



IKM 2015

Weimar, July 20 - 22

20th International Conference on the Applications of Computer Science and Mathematics
in Architecture and Civil Engineering

digital PROCEEDINGS

Proceedings of the 20th International Conference on the
Applications of Computer Science and Mathematics in
Architecture and Civil Engineering

Weimar, July 20-22, 2015

ISSN 1611-4086

Editors: K. Gürlebeck, T. Lahmer

Contents

<u>Zainab Al-Yasiri</u> On boundary value problems for p-Laplace and p-Dirac equations	1
<u>Muyiwa Alalade, Binod Kafle, Frank Wuttke, Tom Lahmer</u> Calibration of cyclic constitutive models for soils by oscillating functions	9
<u>Abd Albasset Almamou, Thomas Gebhardt, Sebastian Bock, Jörg Hildebrand, Willfried Schwarz</u> Quality control of constructed models using 3D point clouds	15
<u>Andrey Volkov, Heiko Kirschke, Pavel Chelyshkov, Artem Sedov, Denis Lysenko</u> The criteria's set with invariant design building elements on the base of three imputations: "convenience", "safety" and "energy-efficiency"	24
<u>Milton dos Santos Ferreira, Nelson Felipe Loureiro Vieira</u> Eigenfunctions and fundamental solutions for the fractional Laplacian in 3 dimensions	30
<u>Luise Goebel, Andrea Osburg, Tom Lahmer</u> Study of analytical models of the mechanical behaviour of polymer-modified concrete	36
<u>Yuri Grigor'ev</u> Regular quaternionic functions and their applications	45
<u>Veronika Hartmann, Kay Smarsly, Tom Lahmer</u> Robust scheduling in construction engineering	51
<u>Raoul Hölter, Elham Mahmoudi, Tom Schanz</u> Optimal sensor location for parameter identification in soft clay	56
<u>Angela Hommel, Klaus Gürlebeck</u> The relationship between linear elasticity theory and complex function theory studied on the basis of finite differences	62
<u>Elena Ignatova, Heiko Kirschke, Eike Tauscher, Kay Smarsly</u> Parametric geometric modeling in construction planning using industry foundation classes	68

<u>Katrin Jahr, Robert Schlich, Kosmas Dragos, Kay Smarsly</u>	76
Decentralized autonomous fault detection in wireless structural health monitoring systems using structural response data	
<u>Zouhour Jaouadi, Tom Lahmer</u>	84
Topology optimization of structures subjected to multiple load cases by introducing the Epsilon constraint method	
<u>Ghada Karaki</u>	91
Selection and scaling of ground motion records for seismic analysis using an optimization algorithm	
<u>Igor Kavrakov, Hans-Georg Timmler, Guido Morgenthal</u>	98
Structural optimization using the energy method with integral material behaviour	
<u>Jens Kersten, Volker Rodehorst</u>	104
Towards stereo vision- and laser scanner-based UAS pose estimation	
<u>Reza Khosravian, Frank Wuttke</u>	111
Qualitative investigation of the effect of soil modeling approach on dynamic behavior of a small-scale 2-DOF structure with pile foundation	
<u>Dmitrii Viktorovich Khristich, Yuri Vladimirovich Astapov</u>	117
Variational posing and solution of coupled thermomechanical problems in a reference configuration	
<u>Rolf Sören Kraußhar, Regina de Almeida</u>	123
Fundamentals of a Wiman Valiron theory for polynomogenic functions	
<u>Nuno Lopes, Daniela Rodrigues, Paulo Vila Real</u>	129
Analysis of steel structural members in fire with slender cross-sections through beam finite elements applying an effective constitutive law	
<u>Joaquim Miguel Macedo, Agostinho Benta, Luís Picado-Santos</u>	135
Use of microsimulation in the adaptation to Portugal of the HCM 2000 methodology for basic freeway segments	
<u>Jörg Meier, Tom Schanz</u>	142
Benchmarking of optimization algorithms	
<u>Michal Musial</u>	148
The influence of cracks and overestimation errors on the deflection of the reinforced concrete beams in the rigid finite element method	

<u>Abdur Rehman Nasir</u> , Hans-Joachim Bargstädt Ameliorating employability in construction through BIM innovation	154
<u>Long Nguyen-Tuan</u> , Tom Lahmer, Maria Datcheva, Eugenia Stoimenova, Tom Schanz Parameter identification applying in complex thermo-hydro-mechanical problems like the design of buffer elements	160
<u>Volker Rodehorst</u> Evaluation of the metric trifocal tensor for relative three-view orientation	166
<u>M. Manuela Rodrigues</u> Operational properties of the Laguerre transform	173
<u>Markus Stokmaier</u> , A.G. Class, T. Schulenberg, R.T. Lahey Jr. Optimizing acoustic resonators for sonofusion experiments with evolutionary algorithms	178
<u>Fengjie Tan</u> , Tom Lahmer, Manju Gyaraganahalll Siddappa Section optimization and reliability analysis of arch-type dams including coupled mechanical-thermal and hydraulic fields	186
<u>Hans-Joachim Bargstädt</u> , Rina Sari Tarigan Rule based expansion of standard construction processes	194
<u>Kay Smarsly</u> , <u>Eike Tauscher</u> IFC-based monitoring information modeling for data management in structural health monitoring	200
<u>Iuliia Vasileva</u> The problem of partial reinforcing an interface crack edge by a rigid patch plate under in-plane and antiplane loads	207
<u>Nelson Vieira</u> Some results in fractional Clifford analysis	212
<u>Jens Wiggenbrock</u> , Kay Smarsly A generic framework supporting distributed computing in engineering applications	218

ON BOUNDARY VALUE PROBLEMS FOR P -LAPLACE AND P -DIRAC EQUATIONS

Z. R. Al-Yasiri*, K. Gürlebeck

**Al-Nahrain University, Baghdad, Iraq. Bauhaus-Universität Weimar, Germany*
E-mail: zainab.al-yasiri@uni-weimar.de, zainab_math_comp@yahoo.com

Keywords: Clifford analysis, p -Dirac equation, p -Laplace equation.

Abstract. *The p -Laplace equation is a nonlinear generalization of the Laplace equation. This generalization is often used as a model problem for special types of nonlinearities. The p -Laplace equation can be seen as a bridge between very general nonlinear equations and the linear Laplace equation. The aim of this paper is to solve the p -Laplace equation for $2 < p < 3$ and to find strong solutions. The idea is to apply a hypercomplex integral operator and spatial function theoretic methods to transform the p -Laplace equation into the p -Dirac equation. This equation will be solved iteratively by using a fixed point theorem.*

1 INTRODUCTION

Monogenic functions are defined as null-solutions of a generalized Cauchy-Riemann system or of a Dirac equation. In this sense the theory of monogenic functions has to be seen as a generalization of the complex function theory (of holomorphic functions). Indeed, monogenic functions share a lot of properties with holomorphic functions [9]. First applications to boundary value problems were considered in [10] in 1990. Based on an operator theoretical approach elliptic boundary value problems could be studied (existence, uniqueness, regularity and integral representations). Recently this approach has been extended to parabolic and (partially) to the treatment of hyperbolic equations. In [11] one can find a lot of integral representation formulas for the solutions to elliptic boundary value problems. Some nonlinear cases like the Navier-Stokes equations and similar equations, containing nonlinearities of the type $u \cdot \text{grad } u$ or u^2 could be also treated by this concept. When looking at more general nonlinear problems one of most important problems is the p -Laplace equation. There has been a surge of interest in the p -Laplacian in many different contexts, from game theory to mechanics, image processing and non-newtonian fluids. There are many unsettled existence, uniqueness and regularity issues. Currently there are many works proposing weak solutions of the p -Laplace equation [1], [2], [3], [5], [6], [7], [8]. This is strongly related to the fact that the p -Laplace equation can be introduced by minimizing the p -Dirichlet integral $\int_{\Omega} |\text{grad } u|^p dx$. This explains on the one hand a lot of similar properties of the solutions, compared with harmonic functions and on the other hand it seems to be natural to apply variational methods for the solution. Due to the fact that the p -Laplace equation degenerates at the zeros of u or will have singularities, depending on p , there are not so many works on strong solutions of the p -Laplace equation. One idea for the treatment of the p -Laplace equation is its transformation into a p -Dirac equation. This leads to the question to generalize the problem to the p -Laplace or the p -Dirac equation for vector-valued functions. The idea behind is that for equations for vector-valued functions often function theoretic methods can be applied. The study of such equations in the Clifford analysis framework began with C. A. Nolder and J. Ryan. They introduced non-linear Dirac operators in \mathbb{R}^N , associated to the p -Laplace equation [14]. The regularity of the p -Laplace equation in the plane has been studied for $p \geq 2$, by E. Lindgren and P. Lindqvist [12]. The infinite Dirac operator has been defined and some of its key properties have been explored by T. Bieske and J. Ryan [4]. P. Lindqvist published several surveys on the p -Laplace equation (see e.g. [13]). We will solve the p -Laplace equation for $2 < p < 3$ and search for strong solutions. The new strategy is to apply a generalized Teodorescu transform to the p -Laplace equation and to transform it into a p -Dirac equation by applying ideas from Clifford analysis. The obtained p -Dirac equation will be solved iteratively by using Banach's fixed point theorem.

2 PRELIMINARIES

Mostly, the p -Poisson equation is studied in the form

$$\Delta_p u = \text{div}(|\nabla u|^{p-2} \nabla u) = f,$$

where u and f are scalar-valued functions, defined in a domain $G \subset \mathbb{R}^N$, $N \geq 1$ with sufficiently smooth boundary ∂G and $1 \leq p \leq \infty$. If $f = 0$ then the equation is called p -Laplace equation. Substituting $w := \nabla u$, the p -Dirac equation will be obtained

$$\text{div}(|w|^{p-2} w) = f. \tag{1}$$

Here w is a vector-valued function. This leads to the idea to work from the very beginning with vector-valued functions u . Replacing the application of the divergence operator and the gradient by the application of a generalized Dirac operator one obtains a p -Laplace (Poisson) equation for vector-valued functions and a corresponding p -Dirac equation. The p -Poisson and the p -Dirac equation will be studied in the scale of Sobolev spaces. The structure of the differential equations shows that some knowledge about the regularity of powers and products of functions belonging to certain Sobolev spaces is necessary. For the values $2 < p < 3$ the Sobolev spaces do not form an algebra and these questions must be studied in detail. Consider $m \geq 0$ and

$p \geq 1$. The norm $\|\cdot\|_{m,p}$ is defined by $\|u\|_{m,p} = \left(\sum_{|\alpha| \leq m} \|\partial^\alpha u\|_{0,p}^p \right)^{1,p}$, where $\|\cdot\|_{0,p}$ is the usual norm of $L_p(G)$.

Let $N \geq 1$ and an orthonormal basis e_0, e_1, \dots, e_N of \mathbb{R}^{N+1} generates the Clifford algebra $\mathcal{Cl}_{0,N}$. For more information we refer to [11]. We recall some basic facts and formulae from spatial function theory:

- A Dirac-type operator is defined by

$$Du = \sum_{i=1}^N e_i \frac{\partial}{\partial x_i} u.$$

The solutions of $Du = 0$ will be called \mathcal{Cl} -holomorphic functions.

- The Teodorescu transform over G is defined by

$$(T_G u)(x) = - \int_G \mathbf{e}(x-y) u(y) dy,$$

with the Cauchy kernel $\mathbf{e}(x) = \frac{1}{\sigma_N} \frac{\bar{\omega}(x)}{|x|^{N-1}}$, $\omega(x) = \frac{x}{|x|}$, $x = \sum_{i=1}^N x_i e_i$. Here σ_N denotes the surface area of the unit ball in \mathbb{R}^N . The Teodorescu transform is a weakly singular operator and the most important algebraic property is that it is a right inverse of the Dirac operator D .

- The Cauchy-Bitsadze operator or Cauchy-Fueter operator is given by

$$(F_\Gamma u)(x) = \int_\Gamma \mathbf{e}(x-y) \alpha(y) u(y) d\Gamma_y,$$

where α stands for the outward pointing unit normal vector at $y \in \Gamma$. A sufficient smoothness of the boundary $\Gamma = \partial G$ has to be assumed.

- The identity I , the Cauchy operator F , the Dirac operator D and its right inverse T are connected through the Borel-Pompeiu formula

$$F_\Gamma u + T_G Du = u,$$

where u is an arbitrary sufficiently smooth function. If u is a \mathcal{Cl} -holomorphic function it means that $F_\Gamma u = u$ and the Cauchy integral reconstructs the \mathcal{Cl} -holomorphic function from its boundary values.

3 THE MAIN RESULT

We will use Banach's fixed-point theorem for proving existence and uniqueness of solutions to the p -Dirac equation. Consider a (Neumann-type) boundary value problem for the p -Poisson equation and rewrite it in terms of the Dirac operator D

$$\Delta_p u = D (|Du|^{p-2} Du) = f \quad \text{in } G, \quad (2)$$

$$Du = 0 \quad \text{on } \Gamma. \quad (3)$$

Let $u \in W^{1,p}(G)$, $1 < p < \infty$. Note that $D^2 = -\Delta$ is the Laplacian in \mathbb{R}^N . Substituting Du by w we obtain the p -Dirac equation

$$D (|w|^{p-2} w) = f. \quad (4)$$

Let G be a bounded domain with smooth boundary $\partial G = \Gamma$ in \mathbb{R}^N , $N \geq 3$. We search for $w \in L_p(G)$, $2 < p < 3$, satisfying

$$D (|w|^{p-2} w) = f \quad \text{in } G \quad (5)$$

$$w = 0 \quad \text{on } \partial G. \quad (6)$$

We assume additionally

$$f \in L_{\tilde{p}}(G) \cap L_q^{loc}(G), \text{ with } \tilde{p} = \frac{p}{p-1}, q > N \text{ and } \text{tr}_\Gamma T_G f = 0.$$

The condition $q > N$ is needed for technical reasons because it guarantees that $T_G f \in C(G)$. We can now apply the operator T_G to equation (5), resulting in

$$T_G(D(|w|^{p-2} w)) = T_G f.$$

By applying the Borel-Pompeiu formula we have

$$T_G(D(|w|^{p-2} w)) = |w|^{p-2} w - F_\Gamma(|w|^{p-2} w) = T_G f.$$

From the boundary condition $w|_\Gamma = 0$ one obtains $F_\Gamma(|w|^{p-2} w) = 0$. Then we have

$$|w|^{p-2} w = T_G f.$$

From now on we assume that $|w|^{p-2} \neq 0$ in G . Dividing the previous equation by $|w|^{p-2}$ we obtain the equation

$$w = \frac{T_G f}{|w|^{p-2}}. \quad (7)$$

This equation will be iterated. Starting from an initial guess w_0 we define for $n = 1, 2, \dots$

$$w_n = \frac{T_G f}{|w_{n-1}|^{p-2}}. \quad (8)$$

We consider the subsequence with even indices and introduce $w_0 = g_0$, $w_2 = g_1$, ..., and $w_{2n} = g_n$. In terms of g_n we get finally the equations

$$g_n = \frac{T_G f}{|T_G f|^{p-2}} |g_{n-1}|^{(p-2)^2}, n = 1, 2, \dots \quad (9)$$

Taking the modulus on both sides of equation (9), one obtains

$$|g_n| = |T_G f|^{3-p} |g_{n-1}|^{(p-2)^2}. \quad (10)$$

We can express all g_n by using only g_0 as follows:

$$g_n = T_G f |T_G f|^{\sum_{k=0}^{n-2} (1-(p-2))(p-2)^{2(k+1)} - (p-2)} |g_0|^{(p-2)^{2n}}.$$

It can be seen from the properties of $T_G f$ that $g_n = w_{2n}$ satisfies the boundary condition if g_0 satisfies it. We study at first the mapping properties of the mapping defined by equation (10). Because of our basic assumption for the right hand side $f \in L_{\tilde{p}}(G)$, where $\tilde{p} = \frac{p}{p-1}$, we can conclude that $T_G f \in W^{1, \tilde{p}}(G)$. For a detailed description of the mapping properties of T we refer to [11]. For the purpose of the paper we need the property $T : W^{p, m}(G) \mapsto W^{p, m+1}(G)$. With the results from [16] we obtain that $|T_G f|^{3-p} \in W^{1, \frac{\tilde{p}}{3-p}}(G)$.

We know that $|g_{n-1}|^{(p-2)^2} \in L_{\frac{p}{(p-2)^2}}(G)$. Using a theorem on products of functions belonging to certain Sobolev spaces (see [15]), we conclude that $|T_G f|^{3-p} |g|^{(p-2)^2} \in L_r(G)$, for $p < r < \frac{Np}{N-p}$. By using embedding theorems we have $L_r(G) \subset L_p(G)$. All together means $g_n \in L_p(G)$, where $2 < p < 3$.

Now, we are ready to study the iteration procedure. To avoid zeros of the iterates in G let us assume that the initial guess satisfies $k_1 |T_G f(x)|^{\frac{3-p}{1-(p-2)^2}} \leq |g_0(x)| \leq |T_G f(x)|^{\frac{3-p}{1-(p-2)^2}}$, for all $x \in G$ with $0 < k_1 < 1$.

Suppose that $|g_k(x)| \leq |T_G f(x)|^{\frac{3-p}{1-(p-2)^2}}$ for $k = 0, \dots, n-1$ and we prove that it holds also for $k = n$. Recalling equation (10) for $k = n$ and substituting $|g_{k-1}(x)| \leq |T_G f(x)|^{\frac{3-p}{1-(p-2)^2}}$ we obtain

$$|g_k(x)| \leq |T_G f(x)|^{3-p} \left(|T_G f(x)|^{\frac{3-p}{1-(p-2)^2} \right)^{(p-2)^2} = |T_G f(x)|^{3-p} |T_G f(x)|^{\frac{(3-p)(p-2)^2}{1-(p-2)^2}}.$$

This proves that for all n

$$|g_n(x)| \leq |T_G f(x)|^{\frac{3-p}{1-(p-2)^2}}. \quad (11)$$

Taking the L_p norm in (11) leads to

$$\|g_n\|_{0,p} \leq \left\| |T_G f|^{\frac{3-p}{1-(p-2)^2}} \right\|_{0,p}. \quad (12)$$

Then the sequence of iterations w_{2n} or g_n is bounded from above by $|T_G f|^{\frac{3-p}{1-(p-2)^2}}$. This bound depends only on p and f .

Additionally, it can be shown that the sequence $|g_n(x)|$ is increasing for all $x \in G$. Recalling equation (11) and taking the $(1 - (p-2)^2)$ -th power on both sides we get $|g_{n-1}|^{1-(p-2)^2} \leq |T_G f|^{3-p}$.

Multiplying both sides of our inequality by $|g_{n-1}|^{(p-2)^2}$ results in

$$|g_{n-1}|^{1-(p-2)^2} |g_{n-1}|^{(p-2)^2} \leq |T_G f|^{3-p} |g_{n-1}|^{(p-2)^2}.$$

This means for all n and $2 < p < 3$, we have proved

$$|g_{n-1}| \leq |g_n|. \quad (13)$$

By taking the L_p norm in inequality (13) we get that also that the sequence of the norms of w_{2n} or g_n is an increasing sequence

$$\|g_{n-1}\|_{0,p} \leq \|g_n\|_{0,p}. \quad (14)$$

We study now the contractivity of the mapping we will collect all obtained estimates for $2 < p < 3$. We have

$$g_n = \frac{T_G f}{|T_G f|^{p-2}} |g_{n-1}|^{(p-2)^2}, |g_{n-1}| \leq |g_n| \leq |T_G f|^{\frac{3-p}{1-(p-2)^2}}, \|g_{n-1}\|_{0,p} \leq \|g_n\|_{0,p} \leq \left\| |T_G f|^{\frac{3-p}{1-(p-2)^2}} \right\|_{0,p}.$$

Now we can conclude that

$$|g_n - g_{n-1}| = \left| \frac{T_G f}{|T_G f|^{p-2}} \left(|g_{n-1}|^{(p-2)^2} - |g_{n-2}|^{(p-2)^2} \right) \right| \leq |T_G f|^{3-p} \left| |g_{n-1}|^{(p-2)^2} - |g_{n-2}|^{(p-2)^2} \right|. \quad (15)$$

Consider the function $y(s) = s^{(p-2)^2}$ for $s > 0$. Fix $x \in G$ and apply the mean value theorem to $y(|g_{n-1}(x)|) = |g_{n-1}(x)|^{(p-2)^2}$ and $y(|g_{n-2}(x)|) = |g_{n-2}(x)|^{(p-2)^2}$. With $|\zeta| \in [|g_{n-2}(x)|, |g_{n-1}(x)|]$, and $|y'(|\zeta|)| = \frac{(p-2)^2}{|\zeta|^{1-(p-2)^2}}$ we have

$$\left| |g_{n-1}(x)|^{(p-2)^2} - |g_{n-2}(x)|^{(p-2)^2} \right| = \frac{(p-2)^2}{|\zeta|^{1-(p-2)^2}} \left| |g_{n-1}(x)| - |g_{n-2}(x)| \right|.$$

We use $|\zeta| \in [|g_{n-2}(x)|, |g_{n-1}(x)|]$, $|g_{n-2}(x)| \leq |g_{n-1}(x)|$ and $|g_0| \geq k_1 |T_G f|^{\frac{3-p}{1-(p-2)^2}}$. Then

$$|\zeta|^{1-(p-2)^2} \geq |g_{n-2}|^{1-(p-2)^2} \geq |g_0|^{1-(p-2)^2} \geq k_1^{1-(p-2)^2} |T_G f|^{3-p}.$$

Then we have

$$\frac{1}{|\zeta|^{1-(p-2)^2}} \leq \frac{1}{|g_0|^{1-(p-2)^2}} \leq \frac{1}{k_1^{1-(p-2)^2} |T_G f|^{3-p}}.$$

By substituting the latter estimates in equation (15) one obtains

$$|g_n - g_{n-1}| \leq \frac{(p-2)^2 |T_G f|^{3-p}}{k_1^{1-(p-2)^2} |T_G f|^{3-p}} \left| |g_{n-1}| - |g_{n-2}| \right| \leq \frac{(p-2)^2}{k_1^{1-(p-2)^2}} |g_{n-1} - g_{n-2}|. \quad (16)$$

It has been shown that with $c_1 = \frac{(p-2)^2}{k_1^{1-(p-2)^2}}$

$$|g_n - g_{n-1}| \leq c_1 |g_{n-1} - g_{n-2}|. \quad (17)$$

The last step is to take the L_p norm in the inequality (17). We obtain

$$\|g_n - g_{n-1}\|_{0,p} \leq c_1 \|g_{n-1} - g_{n-2}\|_{0,p}.$$

That means we have proved for $k_1 > (p-2)^{\frac{2}{1-(p-2)^2}}$, dependent on $p \in (2, 3)$ there is contractivity coefficient $c_1 < 1$. All conditions for the application of Banach's fixed-point theorem are now fulfilled.

Before we are going to state the next theorem, remember that the formula for g_n is given by $g_0 = w_0, g_1 = w_2, \dots, g_n = w_{2n}$. That means we state the theorem in terms of w_{2n} .

Theorem 1 *Let G be a bounded domain with smooth boundary $\partial G = \Gamma$ in \mathbb{R}^N , $N \geq 3$. Let $f \in L_{\tilde{p}}(G) \cap L_q^{loc}(G)$, with $\tilde{p} = \frac{p}{p-1}$, $q > N$, $\text{tr}_\Gamma T_G f = 0$ and $2 < p < 3$. Then the boundary value problem*

$$D(|w|^{p-2}w) = f \quad \text{in } G \quad (18)$$

$$w = 0 \quad \text{on } \partial G = \Gamma, \quad (19)$$

has a unique solution $w \in L_p(G)$. Under the condition

$$k_1 |T_G f|^{\frac{3-p}{1-(p-2)^2}} \leq |w_0(x)| \leq |T_G f|^{\frac{3-p}{1-(p-2)^2}},$$

with $(p-2)^{\frac{2}{1-(p-2)^2}} < k_1 < 1$ the sequence defined by $w_{2n} = \frac{T_G f}{|T_G f|^{p-2}} |w_{2(n-1)}|^{(p-2)^2}$ for $n \in \mathbb{N} \setminus \{0\}$ converges in $L_p(G)$ to the unique solution.

4 CONCLUSIONS

It could be shown in the paper that the p -Poisson equation with certain Neumann-type boundary conditions can be transferred to a Dirichlet boundary value problem for the p -Dirac equation. Main tool was an operator calculus taken from hypercomplex function theory. The obtained p -Dirac equation could be solved iteratively by a fixed-point iteration. This was possible for all $p \in (2, 3)$ and as an estimate for the contractivity constant the value $c_1 = \frac{(p-2)^2}{k_1^{1-(p-2)^2}}$, for $(p-2)^{\frac{2}{1-(p-2)^2}} < k_1 < 1$ was obtained. These results support the idea to reduce as in the linear case the study of the second order differential equation to two equations of first order, where we can apply function theoretic methods. For the first step, discussed in this paper this is visible. The second task, to calculate u from $Du = w$ and to improve the result on the regularity of the solution has still to be solved.

REFERENCES

- [1] T. Adamowicz: On p -Harmonic Mappings in The Plane. *Nonlinear Anal., Theory Methods Appl., Ser. A, Theory Methods* **71**, No. 1-2, 502-511, 2009.
- [2] T. Adamowicz, A. Björn, J. Björn: Regularity of $p(\cdot)$ -Superharmonic Functions, The Kellogg Property and Semiregular Boundary Points. arXiv:1302.0233, DOI:10.1016/j.anihpc, 2013.
- [3] T. Adamowicz, A. Kalamajska: Maximum Principles and Nonexistence Results For Radial Solutions to Equations Involving p -Laplacian. *Math. Methods Appl. Sci.* **33**, No. 13, 1618-1627, 2010.
- [4] T. Bieske, J. Ryan: The Infinite Dirac Operator. *J. Phys.: Conf. Ser.* 254 012003, 2010.
- [5] P. G. Ciarlet: *Linear and Nonlinear Functional Analysis with Applications*. ISBN 978-1-611972-58-0/hbk. xiv, 832, 2013.

- [6] L. Diening, P. Lindqvist, B. Kawohl: The p -Laplacian Operator and Applications. Mathematisches Forschungsinstitut Oberwolfach, Report No. 08/2013, DOI: 10.4171/OWR, 2013.
- [7] A. Edquist, E. Lindgren: A Two-Phase Obstacle-Type Problem for The p -Laplacian. Calc. Var. Partial Differ. Equ. 35, No. 4, 421-433, 2009.
- [8] A. J. M. Ferreira, E. J. Kansa, G. E. Fasshauer and r, V. M. A. Leitão: Progress on Meshless Methods. Computational Methods in Applied Sciences (Springer) 11, Dordrecht: Springer 2009.
- [9] K. Gürlebeck, K. Habetha, W. Sprößig: Holomorphic Functions in the Plane and n -Dimensional Space. Basel: Birkhäuser 2008.
- [10] K. Gürlebeck, W. Sprößig: Quaternionic Analysis and Elliptic Boundary Value Problems. ISNM. International Series of Numerical Mathematics. 89. Basel: Birkhäuser. 1990.
- [11] K. Gürlebeck, W. Sprößig: Quaternionic and Clifford Calculus for Physicists and Engineers. Mathematical Methods in Practice. Chichester: Wiley. 1997.
- [12] E. Lindgren, P. Lindqvist: Regularity of the p -Poisson Equation in The Plane. Department of Mathematical Sciences, Norwegian University of Science and Technology, NO-7491 Trondheim, Norway, REPORT No. 13, fall. ISSN 1103-467X, 2013/2014.
- [13] P. Lindqvist: Notes on The p -Laplace Equation. Department of Mathematics and Statistics (ISBN 951-39-2586-2/pbk). 80 p. 2006.
- [14] C. A. Nolder, J. Ryan: p -Dirac Operators. Adv. Appl. Clifford Algebr. 19, No. 2, 391-402, 2009.
- [15] M. Reed, B. Simon: Methods of Modern Mathematical Physics. Moskva: Izdatelstvo Mir. 430 p. 1982.
- [16] Z. R. Al-Yasiri, K. Gürlebeck: On a Boundary Value Problem for a p -Dirac Equation. to appear in Mathematical Methods in the Applied Sciences.

CALIBRATION OF CYCLIC CONSTITUTIVE MODELS FOR SOILS BY OSCILLATING FUNCTIONS

M. Alalade*, B. Kafle, F. Wuttke and T. Lahmer

**Bauhaus Universität Weimar
Department of Civil Engineering
E-mail: muyiwa.alalade@uni-weimar.de*

Keywords: Model Parameter Identification, Soil Structure Interaction, Elasto-plastic Model, Unsaturated Soil, Cyclic Loading, Model Calibration, Optimization.

Abstract. *In order to minimize the probability of foundation failure resulting from cyclic action on structures, researchers have developed various constitutive models to simulate the foundation response and soil interaction as a result of these complex cyclic loads. The efficiency and effectiveness of these model is majorly influenced by the cyclic constitutive parameters. Although a lot of research is being carried out on these relatively new models, little or no details exist in literature about the model based identification of the cyclic constitutive parameters. This could be attributed to the difficulties and complexities of the inverse modeling of such complex phenomena. A variety of optimization strategies are available for the solution of the sum of least-squares problems as usually done in the field of model calibration. However for the back analysis (calibration) of the soil response to oscillatory load functions, this paper gives insight into the model calibration challenges and also puts forward a method for the inverse modeling of cyclic loaded foundation response such that high quality solutions are obtained with minimum computational effort. Therefore model responses are produced which adequately describes what would otherwise be experienced in the laboratory or field.*

1 INTRODUCTION

The increased awareness in the impact of cyclic actions from natural and man-made sources on a structure during its lifespan necessitates understanding the complex soil structure interaction during these cyclic loads. The stresses induced by these cyclic loads lead to failure patterns such as flow-type failure (liquefaction), cyclic mobility or plastic strain accumulation. The failure type experienced depends on the initial stress state and degree of stress reversal as observed by [1]. In order to design structures such that the effects of these stresses are minimized, various constitutive models based on different formulations such as –plasticity, elasto-plasticity, hypoplasticity and so on, to describe the soil structure interaction during complex cyclic loading on dry, saturated and unsaturated soils have been developed.

The last three decades heralded the development and extension of many constitutive models some of which includes the elasto-plastic strain hardening law model by [2] for monotonic loads which served as a foundation for many other models such as the model by [3] for cyclic loads and model by [4], [5] for monotonic and cyclic loaded footings on unsaturated soil which takes into account the effect of matric suction on the bearing capacity of the soil as observed by [6]. The models in [3] and [5] for cyclic loading is capable of simulating the foundation response under different loading conditions and soil states. However, the quality of the model's response is strongly influenced by certain constitutive parameters, thus in order to apply the models for the actualization of economical and efficient structural design, we have to bridge the gap between model simulation and experimental response. This is achieved by the calibration and optimization of the models' sensitive 'cyclic constitutive parameters' with experimental results.

The importance of these constitutive models cannot be over-emphasized, especially when considering the ease with which it can be incorporated into finite element software for structural analysis, structural design and structural health monitoring as well, therefore in order to yield reliable model responses an in-depth knowledge on the cyclic parameter behavior is required in addition to selecting an efficient optimization strategy.

2 THEORY

2.1 Mathematical Model

The elasto-plastic strain hardening model proposed by [3] for response to cyclic loading on dry soil is an extension of the model proposed by [2] which was developed for monotonic loading. In order to simulate cyclic loading, the model in [3] permits the formation of plastic strains inside the bounding surface. The magnitude of plastic strains induced is a function of the distance between the stress point and the image point I_p on the bounding surface, the memory parameters (ρ_c and ρ_k) and the cyclic constitutive parameters expressed in the Φ term in Equation 1. The parameters $\Lambda(Q_I)$ and $\frac{\delta g}{\delta Q}(Q_I)$ are calculated on the image point and not on the current stress point as would be the case for monotonic loading

$$dq^{pl} = \Lambda(Q_I) \Phi(\delta, \rho_k) \frac{\delta g}{\delta Q}(Q_I) \quad (1)$$

The Φ term which is a function of δ and ρ_k is a diagonal matrix (Equation 2) which acts as a weighting function during cyclic loading. Larger values of δ leads to small diagonal terms and

also smaller plastic displacements [3]

$$\Phi = \begin{bmatrix} \exp\left(-\left(\varsigma_\eta \sqrt{\frac{\delta}{\xi} + \kappa_\eta \rho_k}\right)\right) & 0 & 0 \\ 0 & \exp\left(-\left(\varsigma_\epsilon \sqrt{\frac{\delta}{\xi} + \kappa_\epsilon \rho_k}\right)\right) & 0 \\ 0 & 0 & \exp\left(-\left(\varsigma_\zeta \sqrt{\frac{\delta}{\xi} + \kappa_\zeta \rho_k}\right)\right) \end{bmatrix} \quad (2)$$

Plastic strain caused by cyclic loading is sensitive to the constitutive parameters ς_i and κ_i (where $i = \eta, \epsilon, \zeta$) in the Φ matrix. These parameters regulate the rate at which shakedown occurs in the model and also the the coupling between the horizontal loading and the corresponding vertical displacement at constant vertical force.

The application of this model to unsaturated soil condition was made possible by its extension in [5] which is expressed in Equation 3 where it was observed according to the findings of [7] and [8] that not only the maximum vertical force (V_m) and the initial soil stiffness (R_0) are sensitive to matric suction but also the cyclic constitutive parameters, thus simulating the response that would be expected for unsaturated soil as compared to dry or saturated soils. This model can be seen in Equation 3. Though similar to Equation 1 the parameters are a function of the matric suction ψ

$$dQ^{pl}(\psi) = \Lambda_I(\psi) \Phi(\delta, \rho_k, \psi) \left(\frac{\delta g(\psi)}{\delta Q(\psi)} \right)_I \quad (3)$$

2.2 Calibration and optimization

The quality of any prognosis depends on the quality of the identified cyclic constitutive parameters. Besides accuracy, efficiency is also an important issue as dynamic non-linear models tend to be complex and time consuming, particularly during calibration. Therefore it was necessary to study the cyclic constitutive parameter dependency using contour lines before selecting an optimization strategy. A strong dependency between some parameters was observed and is expressed in Figure 1. The presence of many valleys (indicating minima) can be traced to the structure of the Φ matrix which has addition operations in each of the diagonal terms as seen in Equation 2. Thus different pairs of cyclic constitutive parameters in each diagonal term in the Φ matrix can yield similar results with regards to model response.

In order to minimize now regularized sum of squared error cost functions, the Nelder-Mead method ([10]), which is heuristic based, deterministic and known to be robust with respect to noisy cost function is applied. The objective function being minimized is the sum of squared error with respect to the vertical cyclic displacement, η [3]

$$C'_f(p) = \sum_i^n (\eta_{(t_i,p)}^{mod} - \eta_{(t_i)}^{exp})^2 + \Gamma \sum_{k=1}^4 (\Psi_{(k)}^0 - \Psi_{(k)}^{mod})^2 \quad (4)$$

where:

- C'_f is the cost function to be minimized

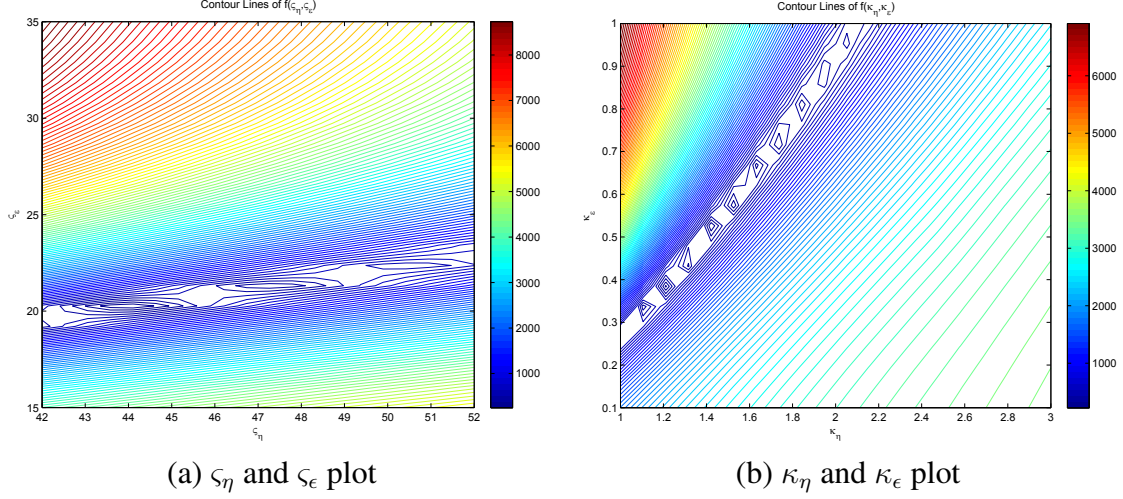


Figure 1: Dependencies between cyclic constitutive parameters [9]

- η^{mod} is the vertical component of the generalized cyclic plastic displacement vector calculated by the model
- η^{exp} is the vertical component of the generalized cyclic plastic displacement vector obtained from the experiment
- p is a vector of $\Lambda_I(\psi)$, $\Phi(\delta, \rho_k, \psi)$ and $\left(\frac{\delta g(\psi)}{\delta Q(\psi)} \right)_I$
- t_i is the time step at each point
- n is the total number of data points
- Γ is a scaling factor for the penalty term
- Ψ^0 is a vector of a priori cyclic constitutive parameters
- Ψ^{mod} is a vector of calculated cyclic constitutive parameters
- k is the total number of cyclic constitutive parameters

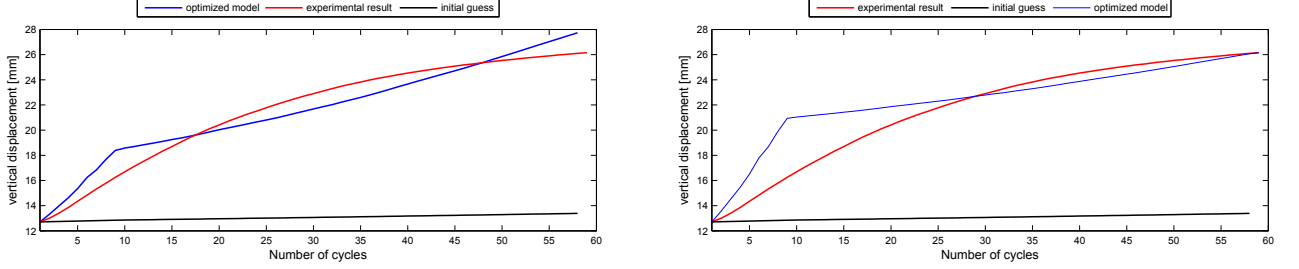
3 RESULTS

Model parameter identification was carried out by calibrating the model to experimental data obtained from [5]. Before the model calibration, it was necessary to filter out measurement errors from the experimental data. The model parameter identification was carried out using the Nelder-Mead algorithm on dry and unsaturated soils, with outcomes shown in Table 1 and Figure 2 to Figure 3.

It is worth noting that as a result of the strong dependency between the cyclic constitutive parameters and the application of a deterministic local optimization strategy, the values used to initiate the optimization plays a major role in the computational time required and the quality of the output result obtained. Although values from literature (values published in [11]) were first used to initiate the optimization process, the quality of fit was not satisfactory, thus other randomly generated values were used as initial values until a best fit was attained.

Table 1: Parameters obtained after model optimization with and without regularization

State	ψ [kPa]	V_m [kN]	R_0 [kN/mm]	ζ_η	κ_η	ζ_ϵ	κ_ϵ	F.value	Iter.
Sat. ($\Gamma = 0$)	0	1.12	0.252	54.3857	0.3435	-59.3968	74.9093	50.77	482
Sat. ($\Gamma \neq 0$)	0	1.12	0.252	52.2103	0.1825	27	55	47.11	328
Unsat. ($\Gamma = 0$)	2.1	6.4	0.822	7.1696	3.3187	12.9429	109.6090	1.143	121



(a) accumulated plastic displacement plot ($\Gamma = 0$) (b) accumulated plastic displacement plot ($\Gamma \neq 0$)

Figure 2: Comparison between non-regularized and regularized optimized model response for saturated soil

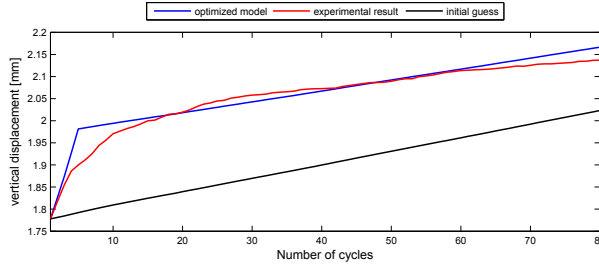


Figure 3: Comparison between the initial model response, experimental response and optimized model response for unsaturated soil

4 CONCLUSION

As observed in Figure 2 and Figure 3 and also corroborated in literature, the unsaturated soil yields lower plastic displacements when compared to other soil states, in addition to this and with respect identifying the model parameters it can be concluded that

- Measurement error (noise) affects quality of fit during calibration and thus have to be filtered out before parameter identification
- The initial guess is a key factor in determining the outcome (quality of parameters obtained) and efficiency of the the inverse modeling computation.
- Though the Nelder–Mead algorithm may converge to a local minima, the process of using random initial values and comparing the quality of fit shows the application of this algorithm to find the global minima with a high probability.
- Better quality fit was observed for unsaturated soil condition with minimal computational effort. This can be attributed to the fact that shakedown occurs earlier and as such the effect of the slight reduction in the accumulated plastic displacement during unloading by soil rebound which the model does not account for is minimized.

- With regularization, calibration yields more reliable results with minimal computational effort for these complex dynamic soil models as seen in Table 1.

REFERENCES

- [1] J Yang and HY Sze. Cyclic strength of sand under sustained shear stress. *Journal of Geotechnical and Geoenvironmental Engineering*, 137(12):1275–1285, 2011.
- [2] R Nova and L Montrasio. Settlements of shallow foundations on sand. *Géotechnique*, 41(2):243–256, 1991.
- [3] Claudio Di Prisco and Clara Zambelli. Cyclic and dynamic mechanical behaviour of granular soils: experimental evidence and constitutive modelling. *Revue française de genie civil*, 7(7-8):881–910, 2003.
- [4] F. Wuttke, B. Kafle, Y. Lins, and T. Schanz. Macroelement for statically loaded shallow strip foundation resting on unsaturated soil. *International Journal of Geomechanics*, 13(5):557–564, 2013.
- [5] B. Kafle and F. Wuttke. Cyclic macroelement for shallow footing over unsaturated soil. pages 521–526, 2013.
- [6] SK Vanapalli, DG Fredlund, DE Pufahl, and AW Clifton. Model for the prediction of shear strength with respect to soil suction. *Canadian Geotechnical Journal*, 33(3):379–392, 1996.
- [7] Sai K. Vanapalli and Fathi M. O. Mohamed. Bearing capacity of model footings in unsaturated soils. In T. Schanz, editor, *Experimental Unsaturated Soil Mechanics*, number 112 in Springer Proceedings in Physics, pages 483–493. Springer Berlin Heidelberg, January 2007.
- [8] T. Schanz, Y. Lins, and S.K. Vanapalli. Bearing capacity of a strip footing on an unsaturated sand. volume 2, pages 1195–1200, 2011.
- [9] Muyiwa Ebenezer Alalade. Extension, calibration and validation of a constitutive model for cyclic loaded shallow footings resting on unsaturated soils. Master’s thesis, Bauhaus Universität Weimar, 2014.
- [10] Saa Singer and John Nelder. Nelder-mead algorithm. *Scholarpedia*, 4(7):2928, 2009.
- [11] C Di Prisco, R Nova, and A Sibilìa. Analysis of soil-structure interaction of towers under cyclic loading. *Proc. NUMOG*, 8:637–642, 2002.

QUALITY CONTROL OF CONSTRUCTED MODELS USING 3D POINT CLOUD

**Abd Albasset Almamou, Thomas Gebhardt, Sebastian Bock, Jörg Hildebrand and
Willfried Schwarz**

Bauhaus-Universität Weimar
Marienstraße 9, 99421 Weimar, Germany
{abd.albasset.almamou, thomas.gebhardt, sebastian.bock, joerg.hildebrand,
willfried.schwarz}@uni-weimar.de

Keywords: Point Cloud Algorithms, Quality Control, Terrestrial Laser Scanning.

Abstract. *Over the last decade, the technology of constructing buildings has been dramatically developed especially with the huge growth of CAD tools that help in modeling buildings, bridges, roads and other construction objects. Often quality control and size accuracy in the factory or on construction site are based on manual measurements of discrete points. These measured points of the realized object or a part of it will be compared with the points of the corresponding CAD model to see whether and where the construction element fits into the respective CAD model. This process is very complicated and difficult even when using modern measuring technology. This is due to the complicated shape of the components, the large amount of manually detected measured data and the high cost of manual processing of measured values. However, by using a modern 3D scanner one gets information of the whole constructed object and one can make a complete comparison against the CAD model. It gives an idea about quality of objects on the whole. In this paper, we present a case study of controlling the quality of measurement during the constructing phase of a steel bridge by using 3D point cloud technology. Preliminary results show that an early detection of mismatching between real element and CAD model could save a lot of time, efforts and obviously expenses.*

1 INTRODUCTION

The tremendous technological advances affect our present social and professional life. This includes machines that have high computational power and software that help people to achieve their tasks quickly and efficiently. From an engineering point of view, this applies to the use of CAD tools that help engineers to model buildings, bridges and other civil engineering structures. The question that comes to the mind is how to check whether the object is produced exactly like the CAD model?

Due to the complexity of some structures such as steel bridges or large industrial plants, is difficult to be combined with the tolerances in the factory and on site (Figure 1). The assembly of large structures made of steel, mainly by welding or bolts, requires observance with relatively small tolerances (in the range of ± 2 mm to ± 5 mm) for components with dimensions of up to several 100 m [1].



(a) In factory



(b) On site

Figure 1: Construction process of a steel bridge

There exists a way to check the accuracy of the comparison process between constructed objects and the modeled CAD object. It uses a Total Station (TS) for manually measuring discrete points, see Figure 2. Later on, the coordinates of the measured points (e.g. corner points) are compared against the respective coordinates of the modeled geometry.

Based on this, one can derive further information of the object, i.e. the distance between measured coordinates to check length, width and height or the absolute position of the coordinates w.r.t. the reference coordinate system, etc.

This way of measuring works well for simple and small construction objects. However, for huge and complicated objects, it can be very inefficient. This is mainly due to the complicated shape of components, the large amount of manually detected measured data, the high cost of manual processing of measured values and the cost of time of the technician who is taking the measurements [2].

A promising method for acquiring the geometry of a 3D object is Terrestrial Laser Scanning (TLS) [3]. By using TLS the complete surface of an object can be measured in short time and with high accuracy [4]. The result of the scanner is generating a cloud of 3D points containing primarily the three dimensional coordinates with additional measuring values, such as the



Figure 2: Quality control by measuring discrete points with total station

reflectance value or the color value of each measured point. There are a lot of concepts to evaluate a 3D point cloud. For instance, this can be done by automated recognition of 3D CAD model objects in the point cloud [5] or by using the Iterative Closest Point (ICP) algorithm to register 3D point cloud against each other or against a CAD model [6, 7]. In our case, CAD model exists, therefore we can immediately use the information of the modeled CAD objects to analyse the scanned data. The gathered scanned data includes information of the geometry (length, width and height), material properties (steel, wood, glass, etc.) or properties of the surface (roughness, reflection, etc.). This paper presents a new strategy of controlling the quality and accuracy of the real geometry by employing 3D laser scanner in collecting data of the constructed objects. This is an alternative method based on the most recent TLS technology of the quality control of large engineering structures that replaces the classical method of measuring discrete points that uses a total station.

2 CONCEPT AND METHODOLOGY

By using TLS the surveyor gathers a big data file of point cloud which describes the surface of an object by a high density of measured 3D points. The distribution of points on the surface depends on the used scan resolution, i.e. the angle increments of the rotating laser. Consequently, there are no directly measured edges or corner points in the data. To get an information about the geometric deviations of the measured object against the target state (CAD model) it is necessary to reconstruct the corner points and edges from the point cloud data. This methodology of measurement which uses TLS is illustrated in the following steps:

2.1 Starting point

At the beginning we have a CAD model and a point cloud that represents the constructed objects from a scanning process with TLS. This point cloud is registered in the coordinate system of CAD model (see [6, 7, 8]) and filtered to remove fake points which come from reflections or multipath effects. The number of 3D scanned points depends on the resolution which is a defined parameter in the scanner, it could be set before starting the scan. It is obvious that the scan resolution plays a vital role in identifying the object as accurate as possible.

2.2 Data representation

Many research and commercial CAD tools are used to deal with point cloud. We are using FreeCAD 0.13 [9]. FreeCAD is an open source parametric 3D modeler. It facilitates modeling and designing CAD objects and it is completely modular. FreeCAD reads and writes many open file formats and runs under all commonly used operating systems. In the first step the user loads CAD model as well as the registered point cloud of the object into the software that uses certain data structure and algorithms. The point cloud is represented by using a data structure called octree [10]. The advantage of using an octree is that the time complexity of building the tree and searching operations in it is efficient. Generally, the time complexity of building the tree is $O(N\log(N))$. Meanwhile, the searching operation requires (for the best case) greater than or equal to $O(\log(N))$. However, this is not an absolute evaluation of Octree performance. The search performance strongly depends on the distribution of points in the point cloud.

2.3 Comparing the scanned object against their CAD model

Once the CAD model is viewed in FreeCAD, the user chooses a geometric primitive which he wants to make a comparison between CAD model and the measured data (point cloud). Currently, this can be a corner point, an edge or a plane or any object. Thereby the selection of the geometric primitive happens on the CAD model. Navigating and working in a 3D point cloud requires a good spatial sense and a good sense of direction. Especially for inexperienced users working in a point cloud is often confusing. Therefore, the engineer is working with CAD which is the technical language he understands. The selection of 3D points to be used and the realization of the comparison are running automatically in the following way: The identification of a corner point or an edge is based on the computation of the intersected planes. The output of intersection could be determined upon to the number of independent planes. i.e. lines (at 2 planes) or points (at 3 planes). With this approach, the algorithm uses the information of all relevant surrounding points of the intersection point or the edge. With the information (coordinates) of the selected part of the CAD model (corner point, edge, or a plane) we search at first for the corresponding planes in the point cloud. To get this, we use adapted bounding box algorithms based on octree data representation of the point cloud [11].

The resulting point cloud subset form the input data set of an Least-Squares Algorithm which computes a plane with its parameters (x, y, z, d) . Calculating plane parameters and their standard deviation is done respectively by [12] along with data snooping [13] to localize and eliminate points that do not belong to the plane. This way is applied for every plane, which is localized by the starting information of the chosen part of CAD model. Finally, the software we developed in FreeCAD for this solution generates a report with information about the reconstructed planes and results of the intersection point(s). From that, the coordinates of a selected corner point can be compared with the corresponding point in the CAD model.

3 CASE STUDY: STEEL BRIDGE

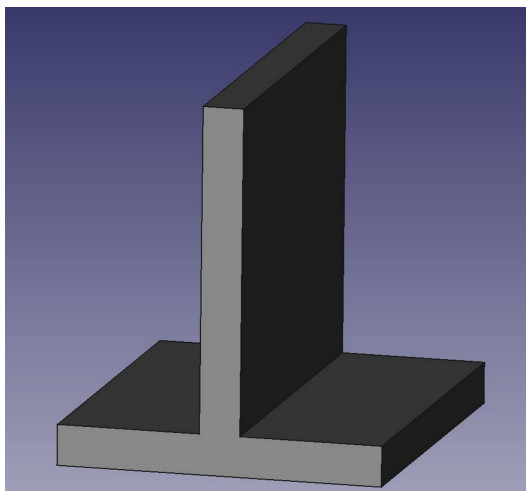
The 3D scanner gives millions of 3D points from different views. For research purposes, we produce a little piece of a steel bridge (T-beam). It is modeled in FreeCAD and scanned with the laser scanner IMAGER 5010 [4]. The T-beam is also measured with a total station, so we have

the real (free of errors) coordinates of the corner points out of it. Figure 3 shows the laboratory setting with the testing object made of steel along with the laser scanner and the total station.

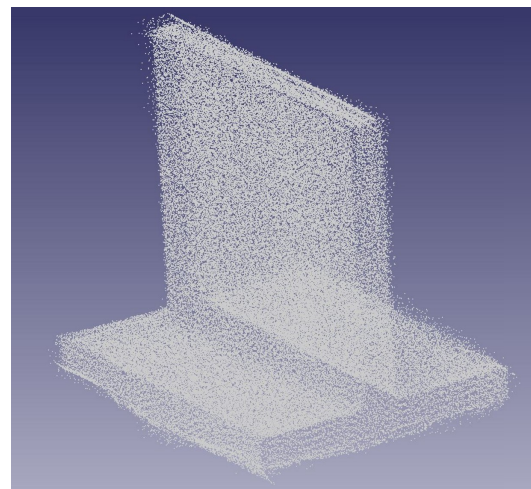


Figure 3: Laboratory setting: T-beam (left), total station (middle) and laser scanner (right)

The modeled T-beam and the scanned point cloud are shown in FreeCAD tool as in figure 4.



(a) CAD model of a T-beam

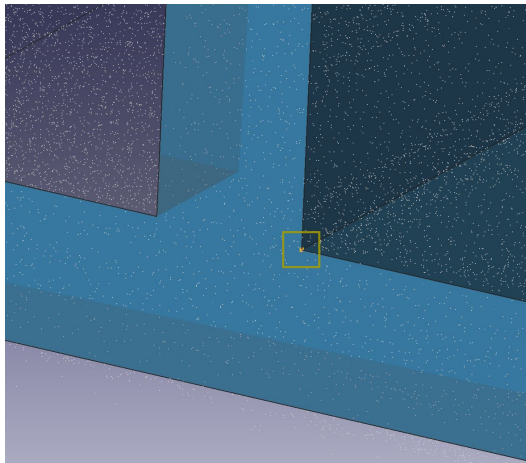


(b) Constructed T-beam out of points cloud

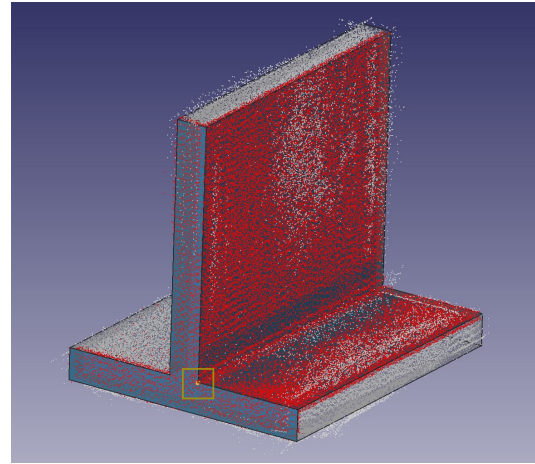
Figure 4: T-beam in CAD and constructed view

The coordinate systems of the CAD model and the scanned objects are identical. To measure the quality of the constructed T-beam, we used a scenario of searching a corner point in the CAD model and compute its corresponding point regarding the mentioned steps in section 2 based on the point cloud.

Figure 5 demonstrates the chosen corner point (yellow box) of the CAD model and the automatically located points of the 3 corresponding planes in red.



(a) Chosen corner point of CAD model



(b) Extracting sub point cloud of the 3 corresponding planes of the corner point

Figure 5: Exemplary chosen corner point

With this subset of points, the calculation algorithm starts. At the end we obtain a report file which includes the parameters of the 3 calculated planes (alternative 2 or 1 plane by choosing an edge or a plane) and the comparison between the calculated (scan based) and modeled (reference) coordinates of the corner point (alternative the comparison between scan based and reference edge or plane). Figure 6 depicts the calculation results of the first plane.

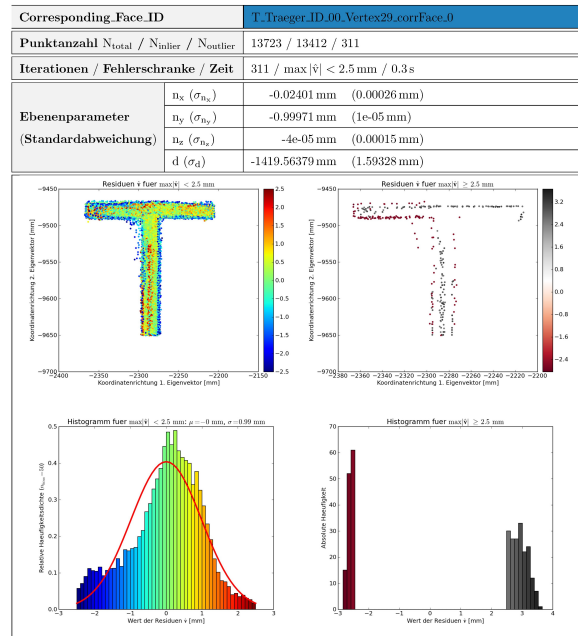


Figure 6: Results of one of the calculated plane (front of T-beam)

Figure 6 contains the most important parameters of the plane fitting, this information is:

- number of points inside (N_{inlier}),

- calculation time,
- parameters of the normal vector (n_x , n_y , n_z and d) and
- their standard deviation (σ_{n_x} , σ_{n_y} , σ_{n_z} and σ_d).

Furthermore, the 4 sub-figures presented in Figure 6 show the distribution of the used and eliminated scanned points. The distribution of the used points is normal and regular and the standard deviation is low, that is why it is a good representation of this plane.

Table 1 shows the results of determining compatibility of the coordinates of the chosen corner point.

		Reference point $P_{CAD}[mm]$	Scan-based point $P_{scan}[mm]$	Δ_{mm}
Point coordinates (Standard deviation)	$x_p(\sigma_{x_p})$	773.25 (-)	774.21 (1.94)	0.96
	$y_p(\sigma_{y_p})$	1356.67 (-)	1357.05 (1.64)	0.38
	$z_p(\sigma_{z_p})$	9511.23 (-)	9511.20 (1.25)	-0.03

Table 1: Coordinates of a corner point from CAD and scan-based calculation

As we see in table 1 that the difference Δ between the coordinates of the reference and calculated scan-based of the studied point P is less than 1 mm. These are very promising results calculated from the algorithms which we are developing. Realistically, these are not optimal results and there are some small errors, these errors could come out of different resources, i.e. the production line, reflections on the steel surface, the coordinate transformation of the point cloud into the reference system (CAD system), etc. This difference is allowed in the construction calculation as it is already taken in consideration. The standard deviations are a bit pessimistic, this is due to the impact of the calculation process.

To check if there are errors coming from the production line, the corner points of the T-beam are measured with a total station with an accuracy of less than 0.1 mm. Table 2 shows the results of the comparison between the scan based and the real coordinates of the chosen corner point.

		Real point $P_{Real}[mm]$	Scan -based point $P_{scan}[mm]$	Δ_{mm}
Point coordinates	x_p	773.86	774.21	0.35
	y_p	1356.78	1357.05	0.27
	z_p	9511.79	9511.20	-0.59

Table 2: Coordinates of a corner point from total station and scan-based calculation

The results shown in table 2 validate the calculation process. The difference Δ between the coordinates is also less than 1 mm. There is no significant serious error coming from the calculation process. The overall number of points we have calculated and compared in this way is 12 points of 2 T-beams. We confirm that more than 80% of the difference values Δ are less than 1 mm.

4 CONCLUSION AND FUTURE WORK

In this paper we have presented a strategy of quality control of constructed models using 3D point clouds. The solution is based on 3D laser scanning. We have shown the work flow of the solution in an applicable way (not mathematics or analytic presentation). The study was conducted with a case study which is an example of how to measure a selected CAD point and its correspondent in the TLS point cloud. The proposed solution demonstrates that it is an efficient and faster way than the traditional one which uses a total station. The advantage of using the laser scanning combined with our application is that the user works only on the CAD model and gather information on the quality of the built object on the whole object. Therefore, the geometry of the object is known from the production line over the construction till the working time.

A rapid detection, comprehensive analysis and reliable evaluation of the construction process is used to improve assembly quality and for reducing essential rework and installation time. In the future and from a perspective view point, we can use it for deformation based monitoring. The measured deformations allow direct determination of injury. To the best of our knowledge, this is the first step of using the information (geometry) of CAD model to evaluate a point cloud of the constructed object. Our another perspective is to continue investigating more searching, selecting and segmentation algorithms that we want to bring to the 3D laser scanning during the real time scan to obtain a better informative point cloud.

REFERENCES

- [1] DIN EN ISO 13920, “General tolerances for welded constructions,” Nov. 1996.
- [2] S. P. Low and H. K. C. Yeo, “A construction quality costs quantifying system for the building industry,” *International Journal of Quality & Reliability Management*, vol. 15, no. 3, pp. 329–349, 1998. [Online]. Available: <http://dx.doi.org/10.1108/02656719810198926>
- [3] H. Wölfelschneider, “Physikalische prinzipien der laserscantechnologie,” in *Terrestrisches Laserscanning (TLS 2009) Yes, we Scan!, DVW-Schriftenreihe, Bd. 60*, F. GOD-HOFF and R. STAIGER, Eds. Wißner.
- [4] “Technical data of laser scanner,” http://www.zf-laser.com/fileadmin/editor/Datenblaetter/Datasheet_Z_F_IMAGER_5010C_E_kompr.pdf, 2012.
- [5] F. Bosché, “Automated recognition of 3d {CAD} model objects in laser scans and calculation of as-built dimensions for dimensional compliance control in construction,” *Advanced Engineering Informatics*, vol. 24, no. 1, pp. 107 – 118, 2010, informatics for cognitive robots. [Online]. Available: <http://www.sciencedirect.com/science/article/pii/S1474034609000482>
- [6] P. J. Besl and N. D. McKay, “A method for registration of 3-d shapes,” *IEEE Trans. Pattern Anal. Mach. Intell.*, vol. 14, no. 2, pp. 239–256, Feb. 1992. [Online]. Available: <http://dx.doi.org/10.1109/34.121791>

- [7] G. Tam, Z.-Q. Cheng, Y.-K. Lai, F. Langbein, Y. Liu, D. Marshall, R. Martin, X.-F. Sun, and P. Rosin, “Registration of 3d point clouds and meshes: A survey from rigid to non-rigid,” *Visualization and Computer Graphics, IEEE Transactions on*, vol. 19, no. 7, pp. 1199–1217, July 2013.
- [8] S. Schuhmacher and J. Böhm, “Georeferencing of terrestrial laserscanner data for applications in architectural modelling,” 2005.
- [9] D. Falck and B. Collette, *FreeCAD*. Packt Publishing, 2012.
- [10] J. Revelles, C. Urena, and M. Lastra, “An efficient parametric algorithm for octree traversal,” in *Journal of WSCG*, 2000, pp. 212–219.
- [11] P. Cloud, “Pcl library,” <http://www.pointclouds.org/>, 2015.
- [12] E. Drixler, *Analyse der Form und Lage von Objekten im Raum*, ser. Deutsche Geodätische Kommission bei der Bayerischen Akademie der Wissenschaften / C: Dissertationen. Beck, 1993. [Online]. Available: <https://books.google.de/books?id=xuE8HAAACAAJ>
- [13] W. Baarda, *A Testing Procedure for Use in Geodetic Networks*, ser. A testing procedure for use in geodetic networks. Netherlands Geodetic Commission, 1968, no. v. 2, no. 5. [Online]. Available: <https://books.google.de/books?id=4Ho-SwAACAAJ>

THE CRITERIA'S SET WITH INVARIANT DESIGN BUILDING ELEMENTS ON THE BASE OF THREE IMPUTATIONS: "CONVENIENCE", "SAFETY" AND "ENERGY-EFFICIENCY"

A. Volkov*, H. Kirschke, P. Chelyshkov, A. Sedov, D. Lysenko

*Moscow State University of Civil Engineering

129337, Russia, Moscow, Yaroslavskoe shosse, 26

E-mail: rector@mgsu.ru

Keywords: energy efficiency, mathematical model, comfort, building automation

Abstract. The paper deals with the formalization of the criteria for constructing building management systems. We consider three criteria - "convenience", "safety" and "energy-efficiency". For each objective proposed method of calculation.

Imputation "Convenience"

«Convenience» - the imputation, characterizing the value degree of conformity to the proposed terms conditions optimal low-rise residential building comfort. The optimality criteria is a complex criteria, containing the characteristics' set . The imputation «Convenience» value depends on the values of comfort characteristics. The comfort characteristics are conditionally abstract objects' parameters, that have a direct or correlation with subjective comfort feeling. The investigated object can contain n comfort points. After that the value of "Convenience" value (K) may be defined as

$$K = \sum_{i=1}^n \left(1 - \frac{|a_i^{opt} - a_i|}{a_i^{opt} + a_i} \right) \quad (1)$$

a_i - the convenience characteristic of investigated object (is measured in actual size);

a_i^{opt} - the optimal investigated object value the convenience characteristic (is measured in actual size);

It is clear, that the convenience concept is subjective and depends on human physiological makers, his/her being in this living quarters. Comfortable conditions for one person could be quite uncomfortable for another one.

Man, being in the room, is exposed by many factors. Consequently, solving the creating problem of a comfortable indoor climate, it is necessary to elaborate such control engineering systems' algorithm, that will take place into account the regulated microclimate parameters' perceptions. In this case the first step is analyzing the effects of individual microclimate parameters and their combinations for person comfort.

Temperature is the most significant indoor climate factor. Aside an obvious effect on the room air temperature, there is a radiant radiation influence. It rises from other room items and from the sun (through the window openings). Thus, it is important to maintain an optimal ratio between the mean radiant and the room air temperatures. Air humidity has a significant impact on most of the processes that may occur in the indoor climate: bacteria, viruses, and dust mites, education fungi infections of the respiratory tract and allergies, intensification of issue of construction materials, peeling dust.

Imputation "Safety"

"Safety" – the imputation based in there components:

- The reliability characteristic of an artificial intelligence system of investigated object S_r
- The engineering security artificial intelligence system characteristic S_e
- Description of the artificial intelligence system protection module S_s

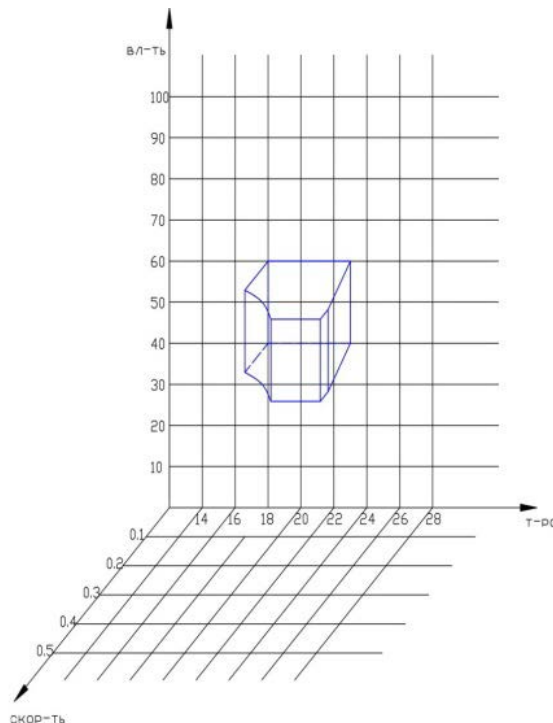


Fig. 1. The optimal comfort conditions space

Thus, the criteria imputation "Safety" is an additive characteristic based on these three components:

$$S = S_r + S_e + S_s \quad (2)$$

Characteristic of artificial intelligence system reliability is analyzed as:

$$S_r = 1 - \frac{|N^{opt} - N|}{N^{opt} + N} \quad (3)$$

N -the abstract investigated object reliability characteristic;

N^{opt} - the optimal value of the abstract investigated object reliability characteristic, defined by the following algorithm.

It is rather easy to determine the reliability of control systems organized on different kind structures. Classic feature of system reliability is the probability of not failure (P). It is calculated as formula (4)

$$P = \frac{N_K}{N_H} \quad (4),$$

where N_H - initial elements' number of the system that is being tested,

N_K - the finite elements' number of the system, remaining be able to work.

For example, the formula for determining the probability of failure-free operation with a decentralized structure will be like (5)

$$P(t) = 1 - \prod_{i=1}^m (1 - P_i) \quad (5)$$

Thus, you can determine the likelihood of a control system with any of the given structures. However, the considered characteristics of reliability not be acceptable for a final decision making on the choice of the particular structure of the control system, because it does not include the criticality of various engineering systems.

To account such heterogeneity influence of various engineering systems on the building possible viability by introducing an abstract characterization of the automatic control systems reliability (N), when it is calculating the probability of non-failure operation of control systems of various engineering systems (P) will be multiplied by the weighting coefficients corresponding criticality of engineering systems.

$$N = 1 - \prod_{i=1}^m (1 - k_i \cdot P_i) \quad (6)$$

Defining the building engineering systems' "weight" seems reasonable to distinguish three characteristics engineering systems: volume of thermal energy consumption (H, GCal), the

volume of electric energy consumption (E, kW) and the number of people (M), whose comfort and effectiveness directly depends on the correctness of the considered systems engineering.

So, abstract weighting criticality factor of engineering systems for offices could be defined by the (7).

$$N = 1 - \prod_{i=1}^m (1 - k_i \cdot P_i) \quad (7)$$

Thus, formalized an abstract characterization of the automatic control systems' reliability and abstract criticality of engineering systems weighting factor. Basing on proposed feature it is possible to determine the optimal look of the automatic building control system structure from the meet the needs of critical engineering systems point of view.

The second characteristic of "Security" is characteristic of engineering security artificial intelligence systems (S_e). That could be defined as:

$$S_e = 1 - \frac{d - d'}{d + d'} \quad (8),$$

d - the unprotected systems risk (cu);

d' - the degree of system risk (cu).

Consider the following description of security systems - a security modules' assessment of the artificial intelligence systems. It is defined as

$$S_S = \sum_{i=1}^m \left(1 - \frac{S_i^{\max} - S_i}{S_i^{\max} + S_i} \right) \quad (9)$$

S_i^{\max} - the largest possible protected sites number of investigated object's consideration module;

S_i - the accepted protected sites number of investigated object's consideration module.

In the system of automation and dispatching of low-rise residential building it is a complex subsystem security that could be divided into subsystems that implement separate functions. Usually there are the following four subsystems in the residential building security system:

- security alarm system;
- fire alarm system;
- access control;
- CCTV.

To save funds of the investor company developing the automation system project it is often provided a consolidated subsystem, for example, security and fire control panels.

Fire alarm system and automatic equipment ensure continuous automatic the system efficiency monitoring by logging events, alarm and their elimination, the determination of the exact address of the fire source and output this information to a display, receiving information about the fire extinguishing system work in the heard of fire.

The most high-tech and science-intensive measure in comprehensive security implementation is monitoring a continuous process of collecting and analyzing information on the value of the object state diagnostic parameters.

Imputation “Energy-efficiency”

Imputation “Energy-efficiency” characterizes the fuel-energy resources and drinking water amount within the low-rise buildings investigation.

$$E = \sum_{i=1}^l \left(1 - \frac{|e'_i - e_i|}{e'_i + e_i} \right) \quad (10)$$

e'_i - the saving volume of the i-th type of the resource (the item of fuel and energy resources and drinking water), implemented by the action of artificial intelligence systems studied buildings, (ton of reference fuel);

e_i - the total consumption volume of the i-th investigated building resource type (the item of fuel and energy resources and water), (ton of reference fuel)..

Under the overall consumption understanding the total volume of savings and volume of total consumption.

The aim of the engineering systems is the required microclimate parameters' maintenance, containing temperature and relative humidity.

REFERENCES

- [1] Volkov A., Sedov A., Chelyshkov P. Usage of building information modelling for evaluation of energy efficiency. Applied Mechanics and Materials Vols. 409-410 (2013) pp 630-633 © (2013) Trans Tech Publications, Switzerland doi:10.4028/www.scientific.net/AMM.409-410.630.
- [2] VolkovAndrey, Sedov Artem, Chelyshkov Pavel, Kulikova Ekaterina Modeling the thermal comfort of internal building spaces in hospital. Applied Mechanics and Materials Vols. 584-586

(2014) pp 753-756 © (2014) Trans Tech Publications, Switzerland
doi:10.4028/www.scientific.net/AMM.584-586.753.

[3] Volkov Andrey, Sedov Artem, Chelyshkov Pavel, Kulikova Ekaterina Modeling the thermal comfort of internal building spaces in kindergarten Applied Mechanics and Materials Vols. 584-586 (2014) pp 757-760 © (2014) Trans Tech Publications, Switzerland
doi:10.4028/www.scientific.net/AMM.584-586.757.

[4] Volkov Andrey, Sedov Artem, Chelyshkov Pavel, Kulikova Ekaterina Modeling the thermal comfort of internal building spaces in school. Applied Mechanics and Materials Vols. 584-586 (2014) pp 761-764 © (2014) Trans Tech Publications, Switzerland
doi:10.4028/www.scientific.net/AMM.584-586.761.

EIGENFUNCTIONS AND FUNDAMENTAL SOLUTIONS FOR THE FRACTIONAL LAPLACIAN IN 3 DIMENSIONS

M. Ferreira^{†,‡}, N. Vieira[‡]

[†] *School of Technology and Management
Polytechnic Institute of Leiria
P-2411-901, Leiria, Portugal.
Email: milton.ferreira@ipleiria.pt*

[‡] CIDMA - Center for Research and Development in Mathematics and Applications
Department of Mathematics, University of Aveiro
Campus Universitário de Santiago, 3810-193 Aveiro, Portugal.
Email: mferreira@ua.pt, nloureirovieira@gmail.com

Keywords: Fractional Laplace operator; Riemann-Liouville fractional derivatives; Eigenfunctions; Fundamental solution; Mittag-Leffler function.

Abstract. *Recently there has been a surge of interest in PDEs involving fractional derivatives in different fields of engineering. In this extended abstract we present some of the results developed in [3]. We compute the fundamental solution for the three-parameter fractional Laplace operator $\Delta^{(\alpha,\beta,\gamma)}$ with $(\alpha, \beta, \gamma) \in]0, 1]^3$ by transforming the eigenfunction equation into an integral equation and applying the method of separation of variables. The obtained solutions are expressed in terms of Mittag-Leffler functions. For more details we refer the interested reader to [3] where it is also presented an operational approach based on the two Laplace transform.*

1 INTRODUCTION

The problems with the fractional Laplacian attracted in the last years a lot of attention, due especially to their large range of applications. The fractional Laplacian appears in probabilistic framework as well as in mathematical finance as infinitesimal generators of the stable Lévy processes [1]. One can find problems involving the fractional Laplacian in mechanics and in elastostatics, for example, a Signorini obstacle problem originating from linear elasticity [2].

The aim of this paper is to present an explicit expression for the family of eigenfunctions and fundamental solutions of the three-parameter fractional Laplace. For the sake of simplicity we restrict ourselves to the three dimensional case, however the results can be generalized for an arbitrary dimension. The two dimensional case was already studied in [10]. Connections between fractional calculus and Clifford analysis were considered recently in [5, 9].

2 PRELIMINARIES

2.1 Fractional calculus and special functions

Let $(D_{a+}^{\alpha} f)(x)$ denote the fractional Riemann-Liouville derivative of order $\alpha > 0$ (see [6])

$$(D_{a+}^{\alpha} f)(x) = \left(\frac{d}{dx}\right)^n \frac{1}{\Gamma(n-\alpha)} \int_a^x \frac{f(t)}{(x-t)^{\alpha-n+1}} dt, \quad n = [\alpha] + 1, \quad a, x > 0. \quad (1)$$

where $[\alpha]$ means the integer part of α . When $0 < \alpha < 1$ then (1) takes the form

$$(D_{a+}^{\alpha} f)(x) = \frac{d}{dx} \frac{1}{\Gamma(1-\alpha)} \int_a^x \frac{f(t)}{(x-t)^{\alpha}} dt. \quad (2)$$

The Riemann-Liouville fractional integral of order $\alpha > 0$ is given by (see [6])

$$(I_{a+}^{\alpha} f)(x) = \frac{1}{\Gamma(\alpha)} \int_a^x \frac{f(t)}{(x-t)^{1-\alpha}} dt, \quad a, x > 0. \quad (3)$$

We recall also the following definition (see [8]):

Definition 2.1 *A function $f \in L_1(a, b)$ has a summable fractional derivatives $(D_{a+}^{\alpha} f)(x)$ if $(I_{a+}^{n-\alpha} f)(x) \in AC^n([a, b])$, where $n = 0, 1, \dots, n-1$ and $AC^n([a, b])$ denote the class of functions $f(x)$, which are continuously differentiable on the segment $[a, b]$ up to order $n-1$ and $f^{(n-1)}(x)$ is absolutely continuous on $[a, b]$.*

If a function f admits a summable fractional derivative, then the composition of (1) and (3) can be written in the form (see [8, Thm. 2.4])

$$(I_{a+}^{\alpha} D_{a+}^{\alpha} f)(x) = f(x) - \sum_{k=0}^{n-1} \frac{(x-a)^{\alpha-k-1}}{\Gamma(\alpha-k)} (I_{a+}^{n-\alpha})^{(n-k-1)}(a), \quad n = [\alpha] + 1. \quad (4)$$

Nevertheless we note that $D_{a+}^{\alpha} I_{a+}^{\alpha} f = f$, for any summable function. This is a particular case of a more general property (cf. [7, (2.114)])

$$D_{a+}^{\alpha} (I_{a+}^{\gamma} f) = D_{a+}^{\alpha-\gamma} f, \quad 0 \leq \gamma \leq \alpha. \quad (5)$$

One important function used in this paper is the two-parameter Mittag-Leffler function $E_{\mu,\nu}(z)$ [4], which is defined in terms of the power series by

$$E_{\mu,\nu}(z) = \sum_{n=0}^{\infty} \frac{z^n}{\Gamma(\mu n + \nu)}, \quad \mu > 0, \nu \in \mathbb{R}, z \in \mathbb{C}. \quad (6)$$

In particular, the function $E_{\mu,\nu}(z)$ is entire of order $\rho = \frac{1}{\mu}$ and type $\sigma = 1$. Two important fractional integral and differential formulae involving the two-parametric Mittag-Leffler function are the following (see [4, p.61,p.87])

$$I_{a^+}^{\alpha} \left((x-a)^{\nu-1} E_{\mu,\nu}(k(x-a)^{\mu}) \right) = (x-a)^{\nu+\alpha-1} E_{\mu,\nu+\alpha}(k(x-a)^{\mu}) \quad (7)$$

$$D_{a^+}^{\alpha} \left((x-a)^{\nu-1} E_{\mu,\nu}(k(x-a)^{\mu}) \right) = (x-a)^{\nu-\alpha-1} E_{\mu,\nu-\alpha}(k(x-a)^{\mu}) \quad (8)$$

for all $\alpha > 0, \mu > 0, \nu \in \mathbb{R}, k \in \mathbb{C}, a > 0, x > a$.

The approach developed in Section 3 leads to the solution of linear Abel integral equations of the second kind.

Theorem 2.2 [4, Thm. 4.2] *Let $f \in L_1[a, b], \alpha > 0$ and $\lambda \in \mathbb{C}$. Then the integral equation*

$$u(x) = f(x) + \frac{\lambda}{\Gamma(\alpha)} \int_a^x (x-t)^{\alpha-1} u(t) dt, \quad x \in [a, b]$$

has a unique solution

$$u(x) = f(x) + \lambda \int_a^x (x-t)^{\alpha-1} E_{\alpha,\alpha}(\lambda(x-t)^{\alpha}) f(t) dt. \quad (9)$$

3 EIGENFUNCTIONS AND FUNDAMENTAL SOLUTION OF THE FRACTIONAL LAPLACE OPERATOR

Consider the eigenfunction equation for the fractional Laplace operator $\Delta^{(\alpha,\beta,\gamma)}$

$$\begin{aligned} & \Delta^{(\alpha,\beta,\gamma)} u(x, y, z) = \lambda u(x, y, z) \\ \Leftrightarrow & \left(D_{x_0^+}^{1+\alpha} u \right) (x, y, z) + \left(D_{y_0^+}^{1+\beta} u \right) (x, y, z) + \left(D_{z_0^+}^{1+\gamma} u \right) (x, y, z) = \lambda u(x, y, z). \end{aligned} \quad (10)$$

where $\lambda \in \mathbb{C}, (\alpha, \beta, \gamma) \in]0, 1]^3, (x, y, z) \in \Omega = [x_0, X_0] \times [y_0, Y_0] \times [z_0, Z_0], x_0, y_0, z_0 \geq 0, X_0, Y_0, Z_0 < \infty$, and $u(x, y, z)$ admits summable fractional derivatives $D_{x_0^+}^{1+\alpha}, D_{y_0^+}^{1+\beta}, D_{z_0^+}^{1+\gamma}$.

Applying the fractional integral operators $I_{x_0^+}^{1+\alpha}, I_{y_0^+}^{1+\beta}$ and $I_{z_0^+}^{1+\gamma}$ from both sides of (10), taking into account (4) and using Fubini's Theorem, we get

$$\begin{aligned} & \left(I_{y_0^+}^{1+\beta} I_{z_0^+}^{1+\gamma} u \right) (x, y, z) + \left(I_{x_0^+}^{1+\alpha} I_{z_0^+}^{1+\gamma} u \right) (x, y, z) \\ & + \left(I_{x_0^+}^{1+\alpha} I_{y_0^+}^{1+\beta} u \right) (x, y, z) - \lambda \left(I_{x_0^+}^{1+\alpha} I_{y_0^+}^{1+\beta} I_{z_0^+}^{1+\gamma} u \right) (x, y, z) \\ & = \frac{(x-x_0)^{\alpha-1}}{\Gamma(\alpha)} \left(I_{y_0^+}^{1+\beta} I_{z_0^+}^{1+\gamma} f_0 \right) (y, z) + \frac{(x-x_0)^{\alpha}}{\Gamma(1+\alpha)} \left(I_{y_0^+}^{1+\beta} I_{z_0^+}^{1+\gamma} f_1 \right) (y, z) \\ & + \frac{(y-y_0)^{\beta-1}}{\Gamma(\beta)} \left(I_{x_0^+}^{1+\alpha} I_{z_0^+}^{1+\gamma} h_0 \right) (x, z) + \frac{(y-y_0)^{\beta}}{\Gamma(1+\beta)} \left(I_{x_0^+}^{1+\alpha} I_{z_0^+}^{1+\gamma} h_1 \right) (x, z) \\ & + \frac{(z-z_0)^{\gamma-1}}{\Gamma(\gamma)} \left(I_{x_0^+}^{1+\alpha} I_{y_0^+}^{1+\beta} g_0 \right) (x, y) + \frac{(z-z_0)^{\gamma}}{\Gamma(1+\gamma)} \left(I_{x_0^+}^{1+\alpha} I_{y_0^+}^{1+\beta} g_1 \right) (x, y), \end{aligned} \quad (11)$$

where we denote the Cauchy's fractional integral conditions by

$$f_0(y, z) = \left(I_{x_0^+}^{1-\alpha} u \right) (x_0, y, z), \quad f_1(y, z) = \left(D_{x_0^+}^\alpha u \right) (x_0, y, z), \quad (12)$$

$$h_0(x, z) = \left(I_{y_0^+}^{1-\beta} u \right) (x, y_0, z), \quad h_1(x, z) = \left(D_{y_0^+}^\beta u \right) (x, y_0, z), \quad (13)$$

$$g_0(x, y) = \left(I_{z_0^+}^{1-\gamma} u \right) (x, y, z_0), \quad g_1(x, y) = \left(D_{z_0^+}^\gamma u \right) (x, y, z_0). \quad (14)$$

We now assume that $u(x, y, z) = u_1(x) u_2(y) u_3(z)$. Substituting in (11) and taking into account the initial conditions (12), (13), and (14) we obtain

$$\begin{aligned} & u_1(x) \left(I_{y_0^+}^{1+\beta} u_2(y) I_{z_0^+}^{1+\gamma} u_3(z) \right) + u_2(y) \left(I_{x_0^+}^{1+\alpha} u_1(x) I_{z_0^+}^{1+\gamma} u_3(z) \right) \\ & + u_3(z) \left(I_{x_0^+}^{1+\alpha} u_1(x) I_{y_0^+}^{1+\beta} u_2(y) \right) (x, y, z) - \lambda \left(I_{x_0^+}^{1+\alpha} u_1 \right) (x) \left(I_{y_0^+}^{1+\beta} u_2 \right) (y) \left(I_{z_0^+}^{1+\gamma} u_3 \right) (z) \\ & = a_1 \frac{(x-x_0)^{\alpha-1}}{\Gamma(\alpha)} \left(I_{y_0^+}^{1+\beta} u_2(y) I_{z_0^+}^{1+\gamma} u_3(z) \right) + a_2 \frac{(x-x_0)^\alpha}{\Gamma(1+\alpha)} \left(I_{y_0^+}^{1+\beta} u_2(y) I_{z_0^+}^{1+\gamma} u_3(z) \right) \\ & + b_1 \frac{(y-y_0)^{\beta-1}}{\Gamma(\beta)} \left(I_{x_0^+}^{1+\alpha} u_1(x) I_{z_0^+}^{1+\gamma} u_3(z) \right) + b_2 \frac{(y-y_0)^\beta}{\Gamma(1+\beta)} \left(I_{x_0^+}^{1+\alpha} u_1(x) I_{z_0^+}^{1+\gamma} u_3(z) \right) \\ & + c_1 \frac{(z-z_0)^{\gamma-1}}{\Gamma(\gamma)} \left(I_{x_0^+}^{1+\alpha} u_1(x) I_{y_0^+}^{1+\beta} u_2(y) \right) + c_2 \frac{(z-z_0)^\gamma}{\Gamma(1+\gamma)} \left(I_{x_0^+}^{1+\alpha} u_1(x) I_{y_0^+}^{1+\beta} u_2(y) \right), \quad (15) \end{aligned}$$

where $a_i, b_i, c_i \in \mathbb{C}$, $i = 1, 2$, are constants defined by the initial conditions (12), (13), and (14). Supposing that $\left(I_{x_0^+}^{1+\alpha} u_1 \right) (x) \left(I_{y_0^+}^{1+\beta} u_2 \right) (y) \left(I_{z_0^+}^{1+\gamma} u_3 \right) (z) \neq 0$, for $(x, y, z) \in \Omega$, we can divide (15) by this factor. Separating the variables we get the following three Abel's integral equations of second kind:

$$u_1(x) - \mu \left(I_{x_0^+}^{1+\alpha} u_1 \right) (x) = a_1 \frac{(x-x_0)^{\alpha-1}}{\Gamma(\alpha)} + a_2 \frac{(x-x_0)^\alpha}{\Gamma(1+\alpha)}, \quad (16)$$

$$u_2(y) + \nu \left(I_{y_0^+}^{1+\beta} u_2 \right) (y) = b_1 \frac{(y-y_0)^{\beta-1}}{\Gamma(\beta)} + b_2 \frac{(y-y_0)^\beta}{\Gamma(1+\beta)}, \quad (17)$$

$$u_3(z) + (\mu - \lambda - \nu) \left(I_{z_0^+}^{1+\gamma} u_3 \right) (z) = c_1 \frac{(z-z_0)^{\gamma-1}}{\Gamma(\gamma)} + c_2 \frac{(z-z_0)^\gamma}{\Gamma(1+\gamma)}, \quad (18)$$

where $\lambda, \mu, \nu \in \mathbb{C}$ are constants. We observe that the equality

$$\left(I_{x_0^+}^{1+\alpha} u_1 \right) (x) \left(I_{y_0^+}^{1+\beta} u_2 \right) (y) \left(I_{z_0^+}^{1+\gamma} u_3 \right) (z) = 0,$$

agrees with (15), (16), (17), and (18) for at least one point (ξ, η, θ) . Solving the latter equations using (9) in Theorem 1.2 and after straightforward computations we obtain a family of eigenfunctions.

Theorem 3.1 A family of eigenfunctions of the fractional Laplace operator $\Delta^{(\alpha,\beta,\gamma)}$ is given by $u_{\lambda,\mu,\nu}(x, y, z) = u_1(x) u_2(y) u_3(z)$ with

$$u_1(x) = a_1 (x - x_0)^{\alpha-1} E_{1+\alpha,\alpha} (\mu(x - x_0)^{1+\alpha}) + a_2 (x - x_0)^\alpha E_{1+\alpha,1+\alpha} (\mu(x - x_0)^{1+\alpha}) \quad (19)$$

$$u_2(y) = b_1 (y - y_0)^{\beta-1} E_{1+\beta,\beta} (-\nu(y - y_0)^{1+\beta}) + b_2 (y - y_0)^\beta E_{1+\beta,1+\beta} (-\nu(y - y_0)^{1+\beta}) \quad (20)$$

$$u_3(z) = c_1 (z - z_0)^{\gamma-1} E_{1+\gamma,\gamma} ((\mu - \lambda - \nu)(z - z_0)^{1+\gamma}) + c_2 (z - z_0)^\gamma E_{1+\gamma,1+\gamma} ((\mu - \lambda - \nu)(z - z_0)^{1+\gamma}), \quad (21)$$

where $\lambda, \mu, \nu \in \mathbb{C}$ are constants.

Corollary 3.2 For $\lambda = 0$, $u_{0,\mu,\nu}(x, y, z) = u_1(x) u_2(y) u_3(z)$ is a family of fundamental solutions for the fractional Laplace operator $\Delta^{(\alpha,\beta,\gamma)}$.

Remark 3.3 In the special case of $\alpha = \beta = \gamma = 1$ the functions u_1, u_2 and u_3 take the form:

$$u_1(x) = a_1 \cosh(\sqrt{\mu}(x - x_0)) + \frac{a_2}{\sqrt{\mu}} \sinh(\sqrt{\mu}(x - x_0)),$$

$$u_2(y) = b_1 \cos(\sqrt{\nu}(y - y_0)) + \frac{b_2}{\sqrt{\nu}} \sin(\sqrt{\nu}(y - y_0)),$$

$$u_3(z) = c_1 \cosh\left(\sqrt{\mu - \lambda - \nu}(z - z_0)\right) + \frac{c_2}{\sqrt{\mu - \lambda - \nu}} \sinh\left(\sqrt{\mu - \lambda - \nu}(z - z_0)\right).$$

which are the components of the fundamental solution of the Laplace operator in \mathbb{R}^3 obtained by the method of separation of variables.

It is also possible to apply an operational approach based on the two dimensional Laplace transform to obtain a complete family of eigenfunctions and fundamental solutions for the fractional Laplace operator. This was done in detail in [3].

Acknowledgement: This work was supported by Portuguese funds through the CIDMA - Center for Research and Development in Mathematics and Applications, and the Portuguese Foundation for Science and Technology (“FCT–Fundação para a Ciência e a Tecnologia”), within project UID/MAT/ 0416/2013. N. Vieira was also supported by FCT via the FCT Researcher Program 2014 (Ref: IF/00271/2014).

REFERENCES

- [1] D. Applebaum: Lévy processes: from probability to finance and quantum groups. Notices Am. Math. Soc., **51**-No.11, 1336-1347, 2004.
- [2] L.A. Caffarelli, S. Salsa and L. Silvestre: Regularity estimates for the solution and the free boundary of the obstacle problem for the fractional Laplacian. Invent. Math., **171**-No.2, 425-461, 2008.

- [3] M. Ferreira and N. Vieira: Eigenfunctions and fundamental solution of the fractional Laplace and Dirac operators: the Riemann-Liouville case. Submitted.
- [4] R. Gorenflo, A.A. Kilbas, F. Mainardi and S. Rogosin: Mittag-Leffler functions. Theory and applications. Springer Monographs in Mathematics, Springer, Berlin, 2014.
- [5] U. Kähler and N. Vieira: Fractional Clifford analysis. S. Bernstein, U. Kähler, I. Sabadini and F. Sommen eds. Hypercomplex Analysis: New perspectives and applications, Trends in Mathematics, Birkhäuser, Basel, 2014.
- [6] A. Kilbas, H.M. Srivastava and J.J. Trujillo: Theory and applications of fractional differential equations. North-Holland Mathematics Studies-Vol.204, Elsevier, Amsterdam, 2006.
- [7] I. Podlubny: Fractional differential equations. An introduction to fractional derivatives, fractional differential equations, to methods of their solution and some of their applications. Mathematics in Science and Engineering-Vol.198, Academic Press, San Diego, CA, 1999.
- [8] S.G. Samko, A.A. Kilbas and O.I. Marichev: Fractional integrals and derivatives: theory and applications. Gordon and Breach, New York, NY, 1993.
- [9] N. Vieira: Fischer Decomposition and Cauchy-Kovalevskaya extension in fractional Clifford analysis: the Riemann-Liouville case. Proc. Edinb. Math. Soc., II. Ser., in press.
- [10] S. Yakubovich: Eigenfunctions and fundamental solutions of the fractional two-parameter Laplacian. Int. J. Math. Math. Sci., Article ID **541934**, 18p, 2010.

STUDY OF ANALYTICAL MODELS OF THE MECHANICAL BEHAVIOR OF POLYMER-MODIFIED CONCRETE

L. Göbel *, A. Osburg and T. Lahmer

* *Research Training Group 1462*
Bauhaus-Universität Weimar
Berkaer Straße 9
99423 Weimar

E-mail: luise.goebel@uni-weimar.de

Keywords: Polymer-modified concrete (PCC), mechanical behavior, modulus of elasticity, tensile strength.

Abstract. *Polymer modification of mortar and concrete is a widely used technique in order to improve their durability properties. Hitherto, the main application fields of such materials are repair and restoration of buildings. However, due to the constant increment of service life requirements and the cost efficiency, polymer modified concrete (PCC) is also used for construction purposes. Therefore, there is a demand for studying the mechanical properties of PCC and entitative differences compared to conventional concrete (CC). It is significant to investigate whether all the assumed hypotheses and existing analytical formulations about CC are also valid for PCC. In the present study, analytical models available in the literature are evaluated. These models are used for estimating mechanical properties of concrete. The investigated property in this study is the modulus of elasticity, which is estimated with respect to the value of compressive strength. One existing database was extended and adapted for polymer-modified concrete mixtures along with their experimentally measured mechanical properties. Based on the indexed data a comparison between model predictions and experiments was conducted by calculation of forecast errors.*

1 INTRODUCTION

Polymer-modified concrete (PCC) has been a widely used material in repair and restoration of buildings. Due to the constant increment of service life requirements and the cost efficiency, it is more and more utilized for construction purposes. This process requires the pronounced investigation of the mechanical performance of polymer-modified concrete. The modification in the composition of the mixture as a result of polymer addition affects the behavior of the concrete in its fresh and hardened state. Therefore, it is important to estimate precisely the fundamental mechanical properties of this material.

The characterization of the mechanical performance of different kinds of concrete has been investigated for many decades (e.g. [1], [2], [3], [4], [5]). Hitherto, numerous constitutive relations for the prediction of properties such as the Young's modulus, the tensile strength or stress-strain curves have been developed. Nonetheless, their fields of application are limited in most cases to conventional concrete (CC) [6]. One crucial question is whether or not the behavior of PCC can be translated to the properties of conventional concrete. More particularly, it is significant to investigate if the assumed hypotheses and existing analytical formulations are applicable for polymer-modified concrete. Present models may not take into account the complexity of PCC and, therefore, may lead to inaccurate predictions of fundamental mechanical properties. Thus, it needs to be clarified if existing design codes should be modified for the application to new construction materials.

Within this paper, analytical expressions for estimating the modulus of elasticity (MOE) were investigated. The so-called Young's modulus of concrete directly affects the stiffness and deformation behavior of structural components. It needs to be known for both the determination of deflections in structures for requirements in serviceability and to calculate prestressing forces in prestressed concretes [7],[8]. There are various factors affecting the Young's modulus of concrete. The most important ones are classified in Figure 1.

To compare the goodness-of-fit of those models, an existing database [9] was used and extended for data from polymer-modified concretes. The comparison between model calculations and experimental data was done by using different quality criteria.

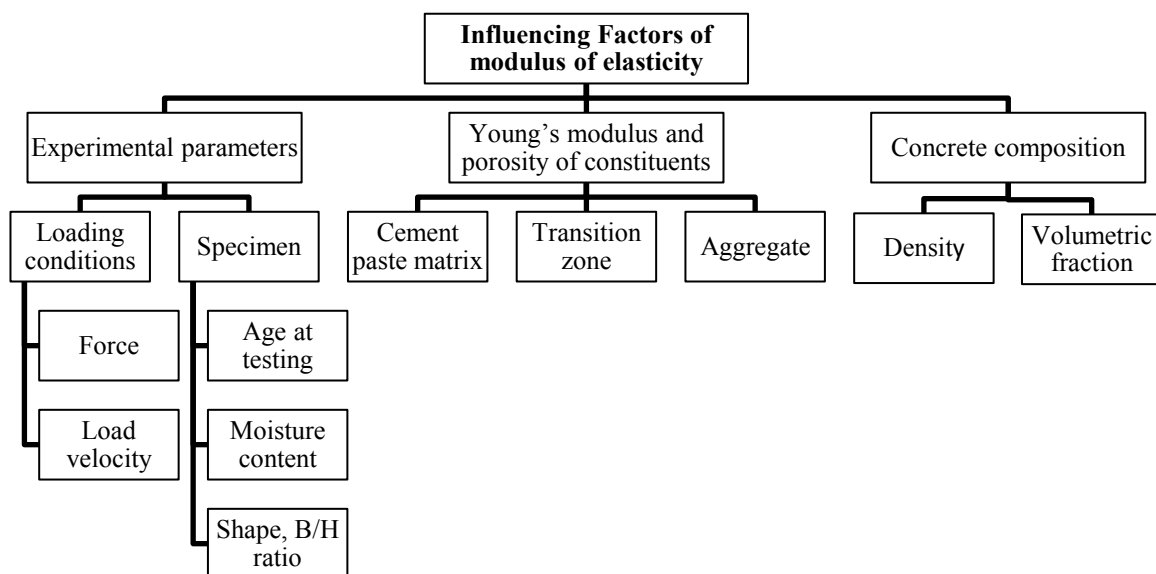


Figure 1: Most important factors affecting the modulus of elasticity of concrete

2 MATERIAL PHENOMENA OF PCC

Polymer-modified concretes exhibit different behavior compared to conventional concretes. The addition of polymers to the concrete mixture varies from 5 % up to 20 % of the cement content in which various types of polymers can be used. For concretes modified with styrene-butadiene and styrene-acrylic acid ester in form of latex dispersion or redispersible powders most studies have been conducted [10]. Besides their chemical nature, the polymers vary regarding their consistency as well as their minimum film formation temperature. Those factors also have a large influence on the properties of fresh and hardened PCC.

A lot of research has been conducted with regard to observations of changes in the microstructure of cementitious systems [11], [12], [13]. Polymer and cement phases interpenetrate each other [14], and they form together the binder matrix. A continuously increasing number of publications considers the changed mechanical behavior of PCC, e.g. [15], [16], [17], [18]. The Young's modulus as well as the compressive strength normally decrease, the material shows a more ductile behavior, and the viscous properties are more conspicuous, resulting in large time-dependent deformations [19–21], [20], [21].

One question is the application of analytical formulas describing the mechanical performance of CC to PCC. KEITEL evaluated the use of existing creep models developed for CC representing PCC. The author compared calculated creep strains to experimental data of PCC, and optimized the model parameters to minimize the differences between them [22], [23]. The adaptation of design codes, aiming at prediction of the Young's modulus of concretes, for the use of PCC is not studied yet.

3 SURVEY OF EXPERIMENTAL DATA AND STRUCTURAL DESIGN CODES

3.1 Existing databases

A large variety of experimental results of mechanical laboratory tests concerning conventional concretes are available in the open literature. LIM et al. [9], ASLANI et al. [24], and CRAEYE et al. [6] provide an overview about existing analytical formulations for different types of concrete and constructed databases to summarize information about mix-design and properties of concretes used in numerous experimental studies.

LIM et al. [9] assembled a database from 209 experimental studies and summarized 4353 datasets. The results were sorted into different groups according to the type of concrete (normal-weight concrete (NWC) and light-weight concrete (LWC)) and the cross-sectional shape of specimen (square or circular). CRAEYE et al. [6] provide an overall view on the mechanical performance of self-compacting concrete (SCC). The database contains results of more than 250 publications. ASLANI et al. [24] assembled around 250 mixtures for a database of CC and SCC and analyzed the mechanical properties for those kinds of concrete.

3.3 Extension of an existing database

The database by LIM et al. [9], which was chosen to be the most complete one, was further expanded by adding more recent experimental results about PCC. A literature study was carried out. The additional data stems from several publications about the mechanical performance of polymer-modified concrete and related laboratory experiments. Entirely, the database contains results of more than 25 papers. It includes information with regard to mix-design, fresh and hardened properties of PCC. The structure of the database is shown in Figure 2. It should be noted that in some of the datasets details were not available from the source documents. To

guarantee comparability between different concretes and for a consistent treatment of the test results inside the database, only datasets from concretes with a circular cross-section were used.

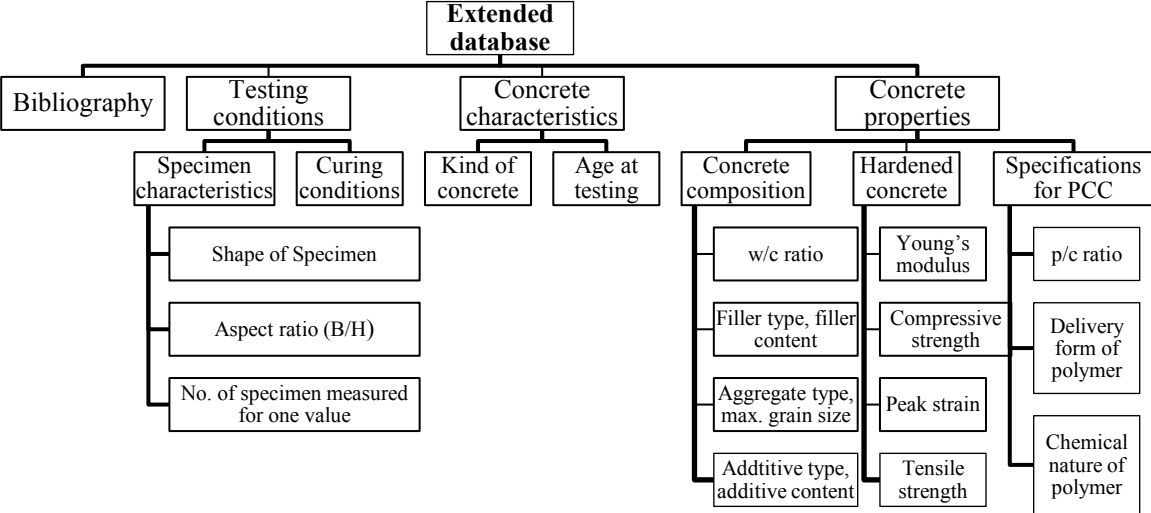


Figure 2: Structure of the database including properties related to PCC

In the database of the polymer-modified concretes, the water-to-cement ratio varied from 0.23 to 0.84, the density of the hardened concrete from 1560 to 2440 kg/m³, the experimentally determined Young’s modulus from 10,000 to 39,500 kN, and the concrete compressive strength from 14 to 68 kN. Figure 3 shows the distribution of the compressive strength of the normal and light weight concrete specimens, and of the polymer-modified concrete specimens. Apparently, the collected PCC specimen have a compressive strength around 40 kN whereas the compressive strengths of the conventional concretes are slightly lower according to this database.

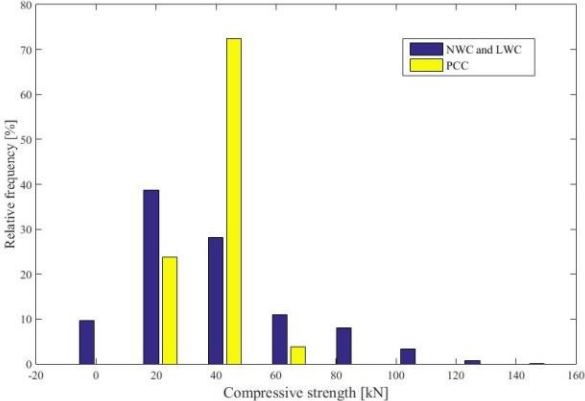


Figure 3: Relative frequencies of compressive strength values of conventional concretes (NWC and LWC) and polymer-modified concretes (PCC) from laboratory experiments

Furthermore, the database was used to investigate some polymer-specific properties. The polymer-to-cement ratio used for modification of the concretes varies between 0.01 and 0.30. So, Figure 4 shows the occurrence of the four most often polymers used for modification

purposes when comparing the datasets of the database. As illustrated, most research results are available about concretes modified with styrene-butadiene.

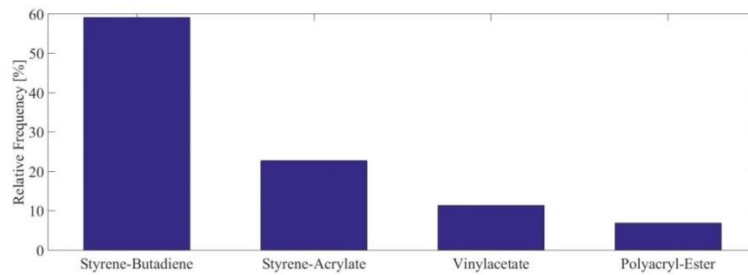


Figure 4: Relative frequencies of polymers used for modification of cementitious systems

3.2 Limitations of the database

Using experimental results from different published sources include problems because often there are information missing regarding the exact composition of the concrete mixtures and the testing regime, respectively. Furthermore, the extraction of relevant results in some cases is difficult because of an incompleteness of the published values. Partly, the data are presented in diagrams and have to be extrapolated from the graphs [24].

Such databases contain datasets from different laboratory experiments and, thus, comprise a great variety of cementitious material. The experimentally determined mechanical properties depend on many influencing factors due to the complex behavior of concretes. The indexed parameters differ from one investigation to another. There are differences in the material composition (aggregate size, type and amount of cement, aggregate, or additive, respectively), the age of the specimen, curing conditions, testing facility, and the measurement equipment. Loading rates, for example, cover several orders of magnitude (from very slow tests up to tests within a few seconds). Therefore, the gathered experimental data scatter significantly, which has to be considered during the interpretation of the results.

3.4 Models for the modulus of elasticity

The modulus of elasticity for concrete can be calculated with empirical equations. The models were developed by several institutions. Many researchers have provided additional recommendations based on evaluation of experimental works. Most of the formulas relate the initial or secant modulus to the compressive strength of concrete. Due to the large influence of the concrete density and the type of aggregates used in the concrete mixtures, some models consider those parameters with correction factors. However, because of many influencing factors, the calculated value never represents the actual value of the modulus of elasticity [8].

Within this paper, existing analytical models were separated into three groups. The formulations in the first group predict the MOE only with the compressive strength of concrete as an input parameter. The second group additionally takes into account the density of the hardened concrete. Many researchers have recognized the determining effect of the aggregate properties in predicting MOE of concrete [24], and, thus, a third class of equations was distinguished, including parameters for different types of aggregates. A more detailed explanation about the models is given in the original publications. The models used in this study are summarized in Table 1, Appendix 1.

4 RESULTS AND DISCUSSION

4.1 Comparison of model outputs and experimental data

The experimental data from the database were used to evaluate how good the models developed for conventional concretes predict the modulus of elasticity for polymer-modified concretes. In a first step, the quotient between the mean values of both the calculated Young's modulus and the experimentally determined Young's modulus were calculated for every model. The calculation was done on the basis of the same value of the compressive strength. The results are shown in Table 2. The closer the values converge to 1, the better fits the model the experiments. The comparison was done for all three types of concrete.

Table 1: Comparison between calculated and experimental results for the Young's modulus

Input parameter	f_c					f_c and γ				f_c and γ and K_1		
	1	2	3	4	5	6	7	8	9	10	11	12
NWC	1.05	0.99	1.21	1.24	1.16	1.08	1.02	0.53	0.75	0.99	1.67	1.21
LWC	1.61	1.92	2.34	2.14	1.99	0.80	1.16	0.46	0.92	1.04	0.86	1.15
PCC	1.14	1.09	1.34	1.35	1.26	1.12	1.14	0.59	0.85	1.00	1.00	1.33

It can be seen that the values of PCC are almost in the same range like the values of NWC. That means that the models developed for CC are able to predict the Young's modulus of PCC. The mean values for LWC are much higher which indicates that the models overestimate the property for this type of concrete.

There are differences between the prediction qualities of the different models. For PCC, the best estimation is derived by application of both the AASHTO and the BAALBAKI model which take into account the type of aggregate. In case of PCC, it therefore seems to be necessary to use a model with more than only one input parameter. For NWC, it is already sufficient to apply the models suggested by almost all national design codes that only use the compressive strength for estimation.

4.2 Quality criteria

To prove the results from the previous section, two other types of quality criteria were calculated to evaluate the goodness-of-fit of the models. The root-mean-squared errors (RMSE) as well as the mean absolute percentage errors (MAPE) were determined. The lower the calculated value of both criteria is, the better is the prediction capability of the model. Table 3 shows the results of the calculations. Due to the bad performance of the models in case of light-weight concretes, only NWC and PCC were considered in this section.

It can be seen that both the calculation of RMSE and MAPE and the direct comparison between calculated and experimental results are almost comparable. Hence, also the use of models that consider the type of aggregates is recommended for application to PCC because results with the least errors can be achieved by applying those types of models. When the forecast errors between the model outputs for NWC and PCC are compared, it becomes obvious that there are almost no differences. In case of the first group of models, the model predictions are better for NWC. Otherwise, if the aggregate type is considered, the forecast errors are similar for both types of concrete.

Table 2: Forecast errors for estimating the Young's modulus of concrete by different models

Input parameter	f_c					f_c and γ				f_c and γ and K_1		
	1	2	3	4	5	6	7	8	9	10	11	12
NWC												
RMSE ($\cdot 10^{-3}$)	4.99	4.93	6.53	8.85	6.84	5.10	5.36	17.77	4.79	6.92	4.89	5.15
MAPE [%]	13.5	13.3	22.5	25.4	19.0	12.9	13.4	46.4	12.2	17.8	10.4	11.2
PCC												
RMSE ($\cdot 10^{-3}$)	4.51	3.44	9.51	9.43	7.34	3.94	4.62	8.26	1.07	4.41	2.88	2.71
MAPE [%]	19.5	16.0	34.1	35.3	27.2	13.3	14.1	40.9	12.1	16.0	11.3	11.2

5 CONCLUSION

The main focus of existing studies about polymer-modified concrete has been related to changes in the microstructure, the mix-design, and durability since it is a relatively new type of concrete. The application of models describing the mechanical behaviour of PCC has not been investigated yet. Nevertheless, in most papers information about the compressive strength, and in some cases, about the modulus of elasticity and the tensile strength are published. So, an existing database, developed for conventional concrete, was extended by addition of datasets for PCC. Results from more than 25 papers were assembled. The database was used to compare experimental data with the results of empirical formulations for estimating the Young's modulus of concrete.

It can be concluded that the models for estimating the modulus of elasticity can be applied to PCC, especially those which consider the type of aggregate. The experimentally determined data of PCC seem to confirm the model predictions and fit well into the bandwidth expected for the secant modulus of elasticity in general. Even the assumed lower Young's modulus of PCC due to the role of polymers in the matrix and the formation of sliding planes inside the microstructure [18] does not deteriorate the capability of the models developed for CC for their application to PCC. However, it should not be neglected that the scatter of the experimentally determined Young's modulus for concretes which have the same compressive strength can be enormous. Hence, a precise determination of the Young's modulus is only possible with laboratory experiments, conduction of static tests, or with ultrasonic measurement methods.

REFERENCES

- [1] P.R. Barnard, Researches into the complete stress-strain curve for concrete, Magazine of Concrete Research 16 (1964) 203–210.
- [2] S. Popovics, A numerical approach to the complete stress-strain curve of concrete, Cement and Concrete Research 3 (1973) 583–599.
- [3] M.A. Mansur, T.H. Wee, M.S. Chin, Derivation of the complete stress-strain curves for concrete in compression, Magazine of Concrete Research 47 (1995) 285–290.
- [4] K. Dahl, Uniaxial stress-strain curves for normal and high strength concrete, Dissertation, Lyngby, 1992.
- [5] B. Baldwin, M.A. North, A stress-strain relationship for concrete at high temperatures, Magazine of Concrete Research 16 (1973) 208–212.

- [6] B. Craeye, P. van Itterbeeck, P. Desnerck, V. Boel, G. de Schutter, Modulus of elasticity and tensile strength of self-compacting concrete: Survey of experimental data and structural design codes, *Cement and Concrete Composites* 54 (2014) 53–61.
- [7] A.A. Tasnimi, Mathematical model for complete stress-strain curve prediction of normal, light-weight and high-strength concretes, *Magazine of Concrete Research* 56 (2004) 23–34.
- [8] I.B. Topcu, A. Ugurlu, Elasticity Theory of Concrete and Prediction of Static E-Modulus for Dam Concrete Using Composite Models, *Digest* 2007 1115–1127.
- [9] J.C. Lim, T. Ozbakkaloglu, Stress–strain model for normal- and light-weight concretes under uniaxial and triaxial compression, *Construction and Building Materials* 71 (2014) 492–509.
- [10] Y. Ohama, V.S. Ramachandran, Polymer-Modified Mortars and Concretes: Properties and Process Technology, in: V.S. Ramachandran (Ed.), *Concrete Admixtures Handbook: Properties, Science, and Technology*, 2nd, 1996.
- [11] A. Dimmig, Einflüsse von Polymeren auf die Mikrostruktur und die Dauerhaftigkeit kunststoffmodifizierter Mörtel (PCC), *Dissertation*, Weimar, 2002.
- [12] A. Beeldens, D. van Gemert, H. Schorn, Y. Ohama, L. Czarnecki, From microstructure to macrostructure: an integrated model of structure formation in polymer-modified concrete, *Materials and Structures* 38 (2005) 601–607.
- [13] A. Jenni, M. Herwegh, R. Zurbruggen, T. Aberle, L. Holzer, Quantitative microstructure analysis of polymer-modified mortars, *Journal of Microscopy* 2012 (2003) 186–196.
- [14] A. Dimmig-Osburg, K.A. Bode, A. Flohr, The influences of different polymers on the deformation behaviour and stiffness processing of concrete, 04--06. September.
- [15] K.A. Bode, A. Dimmig-Osburg, Shrinkage properties of polymer-modified cement mortars (PCM), in: 13. International Congress on Polymers in Concrete (ICPIC), Madeira Islands, Portugal, 2010, pp. 89–95.
- [16] J.M. Gao, C.X. Qian, B. Wang, K. Morino, Experimental study on properties of polymer-modified cement mortars with silica fume, *Cement and Concrete Research* 32 (2002) 41–45.
- [17] H. Ma, Z. Li, Microstructures and mechanical properties of polymer modified mortars under distinct mechanisms, *Construction and Building Materials* 47 (2013) 579–587.
- [18] A. Flohr, K.A. Bode, A. Dimmig-Osburg, The deformation behaviour and stiffness evolution of polymer-modified cement concrete (PCC), in: 13. International Congress on Polymers in Concrete (ICPIC), Madeira Islands, Portugal, 2010, pp. 153–160.
- [19] A. Flohr, A. Dimmig-Osburg, Study on the load-behavior of modified cement concrete, in: *Advanced Materials Research*, pp. 198–203.
- [20] B. Chen, J. Liu, Mechanical properties of polymer-modified concretes containing expanded polystyrene beads, *Construction and Building Materials* 21 (2007) 7–11.
- [21] A.A. Aliabdo, A.M. Abd_Elmoaty, Experimental investigation on the properties of polymer modified SCC, *Construction and Building Materials* 34 (2012) 584–592.
- [22] H. Keitel, A. Dimmig-Osburg, V. Zabel, Characterization of time-dependent Deformations of Polymer Modified Cement Concrete (PCC), 18th International Conference on the Application of Computer Science and Mathematics in Architecture and Civil Engineering Weimar, 07. - 09. Juli 2009.
- [23] H. Keitel, A. Dimmig-Osburg, Prediction of creep deformation of PCC using models of standard cement concrete, in: 13. International Congress on Polymers in Concrete (ICPIC), Madeira Islands, Portugal, 2010.
- [24] F. Aslani, S. Nejadi, Mechanical properties of conventional and self-compacting concrete: An analytical study, *Construction and Building Materials* 36 (2012) 330–347.

- [25] American Concrete Institute, Building Code Requirements for Structural Concrete (ACI 318-11) and Commentary, Farmington Hills, MI, 2008, [April 20, 2015].
- [26] American Concrete Institute, State-of-the-Art Report on High-Strength Concrete. ACI363-R, Farmington Hills, Michigan, 1992.
- [27] Ministerio de Fomento, Spain, Code on Structural Concrete (EHE-08), 2010, [April 20, 2015].
- [28] J. Matos, V. Branco, A.N. Macêco, D. Oliveira, Structural assessment of a RC Bridge over Sororó river along the Carajás railway, Ibracon Structures and Materials Journal 2015 (8) 140–163.
- [29] Mary Beth D. Hueste, Praveen Chompreda, David Trejo, Daren B. H. Cline, Mechanical properties of high strength concrete for prestressed concrete bridge girders, Austin, Texas, USA, 2003.
- [30] D.J. Cook, P. Chindaprasirt, A mathematical model for the prediction of damage on concrete, Cement and Concrete Research 11 (1981) 581–590.
- [31] Comité Euro-International du Béton, CEB-FIP Model Code 1990, Thomas Telford, 1993, [April 20, 2015].

APPENDIX 1

Table 3: Models for the modulus of elasticity developed for conventional concretes

No.	Reference	Model for modulus of elasticity	Input parameter
1	ACI 318 (2008) [25]	$E_c = 4730 \sqrt{f_c}$	f_c ¹
2	ACI363 (1992) [26]	$E_c = 3320 \sqrt{f_c} + 6890$	f_c
3	EHE (2010) [27]	$E_c = 10000 \cdot \sqrt[3]{f_c}$	f_c
4	NBR 6118 (2014) [28]	$E_c = 5600 \sqrt{f_c}$	f_c
5	HUESTE (2004) [29]	$E_c = 5230 \sqrt{f_c}$	f_c
6	AHMAD and SHAH (1985) [24]	$E_c = 3.38 \cdot 10^{-5} \cdot \gamma^{2.5} (\sqrt{f_c})^{0.65}$	f_c and γ^2
7	JOBSE and MOUSTAFA (1984) [24]	$E_c = 0.103 \cdot \gamma^{1.5} (\sqrt{f_c})^{0.5}$	f_c and γ
8	COOK (1989) [30]	$E_c = 3.22 \cdot 10^{-5} \cdot \gamma^{2.5} (\sqrt{f_c})^{0.315}$	f_c and γ
9	LIM (2014) [9]	$E_c = 4400 \sqrt{f_c} \left(\frac{\gamma}{2400}\right)^{1.4}$	f_c and γ
10	AASHTO (2006) [24]	$E_c = 0.043 K_1 \cdot \gamma^{1.5} \cdot \sqrt{f_c}$	f_c and γ and K_1 ³
11	BAALBAKI, W. (1997) [24]	$E_c = K_1 + 0.2 f_c$	f_c and γ and K_1
12	CEB-FIP (1993) [31]	$E = 21500 \cdot K_1 \sqrt[3]{\frac{f_c}{10}}$	f_c and γ and K_1

¹ Cylinder compressive strength of concrete (standard specimens) [kN]

² Unit weight of concrete [kg/m³]

³ Correction factor for source of aggregate, specific values for specific types aggregates

REGULAR QUATERNIONIC FUNCTIONS AND THEIR APPLICATIONS

Yu. Grigor'ev

*North-Eastern Federal University, Academy of Sciences Republic of Sakha
58, Belinsky Str., Yakutsk, 677000 Russia
E-mail: grigyum@yandex.ru*

Keywords: Regular quaternionic functions, Moisil-Theodorescu system, Elasticity.

Abstract. *The theory of regular quaternionic functions of a reduced quaternionic variable is a 3-dimensional generalization of complex analysis. The Moisil-Theodorescu system (MTS) is a regularity condition for such functions depending on the radius vector $\mathbf{r} = \mathbf{i}x + \mathbf{j}y + \mathbf{k}z$ seen as a reduced quaternionic variable. The analogues of the main theorems of complex analysis for the MTS in quaternion forms are established: Cauchy, Cauchy integral formula, Taylor and Laurent series, approximation theorems and Cauchy type integral properties. The analogues of positive powers (inner spherical monogenics) are investigated: the set of recurrence formulas between the inner spherical monogenics and the explicit formulas are established. Some applications of the regular function in the elasticity theory and hydrodynamics are given.*

1 INTRODUCTION

In two-dimensional problems of the mathematical physics the methods of complex variable theory are effectively used. As a generalization in multidimensional problems the methods of hypercomplex functions are developed since 1930s papers by R. Fueter, G.C. Moisil and N. Theodorescu (see [1]–[5] and references therein). In [6] one can find a short survey on applications of hypercomplex functions in the three-dimensional theory of elasticity. In a recent paper [7] a new alternative Kolosov-Muskhelishvili formula for the elastic displacement field by means of a (paravector-valued) monogenic, an anti-monogenic and a ψ -hyperholomorphic function is proposed.

In the three-dimensional space the Moisil-Theodorescu system is an analogue of the Cauchy–Riemann system and its theory was developed in three ways: as a theory of partial differential equations, as a part of Clifford analysis [1], and as the theory of regular quaternionic functions of the reduced quaternionic variable [2], [8]–[10]. In this paper we use the last way and give a short survey of our results.

2 PRELIMINARIES AND NOTATIONS

Let i, j, k be the basic quaternions obeying the following rules of multiplication:

$$i^2 = j^2 = k^2 = -1, \quad ij = -ji = k, \quad jk = -kj = i, \quad ki = -ik = j.$$

An element q of the quaternion algebra \mathbb{H} we write in the form $q = q_0 + iq_x + jq_y + kq_z = q_0 + \mathbf{q}$, where q_0, q_x, q_y, q_z are the real numbers, q_0 is called the scalar part of the quaternion, $\mathbf{q} = iq_x + jq_y + kq_z$ is called the vector part of the quaternion q . The quaternion conjugation is denoted as $\tilde{q} = q_0 - \mathbf{q}$.

Let x, y, z be the Cartesian coordinates in the Euclidean space \mathbb{R}^3 . Let Ω be a domain of \mathbb{R}^3 with a piecewise smooth boundary. A quaternion-valued function or, briefly, \mathbb{H} -valued function f of a reduced quaternionic variable $\mathbf{r} = ix + jy + kz \in \mathbb{R}^3$ is a mapping $f : \Omega \rightarrow \mathbb{H}$, such that

$$f(\mathbf{r}) = f_0(\mathbf{r}) + \mathbf{f}(\mathbf{r}) = f_0(x, y, z) + if_x(x, y, z) + jf_y(x, y, z) + kf_z(x, y, z).$$

The functions f_0, f_x, f_y, f_z are real-valued defined in Ω . Continuity, differentiability or integrability of f are defined coordinate-wisely. For continuously real-differentiable functions $f : \Omega \subset \mathbb{R}^3 \rightarrow \mathbb{H}$, which we will denote for simplicity by $f \in C^1(\Omega, \mathbb{H})$, the operator $\nabla = i\partial_x + j\partial_y + k\partial_z$ is called the generalized Cauchy–Riemann operator.

According to R. Fueter a function f is called left- or right-regular in Ω if $\nabla f = 0$ or $f\nabla = 0$, respectively, for $\mathbf{r} \in \Omega$. From now on in the main part we use only the left-regular functions that, for simplicity, we call regular. With the vectorial notations the regularity condition is given as follows:

$$\nabla f(\mathbf{r}) = -\nabla \cdot \mathbf{f}(\mathbf{r}) + \nabla f_0(\mathbf{r}) + \nabla \times \mathbf{f}(\mathbf{r}) = 0, \quad (1)$$

where $\nabla f_0, \nabla \cdot \mathbf{f}, \nabla \times \mathbf{f}$ are the usual gradient, divergence and curl, respectively.

The equations of elastic equilibrium are called the Lamé equations:

$$L\mathbf{u} \equiv (\lambda + 2\mu)\nabla(\nabla \cdot \mathbf{u}) - \mu\nabla \times (\nabla \times \mathbf{u}) = 0. \quad (2)$$

If we introduce the next notations

$$(\lambda + 2\mu)\nabla \cdot \mathbf{u} = f_0, \quad -\mu\nabla \times \mathbf{u} = \mathbf{f}, \quad (3)$$

then the Lamé equation (2) is transformed into the MTS:

$$\nabla \cdot \mathbf{f} = 0, \quad \nabla f_0 + \nabla \times \mathbf{f} = 0, \quad (4)$$

thus the quaternion function $f = f_0 + \mathbf{f}$ is regular. Such the connection between the Lamé equation and quaternion functions was first pointed by G.Moisil.

3 MAIN THEOREMS OF QUATERNIONIC ANALYSIS

Cauchy's integral theorem, the formula of Borel-Pompeiu, Cauchy's integral formula, Cauchy's integral formula for the derivative and some other main properties are established.

Let us call a \mathbb{H} -valued function F as a primitive of the regular function f if $\nabla F = f$, i.e. $\nabla \cdot \mathbf{F} = -f_0$, $\nabla F_0 + \nabla \times \mathbf{F} = \mathbf{f}$. Obviously, $\nabla(\nabla F) = -\Delta F = \nabla f = 0$ and F is a harmonic function. Such the primitive function is not regular. Another notion of a monogenic primitive function is introduced by means of a hypercomplex derivative of a monogenic function (see [11]).

3.1 Analogues of Powers

In higher dimensions analogues of positive powers are constructed by symmetrization of products of the Fueter variables [2]. Now we show a certain other way for introducing the set of regular polynomials. Let us introduce homogeneous polynomials $P^{l,m}(\mathbf{r})$, $l + m = n$, ($l, m = 0, 1, \dots, n; n = 0, 1, \dots$) by means of recurrent formulas:

$$P^{l,m}(\mathbf{r}) = P^{1,0}(\mathbf{r})P^{l-1,m}(\mathbf{r}) + P^{0,1}(\mathbf{r})P^{l,m-1}(\mathbf{r}), \quad (5)$$

where $P^{1,0}(\mathbf{r}) = x + jz$, $P^{0,1}(\mathbf{r}) = y - iz$, $P^{0,0} = 1$ and it is assumed that $P^{p,q} = 0$, if at least one of the numbers $p, q < 0$.

It can be proved that these polynomials are linearly independent over \mathbb{R} , any finite linear combination $\sum_{l,m} P^{l,m}(\mathbf{r})C_{l,m}$ with $C_{l,m} = \text{const} \in \mathbb{H}$ is regular everywhere. Also the polynomials $P^{l,m}(\mathbf{r})$ form a basis of the space of homogeneous regular polynomials of order n . There exist convenient formulas for derivatives:

$$\begin{aligned} \frac{\partial}{\partial x} P^{l,m}(\mathbf{r}) &= (l+m)P^{l-1,m}(\mathbf{r}), \quad \frac{\partial}{\partial y} P^{l,m}(\mathbf{r}) = (l+m)P^{l,m-1}(\mathbf{r}), \\ \frac{\partial}{\partial z} P^{l,m}(\mathbf{r}) &= (l+m) [-iP^{l,m-1}(\mathbf{r}) + jP^{l-1,m}(\mathbf{r})]. \end{aligned} \quad (6)$$

Some other properties of regular polynomials are investigated: the structure of scalar and vector parts, recurrent formulas for scalar and vector parts, explicit formulas for components etc.

Analogues of negative powers are noted $P^{-l-1,-m-1}(\mathbf{r})$ and are introduced in the usual way:

$$P^{-l-1,-m-1}(\mathbf{r}) = \frac{(-1)^{n+1}}{n!} \frac{\partial^n}{\partial x^l \partial y^m} \frac{\mathbf{r}}{r^3} \quad (l, m = 0, 1, \dots, n; n = 0, 1, \dots) \quad (7)$$

The Taylor and Laurent series generalizations by means of introduced powers are proved.

3.2 Approximation Theorems

Runge's Theorem. Each \mathbb{H} -valued function f that is regular in an open (not necessarily connected) subset D of \mathbb{R}^3 with a connected complement can be uniformly approximated on each compactum $K \Subset D$ arbitrarily closely by regular polynomials.

Lavrent'ev's Theorem. Each \mathbb{H} -valued function $f \in C^0$ on a closed subset D of \mathbb{R}^3 can be uniformly approximated on this set arbitrarily closely by regular polynomials if and only if this set is a nowhere dense compactum in \mathbb{R}^3 that does not separate \mathbb{R}^3 .

Keldysh's Theorem. Each \mathbb{H} -valued function $f \in C^0(\bar{D})$ that is regular in a domain D can be uniformly approximated on a closed domain $\bar{D} \in \mathbb{R}^3$ arbitrarily closely by regular polynomials if and only if the complement of D consists of a single domain G_∞ that contains the point at infinity.

Details can be found in [8].

4 APPLICATIONS

4.1 Three-dimensional Kolosov-Muskhelishvili formulae

In plane problems of theory of elasticity the basis of complex function applications is the representation of the general solution of the equilibrium equations in terms of two arbitrary analytic functions called the Kolosov-Muskhelishvili formulae. In this section a variant of three-dimensional quaternion generalization of the Kolosov-Muskhelishvili formulae is presented, which is effectively applied to solve the basic problems of the theory of elasticity for the ball.

The general solution of the Lamé equation (2) in a star-shaped domain Ω^* is expressed in terms of two regular in Ω^* functions φ, ψ in the form

$$2\mu\mathbf{u}(\mathbf{r}) = \varkappa\Phi(\mathbf{r}) - \mathbf{r}\widetilde{\varphi}(\mathbf{r}) - \widetilde{\psi}(\mathbf{r}), \quad \varkappa = -\frac{3\lambda + 7\mu}{\lambda + \mu}, \quad (8)$$

where as Φ one can take any primitive of function φ , having subordinated ψ to the condition $\varkappa\Phi_0 = \mathbf{r} \cdot \varphi + \psi_0$.

Another form of general solution of the Lamé equation in Ω^* is given in terms of two regular in Ω^* functions $f, \nabla g_0$ by V. V. Naumov (see [12]) in the form:

$$\mathbf{u}(\mathbf{r}) = \frac{\mathbf{r}}{\mu} \times I^1 \mathbf{f} + \nabla \left\{ r^2 \left[\frac{3\lambda + 7\mu}{4\mu(\lambda + 2\mu)} I^{1/2} - \frac{1}{\mu} I^1 \right] f_0 \right\} + \nabla g_0, \quad (9)$$

where $f = (\lambda + 2\mu)\nabla \cdot \mathbf{u} - \mu\nabla \times \mathbf{u}$; I^α is the operator of radial integration:

$$I^\alpha f(\mathbf{r}) = \int_0^1 t^\alpha f(\mathbf{r}t) dt.$$

It can be shown that both representations (8) and (9) are equivalent, in particular cases of plane and axially symmetric deformations both representations go into the Kolosov-Muskhelishvili and Solovyev formulae. Some details can be found in [6].

4.2 Equilibrium problems for elastic ball

Using the representation (9) it is shown that the main problems of elastic ball equilibrium can be obtained in a closed form as analogues of the Poisson and Neumann formulas. Solutions of these problems are also expressed in terms of solutions of the Dirichlet and Neumann problems for three independent harmonic functions in a ball. For example, let us consider the equilibrium of a ball U with a radius R when on its boundary S purely normal displacements are given:

$$\begin{cases} L\mathbf{u}(\mathbf{r}) = 0, & \mathbf{r} \in U, \quad \mathbf{u} \in C^2(U) \cap C^1(\bar{U}) \\ u_r|_{\partial U} = u(\theta, \varphi) \in C^0(\partial U); & u_\theta|_{\partial U} = u_\varphi|_{\partial U} = 0. \end{cases} \quad (10)$$

By mean of the quaternion representation (9) the solution of this problem is obtained in the form

$$\mu \mathbf{u}(\mathbf{r}) = \frac{\mathbf{r}}{R} F + \frac{R^2 - r^2}{2R} \nabla [\varkappa(2\varkappa - 1)I^\varkappa - 2\varkappa - 1] F, \quad \varkappa = \frac{2(\nu - 1)}{3 - 4\nu} \in \left(-1, -\frac{2}{3}\right), \quad (11)$$

where F is a solution of the next Dirichlet problem:

$$\begin{cases} \Delta F(\mathbf{r}) = 0, & \mathbf{r} \in U, \\ F|_{r=R} = \mu u(\vartheta, \varphi) \in C^0(S). \end{cases} \quad (12)$$

Then using the Poisson formula for the solution of the Dirichlet problem (12) and radial integration operator I^α properties, we have the solution of the problem (10) in the closed form:

$$\begin{aligned} u_r(\mathbf{r}) &= \frac{1 - t^2}{4\pi R^2} \oint u(2\varkappa + 1) \left[(2 - \varkappa) \frac{t}{s^3} + \frac{2\varkappa^2 - \varkappa}{2\varkappa + 1} \cdot \frac{c}{s^3} + 3(1 - t^2) \frac{t - c}{2s^5} + \right. \\ &\quad \left. + \frac{\varkappa}{2t} (1 - 2\varkappa) \left(\frac{1}{s} - (\varkappa + 1) I^\varkappa \frac{1}{s} \right) \right] dS; \\ \begin{cases} u_\theta(\mathbf{r}) \\ u_\varphi(\mathbf{r}) \end{cases} &= \frac{1}{4\pi R^2} \oint u \begin{cases} \xi \\ \eta \end{cases} \left(\frac{1}{2} + \varkappa \right) (1 - t^2) \left[3 \frac{t^2 - 1}{s^5} + \frac{4\varkappa^2 - 2\varkappa}{(2\varkappa + 1)s^3} + \right. \\ &\quad \left. + (\varkappa - 2\varkappa^2) I^{\varkappa+1} \frac{1}{s^3} \right] dS, \end{aligned}$$

where $s^2 = 1 - 2tc + t^2$, $t = r/R$, $c = \cos \gamma = \cos \theta \cos \theta' + \sin \theta \sin \theta' \cos(\varphi - \varphi')$, $\xi = c_{,\theta}$, $\eta = c_{,\varphi}(\sin \theta)^{-1}$. Integrals $I^\omega s^{-\alpha}$ are integral representations of the Appell hypergeometric function [6].

Analogous results are obtained for the case of the Stokes flow [13].

5 CONCLUSION

In this paper the theory of the Moisil-Theodorescu system in terms of regular quaternionic functions of reduced quaternionic variable is used. The analogues of positive powers (inner spherical monogenics) are investigated: the set of recurrence formulas between the inner spherical monogenics and the explicit formulas are established in Cartesian coordinates. Unlike [11], we used another notion of primitive of regular function. Therefore, we have another version of three-dimensional quaternionic analogue of the complex Kolosov-Muskhelishvili formulae. As applications the problem of elastic sphere equilibrium in the case of normal displacements is solved. The solution is expressed in terms of one harmonic function, which is the solution of the Dirichlet problem with the boundary condition as in the original problem. This solution is also expressed in terms of quadratures of elementary functions and the Appell hypergeometric function.

The reported study was funded by RFBR according to the research project N 15-41-05081.

REFERENCES

- [1] F. Brackx, R. Delanghe, and F. Sommen: Clifford Analysis, Research Notes in Mathematics No. 76. Pitman, London, 1982.
- [2] K. Gürlebeck, K. Habetha and W. Sprößig: Holomorphic functions in the plane and n-dimensional space. Birkhauser Verlag, Basel–Boston–Berlin, 2008.
- [3] M. Ku, U. Kähler and D.S. Wang: Riemann boundary value problems on the sphere in Clifford analysis. Advances in Applied Clifford Algebras, Volume 22, Issue 2, 365–390, 2012.
- [4] F. Colombo, I. Sabadini and D.C. Struppa: Slice monogenic functions. Israel Journal of Mathematics, vol. 171, no. 1, 385–403, 2009.
- [5] G. Gentili, C. Stoppato and D. Struppa: Regular Functions of a Quaternionic Variable. Springer, Heidelberg–New-York–Dordrecht–London, 2013.
- [6] Yu. Grigor'ev: Three-dimensional Quaternionic Analogue of the KolosovMuskhelishvili Formulae. Hypercomplex Analysis: New Perspectives and Applications. Trends in Mathematics, (Eds. S. Bernstein, U. Kaehler, I. Sabadini, F. Sommen), Birkhauser, Basel, 2014, 145-166.
- [7] S. Bock, K. Gürlebecka, D. Legatiuk and H.M. Nguyen: ψ -Hyperholomorphic functions and a KolosovMuskhelishvili formula. Mathematical Methods in the Applied Sciences, Mart 12, 2015, dx.doi.org/10.1002/mma.3431.
- [8] Yu.M. Grigor'ev and V.V. Naumov: Approximation theorems for the Moisil-Theodorescu system. Siberian Mathematical Journal, September-October, Volume 25, Issue 5, 693–701, 1984.
- [9] Yu.M. Grigor'ev and V.V. Alekhin: A quaternionic boundary element method. Sib. jurn. industr. matem. [in Russian], Vol. 2, No. 1, Inst. Matem. Sib. Otd. Akad. Nauk SSSR, Novosibirsk, 47–52, 1999.
- [10] K. Gürlebeck, K. Habetha and W. Sprößig: Quaternionic Calculus for Engineers and Physicists. John Wiley & Sons, Cinchester, 1997.
- [11] S. Bock and K. Gürlebeck, *On a spatial generalization of the Kolosov–Muskhelishvili formulae*. Mathematical Methods in the Applied Sciences, Vol. 32, Issue 2 (2009), 223–240. DOI: 10.1002/mma.1033.
- [12] Yu.M. Grigor'ev: Solution of a problem for an elastic sphere in a closed form. Dynamics of Continuous Medium [in Russian], Inst. Hidrodin. Sib. Otd. Akad. Nauk SSSR, Novosibirsk, No. 71, 1985, 50–54.
- [13] Yu. Grigoriev: Radial integration method in quaternion function theory and its applications, AIP Conference Proceedings, **1648**, 2015, 440003.

ROBUST SCHEDULING IN CONSTRUCTION ENGINEERING

V. Hartmann^{*1}, **K. Smarsly**¹ and **T. Lahmer**²

¹*Computing in Civil Engineering
Bauhaus University Weimar, Germany
Email: veronika.hartmann@uni-weimar.de*

²*Optimization and Stochastics
Bauhaus University Weimar, Germany*

Keywords: Construction Scheduling, Robustness, Uncertainties, Optimization.

Abstract. *In construction engineering, a schedule's input data, which is usually not exactly known in the planning phase, is considered deterministic when generating the schedule. As a result, construction schedules become unreliable and deadlines are often not met. While the optimization of construction schedules with respect to costs and makespan has been a matter of research in the past decades, the optimization of the robustness of construction schedules has received little attention. In this paper, the effects of uncertainties inherent to the input data of construction schedules are discussed. Possibilities are investigated to improve the reliability of construction schedules by considering alternative processes for certain tasks and by identifying the combination of processes generating the most robust schedule with respect to the makespan of a construction project.*

1 INTRODUCTION

To set up construction schedules, knowledge about construction methods, process durations, resources, and boundary conditions is required. When a construction schedule is set up, much data is not exactly known, i.e. the schedule is created based on estimated data. Nevertheless, the common scheduling method in construction management, the Critical Path Method (CPM), treats all input data as deterministic and thus neglects uncertainties inherent to the input data. Changes and deviations from the initial schedule, which occur in the construction phase, are therefore highly probable and, in fact, construction schedules are known to be unreliable. The unreliability of construction schedules poses a serious problem in construction engineering, because construction projects involve many different stakeholders. Common objectives in construction scheduling are the minimization of costs and time, i.e. the makespan. Due to changes during the construction phase, these optimized values are often not met. Therefore, this study aims at investigating methods to set up more reliable schedules by maximizing schedule robustness with respect to the makespan.

Robustness is a term that is widely used and needs to be specified depending on the context. In this work, a robust schedule is a schedule for which the actually realized makespan deviates only little from the initially determined value, even if the input data deviates significantly from the estimations made during the planning phase. To assess the robustness of a schedule, the uncertainties inherent to the input data must be taken into account. Although these uncertainties are different in nature (e.g. unknown weather conditions, unexpected soil conditions, availability of resources, etc.), their effect can well be modelled by variable instead of deterministic process durations. To quantify the robustness of a schedule, a criterion comparing the makespan determined with deterministic data to the makespan determined with variable process durations needs to be defined.

Optimization of schedule robustness has been investigated in different domains. Usually, the robustness of a schedule is improved by varying the order of tasks. In the case of construction schedules, however, the order of tasks is typically not variable but fixed due to the specific boundary conditions. Instead, there often exist alternative processes for some tasks, but the choice of a certain process is usually made based on cost and time efficiency. In this work, the choice amongst alternative processes is investigated with respect to their influence on schedule robustness. It should be emphasized that not the robustness of separate processes is assessed, but the robustness of the combination of different alternative processes of a certain schedule. In the following, a short overview of existing literature concerning schedule robustness is given, and a method is presented for assessing and improving schedule robustness providing alternative processes.

2 SCHEDULE ROBUSTNESS

A common method in construction management to determine deadlines and makespans is the Critical Path Method (CPM). A network plan is drawn and, with process durations considered deterministic, the makespan is calculated as the length of the longest path in the network. As, at the time of generating the schedule, much input data is not yet exactly known but estimated, deviations from the initial schedule during the realization phase are highly probable. The so called Program Evaluation and Review Technique (PERT) has been developed almost at the same time when CPM has been proposed. PERT chooses a stochastic approach with process durations defined by distribution functions. Due to simplifications made

for the computation of the makespan based on stochastic process durations, the mean value and the standard deviation of the makespan are underestimated. Therefore, although considering uncertainties, PERT does not result in more reliable schedules than the purely deterministic CPM. In addition to stochastic approaches, fuzzy methods have also been investigated for scheduling problems [1]. An overview of scheduling under uncertainties can be found in [2].

Robust scheduling is a term that requires further specification depending on the context. In literature, different robustness criteria have been defined, depending on the characteristics of the schedule that is meant to be robust. In [3], the sum of weighted differences between actual and planned process start times based on process durations defined by distribution functions is used. The author of [4] investigates the number of processes that are affected by changing one process duration. In [5], a criticality index based on fuzzy process durations is defined, which measures the probability for a path to become the critical path. These examples illustrate that robustness has manifold aspects and cannot be assessed by one general criterion.

Optimization of schedules for certain robustness criteria can also be found in the domains of single machine problems and vehicle routing problems, as reported, e.g., in [6], [7], and [8]. Usually, the investigated problems require the identification of the optimal sequence of processes without processes running in parallel. However, in construction scheduling, the sequence of processes is largely predefined and many processes are running in parallel. The presented work investigates the potential of alternative processes and their combinations in order to optimize schedule robustness.

3 ASSESSMENT AND OPTIMIZATION OF THE ROBUSTNESS OF CONSTRUCTION SCHEDULES

In this study, the robustness of construction schedules is assessed as the insensitiveness of the makespan towards changes in process durations. It is assumed that the order of tasks is fixed, but that for some tasks there is an option of choosing between two or more alternative tasks. First, a model is developed to represent a schedule with variable process durations and alternative processes. Second, a criterion is defined to assess the schedule robustness, to be used as objective function in an optimization algorithm, to identify the most robust combination of alternative processes.

3.1 Modelling schedules with uncertainties and alternative processes

The schedule is represented by a simple, directed graph, with the set of vertices being a set of events and the set of edges being a set of tasks. A task represents the transformation from the as-is state into the target state, the states being described in the corresponding start and end events respectively. For the realization of a task, two or more alternative processes may exist, i.e., each task may have a set of processes from which one process is finally chosen. For n tasks with m alternative processes each, this leads to m^n possible combinations of processes. A vector c is defined, with the i -th element of the vector identifying the index of the process that is chosen for task i from its set of alternatives processes. This is an efficient way of representing possible combinations of processes. Uncertainties inherent to the input data are taken into account by assuming all process durations to be normally distributed random variables. Each edge of the graph is weighted by the duration of the represented process.

3.2 Assessing the effect of variable process durations

The effect of variable process durations on deadlines and makespans is investigated. For this purpose, a criterion is defined that compares the makespan determined based on deterministic

process durations, in the following labeled m^{ref} , with the makespan reflecting variable process durations, in the following labeled M^{unc} . The variable process durations are described by normal distributions, with σ , defined by the project manager, describing the risk that the duration will deviate from its most probable value and μ set to the most probable value. m^{ref} is calculated based on the most probable values that are considered to be deterministic; it is therefore a discrete value and corresponds to the value calculated with traditional approaches. M^{unc} is determined via a Monte Carlo simulation and is described by a normal distribution. The mean value of M^{unc} , μ^{unc} , might equal m^{ref} , but only if there is a dominant critical path. As soon as deviations in the process durations trigger a change of the critical path, μ^{unc} becomes larger than m^{ref} . The criterion to quantify the difference between m^{ref} and M^{unc} is defined as the difference of the 95% quantile of the distribution representing M^{unc} and the reference makespan m^{ref} :

$$R = Q_{95}^{unc} - m^{ref} \quad (1)$$

3.3 Optimizing schedule robustness

The robustness criterion defined above is used as objective function for the optimization of the schedule robustness. The most robust combination of processes is identified with a genetic algorithm to avoid the time-consuming computation of each possible combination.

The indices of the chosen processes in one possible combination are contained in the vector \mathbf{c} mentioned above. The i -th element of \mathbf{c} contains the index of the process chosen for task t_i out of its set of alternative processes. The vector \mathbf{c} is considered as an „individual“ within the genetic algorithm, the elements being its „genes“. Eq. (1) is used to evaluate the fitness of the individuals. For each individual, the determination of the fitness value requires the computation of m^{ref} and M^{unc} involving a Monte Carlo simulation for the calculation of M^{unc} . Starting from a randomly generated initial population, the genetic algorithm, through crossover and mutation, identifies the combination of processes that is robust with respect to the criterion defined in Eq. (1).

4 CASE STUDY

To validate the method proposed in this work, several network plans have been tested within a case study. The defined robustness criterion takes into account the susceptibility of the schedule for changes in the critical path, reflected by the difference between m^{ref} and μ^{unc} . It should be mentioned that, as a consequence, the most robust combination is not generated by simply choosing for each task the most robust process from its set of alternative processes. The described method is able to consider the situation appropriately. For details, the interested reader is referred to [9].

5 CONCLUSIONS AND OUTLOOK

The effects of uncertainties inherent to the input data of construction schedules have been discussed. A model has been developed that takes into account these uncertainties, describing the process durations with distribution functions instead of discrete values. At the same time, the model allows for considering alternative processes for each task. For a defined robustness criterion, quantifying the influence of uncertainties in process durations on the makespan, the most robust combination of alternative processes is identified by applying a genetic algorithm. In a case study, the effectiveness of the proposed method could be demonstrated. In future

research efforts, the effect of correlations of processes as well as the effect of different stochastic distributions may be investigated. Given the conflict between the total length of the planned makespan m^{ref} and the schedule robustness, additional work may envisage a reasonable trade-off between minimizing m^{ref} and maximizing the schedule robustness.

6 ACKNOWLEDGMENTS

The authors would like to acknowledge the generous support provided by the *Thüringer Graduiertenförderung*, a program of the Free State of Thuringia, Germany, supporting Ph.D. students.

7 REFERENCES

- [1] F. A. Lootsma (1989). Stochastic and fuzzy PERT. *European Journal of Operational Research*. 43. pp. 174-183.
- [2] W. Herroelen and R. Leus (2005). Project Scheduling Under Uncertainty. Survey and Research Potential. *European Journal of Operational Research*. 165(2). pp. 289-306.
- [3] S. Van de Vonder, F. Ballestin, E. Demeulemeester and W. Herroelen (2007). Heuristic procedures for reactive project scheduling. *Computers and Industrial Engineering*. 52(1). pp. 11-18.
- [4] N. Policella (2005). Scheduling with Uncertainty - A Proactive Approach using Partial Order Schedules. *Ph.D. Thesis*. Rome, Italy: Università degli Studi di Roma La Sapienza.
- [5] S. Chanas and P. Zielinski (2001). Critical path analysis in the network with fuzzy activity times. *Fuzzy Sets and Systems*. 122. pp. 195-204.
- [6] M. Seveaux and K. Sörensen (2002). A genetic algorithm for robust schedules in a just-in-time environment. *Research Report LAMIH/SP-2003-1*. University of Valenciennes, France.
- [7] K. Sörensen and M. Seveaux (2009). A practical approach for robust and flexible vehicle routing using metaheuristics and Monte Carlo sampling. *Journal of Mathematical Modelling and Algorithms*. 8(4). pp. 387-407.
- [8] M. König (2011). Generation of robust construction schedules using evolution strategies. In: *Proceedings of the 2011 EG-ICE Workshop*. University of Twente, Twente, The Netherlands, July 6, 2011.
- [9] V. Hartmann, T. Lahmer and K. Smarsly (2015). Assessment and optimization of the robustness of construction schedules. In: *Proceedings of the 22nd EG-ICE Workshop 2015*. Eindhoven, The Netherlands, July 13, 2015.

OPTIMAL SENSOR LOCATION FOR PARAMETER IDENTIFICATION IN SOFT CLAY

R. Hölter*, E. Mahmoudi and T. Schanz

**Chair for Foundation Engineering, Soil and Rock Mechanics
Ruhr-Universität Bochum, Germany
E-mail: Raoul.Hoelter@rub.de*

Keywords: Parameter identification, Global sensitivity analysis, Variance based method, Sensor localisation, Soft soil behaviour.

Abstract. *Performing parameter identification prior to numerical simulation is an essential task in geotechnical engineering. However, it has to be kept in mind that the accuracy of the obtained parameter is closely related to the chosen experimental setup, such as the number of sensors as well as their location. A well considered position of sensors can increase the quality of the measurement and to reduce the number of monitoring points. This Paper illustrates this concept by means of a loading device that is used to identify the stiffness and permeability of soft clays. With an initial setup of the measurement devices the pore water pressure and the vertical displacements are recorded and used to identify the afore mentioned parameters. Starting from these identified parameters, the optimal measurement setup is investigated with a method based on global sensitivity analysis. This method shows an optimal sensor location assuming three sensors for each measured quantity, and the results are discussed.*

1 INTRODUCTION

Identifying the correct soil parameters is essential to perform a reasonable numerical simulation of a geotechnical problem. As the behaviour of soft clay is very complex, laboratory experiments are required to determinate its parameters. Therefore, for these experiments a correct planning is necessary and can be decisive for the quality of the gained results. The methodology of optimal experimental design (OED) is not established in the field of geotechnical engineering and few examples are known from civil engineering [1]. Other scientific fields use this technique to improve the significance of their experiments (for instance see [2] and [3]) During this study, the question is: “Where should the vertical displacement and the pore water pressure be measured in an experimental device to identify the soil’s parameters most precisely?” Translated to the way of thinking of the OED, the variable parameters are the spacial coordinates of the sensor location and the corresponding parameter space is the boundaries of the loading apparatus. To detect these sensor locations, this study’s approach is to use the global sensitivity analysis (GSA). This method indicates by which parameter a certain output is influenced and is well proven in geotechnical engineering (see [4] and [5]). In this method, to precisely identify parameters, it is necessary that the output of interest has a high sensitivity towards the used parameter. Consequently, when comparing the sensitivity of the same parameter in different points, the point that indicates the highest sensitivity should be most suitable for the parameter identification.

2 EXPERIMENTAL PROGRAM

The numerical model that is presented in the next chapter simulates a cross section of the experimental devise corresponding to the left part of figure 1. This device and its operating mode have been presented first in [6]. The right wall of the box in this cross section is impermeable as well as the left one and the membrane between water and soil area at the top that separates the soil from the water. During the whole process displacement of soil medium is recorded in the cross-marked spots, while the pore water pressure (u_w) is recorded by three pressure transducers below the loading plate. The dark grey area represents the examined reconstituted Kasaoka clay that is initially consolidated by means of the uniformly distributed air and water pressure on top. The main experiment is started by applying 30 kPa by the loading plate on one side of the soil specimen. Afterwards a consolidation time of one hour takes place. Then the process of increasing load and consolidation is repeated two more times, leading to a total loading of 90 kPa. The experiment is concluded by a 100 hours consolidation, leading to a total dissipation of the developed u_w . The dissipation excess pore water pressure occurs via the permeable boundary at the bottom.

3 NUMERICAL FORWARD MODEL

Soft soils and especially clay have an explicit time depending hydro-mechanical behaviour. That means structures built on clayey soils do not only exhibit large settlements right after loading process, but some settlements can take place over a very large time period, known as consolidation. In the present work the modified cam clay model [12] is selected to simulate the current case. It has six constant parameters, as follows: the compression index λ (\equiv loading

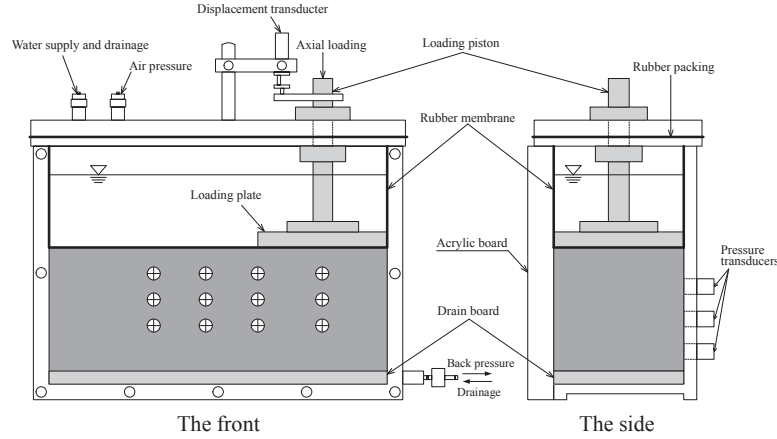


Figure 1: Experimental device [6]

stiffness), the swelling index κ (\equiv unloading stiffness), the slope of critical state line M , the Poisson ratio ν , the permeability $k_x = k_y$ (initially constant in both directions), and the change ratio of permeability due to reduction of void ratio c_k .

The experimental process was simulated in a 2D-model created with the FEM-based code Plaxis 2D. The boundaries on the sides are assumed to be fixed and impermeable, while the bottom allows no deformations but is permeable. The top boundary is impermeable to consider the rubber membrane. The distributed loads that are applied to model the water pressure and the loading plate can cause displacements.

4 PARAMETER IDENTIFICATION

To capture any possible combination, the ranges for the parameter identification were explicitly chosen very large, corresponding to [7] and [8]. Out of these ranges, 100 parameter samples using latin hypercube sampling were created. The numerical model was run for each parameter sample and the u_w and U_y values were recorded at the end of the loading and consolidation phases. As performing parameter identification within an optimisation analysis process needs to run hundreds times the model a huge amount of time or computational effort is needed. Therefore, a metamodel is trained out of the input and output data, based on a mathematical function, namely the least square method to substitute the numerical model. In this way the optimisation algorithm can be applied to any parameter combination in a very short time, without need of running the time consuming FE-code.

To find the optimal parameter set the least square method is defined as objective function, reducing the distance between the simulated and measured values of U_y and u_w in the three points below the loading plate (figure 1). The process of optimisation itself is performed using the generic algorithm within the “Matlab Optimization tool ” [9].

After being identified these parameters are applied in the numerical forward model and the resulting curves for the u_w and U_y are plotted in figure 2. Regarding the curves describing the u_w -distribution, a high agreement can be seen between the measurements and their corresponding simulation data, especially after the last loading. The displacement curves in the right part of figure 2 show qualitatively good result and the final values at the end of the final consolidation are almost matched. During the loading phases the settlement grow to fast indeed. The aspect

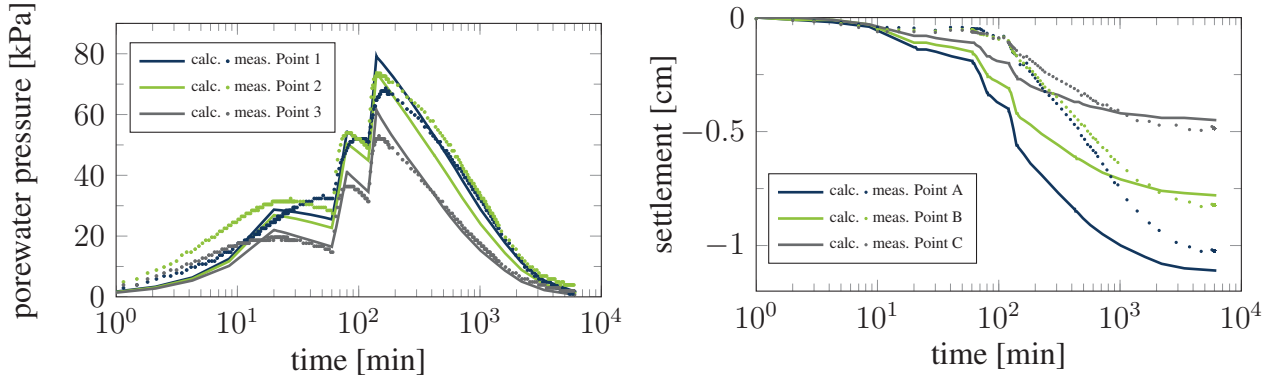


Figure 2: Optimised simulation data for u_w and U_y versus time

that has to be considered is that maybe the measurements from the three points that were used to identify the parameter do not contain enough information to perform a reliable identification. This is the initial thought that motivates the current work.

5 IDENTIFICATION OF OPTIMAL SENSOR LOCATIONS

5.1 Determination of sensitivity distribution

The basic definition of sensitivity analysis is the study of how uncertainty in the output of a model (numerical or otherwise) can be apportioned to different sources of uncertainty in the model input [10]. Global sensitivity analysis was run in this study by variance based method. The main idea of variance based methods VB is to evaluate how the variance of inputs contribute into the variance of the model output. The total effect sensitivity index S_{Ti} is a more comprehensive index which indicates the influence of input factors and their coupling terms with the other input factors. The procedure for calculation of first order and total effect sensitivity indexes has been presented by Saltelli [10].

The results of the GSA in a point below the loading are shown in figure 3. As the most important parameters are the permeability k and the loading stiffness λ , the ongoing work focusses on these parameters. For the GSA, it is necessary to have a variation of the input parameters and therefore changing results. However, as the soil parameters are already identified, the parameter ranges can be reduced and the correlation between stiffness and permeability is considered to have a more accurate soil behaviour description. For the following GSA 100 samples of permeability are created within the reduced range of $[1.3E - 9 - 1.3E - 8]$. The corresponding stiffness values are generated, according to [12] and [11], resulting in a range for λ of $[0.251 - 0.361]$. All of these parameter samples are run in the numerical forward model to create a metamodel as described in section 4. The difference is that this time the results are not only recorded in one point, but for 152 locations, distributed over the whole system, but concentrated below the loading area. Subsequently, GSA is performed in each of these points for U_y and u_w with respect to the permeability k and the stiffness λ to gain the sensitivity indices S_{Ti} .

As the parameter identification is based on real measurement values which include an uncertainty, the results are falsified. Assuming that the uncertainty is a first order error, the larger the measured values are, the higher the reliability of these values are. Therefore it is reasonable to consider not only the sensitivity but also the variance of a certain output by multiplying them with each other.

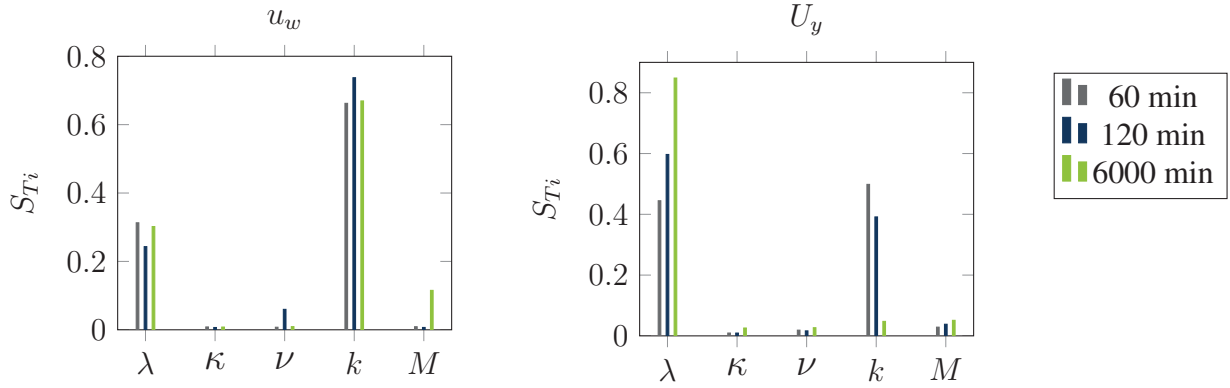


Figure 3: GSA-indices S_{T_i} for point P1

6 RESULTS

The output of the 100 FE- simulations which were used to create the metamodel are also used to compute the variance of both output values of outputs in each of the mentioned 152 points. Finally, the variance of each point is multiplied with the corresponding sensitivity index $S_{T_i}(x, y)$. The results are displayed as contour plots presenting the product, distributed over the whole space of the experimental surface (see figure 4). In case (a) a large area of high sensitivity can be seen below the loading area with even increasing sensitivity in lower areas. Below the loading plate u_w has its highest values, but is strongly related to the applied load on top and less to the permeability k . The only possibility for u_w to dissipate is through the boundary at the bottom of the experimental device. The explanation for the shape of figure 4(b) is closely related to figure 4(a). The time point that is considered is at the end of a simultaneous loading and consolidation phase, which means below the loading plate u_w is high and the presence of excess pressure prevents soil-stiffness induced settlements. In the bottom area u_w can dissipate and soil deformation is again related to the stiffness λ .

At the position $(x = 0.15, y = 0.095)$ the settlements are quite small, as this describes the limit of the loading area. However in this point not only compression takes place, but here there are also shear stress. This shear stress influences the void ratio and according to [11] and [12] the change in void ratio also changes the soil's stiffness and its permeability. This explains the shape of the plots figure 4(c) and (d), as there the most sensitive behaviour is observed in the same mentioned area.

According to the gained results one could suggest measurement devices for the vertical displacements at the positions $(0.15, 0.095)$, $(0.18, 0.03)$, and $(0.21, 0.095)$. The measurement of u_w could be useful at $(0.15, 0.095)$, $(0.18, 0.01)$, and $(0.21, 0.01)$. One should consider that technical feasibility can be limiting when rearranging the sensors, especially in areas near the boundaries. Having such information could help to reduce uncertainties and computational work as the employed data is reduced.

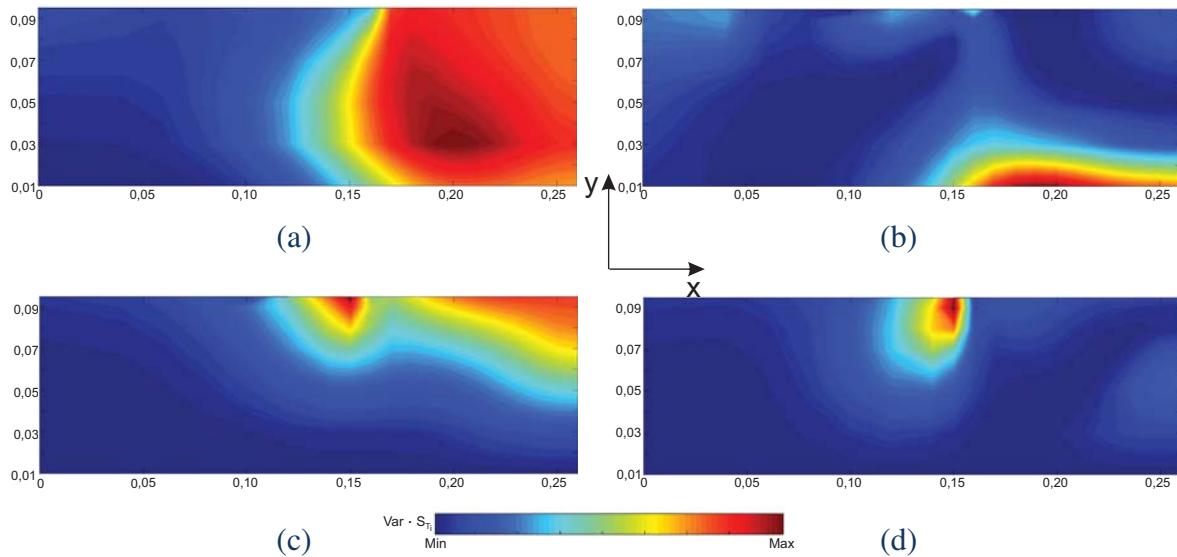


Figure 4: Sensitivity distribution for u_w towards k (a) and λ (b), and for U_y towards k (c) and λ (d)

REFERENCES

- [1] T. Lahmer: Optimal experimental design for nonlinear ill-posed problems applied to gravity dams. *Journal of Inverse Problems*, **27** (12), 2011.
- [2] R. Schenkendorf: Optimal Experimental Design for Parameter Identification and Model Selection. Phd-Thesis, Otto-von-Guericke-Universität Magdeburg, 2014.
- [3] D. Uciński: Optimal Measurement Methods for Distributed Parameter System Identification. CRC Press, Boca Raton, 2005.
- [4] S.Miro, D. Hartmann and T. Schanz: Global sensitivity analysis for subsoil parameter estimation in mechanized tunneling. *Computers and Geotechnics*, **56**, 80–88, 2014
- [5] K. Khaledi, E. Mahmoudi, M. Datcheva, D. König, T. Schanz: Sensitivity analysis and parameter identification of a time dependent constitutive model for rock salt. *J. of Comp. and App. Mathematics*, In Press, Accepted Manuscript.
- [6] S. Nishimura, T. Shuku and K. Fujisama: Prediction of Multidimensional Deformation Behavior Based on Observed Values. *Int. J. Geomech.*, **40** (3), 401–411, 2014.
- [7] J.E. Bowles: *Foundation Analysis and Design*. McGraw-Hill, London, 2001.
- [8] B.M. Das: *Principles of Geotechnical Engineering*. Thomson, Toronto, 2006.
- [9] J.H. Holland: *Adaptive in Natural and Artificial Systems*. University of Michigan Press, Ann Arbor, 1975.
- [10] A. Saltelli et al.: *Global Sensitivity Analysis: The Primer*. John Wiley, New York, 2008.
- [11] D. W. Taylor: *Fundamentals of Soil Mechanics*. John Wiley, New York, 1948.
- [12] A. N. Schofield and C. P. Wroth: *Critical state soil mechanics*, McGraw-Hill, London, 1968.

THE RELATIONSHIP BETWEEN LINEAR ELASTICITY THEORY AND COMPLEX FUNCTION THEORY STUDIED ON THE BASIS OF FINITE DIFFERENCES

A. Hommel* and K. Gürlebeck

**University of Applied Sciences Zwickau
Faculty of Economics; post office box 201037; 08012 Zwickau
E-mail: angela.hommel@fh-zwickau.de*

Keywords: Finite Differences, Discrete Holomorphic Functions, Discrete Polynomials.

Abstract. *It is well-known that the solution of the fundamental equations of linear elasticity for a homogeneous isotropic material in plane stress and strain state cases can be equivalently reduced to the solution of a biharmonic equation. The discrete version of the Theorem of Goursat is used to describe the solution of the discrete biharmonic equation by the help of two discrete holomorphic functions. In order to obtain a Taylor expansion of discrete holomorphic functions we introduce a basis of discrete polynomials which fulfill the so-called Appell property with respect to the discrete adjoint Cauchy-Riemann operator. All these steps are very important in the field of fracture mechanics, where stress and displacement fields in the neighborhood of singularities caused by cracks and notches have to be calculated with high accuracy. Using the sum representation of holomorphic functions it seems possible to reproduce the order of singularity and to determine important mechanical characteristics.*

1 INTRODUCTION

We are interested in problems of fracture mechanics, where stress and displacement fields in the neighbourhood of singularities caused by cracks and notches have to be calculated. The relationship between linear elasticity theory and complex function theory is studied based on finite differences. Using the well-known forward and backward differences we define difference operators and describe discrete harmonic as well as discrete holomorphic functions. An important result is the discrete theorem of Goursat. In order to get a representation formula for the components of the displacement vector near the singularities we use discrete polynomials which fulfill the so-called Appell property with respect to the adjoint discrete Cauchy-Riemann operator and introduce a Taylor expansion of discrete holomorphic functions.

2 THE EQUIVALENCE BETWEEN SOLUTIONS OF EQUATIONS IN LINEAR ELASTICITY THEORY AND SOLUTIONS OF A DISCRETE BIHARMONIC EQUATION

We study the finite difference equations

$$\begin{aligned}\mu \Delta_h u_0 + (\lambda + \mu) D_h^{-1} e &= 0 \\ \mu \Delta_h u_1 + (\lambda + \mu) D_h^{-2} e &= 0,\end{aligned}\tag{1}$$

which approximate the well-known Lamé equations in the bounded domain G . We consider a uniform lattice $\mathbf{R}_h^2 = \{mh = (m_1h, m_2h) \text{ with } m_1, m_2 \in \mathbf{Z}\}$ and the mesh width h and denote by $G_h = (G \cap \mathbf{R}_h^2)$ the discrete domain. The vector components of the external forces are equal to zero and u_0 and u_1 describe the components of the displacement vector u . We define by Δ_h the discrete Laplace operator with

$$\begin{aligned}\Delta_h u(m_1h, m_2h) &= -4h^{-2}u(m_1h, m_2h) + h^{-2}u((m_1 - 1)h, m_2h) \\ &+ h^{-2}u((m_1 + 1)h, m_2h) + h^{-2}u(m_1h, (m_2 - 1)h) + h^{-2}u(m_1h, (m_2 + 1)h)\end{aligned}$$

and consider forward and backward differences in the form

$$\begin{aligned}D_h^1 u(m_1h, m_2h) &= h^{-1}(u((m_1 + 1)h, m_2h) - u(m_1h, m_2h)) \\ &= D_h^{-1} u((m_1 + 1)h, m_2h) \quad \text{and}\end{aligned}$$

$$\begin{aligned}D_h^2 u(m_1h, m_2h) &= h^{-1}(u(m_1h, (m_2 + 1)h) - u(m_1h, m_2h)) \\ &= D_h^{-2} u(m_1h, (m_2 + 1)h).\end{aligned}$$

In detail, $e = D_h^1 u_0 + D_h^2 u_1$ and

$$\mu = \frac{E}{2(1 + \nu)}, \quad \lambda = \frac{E\nu}{(1 + \nu)(1 - 2\nu)}, \quad \lambda + \mu = \frac{\mu}{1 - 2\nu},$$

where E is the elasticity modul, ν the strain number and μ the shear modulus. For the system (1) we use the discretized ansatz of Papkovic-Neuber

$$\begin{aligned}2\mu u_0 &= -D_h^{-1} \Theta + 2\alpha \Phi_1 \\ 2\mu u_1 &= -D_h^{-2} \Theta + 2\alpha \Phi_2\end{aligned}\tag{2}$$

with the stress function Θ , the material constant α and the discrete harmonic functions Φ_1 and Φ_2 . By substituting (2) into (1) we obtain

$$\begin{aligned} D_h^{-1} \left(\frac{2\mu}{(1-2\nu)} e - \Delta_h \Theta \right) &= 0 \\ D_h^{-2} \left(\frac{2\mu}{(1-2\nu)} e - \Delta_h \Theta \right) &= 0, \end{aligned}$$

because Φ_1 and Φ_2 are discrete harmonic. Consequently, the gradient of the expression in parenthesis is equal to zero and therefore the expression must be a constant. Similar to the classical theory it can be assumed that this constant is equal to zero. Therefore we have

$$2\mu e = (1-2\nu)\Delta_h \Theta. \quad (3)$$

From $e = D_h^1 u_0 + D_h^2 u_1$ and (2) it follows

$$2\mu e = -\Delta_h \Theta + 2\alpha (D_h^1 \Phi_1 + D_h^2 \Phi_2). \quad (4)$$

By comparing (3) and (4) we obtain

$$2(1-\nu)\Delta_h \Theta = 2\alpha (D_h^1 \Phi_1 + D_h^2 \Phi_2). \quad (5)$$

Consequently, the solution Θ consists of one part $\Phi_0 \in \ker \Delta_h$ and an inhomogeneous part in relation with equation (5). Based on this result we write the discrete stress function in the form

$$\Theta = \Phi_0 + \Phi_1 \cdot m_1 h + \Phi_2 \cdot m_2 h - A_1$$

with $\Delta_h \Phi_0 = \Delta_h \Phi_1 = \Delta_h \Phi_2 = 0$ and $\Delta_h A_1 = -h D_h^1 D_h^{-1} \Phi_1 - h D_h^2 D_h^{-2} \Phi_2$. We can prove that the equation

$$\Delta_h \Theta = 2(D_h^1 \Phi_1 + D_h^2 \Phi_2)$$

holds and together with (5) we obtain $\alpha = 2(1-\nu)$. Finally it follows from (5)

$$\Delta_h \Delta_h \Theta = 2D_h^1 \Delta_h \Phi_1 + 2D_h^2 \Delta_h \Phi_2 = 0,$$

the important property of the stress function Θ .

Using forward and backward differences we define discrete Cauchy Riemann operators by

$$D^{1h} = \begin{pmatrix} D_h^{-1} & -D_h^2 \\ D_h^{-2} & D_h^1 \end{pmatrix} \quad \text{and} \quad D^{2h} = \begin{pmatrix} D_h^1 & D_h^2 \\ -D_h^{-2} & D_h^{-1} \end{pmatrix}.$$

We remark that we have a factorization of the discrete Laplacian in the form

$$D^{1h} D^{2h} = \begin{pmatrix} \Delta_h & 0 \\ 0 & \Delta_h \end{pmatrix}$$

and D^{1h} approximates the classical operator $\frac{\partial}{\partial x} + i \frac{\partial}{\partial y}$ while D^{2h} approximates $\frac{\partial}{\partial x} - i \frac{\partial}{\partial y}$.

A complex function $\varphi_h(mh) = \begin{pmatrix} p \\ q \end{pmatrix}$ is called *discrete holomorphic* if

$$D^{1h} \begin{pmatrix} p \\ q \end{pmatrix} = \begin{pmatrix} 0 \\ 0 \end{pmatrix}.$$

In detail, we look at the equation system $D_h^{-1} p = D_h^2 q$ and $D_h^{-2} p = -D_h^1 q$ which approximates the classical Cauchy-Riemann equations.

In order to manage the link between linear elasticity and complex function theory we use the discrete version of the Theorem of Goursat.

3 THE DISCRETE THEOREM OF GOURSAT

Using the group homomorphism between complex numbers $a + ib$ and matrices $\begin{pmatrix} a & -b \\ b & a \end{pmatrix}$ we are able to present the discrete version of the Theorem of Goursat.

Theorem 3.1 *Each real-valued solution $u(mh)$ of the difference equation $\Delta_h \Delta_h u(mh) = 0$ in a domain composed by rectangles which are oriented parallel to the axes can be represented by the help of two discrete holomorphic functions $\varphi_h(mh) = \begin{pmatrix} p \\ q \end{pmatrix}$ and $\psi_h(mh) = \begin{pmatrix} p_1 \\ q_1 \end{pmatrix}$ such that*

$$\begin{pmatrix} u \\ 0 \end{pmatrix} = \frac{1}{2} \left(\begin{pmatrix} m_1 h & m_2 h \\ -m_2 h & m_1 h \end{pmatrix} \begin{pmatrix} p \\ q \end{pmatrix} + \begin{pmatrix} m_1 h & -m_2 h \\ m_2 h & m_1 h \end{pmatrix} \begin{pmatrix} p \\ -q \end{pmatrix} + \begin{pmatrix} p_1 - A \\ q_1 \end{pmatrix} + \begin{pmatrix} p_1 - A \\ -q_1 \end{pmatrix} \right).$$

In this notation A is a solution of the Poisson equation $\Delta_h A = -hD_h^1 D_h^{-1} p - hD_h^2 D_h^{-2} q$. For small mesh width h the right hand side of this equation is small. The details of the proof are published in [1].

Consequently, we have on the one hand the solution of the biharmonic equation in the form

$$u = p \cdot m_1 h + q \cdot m_2 h + p_1 - A$$

with $\Delta_h A = -hD_h^1 D_h^{-1} p - hD_h^2 D_h^{-2} q$ and the discrete harmonic functions p, q and p_1 . On the other hand the discrete stress function from section 2 has the form

$$\Theta = \Phi_0 + \Phi_1 \cdot m_1 h + \Phi_2 \cdot m_2 h - A_1$$

with $\Delta_h A_1 = -hD_h^1 D_h^{-1} \Phi_1 - hD_h^2 D_h^{-2} \Phi_2$ and the discrete harmonic functions Φ_0, Φ_1 and Φ_2 . Using (2), the components of the displacement vector can be written in the form

$$\begin{aligned} 2\mu u_0 &= -(D_h^{-1} \Phi_0 + D_h^{-1}(\Phi_1 \cdot m_1 h) + D_h^{-1}(\Phi_2 \cdot m_2 h) - D_h^{-1} A_1) + 2\alpha \Phi_1 \\ &= -(D_h^{-1} \Phi_0 + D_h^{-1} \Phi_1 \cdot m_1 h + D_h^{-1} \Phi_2 \cdot m_2 h - D_h^{-1} A_1) \\ &\quad + 2\alpha \Phi_1(m_1 h, m_2 h) - \Phi_1((m_1 - 1)h, m_2 h) \end{aligned} \quad (6)$$

and

$$\begin{aligned} 2\mu u_1 &= -(D_h^{-2} \Phi_0 + D_h^{-2}(\Phi_1 \cdot m_1 h) + D_h^{-2}(\Phi_2 \cdot m_2 h) - D_h^{-2} A_1) + 2\alpha \Phi_2 \\ &= -(D_h^{-2} \Phi_0 + D_h^{-2} \Phi_1 \cdot m_1 h + D_h^{-2} \Phi_2 \cdot m_2 h - D_h^{-2} A_1) \\ &\quad + 2\alpha \Phi_2(m_1 h, m_2 h) - \Phi_2(m_1 h, (m_2 - 1)h). \end{aligned} \quad (7)$$

In order to get a Taylor expansion of the discrete holomorphic functions we introduce discrete polynomials which fulfill the so-called Appell property. This property means that the complex derivation of a basis function leads to a multiple of another basis function. More precisely, a system of polynomials $\{P^n(z)\}$ is called Appell system, if $\frac{d}{dz} P^n(z) = n P^{n-1}(z)$ with $n = 1, 2, \dots$. For more details see [3].

4 DISCRETE POLYNOMIALS

In the discrete case the polynomials defined in the next theorem fulfill the Appell property.

Theorem 4.1 For polynomials $P^n(m_1h, m_2h) = \begin{pmatrix} P_0^n(m_1h, m_2h) \\ P_1^n(m_1h, m_2h) \end{pmatrix}$ with $n \geq 1$ it holds

$$\frac{1}{2} \begin{pmatrix} D_h^1 & D_h^2 \\ -D_h^{-2} & D_h^{-1} \end{pmatrix} \begin{pmatrix} P_0^n(m_1h, m_2h) \\ P_1^n(m_1h, m_2h) \end{pmatrix} = n \begin{pmatrix} P_0^{n-1}(m_1h, m_2h) \\ P_1^{n-1}((m_1-1)h, m_2h) \end{pmatrix},$$

where

$$P_0^n = \sum_{s=0(2)}^n \binom{n}{s} (-1)^{s/2} \prod_{k=s/2}^{n-s/2-1} (m_1-k)h \prod_{l=1-s/2}^{s/2} (m_2+l)h \quad \text{and}$$

$$P_1^n = \sum_{s=1(2)}^n \binom{n}{s} (-1)^{(s-1)/2} \prod_{k=(s-1)/2}^{n-s/2-3/2} (m_1-k)h \prod_{l=(1-s)/2}^{(s-1)/2} (m_2+l)h.$$

In the following we are interested in the properties of the discrete polynomials. First of all it is easy to prove that these polynomials are discrete holomorphic. From the equation

$$\frac{1}{2} \begin{pmatrix} D_h^{-1} & -D_h^2 \\ D_h^{-2} & D_h^1 \end{pmatrix} \begin{pmatrix} P_0^n(m_1h, m_2h) \\ P_1^n((m_1-1)h, m_2h) \end{pmatrix} = \begin{pmatrix} 0 \\ 0 \end{pmatrix}$$

it follows immediately

$$\begin{aligned} & \frac{1}{4} \begin{pmatrix} D_h^{-1} & -D_h^2 \\ D_h^{-2} & D_h^1 \end{pmatrix} \begin{pmatrix} D_h^1 & D_h^2 \\ -D_h^{-2} & D_h^{-1} \end{pmatrix} \begin{pmatrix} P_0^n(m_1h, m_2h) \\ P_1^n(m_1h, m_2h) \end{pmatrix} \\ &= \frac{n}{2} \begin{pmatrix} D_h^{-1} & -D_h^2 \\ D_h^{-2} & D_h^1 \end{pmatrix} \begin{pmatrix} P_0^{n-1}(m_1h, m_2h) \\ P_1^{n-1}((m_1-1)h, m_2h) \end{pmatrix} = \begin{pmatrix} 0 \\ 0 \end{pmatrix} \end{aligned}$$

such that the polynomials are also discrete harmonic.

In the next step we prove that the discrete polynomials are linearly independent. Especially we show that the identity

$$\begin{pmatrix} P_0(m_1h, m_2h) \\ P_1(m_1h, m_2h) \end{pmatrix} := \sum_{j=0}^n a_j \begin{pmatrix} P_0^j(m_1h, m_2h) \\ P_1^j(m_1h, m_2h) \end{pmatrix} \equiv \begin{pmatrix} 0 \\ 0 \end{pmatrix}$$

is only true for all $(m_1h, m_2h) \in G_h$ with $(0, 0) \in G_h$ iff all a_j with $j = 0, \dots, n$ are equal to zero. Based on the structure of the polynomials we have

$$\begin{pmatrix} P_0(0, 0) \\ P_1(0, 0) \end{pmatrix} = \begin{pmatrix} a_0 \\ 0 \end{pmatrix}.$$

The real part is only in case $a_0 = 0$ equal to zero. By using the Appell property and a small change in the difference operator which realizes a shift from the point $((m_1-1)h, m_2h)$ to (m_1h, m_2h) we get

$$\frac{1}{2} \begin{pmatrix} D_h^1 & D_h^2 \\ -D_h^{-2} - hD_h^1 D_h^{-2} & D_h^{-1} + hD_h^1 D_h^{-1} \end{pmatrix} \begin{pmatrix} P_0(m_1h, m_2h) \\ P_1(m_1h, m_2h) \end{pmatrix} = \sum_{j=0}^n j a_j \begin{pmatrix} P_0^{j-1}(m_1h, m_2h) \\ P_1^{j-1}(m_1h, m_2h) \end{pmatrix} \equiv \begin{pmatrix} 0 \\ 0 \end{pmatrix}.$$

This identity is true at the mesh point $(m_1h, m_2h) = (0, 0)$ iff and only iff $a_1 = 0$. We repeat the application of the modified difference operator in order to prove that for all a_j , $j = 0, \dots, n$ the equation $a_j = 0$ must be fulfilled.

We show now that the polynomials can also be developed in powers of $mh - nh$. We denote by $N = N_1 \cdot N_2$ the number of inner mesh points of a rectangle G_h and investigate for fixed degree of the polynomial $n = N - 1$ the identity

$$\sum_{n_1=1}^{N_1} \sum_{n_2=1}^{N_2} a_{n_1, n_2} \begin{pmatrix} P_0^n((m_1 - n_1)h, (m_2 - n_2)h) \\ P_1^n((m_1 - n_1)h, (m_2 - n_2)h) \end{pmatrix} \equiv \begin{pmatrix} 0 \\ 0 \end{pmatrix}.$$

To this equation we add n more equations by applying step by step the modified difference operator. Based on the Appell property the degree of the polynomials becomes smaller and smaller. If we write the equation system in matrix form with complex elements and a vanishing right hand side it is clear that all a_{n_1, n_2} are equal to zero if the determinant of the matrix on the left hand side is different from zero. From this point of view it is enough to study the structure of the matrix. By transposing it becomes obviously that we consider a Vandermonde matrix. In order to show that the column vectors of the transposed matrix are linear independent we look line by line at the linear combination of these column vectors. In each row we have polynomials with increasing degree in one and the same mesh point. For these polynomials we already proved the linear independence and altogether we get this property for the whole column vector.

5 OUTLOOK

For the discrete holomorphic functions we use the Taylor expansion

$$\Phi(m_1h, m_2h) = \sum_{n=0}^{N-1} b_n P^n(m_1h, m_2h)$$

and substitute this term into the equations (6) and (7). By this way it is possible to describe the components of the displacement vector by the help of a finite sum and our polynomial basis. Another possibility in order to calculate the displacement vector is the use of the discrete Borel Pompeiu formula. For this formula we refer to [4]

REFERENCES

- [1] A. Hommel: A Discrete Theorem of Goursat. *Advances in Applied Clifford Algebras*, Vol.24, Issue 4, 1039–1045, 2014.
- [2] K. Gürlebeck, A. Hommel: Finite Difference Cauchy-Riemann Operators and Their Fundamental Solution in the Complex Case. *Operator Theory–Advances and Applications*, vol.142, 101–115, 2003.
- [3] P.E. Appell: Sur une class de polynomes. *Ann. Sci École Norm. Sup* 9,119–144, 1880.
- [4] K. Gürlebeck, A. Hommel: A Discrete Analogue of the Complex T–Operator and a Proof of the Discrete Borel–Pompeiu Formula. Preprint 1–2003 der Professur Angewandte Mathematik der Bauhaus–Universität Weimar.

PARAMETRIC GEOMETRIC MODELING IN CONSTRUCTION PLANNING USING INDUSTRY FOUNDATION CLASSES

E. Ignatova^{*1}, H. Kirschke², Eike Tauscher², and K. Smarsly²

¹*Moscow State University of Civil Engineering (MGSU)
Department of Information Systems, Technology and Automation in Construction
26 Yaroslavskoye Shosse, Moscow, Russian Federation
Email: eell2009@yandex.ru*

²*Bauhaus University Weimar
Chair of Computing in Civil Engineering
Coudraystr. 7, 99423 Weimar, Germany*

Keywords: Building Information Modeling (BIM), Parametric Geometric Modeling, Information Modeling, Industry Foundation Classes (IFC).

Abstract. *One of the most promising and recent advances in computer-based planning is the transition from classical geometric modeling to building information modeling (BIM). Building information models support the representation, storage, and exchange of various information relevant to construction planning. This information can be used for describing, e.g., geometric/physical properties or costs of a building, for creating construction schedules, or for representing other characteristics of construction projects. Based on this information, plans and specifications as well as reports and presentations of a planned building can be created automatically. A fundamental principle of BIM is object parameterization, which allows specifying geometrical, numerical, algebraic and associative dependencies between objects contained in a building information model. In this paper, existing challenges of parametric modeling using the Industry Foundation Classes (IFC) as a federated model for integrated planning are shown, and open research questions are discussed.*

1 INTRODUCTION

A characteristic feature of building information modeling is the creation of parameterized dependencies between individual objects. Parameterized dependencies allow changes in the building information model to be done automatically and simultaneously. Since, in practice, the planning process is iterative and interactive, parameterized geometric modeling is an invaluable tool to quickly and correctly change construction plans or schedules.

State-of-the-art BIM software, such as Autodesk Revit 2016 [1] and Nemetschek Allplan 2015 [2], provides a large number of default parametric dependencies, such as relationships between the coordinate axes of a building and the position of components or relationships between roof shapes and wall heights. The use of this default parameterization enables easy modifications of BIM models. Furthermore, it becomes possible to modify the description of the model (or of the construction plans or schedules, respectively). BIM software can also be used to create individual relationships between objects of a model and to develop individual data structures. However, for the following reasons, using BIM software requires expert knowledge and is thus limited to IT specialists (“BIM managers”) or to a few BIM enthusiasts:

- High psychological barrier as compared to traditional (and well-known) planning principles
- Implications of object orientation of the software products
- Lack of understanding of parametric modeling

This paper addresses the use of parametric modeling in the context of building information modeling. First, the definition of parameterization is introduced in methodological terms, followed by the description of parameterization types for geometric objects and models. Next, an overview of the parameterization types used in the area of construction planning is given. Then, the type of associative geometric parameterization in conjunction with BIM is analyzed, using an integrated planning scenario as an illustrative example. The paper concludes with a summary and a discussion.

2 METHODOLOGY

Essentially, geometric modeling is the representation of objects with respect to their shapes, dimensions, and orientations. According to Golovanov (2011), computer-aided geometric modeling “teaches the methods to create numerical models using either real geometry or the object to be depicted, as well as the methods of how to deal with such models. The geometric model contains a form description of the object to be depicted and the description of the connections between the model elements” [3].

The foundation of BIM is a 3-dimensional geometric model. However, the geometric model is not only based on some geometric primitives such as cones or cylinders; it is rather based on object-oriented elements that describe the object under construction or elements of the object, such as beams, supports, or ceiling panels. Nevertheless, geometric properties of an object, or of an object’s element, such as shapes, dimensions and orientations, are described similar to the properties of the geometric primitives.

The methodology shown in this paper supports an easy understanding of the major parametric dependencies of geometric modeling. Thus, planners are enabled to easily define simple parametric dependencies, even if only traditional CAD software instead of state-of-the-

art BIM software is used. In the following subsections, a concise literature review on parameterization is provided, followed by an overview of the parameterization types used in the area of construction planning.

2.1 A concise literature review on parameterization

Parameterization is a mathematical term that includes

- i. removal of object properties,
- ii. description of object properties with parameters, and
- iii. determination of the relationships between these parameters.

Borisov, et al. (1998) define parameterization as follows [4]: „Parameterization is a concept that includes all methods of construction planning. One important characteristic of the modern parametric design planning concept is, in particular, the ability to create geometric models with relationships and rules which can be changed and complemented at every stage of its development. The rules are defined as conditions for basic operations“. Thus, parameterization can be considered as a methodology in computer-aided construction planning, which allows, at an early stage, a conceptual design of an object to be created with defined dependencies that can, in a later stage, be adapted to changes and developments of the project. Borisov et al. (1998) have also defined terms describing the technology and the methods for creating parameterization models.

Yermilov et al. (2004) have considered the parameterization of geometric kinematic models in the design process [3]; the authors have described the advantages and foundations of parametric modeling. Koropushkin (2005) has classified parameterized models and proposed calculation algorithms for these models [6]. Erochin (2013) has studied the parameterization of geometric models in aircraft design, particularly models that allow the parameterization of shapes and their orientation in space. Also considering aircraft design, a methodology for the development of parametric models is proposed in [7]. Classifying the tasks of parameterized geometry in geometric constructions, Salkov (2014) has proposed a definition for the term „parameter“, demonstrating that parameterized geometry is founded on the method of iterative design [8]. Butorov and Eresko (2012) have presented an overview of methods for parameterized modeling, including advantages and disadvantages. Widely-used CAD systems that use parameterization have been reviewed and practical applications of computer-aided parameterized modeling have been considered in [9]. As an example of parameterization of geometric models in disciplines apart from engineering, Serjodkin et al. (2014) have investigated models and the methodology of parameterization for computer-aided design approaches in the shoe industry [10].

In summary, parameterization is widely applied in the design process and in several areas within computer-aided design (CAD), computer-aided manufacturing (CAM), and computer-aided engineering (CAE) [11,12].

2.3 Parameterization types for geometric objects and models

This subsection briefly summarizes the of parameterization for geometric objects and models.

Geometric parameterization: Geometric parameterization is the creation of topological relationships, i.e. the generation of relationships between basic geometric elements such as lines, circles, etc. Examples are the parallelism of edges, the coverage of circle centers, or strict horizontal or vertical orientation of lines. The characteristics of geometric parameterization are

not described by numerical parameters, but rather by geometric terms, such as position, alignment, direction, etc.

Numerical parameterization: Numerical parameterization enables the determination of numerical characteristics for geometric objects and their geometric shapes, for example the length of a geometric section, angular dimensions, or distances between points. The characteristics are described through parameters, which can be modified depending on the modeling task. The parameters also influence the geometric shape and the position of an object. In this sense, this type of parameterization is mainly used for describing the geometric dimensions of an object.

Algebraic parameterization: Algebraic parameterization is the creation of mathematical expressions to describe the interrelation between numerical parameters of a geometric object. Examples are the parity of geometric section lengths, the proportionality between height and width of a geometric object, and the limits of object volumes. This type of parameterization allows not only the use of geometric parameters in the algebraic expressions; it also allows considering non-geometric parameters, e.g., time, cost or physical parameters.

Associative parameterization: Associativity implies information linkage between the geometric model and other model types, objects, or processes. Examples are the detailing of model representations in different scales, the reproduction of the geometric model properties in text form, or the mapping of documents into a database. If changes to an object occur, all associated objects will change accordingly.

3 PARAMETERIZATION IN CONSTRUCTION PLANNING

Since state-of-the-art BIM software provides parametrization, the concept of parameterization is widely used in construction planning. In this section, an overview of the parameterization types used in the area of construction planning is given. Then, the types of associative geometric parameterization in conjunction with BIM are analyzed, using the IFC as a federated model within an integrated planning scenario that serves as an illustrative example.

3.1 Overview of parameterization in construction planning

Automation of standard construction procedures: Standard procedures for the geometric modeling of objects, having several dimensions, can advantageously be automated using parameterized relationships between individual objects. The overall set of relationships has to be created for the automatic recalculation of object geometries. In this way, a change in any parameter will be automatically applied to the entire model. For example, the construction of dimension lines and anchoring them to the object contour must be executed only once.

Working with variables: Using variables to parameterize the geometric shape of objects enables a simple and targeted way of model modification. Thus, the planner can quickly design and review alternative design solutions.

Calculating optimum solutions: The possibility of describing a model through parameters allows not only creating alternative options, but also computing optimum solutions, such as dimensions, building volumes, or areas.

Execution of changes: The process of construction planning in engineering practice is a distributed-cooperative process comprising of several iterations and alterations. The geometric parameterization and associative relationships allow developing construction plans or schedules in a way that any alteration can be applied immediately and provided automatically to all

parties participating in the project. At the same time, an automatic representation of all changes is possible.

Parallel planning: Parameterized geometric modeling is the foundation of cooperative work, facilitating architectural and engineering design processes, structural calculations, building installations, and construction works that can be brought together. Conceptual planning on the basis of parameterized geometric modeling enables all processes, even those associated with uncertain or undefined parameters, to be executed faster as compared to conventional approaches.

Parameterization as a programming element of properties: The process of creating and storing analytical relationships between objects is similar to the paradigm of object-oriented programming. The addition of logical and associative relationships supports the generation of project reports, bills of materials, drawings, and other project-related documents.

3.2 Parameterized modeling in the context of BIM

Summarizing the previous sections, it can be concluded that parametric modeling is an important methodology for creating building information models. Considering BIM, it should be emphasized that one of the main objectives of BIM is integrated digital construction planning, which requires the use of a standardized digital data format. This data format serves either as a federated building information model, or it provides a standardized exchange format for all participating planners. However, it is questionable if parametric modeling can be reliably supported through software applications based on a standardized data format. In the following paragraphs, this question is investigated by means of an example using the IFC as a federated model simulating a cooperative construction planning process. In the example, the cooperative construction planning process is simulated as a six-step process including different model imports and model exports, different state-of-the-art software applications (Autodesk Revit 2016 and Nemetschek Allplan 2015), and different model viewers (IFC TOOLS PROJECT Viewer [13] and Solibri Model Viewer v9 [14]).

In the first step, an initial model is created, representing the first story of a building that consists of four walls, two windows, a ceiling, and a door. Using Autodesk Revit 2016, the heights of all walls are parameterized as the distance between level 1 and level 2 (Figure 1). In other words, if the height of the first story changes, the height of all connected walls changes accordingly. Figure 1 illustrates the example, including the parameterized constraints “Base Constraint”, defining the wall’s base being parametrically connected to level 1, and “Top Constraint”, defining the wall’s top being parametrically connected to level 2.

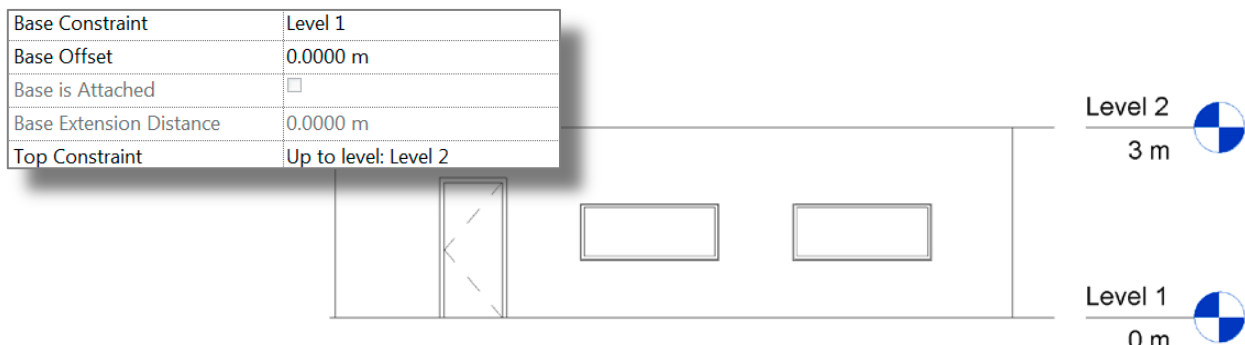


Figure 1: Autodesk Revit 2016 original file: The wall is parametrically connected to level 1 (bottom) and to level 2 (top)

In the second step, the Autodesk Revit 2016 model is exported as an IFC 2X3 file. Then, in the third step, it is reimported into the same (Autodesk Revit 2016) application. As can be seen

from Figure 2, this fairly simple task results in an inconsistent model. Specifically, the previously defined “Top Constraint” is missing, i.e. it is changed from “Up to level: Level 2” to “Unconnected”.

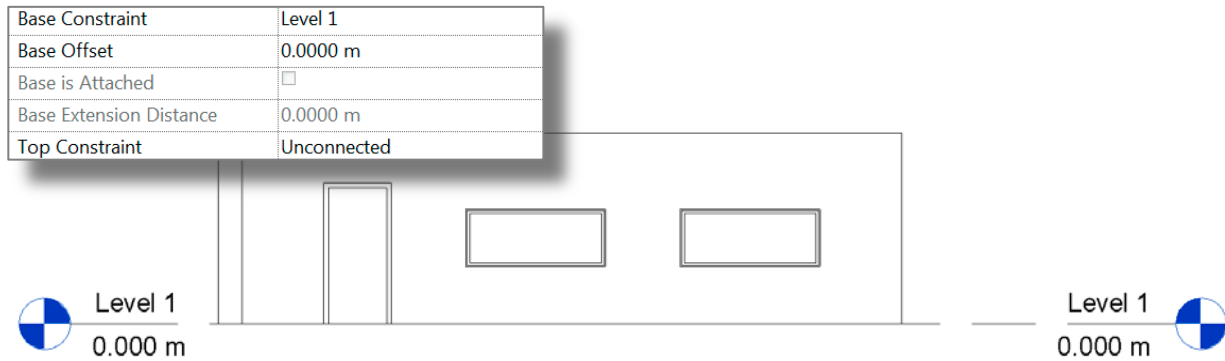


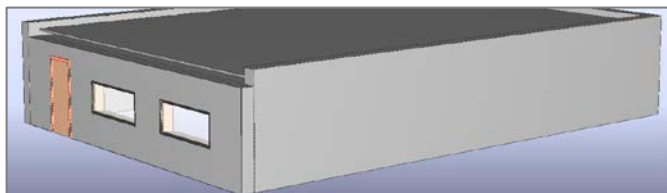
Figure 2: Result after exporting and reimporting the Autodesk Revit 2016 model as IFC 2X3 file: The wall is no longer parametrically connected to level 2 (top), and level 2 is missing

In the fourth step, the exported IFC file is evaluated. The constraints of interest is exported as user-defined IFC Property Sets, where the “Top Constraint”, as shown in Figure 3, is set to “Level: Level 2”. For this reason, the reimport should have been performed properly. However, this is not the case here (which is an assumption, because the information expressed by these Property Sets is not part of the IFC standard).

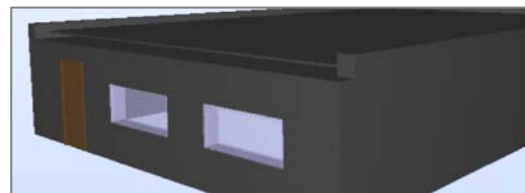
Object/Attribute	Value	Property Set	Type
Base Constraint	Level: Level 1	Constraints	IfcPropertySingleValue
Base Extension Distance	0.0	Constraints	IfcPropertySingleValue
Base Offset	0.0	Constraints	IfcPropertySingleValue
Base is Attached	false	Constraints	IfcPropertySingleValue
Location Line	Core Face: Exterior	Constraints	IfcPropertySingleValue
Related to Mass	false	Constraints	IfcPropertySingleValue
Room Bounding	true	Constraints	IfcPropertySingleValue
Top Constraint	Level: Level 2	Constraints	IfcPropertySingleValue

Figure 3: Connected Property Set of the walls (excerpt): IFC 2X3 export from Autodesk Revit 2016 (screenshot taken using the IFC TOOLS PROJECT Viewer [13])

The further steps describe a more realistic scenario, in which the previously exported IFC model, created by planner A, is provided to another participating planner B (step five). Planner B performs changes to the model using a different software product, Nemetschek Allplan 2015, in which the IFC model is imported. In the Nemetschek Allplan 2015 model, planner B shortens the wall containing the windows and the door by 40 cm. As a result, after exporting the modified Nemetschek Allplan 2015 model as IFC 2X3 file, the geometric model displays correctly (as compared with the Nemetschek Allplan 2015 model resulting from step five) as shown in Figure 4.



(a) IFC TOOLS PROJECT Viewer



(b) Solibri Model Viewer v9

Figure 4: Screenshots visualizing the modified Nemetschek Allplan 2015 model

Evaluating the IFC file exported from the Nemetschek Allplan 2015 model, it can be seen that all Property Sets created in the Autodesk Revit 2016 model are missing. Instead of those Property Sets, new Property Sets (obviously belonging to Nemetschek Allplan 2015) have been inserted. Figure 5 shows the Property Sets connected to the modified wall. Interestingly, an attribute “Top Constraint” with a “Level: Level 2” value still exists. Furthermore, an attribute “Top Offset” is set to “0.0” and an attribute “Unconnected Height” is set to “3.0”, which represents the total height of the modified wall. This height, however, should be reduced by 40 cm, or a corresponding “Top Offset” should be set. Again, it must be noted that this is only an assumption, because the information expressed by these Property Sets is not part of the IFC standard.

Object/Attribute	Value	Property Set	Type
Top Constraint	Level: Level 2	Allplan Attributes	IfcPropertySingleValue
Top Extension Distance	0.0	Allplan Attributes	IfcPropertySingleValue
Top Offset	0.0	Allplan Attributes	IfcPropertySingleValue
Top is Attached	false	Allplan Attributes	IfcPropertySingleValue
Type	Basic Wall: Generic - 375mm	Allplan Attributes	IfcPropertySingleValue
Type Id	Basic Wall: Generic - 375mm	Allplan Attributes	IfcPropertySingleValue
Type Name	Generic - 375mm	Allplan Attributes	IfcPropertySingleValue
Unconnected Height	3.0	Allplan Attributes	IfcPropertySingleValue

Figure 5: Connected Property Sets of the modified wall (excerpt) – IFC 2X3 export from Nemetschek Allplan 2015 (screenshot taken using the IFC TOOLS PROJECT Viewer [13])

In step six, the model is converted back to planner A’s software, i.e. into an Autodesk Revit 2016 model. As can be seen from Figure 6, the geometric model is incorrect: The heights of three out of four walls are changed. Precisely, the heights are reduced by 208.6 cm.

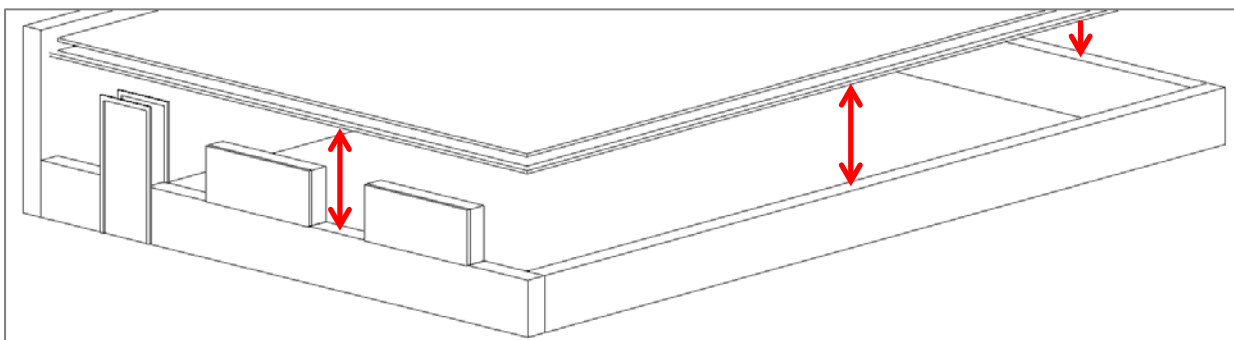


Figure 6: Result after importing the modified IFC file using Nemetschek Allplan 2015 into Autodesk Revit 2016

4 SUMMARY AND DISCUSSION

As demonstrated in this paper, geometric parameterization is a powerful modeling methodology in the context of building information modeling. BIM supports the representation, the storage, and the exchange of various information relevant to construction planning. This information can be used for describing, e.g., geometric/physical properties or costs of a building, for creating construction schedules, or for representing other characteristics of construction projects. Based on this information, plans and specifications as well as reports and presentations of a planned building can be created automatically. In addition, the use of BIM allows for a better way of cooperation within the construction planning process. However, cooperation requires a common digital data format for model exchange. The given example, which illustrates an integrated planning scenario using the IFC standard as federated model, has shown that parametric modeling may lead to inconsistent models if different software applications are used. In conclusion, additional research efforts are required to further

investigate the parameterized geometric modeling in conjunction with building information modeling.

REFERENCES

- [1] Autodesk Inc.: Autodesk Revit 2016. Available at: <http://www.autodesk.com/products/revit-family/overview> [Accessed: June 18, 2015]
- [2] Nemetschek AG: Nemetschek Allplan 2015. Available at: <http://www.allplan.com/en.html> [Accessed: June 18, 2015]
- [3] N. N. Golovanov: Geometric modeling. [Geometricheskoe modellierovanie]. Isdatelski dom, Moscow, Russian Federation, 2011.
- [4] S. A. Borisov, V. V. Smoljaninov, M. N. Terentev: Way of creation geometric models [Sposoby sozdaniya parametrisirovannoi modeli], 1998. Online: <http://www.cosmos.com.ru/articles/param.html#top>.
- [5] V. Yermilov, V. Kharin, M. Shalak: Concepts of geometric models [Концептуальные геометрические модели]. In: Proceedings of the International Conference Graphicon 2004. Online: [http://www.graphicon.ru/2004/Proceedings/Technical_ru/s3\[6\].pdf](http://www.graphicon.ru/2004/Proceedings/Technical_ru/s3[6].pdf), Moscow.
- [6] P. A. Koropushkin: Elaboration of data structure and algorithm for calculation parametric model of geometric objects [Razrabotka struktur dannykh i algoritma rascheta parametricheskikh modelei geometricheskikh objektov], Diss. Ural University Ekatarinburg, Russian Federation, 2005.
- [7] A. P. Erochin: Parametric models in CAD for airplanes [Primenenie parametricheskikh modelei v avtomatisirovannom projektirovanii aviacionnih konstrukzii], 2013. *Novoe slovo v nauke i praktike*, 6, pp. 95-99.
- [8] N. A. Salkov: Parametric geometry in geometric modeling [Parametricheskaja geometria v geometricheskom modellirovanii]. *Geometria i grafika*. 2(3), pp.7-13, 2014.
- [9] V. V. Butorov, S. P. Eresko: Computer-aided modeling in mechanical engineering [Avtomatisazija parametricheskovo modelirovanii v mshinostroitel'nom proizvodstve.]. *Aktualnie problem aviacii i kosmonavtiki*. 1(8), pp.140-141, 2012.
- [10] A. N. Serjodkin, G. L. Vinogradov, V. O. Filipenko: Model and methodology of parameterization in CAD of details with complex shape [Model i metodika parametrisazii pri avtomatisirovannom projektirovanii izdeli so sloshnoi formoi]. *Ingenieurij vestnik dona*. 30(2), pp.85-87, 2014.
- [11] S. Vilgertshofer, A. Borrmann: Automatic Detailing of Parametric Sketches by Graph Transformation. In: Proc. of the 32nd ISARC 2015, Oulu, Finland, 2015.
- [12] S. Vajna, C. Weber, H. Blei, K. Zeman: *CAX für Ingenieure*. Springer-Verlag Berlin Heidelberg, 2009.
- [13] Apstex: IFC Tools PROJECT-Viewer. Available at: <http://www.ifctoolsproject.com> [Accessed: June 18, 2015]
- [14] Solibri Inc.: Solibri Model Viewer v9. Available at: <http://www.solibri.com/products/solibri-model-viewer/> [Accessed: June 18, 2015]

DECENTRALIZED AUTONOMOUS FAULT DETECTION IN WIRELESS STRUCTURAL HEALTH MONITORING SYSTEMS USING STRUCTURAL RESPONSE DATA

K. Jahr^{*}, R. Schlich, K. Dragos and K. Smarsly

Bauhaus University Weimar, Germany
Email: katrin.jahr@uni-weimar.de

Keywords: Structural Health Monitoring, Sensor Fault Detection, Wireless Sensor Networks, Analytical Redundancy, Neural Networks.

Abstract. *Sensor faults can affect the dependability and the accuracy of structural health monitoring (SHM) systems. Recent studies demonstrate that artificial neural networks can be used to detect sensor faults. In this paper, decentralized artificial neural networks (ANNs) are applied for autonomous sensor fault detection. On each sensor node of a wireless SHM system, an ANN is implemented to measure and to process structural response data. Structural response data is predicted by each sensor node based on correlations between adjacent sensor nodes and on redundancies inherent in the SHM system. Evaluating the deviations (or residuals) between measured and predicted data, sensor faults are autonomously detected by the wireless sensor nodes in a fully decentralized manner. A prototype SHM system implemented in this study, which is capable of decentralized autonomous sensor fault detection, is validated in laboratory experiments through simulated sensor faults. Several topologies and modes of operation of the embedded ANNs are investigated with respect to the dependability and the accuracy of the fault detection approach. In conclusion, the prototype SHM system is able to accurately detect sensor faults, demonstrating that neural networks, processing decentralized structural response data, facilitate autonomous fault detection, thus increasing the dependability and the accuracy of structural health monitoring systems.*

1 INTRODUCTION

Structural health monitoring (SHM) systems can be deployed to evaluate the conditions and to ensure the structural integrity of civil engineering structures. To eradicate problems related to cost and installation time in conventional wired SHM systems, wireless sensor nodes are employed. An advantage of wireless sensor nodes is the collocation of processing power with sensing modules; hence, embedded computing can be employed to perform a variety of SHM tasks. Over their lifetime, the wireless sensor nodes can become inaccurate, faulty, or may even break. To ensure the dependability and the accuracy of the SHM system, and the integrity of the structure, sensor faults must be reliably detected in real time [1].

For sensor fault detection, artificial neural networks (ANN) have been used in several engineering disciplines. Smarsly and Law (2014), for example, have proposed the use of ANNs for sensor fault detection by utilizing the analytical redundancy in the correlations between sensor outputs [2]. Obst (April 2009) has presented a distributed recurrent neural network with local communication to detect sensor faults [3]. Basirat and Khan (June 2009) have introduced a neural network approach to distinguish accurate sensor data from faulty sensor data [4]. Yuen and Lam (2006) have presented a method to develop ANN designs for damage detection in structural health monitoring [5]. Venkatasubramanian et al. (1990) have tested various neural network topologies for detecting process failures, such as sensor faults [6].

In this paper, a wireless SHM system with decentralized, autonomous fault detection, producing minimal wireless transmission, is presented. One ANN is embedded into each sensor node and trained to autonomously detect sensor faults by comparing measured data with predicted data. To this end, the measured data collected from the structure is transformed into the frequency domain, and correlated Fourier amplitudes from different sensor nodes at selected frequencies are fed to each ANN. By using only Fourier amplitudes at selected peaks of the frequency spectrum, corresponding to natural frequencies of the structure, a significant reduction in wireless data transmission and storage is achieved. The ANNs are optimized for the test structure used in this study, enabling efficient and accurate sensor fault detection.

In the first part of the paper, background information on sensor fault detection using artificial neural networks is given, followed by a description of the mode of operation of the proposed SHM system. In the second part of the paper, the implementation of the SHM system is shown, and laboratory experiments, devised to validate the SHM system, are presented. Several topologies and modes of operation of the embedded ANNs are tested with simulated sensor faults. The performance of the ANNs is investigated with respect to the dependability and the accuracy of the fault detection approach, the results are discussed and an optimal configuration for the presented test structure is defined. The paper concludes with a summary and a brief outlook on future work directions.

2 SENSOR FAULT DETECTION USING ARTIFICIAL NEURAL NETWORKS

The following section gives a brief overview of sensor fault detection associated with artificial neural networks, and shows the general architecture of the proposed SHM system.

A well-known approach towards fault detection is the installation of physically redundant sensors. Faulty sensors can be identified through the deviation of their measurements from the measurements of correlated sensors. Physical redundancy, although efficient for sensor fault detection, causes increased installation and maintenance costs due to multiple installations

of sensors. Representing a more efficient approach, analytical redundancy typically uses mathematical functions, mapping the characteristics of the structure and the correlations of the installed sensors [7]. Specifically, virtual sensor measurements are computed for each sensor and then compared to the actual measurements. If the properties of a structure are known, physics-based models, e.g. finite element models, can be used in combination with data from adjacent sensor nodes to predict measurements of a sensor. However, to use numerical models, a priori knowledge about the structure is required.

Without a priori knowledge, analytical redundancy can be implemented on wireless sensor nodes based on data-driven models, such as artificial neural networks. ANNs are a class of algorithms that are inspired by biological nervous systems, such as the human brain. ANNs are used to approximate non-linear functions through adaptation to given data sets. Applications of ANNs are used in several areas, i.a. cancer detection, pattern recognition in image analysis, and sensor fault detection.

As depicted in Figure 1, ANNs essentially consist of interconnected data processing units, called “artificial neurons” [8]. Usually, the neurons are grouped in different layers: one input layer, one output layer, and one or more hidden layers. The connections between the neurons, termed “synapses”, have adaptive weights according to the connection strength between two neurons. The connections are used for data exchange between the neurons: the output of the neurons of one layer is used as the input of the neurons of the next layer. ANNs adapt to different applications by learning. Progress in learning is achieved by adjusting the weights of the synapses until a set of given input values results in the desired output values. ANNs can be customized to various objectives by using different topologies, neuron functions, and learning strategies [9].

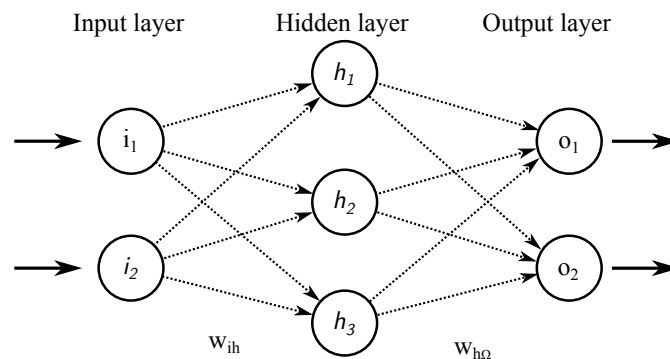


Figure 1: Example for an artificial neural network with two input neurons, two hidden neurons and two output neurons, connected by synapses

The SHM system prototype proposed in this study consists of wireless sensor nodes and a host computer, both linked through a base station. The components of the SHM system perform different tasks, as shown in the data flow in Figure 2. During system operation, the sensor nodes collect acceleration response data. The fundamental frequency as well as the corresponding Fourier magnitude of the acceleration response data of the structure are estimated by the sensor nodes using the fast Fourier transform (FFT) and a peak picking algorithm. For decentralized sensor fault detection, a distinct artificial neural network is embedded into each sensor node. In the ANN, the output of a sensor node is represented either by the input of an input neuron or by the output of an output neuron. The predicted magnitude of a sensor node, used for decentralized fault detection, is returned as output, the calculated magnitudes of neighbor sensor nodes are used as input. The processed data is transmitted wirelessly to the base station and then

to the host computer. On the host computer, the data is stored in a MySQL database. Additional diagnostics and information retrieval are conducted on the host computer in further steps.

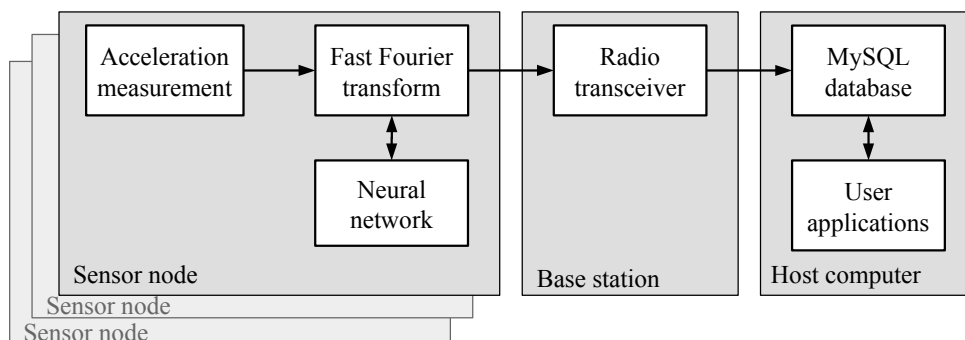


Figure 2: Hardware components and dataflow of the proposed SHM system

3 IMPLEMENTATION AND VALIDATION OF THE PROTOTYPE SHM SYSTEM

In this section, the implementation of the proposed SHM system is described. Laboratory experiments, devised to validate the SHM system, are presented and the test results are discussed.

3.1 Implementation

The proposed SHM system is implemented in an object-oriented way using the Java programming language. The sensor nodes and the base station are of type “Oracle Sun SPOT”. The main board of the Sun SPOTs features a 400 MHz ARM main processor, 1 MB of memory, 8 MB of flash memory and an IEEE 802.15.4 radio transceiver. The application board contains a 3-axis digital output accelerometer, an ambient light sensor, a temperature sensor, and eight tricolor LEDs. The accelerometer ranges between ± 2 g and ± 8 g and has a maximum sampling rate of 125 Hz [10].

3.2 Laboratory experiments

To validate the fault detection approach, the sensor nodes are installed on a test structure, as shown in Figure 3. The test structure is a 4-story frame structure consisting of steel plates of 25 cm \times 50 cm \times 0.75 mm. The plates are mounted on threaded rods with a vertical clearance of 23 cm. At the bottom of the structure, the rods are fixed into a solid block of 40 cm \times 60 cm \times 30 cm. The SHM system is installed on the test structure by mounting one wireless sensor node in the middle of story 3 and story 4, and two sensor nodes on story 2, one in the middle and one shifted aside by 20 cm.

In several test runs, the structure is excited by deflecting the top story. A test run includes a training phase and a data collection phase, each performed simultaneously on every sensor node. The training phase of the SHM system consists of the implementation and the training of an artificial neural network. The training of the ANN is completed through several sampling events used as training input. A sampling event includes the excitation of the structure, sampling of 512 acceleration measurements, on-board estimation of the fundamental frequency and corresponding Fourier magnitude, and wireless data exchange with the other sensor nodes. The data collection phase consists of any desired number of sampling events, sensor fault detection,



Figure 3: Instrumentation of the test structure

and data storage. After every sampling event, the predicted magnitude of each sensor node is predicted by using the measured magnitudes of the other sensor nodes as input to the neural network. The deviation of the measured magnitude and the predicted magnitude is calculated by the sensor node. A deviation exceeding a threshold is indicative of a sensor fault.

To find a suitable artificial neural network architecture for the laboratory test setup, several different topologies and neuron behaviors are tested offline. Finally, the optimal ANN is embedded into each sensor node to validate the fault detection online. To train and to test the ANNs, 100 test samples are generated. To this end, the test structure is excited and acceleration response data is collected and stored in the database. The acceleration response data is split randomly into 70% of training data and 30% of test data. Then, sensor faults are simulated to validate the autonomous sensor fault detection. For each simulated sensor fault, 30 test cases are generated. Different types of sensor faults are simulated through a manipulation of one sensor node by

- a) substituting the sensor readings with randomized values
- b) rotating the sensor node by 45°
- c) shifting the sensor node by 20 cm

The topology of the ANNs is optimized according to three criteria: prediction accuracy, ability of sensor fault detection, and time consumption during training. To optimize the topology, various numbers of hidden layers and hidden neurons per layer are tested. Interlayer connections, allowing only synapses between neurons in adjacent layers, as well as supralayer connections, allowing synapses between neurons in distant layers, are applied. As for the neuron behaviors, different training algorithms, backpropagation [11] and resilient backpropagation [12], are tested. The training and testing of each type of fault is repeated five times. As a performance measure, the root mean square errors (RMSEs) between the measured and the predicted data are calculated and averaged for all repetitions.

3.3 Test results

The efficiency of sensor fault detection depends on the increases of the RMSEs between the measured and the predicted magnitude of the sensor node. Benchmarks for different neural network topologies are shown in Table 1. For non-faulty sensor data, small RMSEs indicate a good approximation. The smallest RMSEs between 0.063 and 0.144, representing the best results, are retrieved with interlayer connected topologies and backward propagation. Using topologies with supralayer connections or the resilient backpropagation training algorithm leads to RMSEs between 0.132 and 0.208. When propagating data of simulated sensor faults through the ANNs, increased RMSE indicate efficient sensor fault detection. The RMSEs of all ANNs increase by a factor of 1.5 to 12 for different simulated sensor faults. Run times during training deviate by a factor of up to 40 between 4.6 s and 172.4 s. In general, the time increases with the number of hidden neurons within an ANN. Using resilient backpropagation, compared to backpropagation, increases the training time considerably by a factor of around 6 for identical topologies.

By comparing the benchmarks of different ANN topologies and taking all criteria and results into consideration, a 3-2-1 interlayer-connected ANN with backpropagation is concluded to be most appropriate for the test structure Figure 4. The results are marked bold in Table 1. The RMSE of 0.102 for the test data is within the lower third of all results. With respect to the simulated sensor faults, the RMSEs of 0.807, 0.603, and 0.410 for randomizing, rotating, and shifting the sensor nodes are within the top quarter of all results. These RMSEs correlate with relative errors of 30.05 %, 27.78 %, and 18.87 % respectively. The training of the 3-2-1 topology, executed in 13 s, was the second fastest.

Table 1: Arithmetic mean of root mean square errors during training and fault detection, and time consumed during training for several network topologies

	Topology	Testing	Simulated sensor faults			Time [s]
			Random	Rotated	Shifted	
Interlayer, backpropagation	3-1	0.149	0.767	0.612	0.334	6.6
	3-2-1	0.102	0.807	0.603	0.410	13.0
	3-3-1	0.144	0.751	0.581	0.283	17.2
	3-5-1	0.081	0.784	0.597	0.370	25.0
	3-7-1	0.063	0.756	0.587	0.294	32.2
	3-2-2-1	0.092	0.813	0.625	0.432	21.0
	3-5-5-1	0.137	1.213	0.752	0.938	46.6
Interlayer and supralayer, backpropagation	3-3-1	0.147	0.762	0.593	0.317	15.2
	3-5-1	0.132	0.764	0.600	0.324	22.6
	3-2-2-1	0.137	0.760	0.601	0.312	19.4
interlayer, resilient backpropagation	3-3-1	0.153	0.783	0.610	0.364	113.0
	3-5-1	0.143	0.729	0.598	0.249	172.4
	3-2-2-1	0.208	0.744	0.607	0.282	120.6

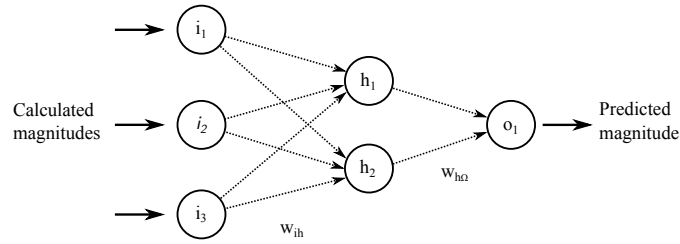


Figure 4: Optimal ANN topology for sensor fault detection: 3-3-1 feedforward neural network with unidirectional interlayer synapses

4 SUMMARY AND CONCLUSIONS

This paper has presented a decentralized autonomous sensor fault detection strategy for wireless structural health monitoring systems based on artificial neural networks. Autonomous sensor fault detection has been implemented by embedding artificial neural networks into the sensor nodes. The ANNs have been trained to predict expected sensor data to be compared to measured sensor data in order to detect sensor faults. To verify the proposed approach, the SHM system has been installed on a test structure for validating tests. Several different network models have been tested to identify an efficient, resource-saving configuration. As a result, an artificial neural network with 3-2-1 interconnected topology and backpropagation training algorithm training has been proven to be the optimal solution for the structure tested in this study. In summary, it can be concluded that sensor fault detection using neural networks can improve the dependability and the accuracy of structural health monitoring systems.

In future work, different types of artificial neural networks and further topologies may be investigated. The SHM system may be tested under varying conditions on test structures with other stimuli or on site. To ensure portability of the proposed fault detection approach, the SHM system may be implemented on other types of sensor nodes.

REFERENCES

- [1] Luke A. Bisby. *An introduction to structural health monitoring*. Department of Civil Engineering, Queen's University, Toronto, ON, Canada, 2014.
- [2] Kay Smarsly and Kincho H. Law. Decentralized fault detection and isolation in wireless structural health monitoring systems using analytical redundancy. *Advances in Engineering Software*, 73:1–10, 2014.
- [3] Oliver Obst. Distributed fault detection using a recurrent neural network. In *Proceedings of the 2009 International Conference on Information Processing in Sensor Networks*, Washington, DC, USA, April 2009.
- [4] Amir H. Basirat and Asad I. Khan. Graph neuron and hierarchical graph neuron, novel approaches toward real time pattern recognition in wireless sensor networks. In *Proceedings of the 2009 International Conference on Wireless Communications and Mobile Computing: Connecting the World Wirelessly*, New York, NY, USA, June 2009.
- [5] Ka-Veng Yuen and Heung-Fai Lam. On the complexity of artificial neural networks for smart structures monitoring. *Engineering Structures*, 28(7):977–984, 2006.

- [6] Venkat Venkatasubramanian, Ravi Vaidyanathan, and Y Yamamoto. Process fault detection and diagnosis using neural networks— 1. steady-state processes. *Computers & Chemical Engineering*, 14(7):699–712, 1990.
- [7] Kay Smarsly and Yuri Petryna. A Decentralized Approach towards Autonomous Fault Detection in Wireless Structural Health Monitoring Systems. In *Proceedings of the 7th European Workshop on Structural Health Monitoring*, Nantes, France, July 2014.
- [8] Emile Fiesler and Russell Beale. *Handbook of neural computation*. Oxford University Press, Oxford, United Kingdom, 1996.
- [9] Kishan Mehrotra, Chilukuri K Mohan, and Sanjay Ranka. *Elements of artificial neural networks*. MIT press, Cambridge, MA, USA, 1997.
- [10] *Sun SPOT Theory of Operation*. Sun Labs, Santa Clara, CA, USA, 1.5.0 edition, 2009.
- [11] David E. Rumelhart, Geoffrey E. Hinton, and Ronald J. Williams. Learning representations by back-propagating errors. *Nature*, 323(6088):533–536, 1986.
- [12] Martin Riedmiller and Heinrich Braun. A direct adaptive method for faster backpropagation learning: The rprop algorithm. In *IEEE International Conference on Neural Networks*, pages 586–591. IEEE, March 1993.

Topology optimization of structures subjected to multiple load cases by introducing the Epsilon constraint method

Zouhour Jaouadi¹

Tom Lahmer²

¹ Graduiertenkolleg 1462, Bauhaus-Universität Weimar,
Berkaer Straße 9, 99425 Weimar, Germany
E-Mail: zouhour.jaouadi@uni-weimar.de

² Institut für Strukturmechanik, Bauhaus-Universität Weimar,
Marienstraße 15, 99423 Weimar, Germany
E-Mail: tom.lahmer@uni-weimar.de

July 7, 2015

1 Abstract

A topology optimization method has been developed for structures subjected to multiple load cases (Example of a bridge pier subjected to wind loads, traffic, superstructure...). We formulate the problem as a multi-criterial optimization problem, where the compliance is computed for each load case. Then, the Epsilon constraint method (method proposed by Chankong and Haimes, 1971) is adapted. The strategy of this method is based on the concept of minimizing the maximum compliance resulting from the critical load case while the other remaining compliances are considered in the constraints. In each iteration, the compliances of all load cases are computed and only the maximum one is minimized. The topology optimization process is switching from one load to another according to the variation of the resulting compliance.

In this work we will motivate and explain the proposed methodology and provide some numerical examples.

Keywords: Topolgy optimization, multiple load cases, Epsilon constraint method

2 Introduction

The objective function of topology optimization problems is to minimize the compliance of the structure due to a given applied force. When the structure is subjected to multiple load cases, the objective function becomes a set of multi-objective functions where the aim is to minimize the compliances due to each load case, seperately.

To deal with the multi-load case, traditional methods [8] propose to minimize the worst case, which means to minimize the maximum compliance corresponding to the load case corresponding to the worst stress state. Another approach consists in combining the different objective functions, so the problem is changed to a scalar optimization problem. A famous example is the weighted sum method where the objective functions are summed with a preference ratio of importance, but the difficulty of this method lies on finding the correct value of the weight ratios prior to optimization, because small perturbations (of these ratios) leads to very different solutions.

3 State of the Art

3.1 Topology optimization

The topology optimization problem aims in finding the optimal layout of a given structure within a specified region, which can be interpreted as finding the adequate design that stores the minimum amount of the strain energy for a given structure. This is equivalent to minimizing the external work done by the applied load. Many methods were used to solve the topology optimization problems. The most famous one is the SIMP method, and compared to other methods, it is based on mathematical theories and permits to convert the optimal topology problem into a sizing problem on a fixed domain [3].

The mathematical formulation of the optimization problem for isotropic material is written as [3]:

$$\begin{aligned} \min_x c(x) = \min_x U(x)^T K(x) U(x) = \min_x \sum_{e=1}^N (x_e)^p u_e^T k_0 u_e \\ \text{subjected to the prescribed volume fraction: } V(x)/V_0 = f \\ \text{subjected to the loads: } KU = F. \end{aligned} \quad (1)$$

Where c is the compliance of the structure. U is the global displacement vector, K is the global stiffness matrix, F is the vector of applied loads, N is the number of the elements, x is the density and p is the penalization factor.

$V(x)$ and V_0 are the volume and the design domain volume, respectively and f is the prescribed volume fraction.

SIMP method is an interpolation scheme that penalizes intermediate densities to realize a black and white design; ($p \geq 3$) is always required. The sensitivity of the objective function with respect to the element densities x_e is formulated as:

$$\frac{\partial c}{\partial x} = -p(x_e)^{p-1} u_e^T k_0 u_e. \quad (2)$$

In order to ensure existence of solutions and to avoid the formation of checker-board patterns, filters are applied to the sensitivities or the densities.

The optimization problem is solved by means of the standard optimality criteria method.

3.2 Robust Topology Optimization

When considering the real engineering world, the solutions obtained from deterministic settings in topology optimization problems may not be practical and do not reflect the real behavior of the structure. This is due to the variabilities in the manufacturing process and the operating conditions. These variabilities lead to uncertainties in geometry and material properties. The material property uncertainty was limited to Young's modulus and perturbations are made on the stiffness matrix to quantify the effect of uncertainties on structural response [2].

Applied loading is often considered as uncertain parameter and uncertainty may include loading direction uncertainty and uncertainty in the magnitudes [9] and [4].

The treatment of uncertainties can be categorized into two types: the robust design optimization (RDO) and the reliability based topology optimization (RBTO). The RDO aims to minimize the influence of the stochastic variabilities. However, the reliability based design optimization figures out the probability of failure and aims to ensure that the reliability of a structure is greater than the required value. The uncertainty is introduced as a constraint on the probability of failure. Kharmanda ([6] and [5]) integrated the reliability analysis into topology optimization problem where the randomness of the applied loads and the geometry have been

taken into account. Also, Zhao and Wang [9] proposed an efficient approach to solve robust topology optimization problem of structures under loading uncertainty and showed the effect of loading magnitude and directional uncertainty on the robust designs.

3.3 Epsilon Constraint method

The Epsilon method is one of the scalarization method [7]. It was proposed first by Chankong and Haimes in 1983, and its concept is to optimize one objective functions among others, while the remaining objectives are constrained to be less than or equal to given target values.

4 Proposed Epsilon Constraint method

4.1 Problem formulation and algorithm

When the structure is subjected to multiple load cases, each load case is considered as an objective function to be optimized and the global optimization problem consists in finding of a single optimal solution that optimizes simultaneously all the objectives functions. Then, the topology optimization problem changes to a problem of minimizing the resulted compliance of the different loads. However, available methods propose to minimize the maximum compliance corresponding to the worst case. These methods seem not to be relevant since they didn't take into consideration the contribution of the other loads. The proposed "adapted" Epsilon method deals with such case, its strategy consists in calculating the compliance corresponding to each load, and in each iteration the maximum compliance should be minimized. The concept of this method can be written mathematically as:

In each iteration:

$$\min_x c_r(x) = \min_x \left\{ \max_{\{r \in 1, \dots, m\}} \left(\sum_{e=1}^N (x_e)^p u_e^T k_0 u_e \right) \right\} \quad (3)$$

subjected to: $c_i(x) \leq \epsilon_i; i=1, \dots, m; i \neq r$

subjected to the the prescribed volume fraction: $V(x)/V_0 = f$

Where m is the numbers of the loads applied in the structure, r is the load case where the compliance reaches its maximum in the iteration. ϵ_i are the upper bounds for the constraints and used to obtain weak Pareto optima, and it is the task of the decision maker to choose the appropriate values.

What characterizes this method is the jumping of the optimization process; while minimizing the first calculated maximum compliance, the optimization is then moved to cover the compliance of the other loads basing on the maximum calculated value of the compliance in each iteration. The optimization stops when the convergence is assured.

This method is described in the following algorithm:

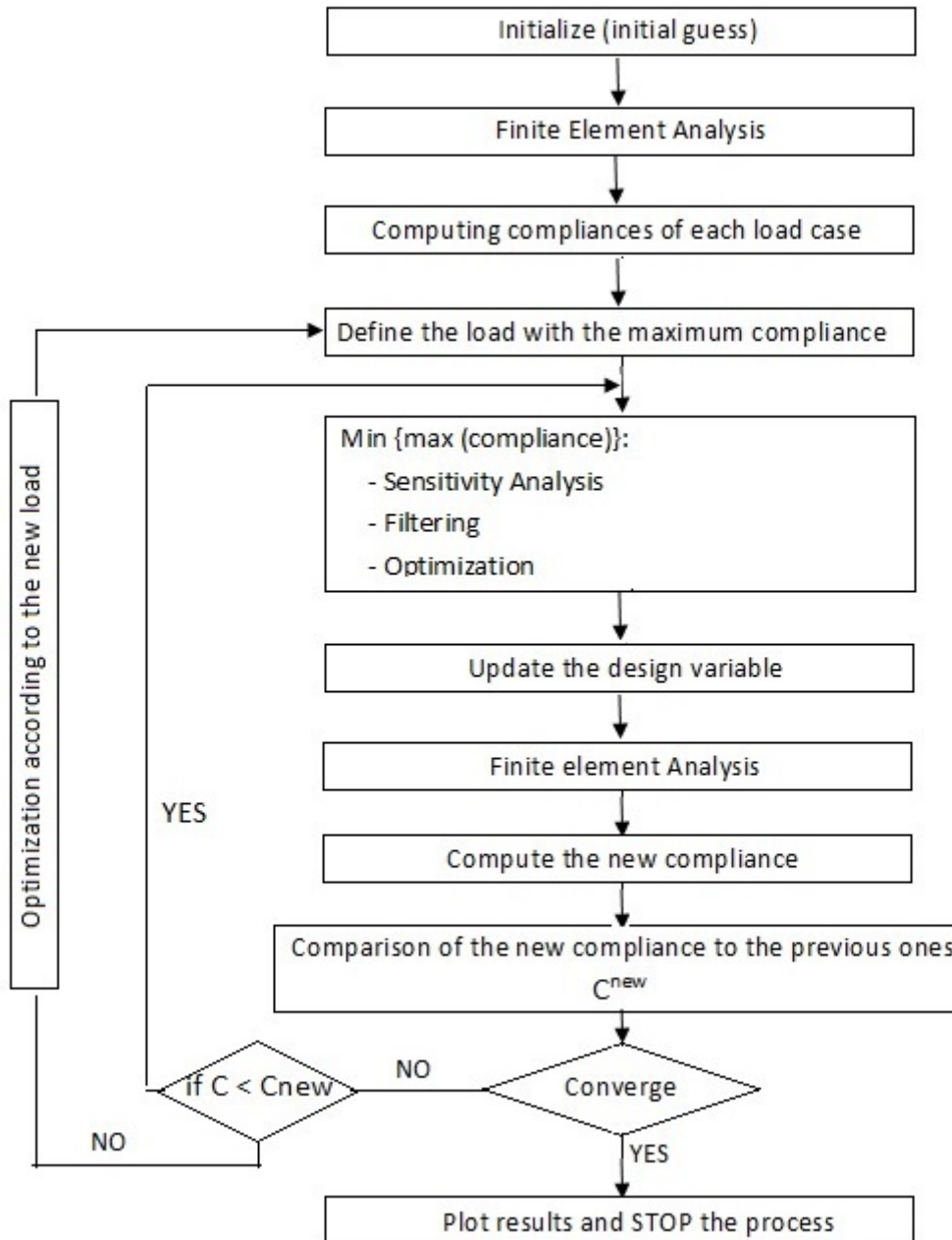


Figure 1: Algorithm of the Epsilon constraint method

4.2 Numerical examples

Consider a cantilever beam where the design domain, the boundary conditions and the external loads are shown in the following table. The aim of the topology optimization is to find the optimal material distribution, with a constraint on the total amount of the material.

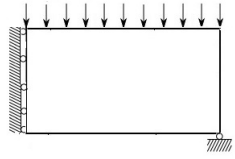
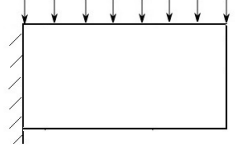


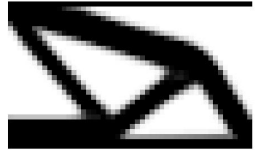

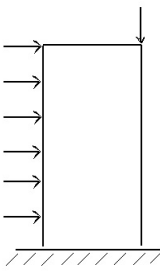
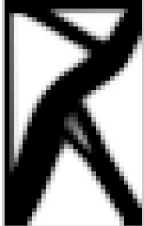

	Initial design	Optimized design (1)	Optimized design (2)
cantilever beam	 	 	 
Column			

Table 1: Optimized structures via Epsilon constraint method
1- without passive elements; 2- with passive elements

From the previous table, in the two examples of the cantilever beam, the distribution of the material depends on two principal factors: the initial boundary conditions and the process of optimization of the Epsilon Constraint method itself. In the first example, and however the upper part is subjected to nodal loads, the final optimized design does not contain that part. This can be explained by the fact that the optimization converged from the first stage and only the important loads were considered (those who have bigger compliance and they are located in the left part: near the boundary condition). Unlike this case, the distribution of material in the second example of the fixed cantilever beam involves the upper part of the structure where the loads were applied. Also, the third example of the fixed column shows the same results. So, the optimal design depends also on the boundary conditions.

In order to ensure the existence of material on the parts where loads are applied and because of the uncertainty of the magnitude and the direction of the loads in the structure, the designer can implement passive elements in those parts with density equal to one (solid part) as it shown in the previous table[1].

The following table shows the effect of considering only 5 loads on the final optimized design while considering the Epsilon constraint method.

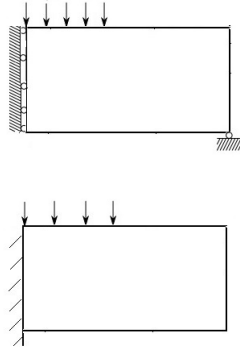

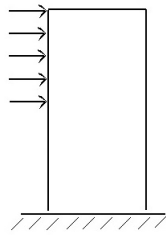

	Initial design	Optimized design without passive elements
cantilever beam		
Column		

Table 2: Effect of the loads on the optimization process of the Epsilon constraint method

5 Conclusion

This paper proposed a new method dealing with structures subjected to multiple loads. An "adapted" Epsilon Constraint method have been implemented as a tool for the optimization process, and, unlike the traditional methods that consider only the optimization of the structure according to critical load case, this method consider the contribution of the different applied loads. This method presents as well a faster convergence and the optimal layout depends principally on the initial boundary conditions and the process of optimization of the Epsilon Constraint method itself.

As outlook, the new designs need to be checked for their structural reliability and compared to those obtained by classical topology optimization. This may lead to adaptations of the proposed method in terms of reliability based structural multi-objective optimization.

Acknowledgements: The work was partly supported by the German Research Foundation (DFG) through the Research Training Group 1462 in Weimar. The authors gratefully acknowledge this support.

References

- [1] Erik Andreassen, Anders Clausen, Mattias Schevenels, Boyan S Lazarov, and Ole Sigmund. Efficient topology optimization in matlab using 88 lines of code. *Structural and Multidisciplinary Optimization*, 43(1):1–16, 2011.
- [2] Alireza Asadpoure. *Topology optimization under stochastic stiffness*. 2011.

- [3] Martin Philip Bendsoe and Ole Sigmund. *Topology optimization: theory, methods and applications*. Springer Science & Business Media, 2003.
- [4] Peter D Dunning, H Alicia Kim, and Glen Mullineux. Student paper: Introducing uncertainty in direction of loading for topology optimization. 2010.
- [5] G Kharmanda, N Kourdi, A Daboul, and A Elhami. Reliability-based topology optimization for different engineering applications. *International Journal of CAD/CAM*, 7(1), 2009.
- [6] G Kharmanda, Niels Olhoff, A Mohamed, and M Lemaire. Reliability-based topology optimization. *Structural and Multidisciplinary Optimization*, 26(5):295–307, 2004.
- [7] George Mavrotas. Effective implementation of the ε -constraint method in multi-objective mathematical programming problems. *Applied mathematics and computation*, 213(2):455–465, 2009.
- [8] R Zakhama, MM Abdalla, Z Gürdal, and H Smaoui. Wind load effect in topology optimization problems. In *Journal of Physics: Conference Series*, volume 75, page 012048. IOP Publishing, 2007.
- [9] Junpeng Zhao and Chunjie Wang. Robust structural topology optimization under random field loading uncertainty. *Structural and Multidisciplinary Optimization*, 50(3):517–522, 2014.

SELECTION AND SCALING OF GROUND MOTION RECORDS FOR SEISMIC ANALYSIS USING AN OPTIMIZATION ALGORITHM

G. J. Karaki*

**Department of Civil Engineering, Faculty of Engineering & Technology
Birzeit University, Palestine
E-mail: gkaraki@birzeit.edu*

Keywords: ground motions, selecting and scaling, nonlinear analysis, Dijkstra's algorithm.

Abstract. *The nonlinear time history analysis and seismic performance based methods require a set of scaled ground motions. The conventional procedure of ground motion selection is based on matching the motion properties, e.g. magnitude, amplitude, fault distance, and fault mechanism. The seismic target spectrum is only used in the scaling process following the random selection process. Therefore, the aim of the paper is to present a procedure to select a sets of ground motions from a built database of ground motions. The selection procedure is based on running an optimization problem using Dijkstra's algorithm to match the selected set of ground motions to a target response spectrum. The selection and scaling procedure of optimized sets of ground motions is presented by examining the analyses of nonlinear single degree of freedom systems.*

1 INTRODUCTION

In the last two decades, seismic analysis and design procedures shifted from the conventional force based methods to displacement based methods. The main advantage of the displacement based methods is the detailed information provided for the structural systems in terms of deformation and damage levels. Such high level of information helps the stakeholder to assess and evaluate the buildings' stock when hit by a specified seismic hazard. Performance based method is one of the popular approaches used for seismic displacement based design and assessment. The method is iterative in its nature and needs extensive analysis methods in order to verify the structural performance levels. An example of such methods of analysis is the nonlinear dynamic analysis, which requires an appropriate set of ground motion records. The selection and scaling of these ground motion records is very important as it affects significantly the analysis results and consequently the design recommendations [1, 2, 3]. In the last decade, there has been work concerned with the selection and scaling of existing ground motions. Naeim et al. [4] used a genetic algorithm to create the appropriate set of time histories for nonlinear analysis based on a target design response spectrum, whereas, [5] used a greedy algorithm to determine the set of ground motions using a probabilistic definition of a target response spectrum in terms of mean and variance. This study is concerned with the selection and scaling of ground motions considering two part optimization objective, and furthermore, test the optimized sets using a nonlinear analysis of Single Degree of Freedom System (SDOF) and draw recommendations for the selection process.

2 SELECTION & SCALING OF GROUND MOTIONS USING AN OPTIMIZATION ALGORITHM

2.1 Ground motion database

Ground motions are collected from the Next Generation Attenuation (NGA) database [6]. For each ground motion, the two horizontal components are retrieved and stored, and for each of these components a response spectrum is derived. In total, a 3551 ground motion records are stored in the database and these are used in the optimization problem. Furthermore, subsets of ground motions based on the earthquake's magnitude, fault mechanism and epicenter distance can be obtained from the database, and these subsets can be used in the optimization problem.

2.2 Selection & Scaling algorithm

The objective of the selection of ground motions is to identify the best combination of ground motions and the corresponding scaling factors for the ground motions to minimize the difference between the given design spectrum and the average of scaled ground motions. Furthermore, in the selection process the condition of having the records spectrum between T_o and T_n higher than the target spectrum is accounted for. The first part of the optimization objective (Case 1) is formulated as the minimization of the error term (R) defined by the following relation,

$$R = \sum_{T_o}^{T_n} \left(\frac{\sum_{i=1}^m (S_i \cdot S a_i)}{m} - F_t(T) \right)^2 \quad (1)$$

in which, T is the vibration period, S_i is the scaling factor for the time record i , $S a_i(T)$ is value of spectral acceleration of record i at period T , $F_t(T)$ is the value of the target design spectrum

at period T , T_o is the initial period to consider, T_n is final period to consider, and m is number of records considered. Moreover, the following must be satisfied

$$S_{min} \leq S_i \leq S_{max} \quad (2)$$

where, S_{min} is the minimum acceptable scaling factor, and S_{max} is the maximum acceptable scaling factor. The second part of the optimization objective (Case 2) adds a penalty on the time records which its spectrum values lie below the target design spectrum, satisfying the following relation for all periods $T_o < T < T_n$

$$((S_i \cdot Sa_i) - F_t(T)) < 0 \quad (3)$$

This penalty add an additional error term to the error in equation 1.

The optimization problem is solved using Dijkstra's algorithm, which is also known as the shortest path algorithm. The algorithm repeatedly executes a procedure which tries to maximize/minimize the return based on examining local conditions, with the hope that the outcome will lead to a desired outcome for the global problem. Typically, such algorithms employ simple strategies that are simple to implement and require minimal amount of resources and time, and this is attractive for the problem at hand. Dijkstra's establishes the shortest path (minimum of objective function) between a set of options (required number in each ground motion set) form the total population of choices (ground motion database). The followings constitute the steps for the optimization algorithm:

1. Create a set StdSet (shortest path set - ground motions set) that keeps track of selected ground motions, i.e. error calculated by equation 1 is calculated to be the minimum. Initially, this set is empty
2. Initialize an error value of very large value
3. While StdSet does not include the required number of ground motions in each set, the followings determine the i^{th} component in StdSet
 - Pick a ground motion (j) from the database and which is not in StdSet, calculate the error term equation 1 and satisfy equation 3 with its penalty
 - If the error term calculated with the j^{th} component of database is the minimum so far, then include ground motion(j) to StdSet as i^{th} entry
 - Repeat through all ground motions in database

3 NUMERICAL EXAMPLE I: SELECTED SET OF GROUND MOTIONS

A design spectrum is used as the target spectrum, the full built database is used in the optimization algorithm. As each of the earthquake records are of two horizontal components, Square Root of Sum of Squares (SRSS) of the two spectrum components of every time record is used in the optimization. Most building codes state the need of seven ground motions to be used in the structural analysis, thus, the optimization problem is run to find the set of seven ground motions. Figure 1 shows the optimization results of the spectra matching the target spectrum using the average spectra, equation 1, without the extra condition on the values of the spectra being above the target spectrum (Case 1). Table 1 documents the identified ground motions for this case. Figure 2 shows the optimization results of the spectra matching the target spectrum

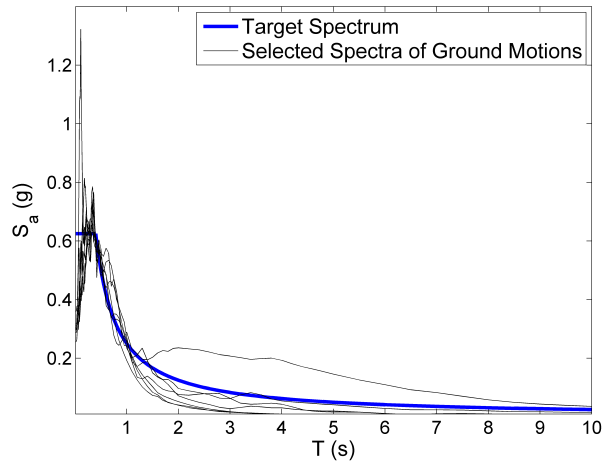


Figure 1: Selected and Scaled Spectra of Ground Motions for Case 1

No.	Year	Earthquake Name	Station	Scale Factor
1.	1999	Chi-Chi Taiwan	HWA032	1.6
2.	1971	San Fernando	Castaic	0.7
3.	1980	Livermore-02	San Ramon	1.0
4.	1994	Northridge-01	Manhattan Beach	1.2
5.	1987	Whittier Narrows-02	LA 116 St School	1.6
6.	1989	Loma Prieta	Fremont	1.3
7.	1999	Chi-Chi Taiwan	TCU075	0.6

Table 1: Selected Time Records for Case 1

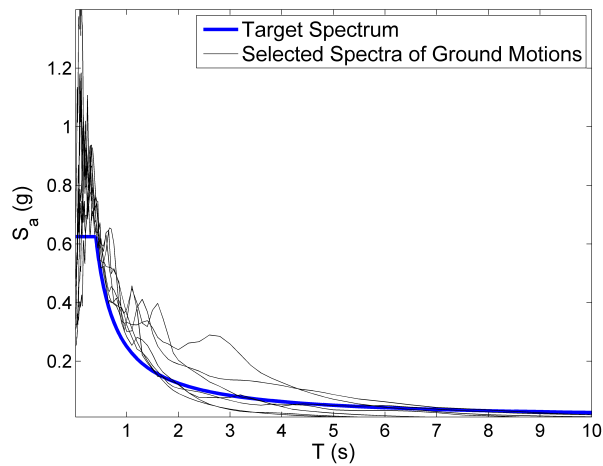


Figure 2: Selected and Scaled Spectra of Ground Motions for Case 2

No.	Year	Earthquake Name	Station	Scale Factor
1.	1979	Imperial Valley-06	EL Centro Array No.8	0.6
2.	1979	Imperial Valley-06	Aeropuerto Mexicali	0.8
3.	1980	Irpinia, Italy-01	Sturno	0.5
4.	1999	Chi-Chi, Taiwan	TCU129	0.4
5.	1979	Imperial Valley-06	Cerro Prieto	1.1
6.	1987	Baja California	Cerro Prieto	0.4
7.	1979	Coyote Lake	Gilroy Array No.6	0.6

Table 2: Selected Time Records for Case 2

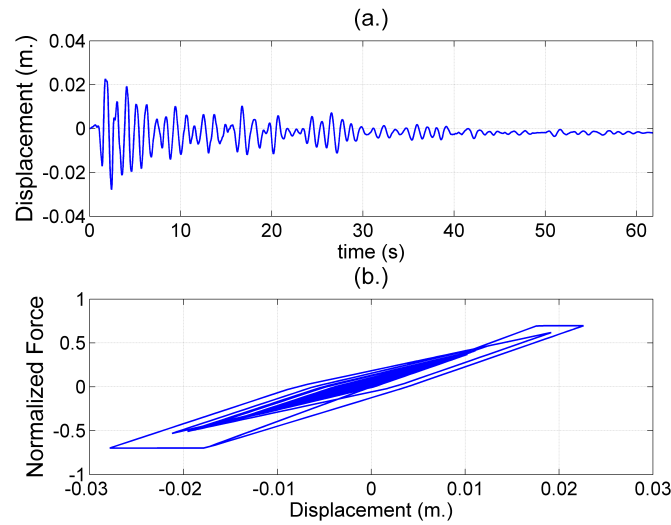


Figure 3: Nonlinear Analysis; a. displacement time history, b. force-deformation relation for the SDOF system

using the average spectra with the extra condition on the values of spectra being above the target spectrum; equations 1 & 3 (Case 2). Table 2 documents the identified ground motions for this case. It can be noticed that the optimized set of ground motions differed when using the condition on the values of the ground motions spectra, i.e. being above target spectrum. This highlights the importance of running an optimization problem to choose the ground motion records over the conventional way which is used extensively in the current engineering practice for seismic design and analysis.

4 NUMERICAL EXAMPLE II: NONLINEAR DYNAMIC ANALYSIS

A nonlinear analysis of SDOF system is performed to test the selected set of ground motions with their scaling factors. The nonlinearity of the system is modeled using an equivalent force-deformation relationship, the Takeda model is used to define the hysteresis model for the nonlinear dynamic problem. The definition of Takeda model needs various parameters to define the system at hand. The followings are the used parameters to define the Takeda model, it follows the equivalent force-deformation relationship for a moment resisting frame system; the unloading stiffness degradation parameter (α) is taken as 0.25, the reloading stiffness parameter (β) is taken as 0.0, post yield stiffness parameter (γ) is taken as 0.25, and elastic displacement limit is taken as 0.15m. The tested SDOF systems have 1 Hz as the natural frequency of vibration. A sample of the analysis results in terms of the displacement history and the system's hysteresis is presented in Figure 3. Furthermore, the maximum displacements and accelerations are illustrated in Table 4.

No.	Earthquake Name	Maximum Displacement (m.)	Maximum Acceleration (m/sec ²)
1.	Chi-Chi Taiwan	0.0298	2.3748
2.	San Fernando	0.0278	2.4799
3.	Livermore-02	0.0208	1.0824
4.	Northridge-01	0.0329	2.0273
5.	Whittier Narrows-02	0.0336	2.8466
6.	Loma Prieta	0.0346	2.6798
7.	Chi-Chi Taiwan	0.0344	1.5097

Table 3: Record of nonlinear analysis for selected ground motions for Case 1

No.	Earthquake Name	Maximum Displacement (m.)	Maximum Acceleration (m/sec ²)
1.	Imperial Valley-06	0.0479	3.4320
2.	Imperial Valley-06	0.0395	2.6328
3.	Irpinia, Italy-01	0.0399	1.6733
4.	Chi-Chi, Taiwan	0.0490	2.7881
5.	Imperial Valley-06	0.0358	2.1193
6.	Baja California	0.0621	3.6545
7.	Coyote Lake	0.0277	2.1094

Table 4: Record of nonlinear analysis for selected ground motions for Case 2

The design values are obtained by finding the average of the maximum responses of the seven records following most of the design codes. For Case 1:

- The average maximum displacements due to seven ground motions is (0.0308 m.) having a coefficient of variation of (0.168)
- The average maximum accelerations due to seven ground motions is (2.143 m/sec²) having a coefficient of variation of (0.300)

For Case 2:

- The average maximum displacements due to seven ground motions is (0.0428 m.) having a coefficient of variation of (0.260)
- The average maximum accelerations due to seven ground motions is (2.629 m/sec²) having a coefficient of variation of (0.276)

Two design values are used to compare the selection of ground motions following the case used in the optimization problem. The displacement indicates the damage level and the acceleration indicates the seismic forces. For the same optimization case, each design value has a different level of accuracy, this highlights the effect of target spectrum's type on the results. Acceleration spectrum is extensively used in seismic design and analysis, therefore, further research is needed to include displacement spectrum in the selection process. Furthermore, examining the accelerations' coefficient of variation in Case 1 and Case 2, it is noticed that the value dropped for Case 2. When adding the condition on the spectra values, the optimization problem yields, in general, different station records for the same earthquake that offers a good match to the target design spectrum, this may be the reason for the lower dispersion in Case 2, and showcases the power of the optimization problem formulated.

5 SUMMARY & CONCLUSION

The study offers an algorithm to create a set of ground motions using an optimization problem. The average of the selected ground motions over different periods is used in the optimization problem. Furthermore, a condition on the spectra values of selected ground motions is also included. It can be noticed that the set of ground motions differed when using the condition on the values of the ground motions spectra, i.e. being above target spectrum, which highlights the importance of running an optimization problem to choose the ground motion records over the conventional way which is used extensively in the current engineering practice for seismic design and analysis. Furthermore, for the same optimization case, each design value has a different level of accuracy, this highlights the effect of the target spectrum's type on the results. Therefore, further research is needed to include the displacement spectra in the selection and scaling process.

REFERENCES

- [1] Browning J., Li R., Lynn A., Moehle J. P., *Performance Assessment for a Reinforced Concrete Building*, Earthquake Spectra 16(3), 2000 541–555
- [2] Yakut A., Erduran E., *A Detailed Seismic Performance Assessment Procedure for RC Frame Building*, Advances in Earthquake Engineering for Urban Risk Reduction, Nato Science Series: IV: Earth and Environmental Sciences 66, 2006 135–150
- [3] Kappos A. J., Panagopoulos G., *Performance Based Seismic Design of 3D R/C Buildings Using Inelastic Static and Dynamic Analysis Procedures*, ISET Journal of Earthquake Technology 41(1), 1411–148 2004
- [4] Naeim F., Alimoradi A., Pezeshk S., *Selection and Scaling of Ground Motion Time Histories for Structural Design Using Genetic Algorithm*, Earthquake Spectra 20(2), 413–426 2004
- [5] Jayarm N., Lin T., Baker J. W., *A Computationally Efficient Ground Motion Selection Algorithm for Matching a Target Response Spectrum Mean and Variance* Earthquake Spectra 27(3) 797–815 2011
- [6] PEER. *Next Generation Attenuation Database* [Online] Available from <http://peer.berkeley.edu/ngawest/> [Accessed: 10th May 2015]

STRUCTURAL OPTIMIZATION USING THE ENERGY METHOD WITH INTEGRAL MATERIAL BEHAVIOUR

I.Kavrakov *, H.-G. Timmler and G. Morgenthal

* *Research Training Group 1462*
Bauhaus-Universität Weimar
Berkaer Straße 9
99423 Weimar

E-mail: igor.kavrakov @ uni-weimar.de

Keywords: Structural optimization, energy method, composite structures, truss optimization.

Abstract. *With the advances of the computer technology, structural optimization has become a prominent field in structural engineering. In this study an unconventional approach of structural optimization is presented which utilize the Energy method with Integral Material behaviour (EIM), based on the Lagrange's principle of minimum potential energy. The equilibrium condition with the EIM, as an alternative method for nonlinear analysis, is secured through minimization of the potential energy as an optimization problem. Imposing this problem as an additional constraint on a higher cost function of a structural property, a bilevel programming problem is formulated. The nested strategy of solution of the bilevel problem is used, treating the energy and the upper objective function as separate optimization problems. Utilizing the convexity of the potential energy, gradient based algorithms are employed for its minimization and the upper cost function is minimized using the gradient free algorithms, due to its unknown properties. Two practical examples are considered in order to prove the efficiency of the method. The first one presents a sizing problem of I steel section within encased composite cross section, utilizing the material nonlinearity. The second one is a discrete shape optimization of a steel truss bridge, which is compared to a previous study based on the Finite Element Method.*

1 INTRODUCTION

Structural optimization has gained considerable attention in the design of structural engineering structures, especially in the preliminary phase. The application of optimization in design would enable optimal and efficient shape of structures and to utilize properties which are not feasible with conventional design techniques. In structural optimization a cost function is minimized under design and equilibrium constraints. Mechanical systems are typically formulated by partial differential equations describing the equilibrium, compatibility and constitutive relations. Alternatively the state of equilibrium can be also formulated by a variational formulation, in which a variation of a given functional with respect to certain state variable is zero. Conventionally the equilibrium condition is secured by the Finite Element Method (FEM). In this work the Energy method with Integral Material behaviour (EIM) is employed, which ensures equilibrium through minimization of the potential energy. With an additional cost function, this constitutes a bilevel optimization problem. The outline of this paper is the following: initially a brief outline of the EIM is given, followed by formulation of the structural optimization and finally the method is applied on two practical examples.

2 STRUCTURAL OPTIMIZATION USING EIM

2.1 Formulation of the EIM

Lagrange's theorem of minimum of potential energy is a variational principle in which the sum of the internal, Π_i and external energy, Π_e is minimized with respect to a state variable, and it represents the fundamental principle of the EIM:

$$\Pi = \Pi_i + \Pi_e \rightarrow \min. \quad (1)$$

In the latter formulation the equilibrium, compatibility and constitutive relations are incorporated; therefore they should be represented accordingly with respect to a certain state variable. In case of formulation on cross section level this is the deformation vector containing the strain ε_0 at the origin and the two curvatures and $\boldsymbol{\varepsilon} = [\varepsilon_0, \kappa_y, \kappa_z]^T$. The constitutive law is described using the integral description of the material, introduced by Raue in [1]. This is obtained by integration over the uniaxial stress-strain relationship resulting in the specific strain energy W , the F and Φ which describe the same behaviour of one specific material. The latter two functions are used within the strain integration over complex geometries, in order the internal potential energy to be obtained:

$$W = W(\boldsymbol{\varepsilon}) = \int_0^\varepsilon \sigma(\varepsilon) d\varepsilon, \quad F = F(\boldsymbol{\varepsilon}) = \int_0^\varepsilon W(\boldsymbol{\varepsilon}) d\varepsilon, \quad \Phi = \Phi(\boldsymbol{\varepsilon}) = \int_0^\varepsilon F(\boldsymbol{\varepsilon}) d\varepsilon. \quad (2)$$

Taking into account Bernoulli's hypothesis, the strain at arbitrary point of a deformed cross section could be described by a linear function of ε_0 , κ_y and κ_z with respect to y and z coordinates respectively as:

$$\varepsilon_x(y, z) = \varepsilon_0 + \kappa_y y + \kappa_z z. \quad (3)$$

In case of biaxial bending, there is a second system of Cartesian coordinates η and ζ , at which along the η axis, the strain is constant as displayed on Figure 1. Here, standard relations are employed for the transformation between coordinate systems. The strain energy Π_i^C of a cross section with area A can be obtained by integrating the specific strain energy over the area $W(y, z)$:

$$\Pi_i^C = \iint_A W[\varepsilon(y, z)] dy dz = \oint_L -\frac{\kappa_z}{\kappa^2} F dy + \frac{\kappa_y}{\kappa^2} F dz = -\frac{1}{\kappa} \oint_L F d\eta. \quad (4)$$

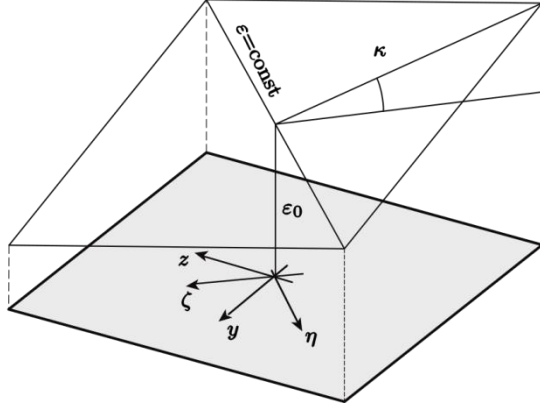


Figure 1. Coordinate transformation.

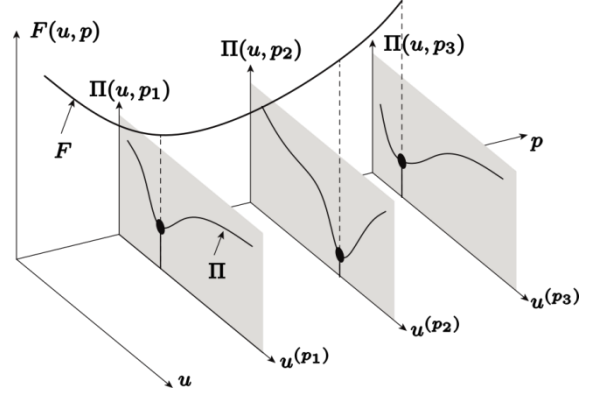


Figure 2. Bilevel optimization.

The proof of equation (4) is obtained by taking the divergence of the gradient of the $\Phi(\mathbf{y}, \mathbf{z})$ function, which is a 2-dimensional vector field, $\nabla \cdot \nabla \Phi$ and using Green's divergence theorem to transfer the integral over the area into a line integral over the contour L . Within this study, the proof will not be presented; however it is discussed in detail in [1] along with the proof of the curl of the gradient $\nabla \times \nabla \Phi = 0$, which ensures the conservation of the energy. The external energy as a result of external N, M_y, M_z forces acting on a cross section is obtained as:

$$\Pi_e^C = -(N\varepsilon_0 + M_y\kappa_z + M_z\kappa_y). \quad (5)$$

With the last relation, equation (1) is completed and with unconstrained optimization algorithm the energy is minimized with the deformation vector $\boldsymbol{\varepsilon}$ as unknown variable. In case of element beam formulation, the internal energy has to be integrated over the length l :

$$\Pi_i^E = \int_0^l \Pi_i^C(x) dx. \quad (6)$$

The state variable in this case is the displacement vector $\mathbf{u}(x) = [u \ v \ w \ v' \ w']^T$, which is composed of the displacements u, v, w in x, y and z direction respectively and their first derivatives v' and w' with respect to x , representing the rotations. The relation between the deformation and displacement vector for geometrically linear Bernoulli beam is defined by the compatibility conditions:

$$\varepsilon_0 = u', \quad \kappa_y = -v'', \quad \kappa_z = -w''. \quad (7)$$

By integrating the product of the external force vector $\mathbf{p}(x) = [p_x \ p_y \ p_z \ m_y \ m_z]^T$ and displacement vector $\mathbf{u}(x)$ over the length, the external energy yields into:

$$\Pi_e^E = \int_0^l \mathbf{p}^T(x) \mathbf{u}(x) dx. \quad (8)$$

The numerical implementation, discretization and suitable shape functions are discussed in the aforementioned literature.

2.1 Formulation of the structural optimization problem

A general structural optimization problem is formulated in a way to minimize an objective function which usually in mechanical problems represents the weight, the displacements, or the

cost of production. Constraints imposed are the behavioural constraints with respect to the state variable (vector representing the response of a structure), design constraints on the design variable (vector or function describing geometry or material properties) and equilibrium constraints [3]. The behavioural and design constraints can relate to bounds, equality and inequality constraints with respect to mathematical optimization, while the equilibrium constraints are usually equality constraints. The EIM secures the equilibrium through optimization and therefore a Bilevel Optimization Problem (BOP) is formulated in which the minimization of the potential energy $\Pi(\mathbf{u}, \mathbf{p})$ represents the lower objective function and an additional cost function $F(\mathbf{u}, \mathbf{p})$:

$$BOP: \begin{cases} \min_{\mathbf{u}, \mathbf{p}} F(\mathbf{u}, \mathbf{p}) \\ s. t. \begin{cases} G(\mathbf{u}, \mathbf{p}) \leq \mathbf{0}, \\ \min_{\mathbf{u}} \Pi(\mathbf{u}, \mathbf{p}), \end{cases} \end{cases} \quad (8)$$

where $F, \Pi: R^m \times R^n \rightarrow R$; and $G: R^m \times R^n \rightarrow R^l$. The design vector \mathbf{p} contains the design variables in the upper optimization task, while the displacement vector \mathbf{u} represents the state variables. The behavioural and design constraints are defined by a set of functions $G(\mathbf{u}, \mathbf{p})$. Figure 2 depicts a simple nested bilevel optimization problem, with one state variable u and one design variable p , where the lower problem is only represented at sequences p_1, p_2 , and p_3 . In case of cross section optimization, the deformation vector would replace the displacement vector as a state variable. There is a vast application field of the bilevel programming problem; thus, the solution strategies depend on the properties of the lower and upper objective function. In this case the nested method is used, which deals with both optimization problems separately i.e. for each iteration of the upper objective, a separate optimization task is solved for the lower objective function. Assuming geometrically linear and unlimited deformation capacity, the potential energy might be considered as convex and smooth function; therefore, for its minimization the unconstrained gradient methods are very effective. In this case the Broyden-Fletcher-Goldfarb-Schano (BFGS) method is used from the Quasi-Newton algorithms with a line search for step size control from the Matlab Optimization toolbox. The properties of the upper objective are usually unknown, therefore gradient free, deterministic and stochastic represent a good choice. Here, the deterministic Nelder-Mead downhill simplex algorithm and the stochastic genetic algorithm from the evolutionary computing field are utilized. It should be noted that there exists a special class of problems which include variational inequality, i.e. the Mathematical Programs with Equilibrium Constraints (MPEC). However, these were not used in this case and the formulation using MPEC with EIM is a further research topic.

3 APPLICATION

3.1 Composite column

Composite cross sections using steel profile are commonly used in practice due to their efficiency to withstand high loads with relatively small area. This example presents optimization of completely encased steel I profile cross section by concrete with circular form typical for columns. The problem is formulated to compute the rotated shape of the I section with respect to the bending moment axes under biaxial bending and axial force, for minimum thickness of the flange t_w of the steel profile. The section geometry with the external forces is depicted on Figure 3 (left). The materials used in this case were concrete C30/37 with parabolic rectangular material law according to Eurocode 2 and steel S235 with bilinear constitutive law. The objective function was to minimize t_w , by changing the design variables t_w and α with

constraints imposed on the strain in compression in concrete $\epsilon_c \geq -3.5\%$ and on the strain of the steel $|\epsilon_s| \leq 25\%$. The contribution of the concrete in tension was neglected.

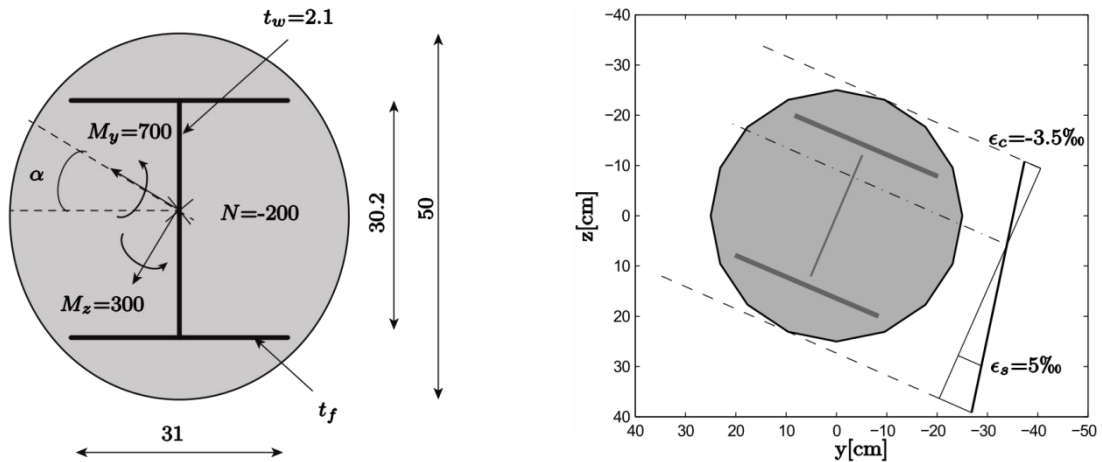


Figure 3. Circular section (left; units: [cm]; [kN]; kNm). Computed curvature and optimized position (right).

The simplex algorithm was utilized and the constraints were imposed as penalty functions. The optimized cross section is depicted on Figure 3 (right), for which $t_w = 2.61$ cm and $\alpha = 23.13^\circ$. As expected, the I profile rotated so its web is perpendicular to the neutral axis with failure in compression.

3.2 Truss bridge

The second example presents discrete shape optimization and a sizing problem. It is based on a previous study by Soh & Yang in [2] who compared a solution of a truss bridge with previous work. Shape optimization problem has been identified as more difficult but more important task than mere sizing problems, since the potential savings in material can be far better improved by the latter [2]. The structure is a 24m spanned truss bridge depicted in Figure 4, for which the total weight should be minimized. Design variables are the area of the bars A_i ($i = 1, 2, \dots, 5$), horizontal coordinates x_2, x_3, x_6, x_7 and vertical coordinates z_7, z_8 . Constraints are imposed on the vertical and horizontal displacements ($u < 1$ cm, $w < 5$ cm), on the axial stresses ($\sigma < 14$ kN/cm²) and on the area of the bars ($A_i > 0.5$ cm²). The bridge is modelled with truss elements, using the symmetry. The material is considered as linear elastic with Young's modulus of $E = 2.1E6$ kN/cm² and density $\rho = 7850$ kg/m³. Soh & Yang also include x_2 and x_3 as design variables without any notice of constraints, which resulted in this work with meaningless results as the node is moving to the support, thus the force has no influence. In order to compare the results, these variables were taken from the cited authors solution as fixed. For the optimization of the outer objective function, initially the GA was implemented, and after 200 generations with a population size of 20 individuals, the simplex was used to refine the results. Favorable results were obtained which resulted in weight reduction of 2.35%. The values of the design parameters are depicted in Table 1 and comparison of the shapes is displayed in Figure 5. The layout conform an arch which is close to the theoretical shape.

Study	Area [mm ²]					Coordinates [cm]						
	A_1	A_2	A_3	A_4	A_5	x_2	x_3	x_6	x_7	z_6	z_7	z_8
[3]	27.2	5136.5	106.7	1433.2	1420.8	162.2	579.3	167.3	435.0	581.2	184.1	61.4
Current	9.30	4676.5	389.8	1460.8	1475.9	fixed	fixed	176.5	433.4	604.9	158.6	38.4

Table 1. Truss bridge optimization results. Total weight: This work – 1235.6kg; Soh&Yang – 1265.32kg.

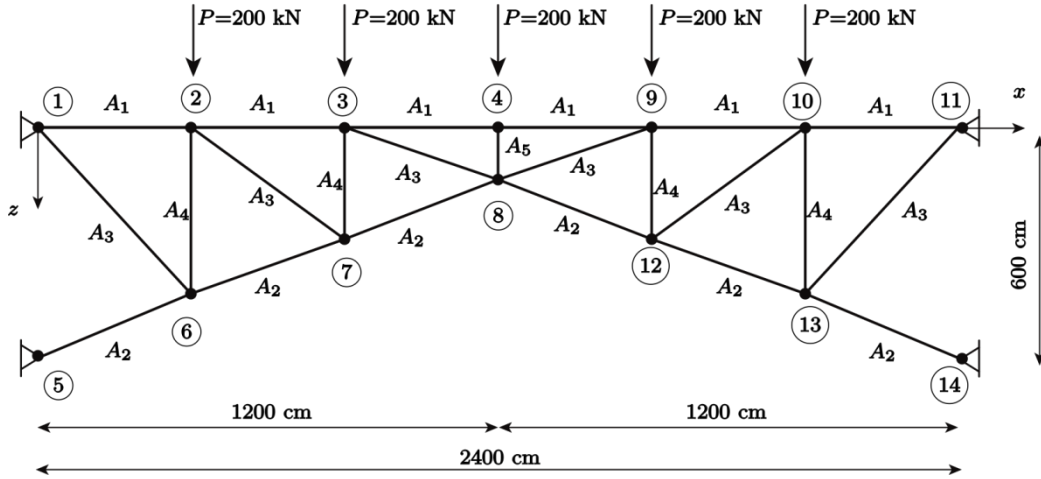


Figure 4. Truss bridge. Units: [cm]; [kN].

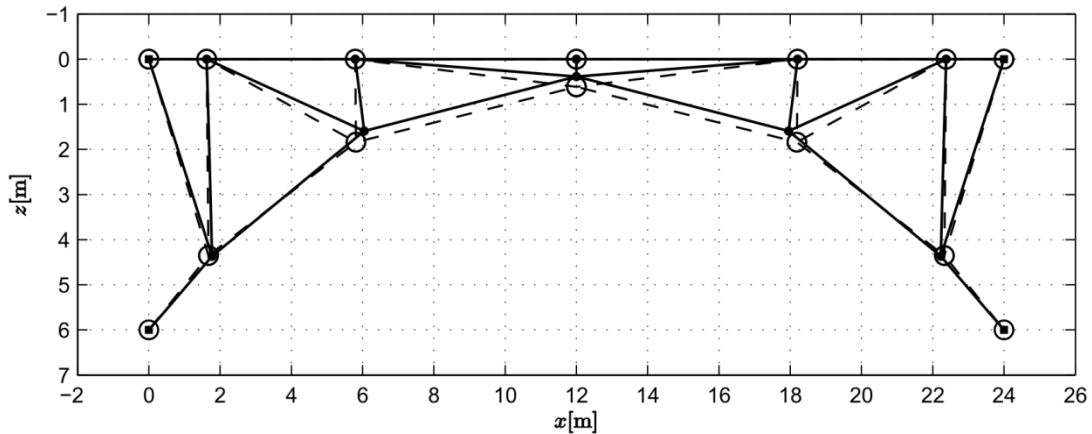


Figure 5. Comparison of truss bridge optimal shape: this work (-●-), Soh&Yang (-○-).

4 CONCLUSION

The future of design of attractive and efficient structures may be very closely related to structural optimization. In this paper, a structural optimization problem using EIM was formulated using bilevel optimization. Although computationally expensive, the EIM could be used as an alternative to the standard FEM for structural optimization, especially in case of physical nonlinearity. However, this limitation could be approached by formulating a MPEC.

REFERENCES

- [1] Raue E.: Non-linear analysis of cross-sections by mathematical optimization. *Bautechnik*, **82**, 896-809, 2005.
- [2] Soh C.-K., and Yang J.: Optimal layout of bridge trusses by genetic algorithms. *Computer-Aided Civil and Infrastructure Engineering*, **13**, 247-254, 1998.
- [3] Christensen P.W., and Klöppel A.: *An introduction to structural optimization*. Springer, Berlin, 2007.
- [4] Kavrakov I.: *Structural optimization of composite cross-sections and elements using energy methods*. Master's thesis, Bauhaus University-Weimar, 2014.

TOWARDS STEREO VISION- AND LASER SCANNER-BASED UAS POSE ESTIMATION

J. Kersten * and V. Rodehorst

* *Bauhaus-University Weimar*
Bauhausstr. 11, 99423 Weimar
E-mail: jens.kersten@uni-weimar.de

Keywords: Unmanned Aircraft Systems (UAS), Pose Estimation, Odometry.

Abstract. *A central issue for the autonomous navigation of mobile robots is to map unknown environments while simultaneously estimating its position within this map. This chicken-egg-problem is known as simultaneous localization and mapping (SLAM).*

Asctec's quadrotor Pelican is a powerful and flexible research UAS (unmanned aircraft system) which enables the development of new real-time on-board algorithms for SLAM as well as autonomous navigation.

The relative UAS pose estimation for SLAM, usually based on low-cost sensors like inertial measurement units (IMU) and barometers, is known to be affected by high drift rates. In order to significantly reduce these effects, we incorporate additional independent pose estimation techniques using exteroceptive sensors. In this article we present first pose estimation results using a stereo camera setup as well as a laser range finder, individually. Even though these methods fail in few certain configurations we demonstrate their effectiveness and value for the reduction of IMU drift rates and give an outlook for further works towards SLAM.

1 INTRODUCTION

Light-weight unmanned aircraft systems (UAS) are small flying robots which can be used for many different civil-engineering applications like monitoring, assessment and inspection of built-up structures [1]. Besides a camera, standard out of the box UAS are often equipped with a GPS receiver and an inertial measurement unit (IMU) for navigation. Image acquisition is usually done by hand either during manual flights or automatically during pre-planned flights based on GPS waypoints. The latter approach requires prior knowledge about the on-site setting and is restricted to outdoor applications.

Simultaneous localization and mapping (SLAM) [2, 3, 4] enables autonomous exploration of unknown indoor and outdoor environments without or few manual interaction as well as preliminary information. SLAM approaches solve the problem of mapping unknown environments while simultaneously estimating the UAS pose within the map. Pose estimation can be tackled by the fusion of measurements from GPS, IMU and further sensors, for example a compass or a barometer, based on Kalman filtering, extended Kalman filtering [5] or particle filters [6]. Especially in GPS-denied environments pose estimation based on the aforementioned sensors is known to be affected by high drift rates due to dead reckoning. Hence, several systems which additionally incorporate laser range finders and cameras were proposed [7, 8, 9, 10]. These exteroceptive sensors are often used in conjunction since they rely on different measurement principles and therefore offer complementary failure modes.

As a first step in setting up an autonomous indoor UAS, we implemented and tested existing pose estimation approaches using a stereo camera setup as well as a laser range finder.

2 SYSTEM OVERVIEW

We use the off-the-shelf research quadrotor *Pelican* from *Ascending Technologies GmbH* since it is well suited to specific requirements in terms of size, payload, computational power and sensor integration. System implementation is here mainly reduced to method development and algorithm implementation. The stereo camera system consists of two forward looking *BlueFox-MLC200wC* cameras with a resolution of $752 \times 480 \text{ pix}$, a field of view of 100° and a 90 Hz framerate. The *Hokuyo* laser range finder *UST-20LX* has a scanning range up to $20 \text{ m} \pm 4 \text{ cm}$, an angular resolution of 0.25° , a horizontal scan coverage of 270° and a scanning frequency of 40 Hz . Since method optimization and system implementation is not finished yet, all experiments were conducted manually instead of using data from real test flights.

3 VISUAL ODOMETRY

The essential matrix \mathbf{E} describes the relative orientation of two calibrated cameras and can be estimated based on corresponding image points using for example the well-known normalized 8-point algorithm [11]. A singular value decomposition (SVD) of \mathbf{E} yields the relative 3D pose (6DOF: relative translation \mathbf{T} and rotation \mathbf{R}) of the cameras. Since \mathbf{E} is projectively invariant and independent from the chosen world coordinate system, \mathbf{T} can only be estimated up to an unknown scale factor. When a fixed stereo camera setup is used, the scaled \mathbf{T} can be computed without additional knowledge, for example ground control points. In a preliminary calibration step the camera intrinsics as well as the relative orientation between

the left and right camera, represented by the rotation matrix $\mathbf{R}_{r,l}$ and the translation vector $\mathbf{T}_{r,l}$, have to be estimated once. Since the relative pose estimation between consecutive stereo frames is based on the relative orientations $\mathbf{E}_l^{1,2}$ and $\mathbf{E}_r^{1,2}$, the scale factors μ and λ for the corresponding translations $\mathbf{T}_l^{1,2}$ and $\mathbf{T}_r^{1,2}$ of the left and right camera are in turn unknown. If temporally tracked points in two subsequent stereo frames are available, the factors can be computed according to the fixed camera pose of the stereo rig [12]: The 3D points $\mathbf{X}_{r,l}^1$, triangulated from the stereo setup in the first frame, define a reference scale, whereas the 3D points $\mathbf{X}_l^{1,2}$ and $\mathbf{X}_r^{1,2}$, triangulated from two subsequent frames of the left and right camera, respectively, can be scaled to $\mathbf{X}_{r,l}^1$. The authors of [12] propose to use the nearest five object points for a reliable computation of μ and λ :

$$\mu = 0.2 \cdot \sum_{i=1}^5 \frac{\|\mathbf{X}_{l,r}^1\|}{\|\mathbf{X}_l^{1,2}\|}, \lambda = 0.2 \cdot \sum_{i=1}^5 \frac{\|\mathbf{X}_{l,r}^1\|}{\|\mathbf{X}_r^{1,2}\|} \quad (1)$$

Whereas this stereo approach (in the following denoted as SVO) is based on 3D correspondences, Perspective-n-Points methods (PnP) use 2D-to-3D correspondences [13]. For the solution of the P3P problem the unknown distances $d_i = \|\mathbf{X}_i - \mathbf{C}\|$ between 3D points and the camera position \mathbf{C} , the inter-point distances $d_{ij} = \|\mathbf{X}_i - \mathbf{X}_j\|$ as well as the angle θ between each pair of rays between \mathbf{C} and \mathbf{X} can be used to form

$$d_{ij}^2 = d_i^2 + d_j^2 - 2d_i d_j \cos(\theta_{ij}), \quad \forall (i, j) \in \{\{1,2\}, \{1,3\}, \{2,3\}\}. \quad (2)$$

This system can be solved by eliminating the unknowns of one equation using the remaining equations, which finally leads to a quartic polynomial.

In this work, the EPnP algorithm [14], which provides a non-linear solution within a linear time, is utilized, since it is known to provide good results compared to other iterative algorithms and is well suited for real-time systems.

Using the aforementioned concepts, visual odometry (VO) consists of two main steps: Feature detection and motion estimation. As stated in [8, 9] an overall estimation frequency of at least 10–15 Hz should be achieved due to the fast flight dynamics. Inspired by [15], we use the Harris-based Shi-Tomasi corner detector [16] along with the Lucas-Canade method [17] for a fast matching of features in all four images of two subsequent stereo frames. The essential matrices for the moving left and right camera are computed using the normalized 8-point algorithm with RANSAC [12] outlier detection. An SVD of $\mathbf{E}_l^{1,2}$ and $\mathbf{E}_r^{1,2}$ yields four possible stereo camera configurations each, where the wanted parameters are those who lead to triangulated points in front of both cameras. μ and λ can then be computed according to (1).

The aforementioned essential matrices are also used for the PnP approach. Further inputs are the triangulated point cloud $\mathbf{X}_{l,r}^1$, the corresponding image coordinates in the second frame, the camera intrinsics as well as an optional initial guess of the pose obtained by SVO. Based on homogeneous transforms the current pose $P_{current}$ can then be computed by

$$P_{current} = P_0 \cdot \Delta P_1 \cdot \dots \cdot \Delta P_{t-1} \cdot \Delta P_t = P_{previous} \cdot \Delta P_t, \quad \text{with } \Delta P = \begin{bmatrix} \mathbf{R}^T & -\mathbf{R}^T \cdot \mathbf{T} \\ \bar{\mathbf{0}} & 1 \end{bmatrix}, \quad P_0 = \begin{bmatrix} I & \bar{\mathbf{0}} \\ \bar{\mathbf{0}} & 1 \end{bmatrix}, \quad (3)$$

where t represents number of frames.

The drawback of (3) is that each pose estimate solely depends on the previous pose as well as the previous and the current view. Therefore, in [9] the UAS motion is estimated across several frames using a bundle adjustment. However, in order to analyze the properties of the above described basic approach no further optimization is done here.

4 LASER ODOMETRY

For the laser scanner-based odometry the hector SLAM approach [18] is utilized, since it enables the processing of measurements acquired with a scan rate of up to 100 Hz . While a navigation filter is used for the 6DOF pose estimation, a 2D SLAM module provides a map as well as the positioning and heading of the UAV related to this map (see figure 1). Please note that for a full 3D pose estimation additional sensors, e.g. a downward looking sonar, is required. Since the used implementation¹ solely uses scan data as well as optional additional IMU data, only 2D pose estimations are possible here.

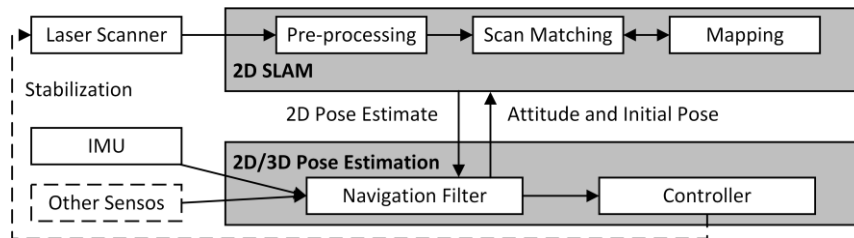


Figure 1: Workflow of hector SLAM [11]. Dashed lines represent optional interfaces.

In order to ensure a real-time pose estimation, SLAM and pose estimation are loosely coupled, i.e., update delays of the SLAM are allowed but don't affect the pose estimation. The motion of a rigid body can in general be described by a nonlinear equation system. Hence, for the pose estimation an extended Kalman filter (EKF) is used. Because IMU-based integrated velocities and positions are known to be affected by high drift rates, the 2D pose estimate from SLAM is used as additional information in EKF filtering.

In the pre-processing step of the SLAM module the scanned point cloud can optionally be filtered or down-sampled. The environment is represented by a 2D occupancy grid map and scan matching aligns laser scans with this map. The scan-based estimation of the current 2D pose is based on a Gauss-Newton approach, where a 3DOF transform of the scanned world coordinates that fits best to the current map is obtained. In order to improve this step, the pose estimate of the EKF is projected to the (x, y) -plane and is used to initialize the scan matching. For more detailed information the reader is kindly referred to [11].

5 EXPERIMENTS

In order to securely test the quality and reliability of the approaches, all experiments were conducted manually, i.e., the UAS equipped with the sensors was carried by hand along pre-defined paths. Since the paths are closed loops, the coordinate differences between the starting and end positions represent a quality measurement. Whereas the 2D/3D SVO and PnP trajectories are compared in the first experiment, the 2D trajectories obtained by hector SLAM

¹ http://wiki.ros.org/hector_slam (June 24, 2015)

with and without IMU fusion are compared. In figure 2 the corresponding results are visualized.

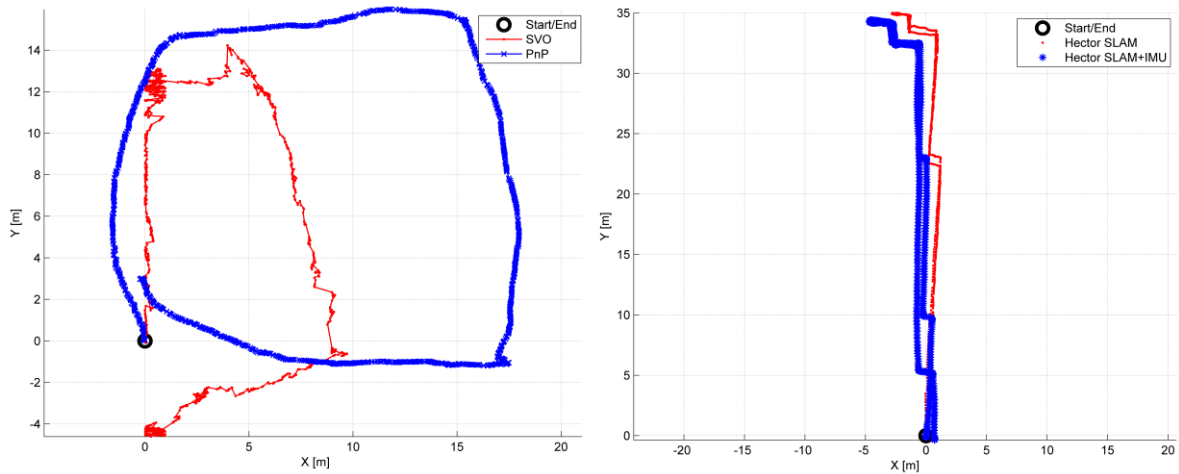


Figure 2: Trajectories of the SVO and PnP method (left) and the Hector SLAM approach with and without IMU fusion (right).

For the VO experiment an outdoor path around a house with a size of approximately $19 \times 12 \text{ m}$ was chosen. As can be seen in figure 2 (left) SVO yielded very inaccurate results. Even though the rough moving directions are correct, the estimated path differs significantly from the expected result of a smooth rectangular path. Due to an unstable scale factor estimation according to (1), the resulting trajectory tends to be very jagged. Furthermore, the path is too short to circuit the building which implies that the factors tend to be underestimated. Nonetheless, the distances between the start- and endpoint are 4.13 m (2D) and 6.51 m (3D). Based on the PnP approach a much smoother and realistic trajectory could be obtained, whereas a slight underestimation of the relative movements can also be observed here. The start-end differences with 2.97 m (2D) and 5.20 m are slightly but not significantly smaller than using VO. The results confirm the observation that the estimation of the rotation is more stable and precise than the translation [13].

Both approaches solely use point correspondences from two consecutive stereo-frames. Disadvantageous configurations, for example very small or zero translations, therefore lead to errors which accumulate over time. The Lukas-Canade feature matching approach in turn fails for large translations which suggests that another matching method should be used here.

For the Hector SLAM experiment a closed indoor trajectory along a straight corridor was chosen, since the laser range finder is sensitive to sunlight. The results solely using the mapping module of Hector SLAM produced a smooth trajectory which is close to the true path. With a 2D start-end difference of 0.39 m , the estimated path intends to be a very good solution. Nonetheless, compared to the result with additionally incorporated IMU measurements, the red path is slightly curved, which indicates a drift caused by the scan matching. The start- to endpoint difference of 0.72 m is surprisingly larger here.

6 CONCLUSION

In this work results of visual and laser scanner-based pose estimation techniques are presented. The PnP approach as well as the Hector SLAM approach using additional IMU data

yielded the best results in our experiments. Nonetheless, the loop closure test and other findings demonstrate that odometry estimates can rapidly exceed drift tolerances defined by the dimensions and richness of detail of the indoor environment to explore.

A careful optimization of the single VO steps, especially the feature matching, will be part of the next works and these techniques will be implemented on our quadrotor. Even though the estimated poses can directly be used as additional input for Asctec's on-board autopilot, the application and implementation of other data fusion methods is planned.

REFERENCES

- [1] N. Hallermann, G. Morgenthal and V. Rodehorst: Vision-based deformation monitoring of large scale structures using Unmanned Aerial Systems. 37th IABSE Symposium, Engineering for Progress, Nature and People, Madrid, Spain, 2014.
- [2] M. Montemerlo: FastSLAM – a factored solution to the simultaneous localization and mapping problem with unknown data association, Ph.D. thesis, Robotics Institute, Carnegie Mellon University, 2003.
- [3] H. Durrant-Whyte and T. Bailey: Simultaneous localization and mapping: part I. IEEE Robotics & Automation Magazine, **13-2**, 99-110, 2006.
- [4] T. Bailey and H. Durrant-Whyte: Simultaneous localization and mapping: part II. IEEE Robotics & Automation Magazine, **13-3**, 108-117, 2006.
- [5] S. S. Haykin. Kalman Filtering and Neural Networks. John Wiley & Sons, Inc., New York, NY, USA, 2001.
- [6] B. Ristic, S. Arulampalam and N. J. Gordon. Beyond the Kalman filter: Particle filters for tracking applications. Artech house, 2004.
- [7] R. Brockers, M. Hummenberger, S. Weiss and L. Matthies: Towards Autonomous Navigation of Miniature UAV. IEEE Conference on Computer Vision and Pattern Recognition, Workshops (CVPRW), 645-651, 2014.
- [8] K. Schmid, T. Tomic, F. Ruess, H. Hirschmuller and M. Suppa: Stereo vision based indoor/outdoor navigation for flying robots. IEEE/RSJ International Conference on Intelligent Robots and Systems (IROS), 3955-3962, 2013.
- [9] M. Achtelik, A. Bachrach, R. He, S. Prentice and R. Nicholas: Stereo vision and laser odometry for autonomous helicopters in GPS-denied indoor environments. G. R. Grant, D. W. Gage and C. M. Shoemaker eds. Unmanned Systems Technology XI. SPIE-The International Society for Optical Engineering, Orlando, FL, USA, 2009.
- [10] S. Huh, D.H. Shim and J. Kim: Integrated navigation system using camera and gimbaled laser scanner for indoor and outdoor autonomous flight of UAVs. IEEE/RSJ International Conference on Intelligent Robots and Systems (IROS), 3158-3163, 2013.
- [11] R. I. Hartley and A. Zisserman: Multiple view geometry in computer vision. Cambridge University Press, 2nd edition, 2004.
- [12] V. Rodehorst, M. Heinrichs and O. Hellwich: Evaluation of Relative Pose Estimation Methods for Multi-Camera Setups. Proc. of the XXI Congress of the Int. Society for Photogrammetry and Remote Sensing (ISPRS), Int. Archives of Photogrammetry,

- Remote Sensing and Spatial Information Science (IAPRS), **37-B3b**, 135-140, Peking, China, 2008.
- [13] L. Quan and Z. Lan: Linear n-point camera pose determination. PAMI, **21-8**, 774-780, 1999.
- [14] F. Moreno-Noguer, V. Lepetit and P. Fua: Accurate non-iterative $O(n)$ solution to the pnp problem. In ICCV, Rio de Janeiro, Brazil, 2007.
- [15] V. More, H. Kumar, S. Kaingade, P. Gaidhani and N. Gupta: Visual odometry using optic flow for Unmanned Aerial Vehicles. International Conference on Cognitive Computing and Information Processing (CCIP), 1-6, 2015.
- [16] J. Shi and C. Tomasi: Good Features to Track. 9th IEEE Conference on Computer Vision and Pattern Recognition, Springer, 1994.
- [17] B. D. Lucas and T. Kanade: An iterative image registration technique with an application to stereo vision. In Proceedings of the 7th international joint conference on Artificial intelligence (IJCAI'81), Morgan Kaufmann Publishers Inc., San Francisco, CA, USA, **2**, 674-679, 1981.
- [18] S. Kohlbrecher, O. von Stryk, J. Meyer and U. Klingauf: A flexible and scalable SLAM system with full 3D motion estimation. IEEE International Symposium on Safety, Security, and Rescue Robotics (SSRR), 155-160, 2011.

QUALITATIVE INVESTIGATION OF THE EFFECT OF SOIL MODELING APPROACH ON DYNAMIC BEHAVIOR OF A SMALL-SCALE 2-DOF STRUCTURE WITH PILE FOUNDATION

R. Khosravian*, F. Wuttke

**Research Training Group 1462
Berkaerstr. 9, 99425 Weimar, Germany
E-mail: Reza.Khosravian.Champiri@uni-weimar.de*

Keywords: Soil Structure Interaction, Impedance Functions, Pile Foundations, FEM, Numerical Methods.

Abstract. *Known as a sophisticated phenomenon in civil engineering problems, soil structure interaction has been under deep investigations in the field of Geotechnics. On the other hand, advent of powerful computers has led to development of numerous numerical methods to deal with this phenomenon, resulting in a wide variety of methods trying to simulate the behavior of the soil stratum. This survey studies two common approaches to model the soil's behavior in a system consisting of a structure with two degrees of freedom, representing a two-storey frame structure made of steel, with the column resting on a pile embedded into sand in laboratory scale. The effect of soil simulation technique on the dynamic behavior of the structure is of major interest in the study. Utilized modeling approaches are the so-called Holistic method, and substitution of soil with respective impedance functions.*

1 INTRODUCTION

Among various methods used to simulate the effect of soil-structure interaction (henceforth referred to as SSI), substitution of the substructure with appropriate springs and dashpots has attracted considerable attention. Relative ease of modeling and compared to many common methods, less computational power demand are mentioned among the major reasons of popularity of this approach [1, 2, 3]; however, simulating the problem with a full three dimensional finite elements (FE) model is another common approach in practice. This approach, also called Holistic method, has been developed since the promotion of computing power, as long as the usually high number of degrees of freedom (DOF) requires fairly high computational demand. Impedance functions, which in fact represent the springs and dashpots modeling the substructure, have been extensively investigated in literature; however, the work presented by Novak et al. [4] is one of the pioneers in the field. Hence, the methodology proposed there is adopted here, shortly explained and tested on a case study. Finally, judgment is made on the prediction capability of the model when compared to the Holistic method.

2 IMPEDANCE FUNCTIONS OF SINGLE PILES

Presented in [4], Novak proposes stiffness constants and constants of equivalent viscous damping for single vertical piles. The soil's shear modulus is considered to be either constant or varying with depth according to a quadratic parabola, the tip of the pile could be either fixed or pinned and the constants are given for both end-bearing and floating piles. Figure 1 provides an illustration of global directions and naming conventions used in this work.

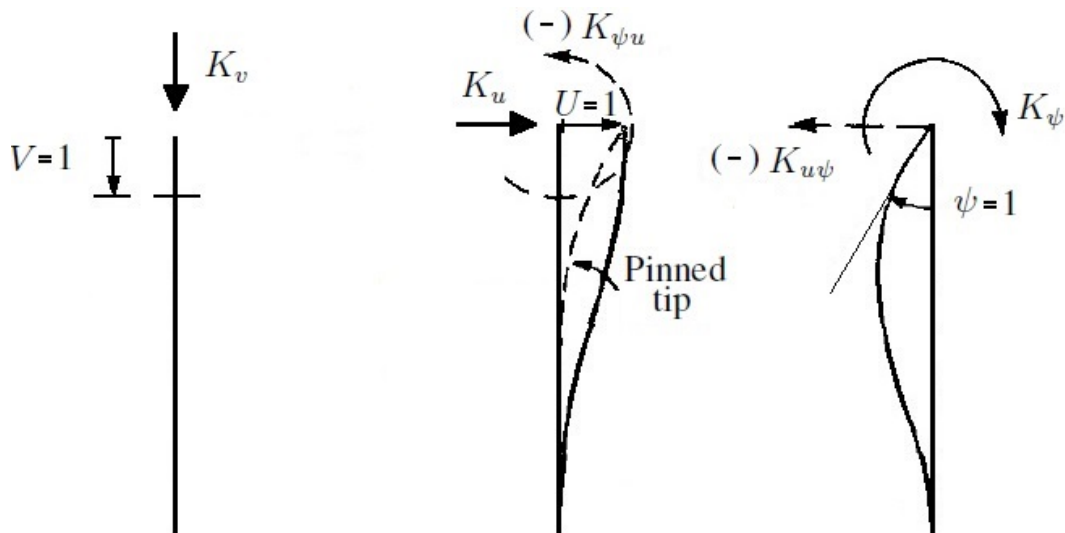


Figure 1: Introduction of Stiffness & Damping Constants for Individual Directions [4]

The stiffness and damping constants in different degrees of freedom are mentioned in Equation 1 to Equation 4.

$$K_v = \frac{E_p \cdot A}{R} \cdot f_{v1}, C_v = \frac{E_p \cdot A}{V_s} \cdot f_{v2} \quad (1)$$

$$K_u = \frac{E_p \cdot I}{R^3} \cdot f_{u1}, C_u = \frac{E_p \cdot I}{R^2 \cdot V_s} \cdot f_{u2} \quad (2)$$

$$K_\psi = \frac{E_p \cdot I}{R} \cdot f_{\psi1}, C_\psi = \frac{E_p \cdot I}{V_s} \cdot f_{\psi2} \quad (3)$$

$$K_c = \frac{E_p \cdot I}{R^2} \cdot f_{c1}, C_c = \frac{E_p \cdot I}{R \cdot V_s} \cdot f_{c2} \quad (4)$$

where E_p , A , R and I represent, respectively, the pile's Young's modulus of elasticity, cross-section area, radius and moment of inertia, and $V_s = (G_s/\rho)^{0.5}$ is the characteristic shear wave velocity of the soil, with G_s being the soil's shear modulus and ρ representing its density. Index c represents ψu and $u\psi$, i.e. the coupling terms between horizontal translation and rotational degrees of freedom.

In their work, Novak neglects the torsional behavior around the pile's axis since he states that this motion is not only strongly frequency dependent, but also consequential just for caisson foundations or groups of massive piles.

The coefficients f_{ij} (with i representing the direction and $j = 1$ for stiffness and $j = 2$ for damping) are extensively introduced and studied in their research for various cases examined with different assumptions in the mentioned survey. Novak argues that excitation frequency does not considerably influence the coefficients for slender piles, and the relative mass ratio of soil to pile is only important for extremely heavy piles. Furthermore, he claims relative stiffness of pile to soil and also the soil's profile to be of major importance for determination of the factors f_{ij} in general, while the pile's slenderness and bottom conditions (floating or end-bearing) are decisive in its vertical behavior. Parabolic variation of soil's shear modulus, versus a constant modulus in the entire soil profile, represents the physically homogeneous soil stratum with its shear modulus increasing downward as the confining pressure enlarges. It is worth noting that for non-circular cross sections, utilization of an equivalent pile radius is possible [4].

3 EXAMPLE

3.1 Case study

The 2-DOF system with first and second eigenfrequencies of $4.0217Hz$ and $10.563Hz$ (fixed case), illustrated in Figure 2, is modeled when put on a pile resting in a homogeneous soil stratum. The rotation DOF is fixed in the lumped mass levels, so that the structure represents the behavior of a small-scale 2-storey steel frame. The circular cross section of the columns has a diameter of $7mm$. Table 3.1 exhibits the exact dimensions and material properties of the pile, the structure and the soil which, in the Holistic approach, is modeled as a linear elastic homogeneous material.

The system is modeled once with a full 3D continuum FE method (Holistic) as a reference (REF). The soil stratum together with the pile is then replaced by the springs proposed by Novak, assuming once a constant (C1) and once a parabolic (C2) soil profile as mentioned in section 2. The same procedure with the models using springs is repeated with the columns simulated by 2D beam elements (B1 for constant and B2 for parabolic soil profile).

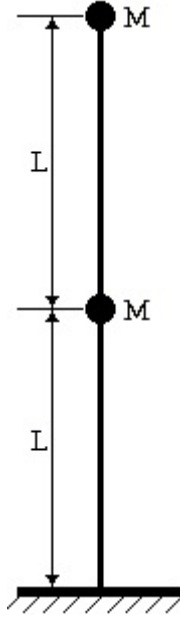


Figure 2: The Structural System

Property	Unit	Value
Pile		
Young's modulus	Pa	$1.89 * 10^{11}$
Radius	m	$5.00 * 10^{-3}$
Length	m	0.15
Soil		
Young's modulus	Pa	$4.74 * 10^8$
V_s	m/s	$3.2 * 10^2$
ρ	Kg/m^3	$1.85 * 10^3$
Poisson ratio	-	0.25
Structure		
Young's modulus	Pa	$2.0 * 10^{11}$
L	m	0.45
M	Kg	1.7

Table 1: The Problem's Parameters

Direction	Stiffness	Damping
v	$5.95 * 10^7$	$2.62 * 10^3$
u	$1.76 * 10^7$	$6.73 * 10^2$
ψ	$6.96 * 10^3$	$7.55 * 10^{-2}$
c	$-2.48 * 10^5$	$-5.72 * 10^0$

Table 2: Springs' Stiffness & Damping Properties for Constant Soil Profile (SI Units)

Direction	Stiffness	Damping
v	$4.46 * 10^7$	$2.09 * 10^3$
u	$6.40 * 10^6$	$3.52 * 10^2$
ψ	$5.58 * 10^3$	$7.26 * 10^{-2}$
c	$-1.49 * 10^5$	$-4.28 * 10^0$

Table 3: Springs' Stiffness & Damping Properties for Parabolic Soil Profile (SI Units)

The five cases undergo an eigenfrequency calculation, accompanied by a 1-second forced vibration ($F(t) = 10 \sin(31.4t)$) followed by 10 seconds of free vibration, while the structure experiences a damping ratio of 2%. Keeping in mind the required calculation time and modeling complexity, together with examining the responses in different cases, will finally lead to a qualitative comparison between different modeling techniques which address this problem.

3.2 Results

Based on the theory and problem dimensions explained in previous sections, the calculated stiffness and damping constants are presented in Table 2 and Table 3 for the constant and parabolic soil profile respectively.

Firstly, the error (here defined as the percentage of difference between a model's specific output and that of the reference model) in eigenfrequencies calculated by the four modeling approaches (C1, C2, B1 and B2 as previously defined in subsection 3.1) are presented in Figure 3. As can be seen, the C1 (3D elements for the beam and constant soil profile) model has a relatively more accurate prediction capability for both modes. It is also worth mentioning that both modes are most accurately predicted by C1, followed by C2 and finally B2 followed by B1 (beam elements and constant soil profile).

Finally, Figure 4 demonstrates the horizontal displacement of the top level of the structure in the first 8 seconds when excited by the load mentioned in subsection 3.1, comparing the reference (Holistic) and the B1 models. Fitting on the response of the reference model at almost every

point, C1 proved to have the highest capability in simulating the problem. When compared to the REF, C2 model tends to predict lower displacement values in the excitation phase (the first second), and higher values in the free vibration phase, while a slight phase difference is also detectable. In contrast, B2 approach calculates higher displacement values in the excitation phase and lower values in the free vibration phase compared to the reference model. The phase difference is also intensified compared to the C2 model.

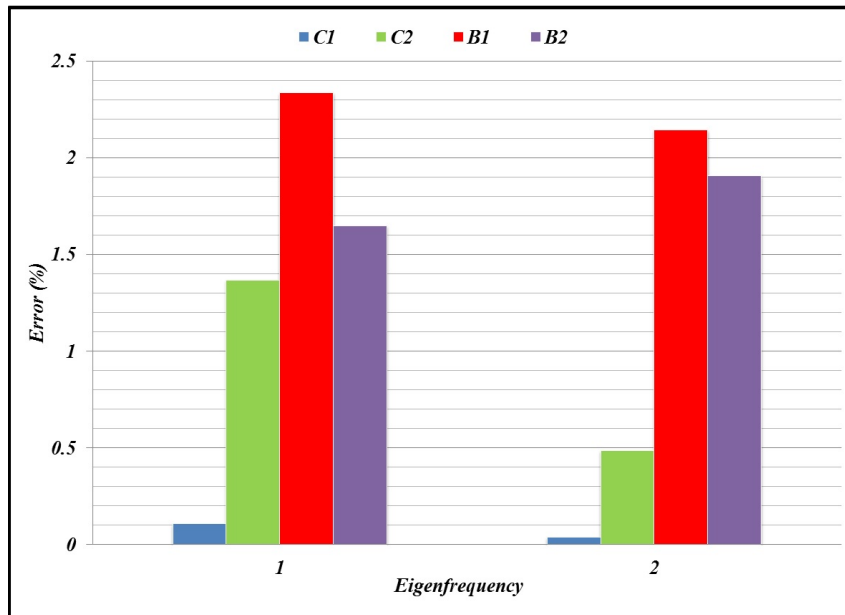


Figure 3: The Error of the Modeling Methods in Predicting the Eigenfrequencies

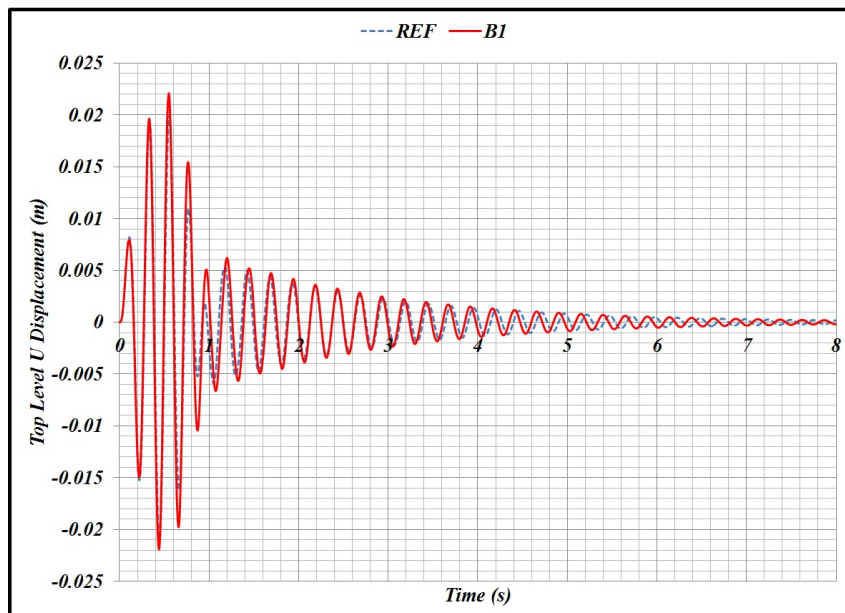


Figure 4: The Structure's Response Calculated with REF and B1 Models

4 CONCLUSION & REMARKS

Based on this study, it can be deduced that the substructure part of the full 3D FE model (Holistic) of a 2-DOF structure illustrated in Figure 2 resting on a pile embedded in a homogeneous elastic soil stratum can be best replaced by springs proposed by Novak [4], when the soil is assumed to have a constant profile and the columns are modeled with 3D (volume) elements. This approach, when compared with the Holistic model, predicts reasonably precise eigenfrequencies and structural response when excited by a 1-second harmonic load followed by a free vibration.

By performing an uncertainty analysis, however, a more accurate comparison between the methods could be made, leading to quantitative measures rather than qualitative comments.

Substitution of the soil layer and the pile with certain springs and dampers drastically reduces the computational effort and modeling complexity; however, one should keep in mind that a major drawback of application of such impedance functions is their incapability of capturing plastification and other phenomena not accounted for in an elastic modeling technique.

5 ACKNOWLEDGMENT

This research is supported by the German Research Foundation (DFG) via Research Training Group "Evaluation of Coupled Numerical Partial Models in Structural Engineering (GRK 1462)", which is gratefully acknowledged.

REFERENCES

- [1] J.P. Wolf: Soil-Structure-Interaction Analysis in Time Domain. Prentice Hall International Series in Civil Engineering and Engineering Mechanics, New Jersey, 1988.
- [2] J.S. Mulliken, D.L. Karabalis: Discrete Model for Dynamic Through-the-Soil Coupling of 3-D Foundations and Structures. *Earthquake Eng. and Structural Dynamics*, **27**, 687–710, 1998.
- [3] A. Maravas, G. Mylonakis, D.L. Karabalis: Simplified Discrete Systems for Dynamic Analysis of Structures on Footings and Piles. *Soil Dynamics and Earthquake Engineering*, **61-62**, 29–39, 2014.
- [4] M. Novak, M. ASCE, B. El Sharnouby: Stiffness Constants of Single Piles. *Journal of Geotechnical Engineering*, **109**, 961–974, 1983.

VARIATIONAL POSITING AND SOLUTION OF COUPLED THERMOMECHANICAL PROBLEMS IN A REFERENCE CONFIGURATION

D.V. Khristich* and Yu.V. Astapov

**Tula State University*
300012, Russian Federation, Tula, prospect Lenina, 92
E-mail: dmitrykhristich@rambler.ru

Keywords: Thermomechanics, Reversible Deformations, Finite Deformations, Variational Principles, Coupled Boundary-Value Problems

Abstract. *Variational formulation of a coupled thermomechanical problem of anisotropic solids for the case of non-isothermal finite deformations in a reference configuration is shown. The formulation of the problem includes: a condition of equilibrium flow of a deformation process in the reference configuration; an equation of a coupled heat conductivity in a variational form, in which an influence of deformation characteristics of a process on the temperature field is taken into account; tensor-linear constitutive relations for a hypoelastic material; kinematic and evolutionary relations; initial and boundary conditions. Based on this formulation several axisymmetric isothermal and coupled problems of finite deformations of isotropic and anisotropic bodies are solved. The solution of coupled thermomechanical problems for a hollow cylinder in case of finite deformation showed an essential influence of coupling on distribution of temperature, stresses and strains. The obtained solutions show the development of stress-strain state and temperature changing in axisymmetric bodies in the case of finite deformations.*

Within posing of a coupled thermomechanical problem for the case of finite deformations, which was introduced in articles [1-3], the problem of non-isothermal punching of a preliminarily crimped rubber sphere through an aperture of less diameter was numerically solved.

A numerical solution is based on a system of equations of nonlinear thermoelasticity in the reference configuration for isotropic bodies, obtained in [4]. This system includes:

a condition of an equilibrium flow of a deformation process in a variational form

$$\int_{V_0} \left(\left(\underline{U}^{-1} \right)' \cdot \underline{\Sigma}_R \cdot \underline{R} + \underline{U}^{-1} \cdot \dot{\underline{\Sigma}}_R \cdot \underline{R} + \underline{U}^{-1} \cdot \underline{\Sigma}_R \cdot \dot{\underline{R}} \right) \cdot \delta \left(\vec{v} \overset{\circ}{\nabla} \right) dV_0 = \int_{\Sigma_0} \vec{P}_0 \cdot \delta \vec{v} d\Sigma_0 + \int_{V_0} \vec{F}_0 \cdot \delta \vec{v} dV_0, \quad (1)$$

where $\underline{\Sigma}_R = \sqrt{\frac{G}{g}} \underline{R} \cdot \underline{S} \cdot \underline{R}^{-1}$, \underline{S} — Cauchy true stress tensor; \underline{G} and \underline{g} — metric tensors in current and initial configurations respectively; \underline{U} — left measure of distortion, \underline{R} — orthogonal tensor in a polar decomposition of a strain affiner $\underline{\Phi} = \underline{U} \cdot \underline{R}$; \vec{v} — velocity vector; \vec{P}_0 and \vec{F}_0 —

external fields of surface and mass forces respectively; $\overset{\circ}{\nabla} = \vec{e}^i \frac{\partial}{\partial X^i}$ — Hamiltonian operator in the original coordinate system;

an equation of a coupled heat conductivity in a variational form

$$\int_{V_0} \left(3K\alpha\dot{\theta}T + c_\varepsilon\rho_0\dot{T} \right) \delta T dV_0 = - \int_{\Sigma_0} \vec{n}_0 \cdot \vec{q}_0 \delta T d\Sigma_0 - \int_{V_0} \lambda \overset{\circ}{\nabla} T \cdot \delta \left(\overset{\circ}{\nabla} T \right) dV_0, \quad (2)$$

where c_ε — heat capacity at constant strain, ρ_0 — initial density, λ — thermal conductivity coefficient, α — linear coefficient of a thermal expansion, K — bulk modulus of the medium, \vec{q}_0 — heat flux vector on the body's bound, \vec{n}_0 — external unit normal with respect to Σ_0 ; $\dot{\theta}$ — rate of relative volume changing; T — temperature;

constitutive relations

$$\dot{\underline{\Sigma}}_R = \left(K - \frac{2}{3}G \right) \dot{\theta} \underline{E} + 2G\dot{M} - 3K\alpha(T - T_0)\underline{E}, \quad (3)$$

where M — non-holonomic strain measure, defined from a differential equation [5] $\dot{M} = \frac{1}{2} \left(\dot{\underline{U}} \cdot \underline{U} + \underline{U} \cdot \dot{\underline{U}} \right)$, G — shear modulus of the material;

kinematic relations

$$\begin{cases} \vec{v} = \frac{d\vec{u}}{dt}, \\ \dot{\underline{\Phi}} = \overset{\circ}{\nabla} \vec{v}, \\ \dot{\underline{U}} \cdot \underline{U} + \underline{U} \cdot \dot{\underline{U}} = \left(\overset{\circ}{\nabla} \vec{v} \right) \cdot \underline{\Phi}^T + \underline{\Phi} \cdot \left(\vec{v} \overset{\circ}{\nabla} \right), \\ \dot{T} = \frac{dT}{dt}; \end{cases} \quad (4)$$

initial conditions

$$\vec{u}|_{t=t_0} = \vec{u}_0(\vec{x}), \quad \underline{U}|_{t=t_0} = \underline{U}_0(\vec{x}), \quad \underline{\Sigma}_R|_{t=t_0} = \underline{\Sigma}_{R0}(\vec{x}), \quad T|_{t=t_0} = T_0(\vec{x}). \quad (5)$$

The boundary conditions of the static type require the definition at each point of the surface Σ_P the law of changes of the external forces as a function of time

$$\vec{P} = \vec{P}_0(\vec{x}, t) \quad \vec{x} \in \Sigma_P \quad \forall t > t_0. \quad (6)$$

When defining the boundary conditions of the kinematic type at each point of the surface Σ_u we determine the law of variation of the displacements of material points

$$\vec{u} = \vec{u}_0(\vec{x}, t) \quad \vec{x} \in \Sigma_u \quad \forall t > t_0. \quad (7)$$

The functions \vec{P}_0 and \vec{u}_0 are assumed to be differentiable with respect to time.

For the temperature field the conditions of free heat exchange on the surface Σ_T are accepted in the form of Newton's law:

$$\lambda \frac{\partial T}{\partial n_0} + a(T - T_e) = 0 \quad \vec{x} \in \Sigma_T \quad \forall t > t_0, \quad (8)$$

where a — heat exchange coefficient, T_e — temperature of external medium.

The initial boundary value problem (1)–(8) is solved using finite element method and method of step-by-step loading.

We list the initial data and the results of solving. The sphere's radius in unstrained state is $r_0 = 10mm$. The material of the sphere is isotropic and has the following characteristics: Young's modulus is $E = 8 \cdot 10^6 Pa$, Poisson's ratio is $\nu = 0,4$, linear coefficient of thermal expansion $\alpha = 2,3 \cdot 10^{-4} K^{-1}$, initial density $\rho_0 = 1,2 \cdot 10^3 \frac{kg}{m^3}$, specific heat $c_\varepsilon = 1,42 \cdot 10^3 \frac{J}{kg \cdot K}$, thermal conductivity coefficient $\lambda_0 = 0,16 \frac{W}{K \cdot m}$.

The process of the sphere's deformation consists of two phases. During the first phase axisymmetric compressing took place. As the result, sphere is placed inside the cylinder with the inner radius $r_1 = 9mm$. Second phase is accompanied by the action of linearly increasing in time pressure p , applied to the sphere under consideration.

Figure 1 contains the scheme of the sphere's loading on the second phase: $r_1 = 9mm$, $r_2 = 8,16mm$, $\beta = 60^\circ$. Initial temperature at each point of the medium is $T_0 = 293K$. Calculations were interrupted, when the pressure acting on the surface Σ_1 of specimen achieved the value $p = 3,36 \cdot 10^6 Pa = 1,176G$ (G — shear modulus of the sphere's material) at the rate of changing $\dot{p} = 2,4 \cdot 10^7 \frac{Pa}{s}$.

Boundary conditions (1)–(8) with the scheme of loading under consideration take the following form:

$$\vec{x} \in \Sigma_1 : \quad \vec{P} = -\dot{p}t\vec{n}_0, \quad T_e = 2000K;$$

$$\vec{x} \in \Sigma_2 : \quad v_n = 0, \quad P_\tau = 0, \quad T_e = 293K;$$

$$\vec{x} \in \Sigma_3 : \quad P_0^{(r)} = P_0^{(\varphi)} = P_0^{(z)} = 0, \quad T_e = 293K.$$

The results of calculations of the stress-strain state of the rubber sphere in the form of stress distributions with respect to shear modulus are presented on figures 2–5.

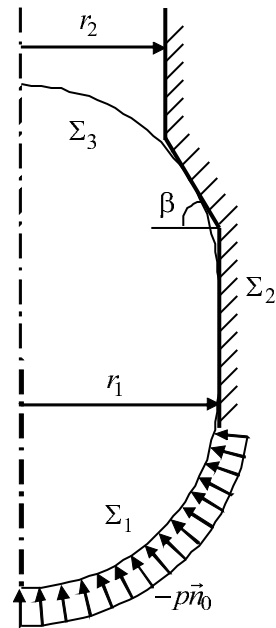


Figure 1. The scheme of the rubber sphere loading

At $p = 0$ the compressing stresses, caused by the strains from the first phase of the deformation process act on the sphere. Maximum in absolute magnitude of stresses at this phase of deformation takes place in the equatorial section of the sphere, which is in contact with the inner surface of the cylinder.

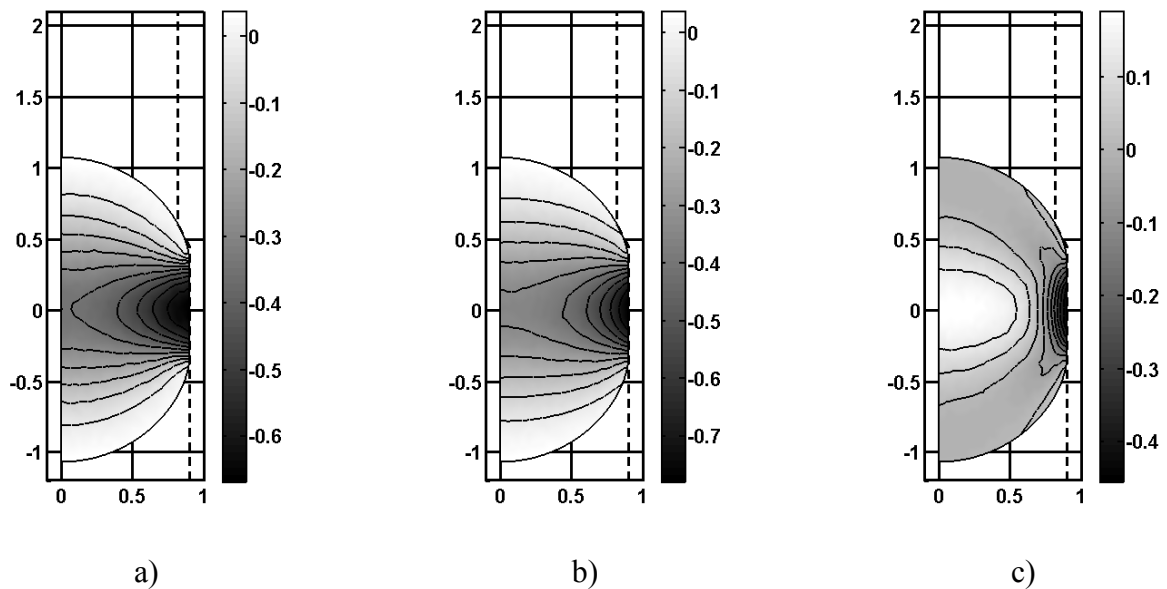


Figure 2. Stress distribution in the sphere at $p = 0$:
 a) radial stresses; b) tangential stresses; c) axial stresses

With the pressure growth the absolute values of stresses in the body also increase, and the character of their distribution in the sphere's cross-section changes. The redistribution of stresses occurs in the area of the contact of the specimen with the conic surface, which merges cylinders with inner radiuses r_1 and r_2 .

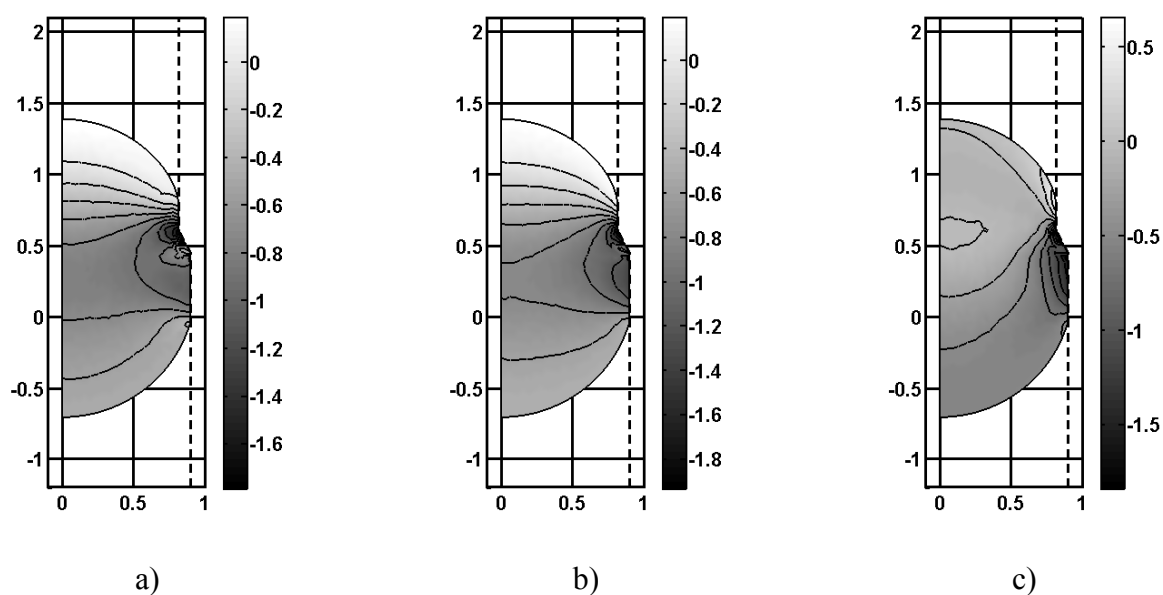


Figure 3. Stress distribution in the sphere at $p = 0, 496G$:
 a) radial stresses; b) tangential stresses; c) axial stresses

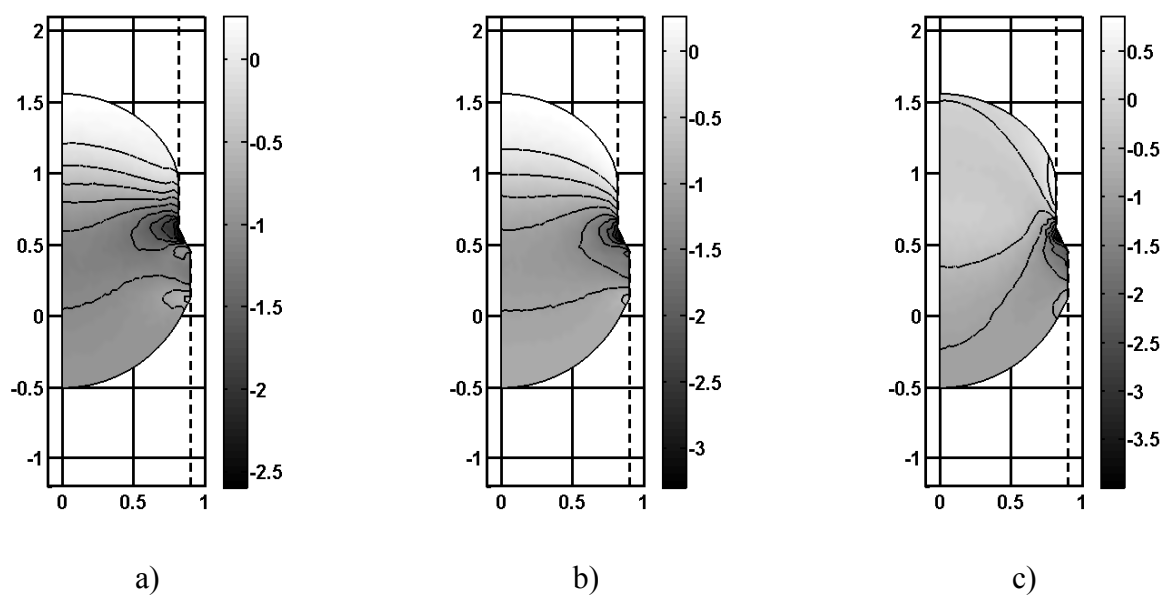


Figure 4. Stress distribution in the sphere at $p = 0, 832G$:
 a) radial stresses; b) tangential stresses; c) axial stresses

The surface form of the deformed body under consideration is significantly changing during movement inside the cylinders and the frustum of the cone. The magnitudes of arising stresses and strains depend on initial radius of the sphere and geometrical parameters of the surface Σ_2 .

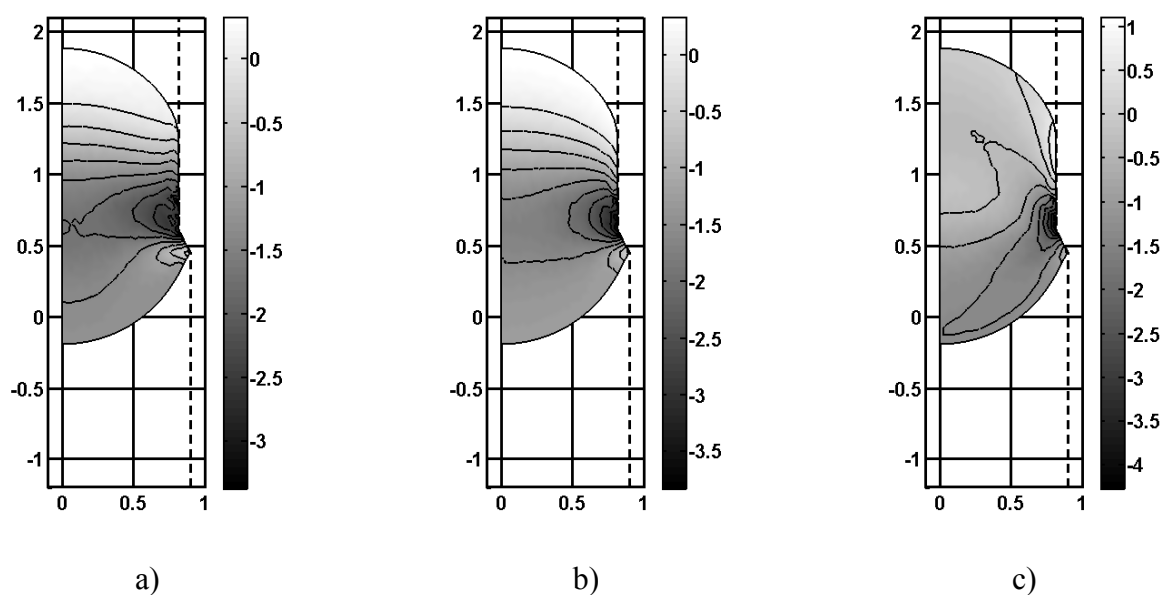


Figure 5. Stress distribution in the sphere at $p = 1, 176G$:
a) radial stresses; b) tangential stresses; c) axial stresses

In spite of the large strains, temperature field does not almost change in deformation due to small time of process flow and selected thermomechanical constants of the material.

Acknowledgements. The reported study was supported by RFBR (research projects No. 13-01-97501-p_tsentr_a, 14-01-31138-mol_a, 15-01-01875_a) and by the Ministry of Education and Science of the Russian Federation (state order No. 467).

REFERENCES

- [1] M.Yu. Sokolova and D.V. Khristich: Description of finite deformations of solids in the reference configuration. Prikl. Mekh. Tekh. Fiz., **53**, 2, 156–166, 2012. [J. Appl. Mech. Tech. Phys. **53**, 2, 283–291, 2012.]
- [2] D.V. Khristich, Yu.V. Astapov and L.V. Glagolev: Positing of the problem of finite deformations of anisotropic solids in the terms of initial configuration. Izv. of Tula State University. Natural sciences, 3, 148–157, 2014.
- [3] D.V. Khristich and M.Yu. Sokolova: Boundary value problem of non-linear thermoelasticity solving. Izv. of Tula State University. Natural sciences, 1, 123–136, 2010.
- [4] D.V. Khristich and Yu.V. Astapov: The accounting of mutual influences between the fields of stresses, strains and temperature in Lamé problem. Izv. of Tula State University. Natural sciences, 1, 67–73, 2015.
- [5] A.A. Markin, M.Yu. Sokolova: Thermomechanics of elastoplastic deformation. FIZ-MATLIT, Moscow, 2013.

FUNDAMENTALS OF A WIMAN VALIRON THEORY FOR POLYMONOGENIC FUNCTIONS

R. De Almeida and R.S. Kraußhar*

* *University of Erfurt*

Fachgebiet Mathematik, Nordhäuser Str. 63, D-99089 Erfurt

E-mail: soeren.krausshar@uni-erfurt.de

Keywords: Wiman-Valiron theory, polymonogenic functions, growth orders

Abstract. *In this paper we present some rudiments of a generalized Wiman-Valiron theory in the context of polymonogenic functions. In particular, we analyze the relations between different notions of growth orders and the Taylor coefficients. Our main intention is to look for generalizations of the Lindelöf-Pringsheim theorem. In contrast to the classical holomorphic and the monogenic setting we only obtain inequality relations in the polymonogenic setting. This is due to the fact that the Almansi-Fischer decomposition of a polymonogenic function consists of different monogenic component functions where each of them can have a totally different kind of asymptotic growth behavior.*

1 THE CLASSICAL SETTING

Suppose that $f(z) = \sum_{n=0}^{\infty} a_n z^n$ is an entire holomorphic function, this means that its convergence radius r is infinite. In the special case where f is a polynomial, there exists an $N \in \mathbb{N}$ such that $a_n = 0$ for all $n > N$, and one has that $|f(z)| \sim |a_N||z|^N$ for $|z|$ large.

Now, to describe the growth behavior of general transcendental entire functions one defines the growth order of f by

$$\rho(f) := \limsup_{r \rightarrow \infty} \frac{\log^+ \log^+ M(r, f)}{\log r}$$

where $M(r, f) := \max\{|f(z)| \mid |z| = r\}$. The classical Lindelöf-Pringsheim theorem provides us with an explicit relation between the Taylor coefficients a_n and the growth order ρ :

$$\rho(f) = \limsup_{n \rightarrow \infty} \frac{n \log(n)}{-\log |a_n|}.$$

2 THE MONOGENIC CASE

In this section we briefly summarize the corresponding result for the higher dimensional monogenic case where one considers a first order operator generalizing straightforwardly the standard Cauchy-Riemann operator. For the general facts about Clifford algebras and Clifford analysis we refer for instance to [1].

2.1 Basic notation

By Cl_n we denote the real Clifford algebra Cl_n over \mathbb{R}^n defined by $e_0 := 1$, $e_i^2 = -1$, $i = 1, \dots, n$ and $e_i e_j = -e_j e_i$ for all $i, j = 1, \dots, n$ such that $i \neq j$.

A basis for Cl_n is given by the elements $1, e_1, \dots, e_n, e_1 e_2, \dots, e_{n-1} e_n, \dots, e_1 \cdots e_n$. A vector space basis for Cl_n is given by the set $\{e_A : A \subseteq \{1, \dots, n\}\}$ with $e_A = e_{l_1} e_{l_2} \cdots e_{l_r}$, where $1 \leq l_1 < \cdots < l_r \leq n$, $e_\emptyset = e_0 = 1$. Each element $a \in Cl_n$ can be written in the form $a = \sum_A a_A e_A$ with $a_A \in \mathbb{R}$. The standard Clifford norm, defined by $\|a\| = (\sum_A |a_A|^2)^{1/2}$.

Next, each non-zero paravector $z = x_0 + x_1 e_1 + \cdots + x_n e_n \in \mathbb{R}^{n+1} \setminus \{0\}$ has an inverse $z^{-1} = \frac{x_0 - x_1 e_1 - \cdots - x_n e_n}{x_0^2 + x_1^2 + \cdots + x_n^2}$.

For simplicity we also apply the standard multi-index notation, namely for an index $\mathbf{m} = (m_1, \dots, m_n) \in \mathbb{N}_0^n$ we write:

$$\mathbf{x}^{\mathbf{m}} := x_1^{m_1} \cdots x_n^{m_n}, \quad \mathbf{m}! := m_1! \cdots m_n!, \quad |\mathbf{m}| := m_1 + \cdots + m_n.$$

Further we denote by $\tau(i)$ the particular index (m_1, \dots, m_n) with $m_j = \delta_{ij}$ for $1 \leq j \leq n$ where δ_{ij} stands for the Kronecker symbol.

2.2 Monogenic functions

Definition 1. (cf. [1]). A function $f : \mathbb{R}^{n+1} \rightarrow Cl_n$ is called entire (left) monogenic if $Df(z) = 0$ for all $z \in \mathbb{R}^{n+1}$ where $\mathcal{D} := \frac{\partial}{\partial x_0} + \sum_{i=1}^n e_i \frac{\partial}{\partial x_i}$ is the generalized Cauchy-Riemann operator.

The null-solutions to this first order operator exhibit some nice analogies to complex holomorphic functions, for instance:

- the maximum principle holds
- we have a Cauchy integral formula
- we have an overall convergent Taylor series representation of the form

$$f(z) = \sum_{|\mathbf{m}|=0}^{\infty} V_{\mathbf{m}}(z)a_{\mathbf{m}},$$

where $V_{\mathbf{m}}$ are the usual Fueter polynomials, for example: $V_{\mathbf{0}}(z) := 1$, $V_{\tau(i)}(z) = x_i - e_i x_0$, $V_{2\tau(i)}(z) = V_{\tau(i)}(z)^2$, $V_{\tau(i),\tau(j)} = \frac{1}{2} \left(V_{\tau(i)}(z)V_{\tau(j)}(z) + V_{\tau(j)}(z)V_{\tau(i)}(z) \right)$.

In [2] we proved an analogous relation of the classical Lindelöf-Pringsheim theorem for entire monogenic functions. For $n > 1$ one has exactly, that

$$\rho(f) = \limsup_{|\mathbf{m}| \rightarrow \infty} \frac{|\mathbf{m}| \log |\mathbf{m}|}{-\log \left\| \frac{1}{c(n, \mathbf{m})} a_{\mathbf{m}} \right\|},$$

where

$$c(n, \mathbf{m}) := \frac{n(n+1) \cdots (n + |\mathbf{m}| - 1)}{\mathbf{m}!}.$$

This constant $c(n, \mathbf{m})$ does not appear in the complex case $n = 1$. It is a novelty in the higher dimensional setting. The reason for the appearance of $c(n, \mathbf{m})$ is that in the higher dimensional case the sharp upper bound for the Taylor coefficients (Cauchy inequality) has the following different form

$$\|a_{\mathbf{m}}\| \leq c(n, \mathbf{m}) \frac{M(r, f)}{r^{|\mathbf{m}|}}.$$

In the case $n = 1$ the constant $c(n, \mathbf{m})$ simply equals 1 and thus turns out to be independent from \mathbf{m} .

3 THE GROWTH OF POLYMONOGENIC FUNCTIONS

Now we consider entire functions in \mathbb{R}^n that are null-solutions to the higher dimensional poly-Cauchy-Riemann equation $\mathcal{D}^k f(z) = 0$ where k is an arbitrary positive integer. These are called left polymonogenic functions, or k -monogenic for short. The starting point of our consideration is the well-known Almansi-Fischer decomposition, cf. [1]: One can represent every k -monogenic function $f(z)$ in terms of $f(z) = \sum_{j=0}^{k-1} x_0^j f_j(z)$ where f_j are monogenic functions. Each entire k -monogenic function has the special Taylor series representation

$$f(z) = \sum_{|\mathbf{m}|=0}^{+\infty} \sum_{j=0}^{k-1} x_0^j V_{\mathbf{m}}(z) a_{\mathbf{m},j}. \quad (1)$$

The Cauchy type estimate for the Taylor coefficients $a_{\mathbf{m},j}$ is given by

$$\|a_{\mathbf{m},j}\| = \left\| \frac{\partial^{|\mathbf{m}|}}{\partial \mathbf{x}^{\mathbf{m}}} f_j \right\| \leq \frac{c(n, \mathbf{m})}{r^{|\mathbf{m}|}} M(r, f_j). \quad (2)$$

Problems of the polymonogenic setting:

- Polymonogenic functions do **not** obey a sharp maximum principle
- Each monogenic component function can have a totally different growth
- **Consequence:** There will be **no direct analogue** of the Lindelöf-Pringsheim theorem; one only gets a series of inequality relations and lower and upper bound estimates.

3.1 Cauchy type estimates

In the following example one can see that polymonogenic functions do not obey a sharp maximum principle:

The function $f(x_0, x_1, x_2) = 1 - x_0^2 - x_1^2 - x_2^2$ satisfies $\mathcal{D}^3 f = 0$ but $f(0, 0, 0) = 1$ and $f(x_0, x_1, x_2) = 0$ for all $x \in \mathbb{R}^3$ with $\sum_{i=0}^2 x_i^2 = 1$. Therefore, we define $M(r, f) := \max\{\|f(z)\| \mid \|z\| = r\}$ and $\mathcal{M}(r, f) := \max\{\|f(z)\| \mid \|z\| \leq r\}$.

To achieve our goal we need to set up relations between the maximum modulus of a k -monogenic function and the monogenic component functions of the Almansi-Fischer decomposition. We can prove the following lemmas, cf. [3]:

Lemma 1. Let $f : \mathbb{R}^{n+1} \rightarrow Cl_n$ be entire k -monogenic where the associated 1-monogenic component functions are denoted by f_0, f_1, \dots, f_{k-1} . Define $M_0(r, f) = \max_{0 \leq j \leq k-1} \{\mathcal{M}(r, f_j)\}$.

Then, for $r \geq 1$ we have

$$\mathcal{M}(r, f) \leq kr^k M_0(r, f). \quad (3)$$

Lemma 2. Let $\mathcal{M}^*(r, f) = \max_{0 \leq q \leq k-1} \mathcal{M}(r, \mathcal{D}^q f)$. Then, for $r > 1$ and $l \in \{0, \dots, k-1\}$ we have

$$\mathcal{M}(r, f_l) \leq kr^k \mathcal{M}^*(r, f) \quad (4)$$

and

$$\mathcal{M}(r, f) \leq k^2 r^{2k} \mathcal{M}^*(r, f). \quad (5)$$

Proof. The monogenic components f_0, \dots, f_{k-1} can be reconstructed from f by

$$x_0^l f_l = P_l f \quad (6)$$

with

$$P_l = \sum_{q=l}^{(+\infty)} (-1)^{l-q} \frac{1}{l!(q-l)!} x_0^q \mathcal{D}^q. \quad (7)$$

Therefore,

$$\|f_l(z)\| \leq \sum_{q=l}^{k-1} \frac{1}{l!(q-l)!} |x_0|^{q-l} \|\mathcal{D}^q f\|.$$

Since $\frac{1}{l!(q-l)!} \leq 1$ we obtain

$$\begin{aligned} M(r, f_l) &\leq \sum_{q=l}^{k-1} \frac{1}{l!(q-l)!} r^{q-l} \mathcal{M}(r, \mathcal{D}^q f) \leq \mathcal{M}^*(r, f) \sum_{q=l}^{k-1} \frac{1}{l!(q-l)!} r^{q-l} \\ &\leq \mathcal{M}^*(r, f) \sum_{q=l}^{k-1} r^{q-l}. \end{aligned}$$

Therefore, for $r > 1$ we have

$$M(r, f_l) \leq kr^{k-2l} \mathcal{M}^*(r, f) \leq kr^k \mathcal{M}^*(r, f). \quad (8)$$

Using (8) and applying the Almansi-Fischer decomposition of f , we may derive inequality (5)

$$\mathcal{M}(r, f) \leq \sum_{j=0}^{k-1} r^j M(r, f_j) \leq k^2 r^{2k} \mathcal{M}^*(r, f). \quad \square$$

Using Lemma 2, we obtain for $r > 1$ the following Cauchy-type estimate

$$\|a_{\mathbf{m}, l}\| \leq \max_{0 \leq l \leq k-1} \|a_{\mathbf{m}, l}\| \leq \frac{c(n, \mathbf{m})k}{r^{|\mathbf{m}|-k+1}} \mathcal{M}^*(r, f). \quad (9)$$

Next we can prove

Lemma 3. *Let $\widetilde{\mathcal{M}}(r, f) := \max_{0 \leq q \leq k-1} \left\{ \max_{\|z\| \leq r} \left\{ r^q \|D^q f(z)\| \right\} \right\}$. Then, for any $r > 1$, we have*

$$M(r, f_l) \leq \widetilde{\mathcal{M}}(r, f) r^{-l} k, \quad (10)$$

for $l \in \{0, \dots, k-1\}$ and

$$\mathcal{M}(r, f) \leq k^2 \widetilde{\mathcal{M}}(r, f). \quad (11)$$

Summarizing we may formulate:

Lemma 4. *For $r > 1$ we have*

$$\mathcal{M}(r, f) \leq kr^k M_0(r, f) \leq k^2 r^k \widetilde{\mathcal{M}}(r, f), \quad (12)$$

and

$$\mathcal{M}(r, f) \leq kr^k M_0(r, f) \leq k^2 r^{2k} \mathcal{M}^*(r, f). \quad (13)$$

3.2 Growth orders

Based on the previously introduced definitions it makes sense to introduce the following slightly different notions of growth orders in the polynogenic settings.

Definition 2. *Let $f : \mathbb{R}^{n+1} \rightarrow Cl_n$ be an entire k -monogenic function. Then*

$$\rho(f) := \limsup_{r \rightarrow \infty} \frac{\log^+(\log^+ \mathcal{M}(r, f))}{\log(r)}, \quad 0 \leq \rho \leq \infty \quad (14)$$

is called the order of growth of the function f .

Theorem 1. Define $\rho_0(f) := \limsup_{r \rightarrow \infty} \frac{\log^+(\log^+(M_0(r, f)))}{\log(r)}$. Then

$$\rho(f) \leq \rho_0(f). \quad (15)$$

Note that in the monogenic case, one has: $\rho(f) = \rho_0(f)$. Using Lemma 1, 2 and Lemma 3 we may establish

Theorem 2. Let $\tilde{\rho}(f) := \limsup_{r \rightarrow \infty} \frac{\log^+(\log^+(\tilde{\mathcal{M}}(r, f)))}{\log(r)}$. Then

$$\rho(f) \leq \rho_0(f) \leq \tilde{\rho}(f). \quad (16)$$

Theorem 3. Let $\rho^*(f) := \limsup_{r \rightarrow \infty} \frac{\log^+(\log^+(\mathcal{M}^*(r, f)))}{\log(r)}$. Then

$$\rho(f) \leq \rho_0(f) \leq \rho^*(f). \quad (17)$$

3.3 Explicit relations between growth orders and Taylor coefficients

In contrast to the monogenic setting where one gets a direct analogue of the Lindelöf-Pringsheim theorem in terms of an equality relation between the growth order and the Taylor coefficients. In the polymonogenic one only gets inequality relations. In [3] we were able to prove the following main results:

Theorem 4. For an entire k -monogenic function with Taylor series representation of the form (1) let

$$\Pi_j = \limsup_{|\mathbf{m}| \rightarrow +\infty} \frac{|\mathbf{m}| \log |\mathbf{m}|}{-\log \left\| \frac{a_{\mathbf{m}, j}}{c(n, \mathbf{m})} \right\|}, \quad 0 \leq j \leq k-1. \quad (18)$$

Then $\tilde{\rho}(f) \geq \Pi_{\min} = \min_{0 \leq j \leq k-1} \Pi_j$ and $\Pi_{\max} = \max_{0 \leq j \leq k-1} \Pi_j \geq \rho(f)$.

Theorem 5. For an entire k -monogenic function $f : \mathbb{R}^{n+1} \rightarrow Cl_n$ with a Taylor series representation of the form (1) let

$$\Pi_j = \limsup_{|\mathbf{m}| \rightarrow +\infty} \frac{|\mathbf{m}| \log |\mathbf{m}|}{-\log \left\| \frac{1}{c(n, \mathbf{m})} a_{\mathbf{m}, j} \right\|}, \quad 0 \leq j \leq k-1. \quad (19)$$

Then $\rho^*(f) \geq \Pi_{\min} = \min_{0 \leq j \leq k-1} \Pi_j$ and $\Pi_{\max} = \max_{0 \leq j \leq k-1} \Pi_j \geq \rho(f)$.

In the monogenic case, one simply has $\Pi_{\min} = \Pi_{\max} = \Pi_j$.

REFERENCES

- [1] R. Delanghe, F. Sommen and V. Souček. *Clifford Algebra and Spinor Valued Functions*. Kluwer, Dordrecht-Boston-London, 1992.
- [2] D. Constales, R. de Almeida and R.S. Kraußhar. On the relation between the growth and the Taylor coefficients of entire solutions to the higher dimensional Cauchy-Riemann system in \mathbb{R}^{n+1} , *Journal of Mathematical Analysis and Applications*, 327 (2007), 763–775.
- [3] R. De Almeida and R.S. Kraußhar. Basics on growths orders of polymonogenic functions. Accepted for publication (14/3/2015) in *Complex Variables and Elliptic Equations*, 27pp.

ANALYSIS OF STEEL STRUCTURAL MEMBERS IN FIRE WITH SLENDER CROSS-SECTIONS THROUGH BEAM FINITE ELEMENTS APPLYING AN EFFECTIVE CONSTITUTIVE LAW

N. Lopes *, D. Rodrigues and P. Vila Real

* *RISCO – Civil Engineering Department of the University of Aveiro
Campus universitário de Santiago, 3810-193 Aveiro, Portugal
E-mail: nuno.lopes@ua.pt*

Keywords: Steel structural elements, numerical modelling, slender cross-sections, fire.

Abstract. *Steel profiles with slender cross-sections are characterized by their high susceptibility to instability phenomena, especially local buckling, which are intensified under fire conditions. This work presents a study on numerical modelling of the behaviour of steel structural elements in case of fire with slender cross-sections. To accurately carry out these analyses it is necessary to take into account those local instability modes, which normally is only possible with shell finite elements. However, aiming at the development of more expeditious methods, particularly important for analysing complete structures in case of fire, recent studies have proposed the use of beam finite elements considering the presence of local buckling through the implementation of a new effective steel constitutive law. The objective of this work is to develop a study to validate this methodology using the program SAFIR. Comparisons are made between the results obtained applying the referred new methodology and finite element analyses using shell elements. The studies were made to laterally restrained beams, unrestrained beams, axially compressed columns and columns subjected to bending plus compression.*

1 INTRODUCTION

The use in construction of steel structures with slender cross-sections has been increasing in recent years as they provide a good weight/resistance relationship. However, these structures are more susceptible to the occurrence of instability phenomena jeopardizing their stability. The existence of local buckling is due to the high slenderness of the different parts of the cross-section (web and flanges). Slender sections with high susceptibility to local buckling are classified according to the Eurocode 3 [1] as Class 4. Global instability is associated to members that are not properly restrained and can occur for example by flexural buckling or lateral-torsional buckling (LTB).

In addition, fire safety is often decisive in the design of steel structures, especially to those who are composed of thin walled sections. The reduced thickness of the profiles combined with the high thermal conductivity of steel, impose high steel temperatures when these profiles are submitted to fire, which directly affect the steel mechanical properties [1, 2]. Due to the high cost and sizes limitation of experimental fire resistance tests, in recent years, numerous studies have been conducted based on numerical simulation, especially through the finite element method (FEM) [2]. There are several programs with geometrically and materially non-linear analysis based on the FEM, as the one used in this study, SAFIR [3]. This program was developed especially for the analysis of structures subjected to fire.

The application of shell finite elements corresponds to one of the most accurate methods for the study of the behavior of structures with slender sections because they can reproduce the local buckling phenomenon. But, when they are applied, the calculating time is too high, being its use limited to small structures and isolated structural elements. In the numerical analysis of complete structures subjected to fire [4], beam finite elements are more used, however, they cannot reproduce local buckling phenomenon. Some studies have been addressing this limitation [5, 6]. The most commonly used approach for analyzing the local buckling is based on the concept of effective width [7], however applying this methodology in beam finite elements introduces some difficulties in the code formulation [5]. The studies conducted in this work are based on a recent study by Franssen and Cowez [5] who have proposed the use of an effective constitutive law to enable the study of structures with Class 4 sections subjected to fire using beam finite elements.

The main objective of this study is to evaluate the accuracy of this method in different types of structural elements. The results obtained with this methodology are compared to analysis performed using shell finite elements, which are taken as the reference values.

This work is included in the European research project FIDESC4 “Fire Design of Steel Members with Welded or Hot-rolled Class 4 Cross-section” [8, 9]. Some of the chosen case studies also correspond to benchmark cases proposed under the COST Action TU0940 - IFER “Integrated Fire Engineering and Response” [10]. Those numerical models (applying shell finite elements) were validated using experimental tests in the project FIDESC4.

2 EFFECTIVE STRESS-STRAIN RELATIONSHIP FOR CONSIDERING LOCAL BUCKLING IN BEAM FINITE ELEMENTS

Franssen and Cowez [5] presented a proposal for numerical modeling of steel structures subjected to fire with beam finite elements, which takes into account the local instability of structural elements with slender section through an effective constitutive law. This new approach uses the constitutive law from EN 1993-1-2 [1], and is based on the effective stresses

method that has the following advantages: application of the correct value of stiffness; no need to predetermine the tensioned and compressed areas; and no need for the classification of the cross sections [5].

Because the local buckling develops only when the element is subject to compression, the stress-strain relationship is changed only with respect to compression, and remains unchanged in tension. This results in a non-symmetrical law (tension / compression), as shown in Figure 1. The effective stress-strain relationship in compression depends on the slenderness of the element, on the boundary conditions of the element (plate supported on four sides for the web, or three for the flange) and on the steel grade.

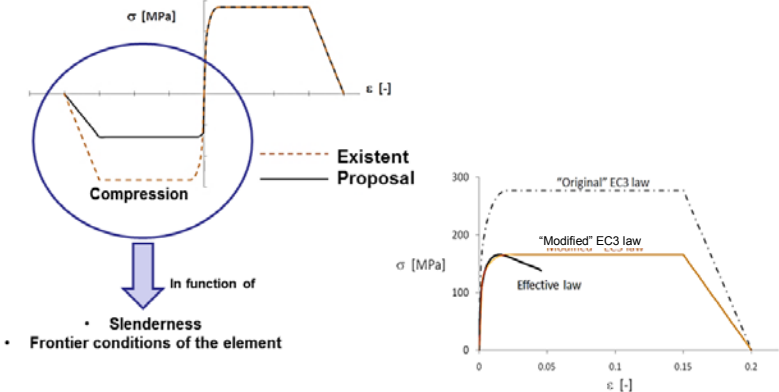


Figure 1. Effective constitutive law modifying EC3 law [5].

This effective constitutive law also depends on the temperature by the same reduction proposed in EC3 [1]. Knowing the slenderness, steel grade and support conditions of the elements, which corresponds to new material properties, the user introduces these new materials on the web and flanges (Figure 2) and the program automatically determines the amount and direction of tensile or compression stresses in each integration point [5].

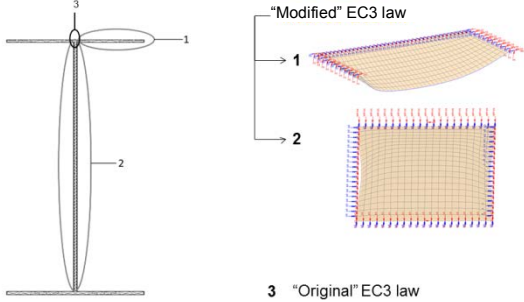


Figure 2. Materials definition: 1 - flanges; 2 - web; 3 – intersection between the flange and web.

3 NUMERICAL MODELS

The study cases were chosen from the following types of members [8, 9]: laterally restrained beams; unrestrained beams; axially compressed columns; and columns subjected to compression plus bending (about the strong axis). The members have different cross sections, length, loading type (bending moment diagrams) and restrained conditions (LTB restriction). The considered cross sections are I welded profiles named $h_w t_w + b t_f$ (h_w - height of the web, t_w - web thickness, b - profile width, t_f - thickness of flange). One test was made using a hot-rolled section HE340AA. The elements are of steel grade S355 at 450 °C (some tests were also performed at 500 and 650 °C). Other members typologies were also analyzed: as for exemple tapered members designated by $h_{w,MAX} - h_{w,min} t_w + b t_f$ ($h_{w,MAX}$ - maximum height of the web,

$h_{w,min}$ - minimum height of the web). These cases were chosen in order to be a reasonable representation of the common application of steel profiles with slender sections.

On the models with beam finite elements only global geometric imperfections were considered, in accordance with Annex C of Part 1-5 of EC3 [7], 80% of the geometric manufacturing tolerances described in the standard EN 1090-2 [11] were used. In the models with shell finite elements local imperfections were also considered according to the same recommendations of Part 1-5 of EC3 and EN 1090-2. Residual stresses were also introduced following the typical distributions on I welded sections [12].

4 RESULTS AND DISCUSSION

This section presents the obtained results using shell finite elements, beam finite elements with EC3 constitutive law and beam finite elements with the effective constitutive law.

First, the obtained results for beams subject to pure bending without LTB are presented. A case corresponding to an experimental test [8] is here detailed (first row in Table 1). This beam is subjected to two concentrated loads, being only the central span at 450 °C. Figure 3 shows the models with shell and beam finite elements and the obtained load-displacement curves.

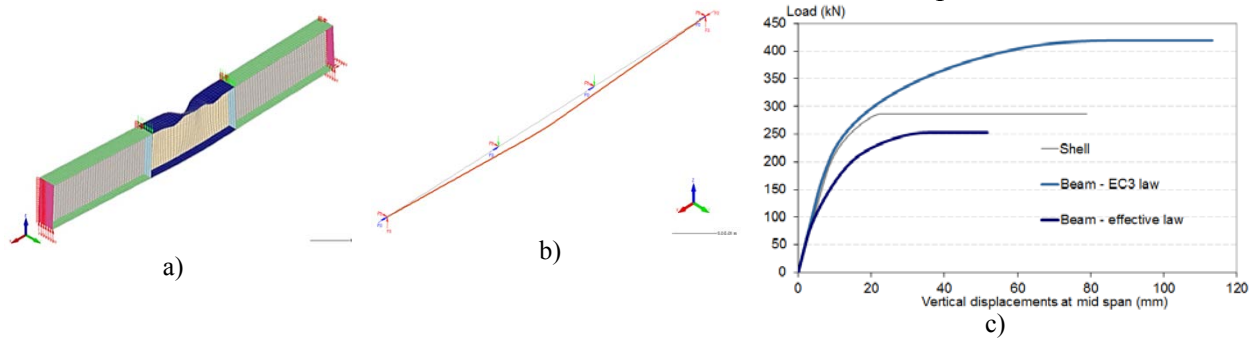


Figure 3. a) Model with Shell FE; b) Model with beams FE; c) Obtained load-displacements relations.

Table 1 summarizes all the obtained ultimate bending moments with all methodologies.

Sectiono	L [m]	Mult (kNm)			b/a	c/a
		a) Shell	b) Beam EC3 law	c) Effective law		
656x4+250x12	1.5	286.91	419.04	252.83	1.46	0.88
1000x14+300x22	10	2496.46	2936.89	2089.21	1.18	0.84
1000x12+300x18	10	1843.62	2445.86	1607.81	1.33	0.87
1000x12+300x14	10	1422.02	2074.32	1275.53	1.46	0.90
1000x8+300x18	10	1608.47	2153.67	1370.39	1.34	0.85
1000x6+300x13	10	943.87	1566.21	859.62	1.66	0.91
450x6+150x11	5	251.52	318.50	229.37	1.27	0.91
450x6+150x9	5	195.33	277.05	188.53	1.42	0.97
450x5+150x8	5	157.57	239.95	154.20	1.52	0.98
450x4+150x6	5	106.00	183.28	103.25	1.73	0.97
450x4+150x5	5	89.33	162.31	85.16	1.82	0.95

Table 1 – Obtained ultimate bending moments for restrained beams.

It can be concluded that the models with the effective law provide similar results to those obtained with the shell finite element models. As expected, the models with beam finite

elements using the EC3 constitutive law provided higher results, due to the local buckling.

Table 2 presents the obtained results for laterally unrestrained beams.

Section	L [m]	psi	Mult (kNm)			b/a	c/a
			a) Shell	b) Beam EC3 law	c) Effective law		
610-450x4+150x5	2.8	1	31.19	38.58	18.76	1.24	0.60
610-450x5+150x5	5	1	45.87	37.20	27.5	0.81	0.60
610-450x5+150x5	5	0	85.36	63.66	46.51	0.75	0.54
610-450x5+150x5	5	-1	97.9	92.80	68.60	0.95	0.70
450x5+250x5	8	1	52.2	51.84	37.05	0.99	0.71
450x5+250x5	11	0	73.29	66.65	48.52	0.91	0.66
450x5+250x5	13	-1	80.12	82.95	59.45	1.04	0.74
1000x7+300x12	8	1	381.42	378.95	225.00	0.99	0.59
1000x7+300x12	10	0	510.45	537.82	311.34	1.05	0.61
1000x7+300x12	12.5	-1	475.51	595.88	383.50	1.25	0.81

Table 2 – Obtained ultimate bending moments for unrestrained beams.

The models with the effective law provide too conservative results. The models with beam finite element using the EC3 constitutive law provide results that are close to those obtained with the shell finite elements, due to the high susceptibility to LTB of these beams.

Table 3 presents the results for axially compressed columns.

Section	L [m]	Nult (kN)			b/a	c/a
		a) Shell	b) Beam EC3 law	c) Effective law		
500x6+250x10	8	441.61	419.92	282.27	0.95	0.64
500x4+250x6	6	328.86	377.75	191.35	1.15	0.58
500x4+250x6	4	421.26	575.13	313.82	1.37	0.74
500x4+250x12	6	677.78	563.07	392.95	0.83	0.58
500x4+250x12	4	940.59	945.53	673.88	1.01	0.72
500x10+250x6	6	405.91	460.07	381.56	1.13	0.94
500x10+250x6	4	627	775.56	528.16	1.24	0.84

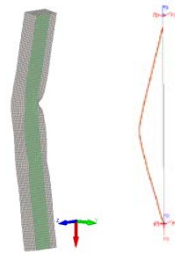


Table 3 – Obtained ultimate axial efforts for axially compressed columns.

Once again, it was observed that the models with the effective law provide too low results.

The obtained results for columns subjected to compression plus bending (about the strong axis) with and without the possibility of LTB occurrence are presented in Table 4.

Section	L [m]	psi	LTB	a) Shell		b) Beam EC3 law		c) Effective law		b/a	c/a
				Nult	Mult	Nult	Mult	Nult	Mult		
350x4+150x5	2.7	1	sim	226.56	16.09	326.01	23.14	184.40	13.09	1.44	0.81
440-340x4+150x5	2.7	0	sim	227.94	34.42	314.95	47.56	157.98	23.85	1.38	0.69
450x4+250x6	10	1	não	192.66	62.35	348.89	113.04	178.94	57.98	1.81	0.93
450x4+250x6	10	0	não	238.62	77.22	454.14	147.14	225.72	73.13	1.90	0.95
450x4+250x6	10	1	sim	92.80	30.03	125.97	40.81	71.32	23.11	1.36	0.77
450x4+250x6	10	0	sim	125.72	40.69	147.04	47.64	82.09	26.60	1.17	0.65
450x4+250x6	10	1	sim	169.43	22.94	158.66	22.85	84.67	12.19	0.94	0.50
1000x5+300x10	10	1	não	486.47	349.98	1112.19	800.78	476.96	343.41	2.29	0.98
HE340AA	10	1	sim	312.09	57.48	385.42	70.15	317.29	57.75	1.23	1.02
1000-750x5+300x10	10	1	sim	305.49	165.13	229.43	124.12	154.04	83.33	0.75	0.50

Table 4 – Obtained ultimate bearing capacities for columns with compression plus bending.

The results obtained with the effective law are not consistent, in some cases the approximation is good but in other cases they are not satisfactory.

5 CONCLUSIONS

A study on the evaluation of the fire resistance of members with slender cross-sections, modeled with beam finite element with a new effective constitutive law, was presented. The obtained results were compared with those obtained through the application of shell finite elements. Laterally restrained beams, unrestrained beams, axially compressed columns and columns subjected to compression plus bending were modeled using the program SAFIR.

Reproducing the same structural element or structure with numerical models considering beam elements and shell elements, can lead to several difficulties, which may range from the reproduction of the supports and loads application to the modeling of the profile geometry (e.g. tapered members), affecting the degree of accuracy of the respective comparisons.

It can be concluded that this new methodology complies with the intended purpose for cross-section bending resistance. On the other hand, regarding the resistance of members with greater susceptibility to global buckling, the ultimate bearing capacities obtained with the effective law proposed by Franssen and Cowez [5] are much lower than the values obtained with shell finite elements. Thus, this approach can be applied to similar elements to the ones studied here, due of its conservative nature.

REFERENCES

- [1] CEN. EN 1993-1-2 Eurocode 3: Design of Steel Structures - Part 1-2: General rules - Structural fire design, Brussels, Belgium, 2005.
- [2] J.-M. Franssen, P. Vila Real, Fire Design of steel Structures, ECCS, Ernst & Sohn, 2010.
- [3] J.-M. Franssen, "SAFIR. A Thermal/Structural Program Modelling Structures under Fire", Engineering Journal, A.I.S.C., Vol 42, N 3, 143-158, 2005.
- [4] P. Vila Real, N. Lopes, "Evaluation of the fire resistance of the steel structure of an exhibition centre using structural fire safety engineering", proceedings of Nordic Steel Construction Conference 2012, pp. 441-450, Oslo, 2012.
- [5] J.-M. Franssen e B. Cowez, "Consideration of local instabilities in beam finite elements by means of effective constitutive law", 7th Structures in Fire, Zurich, 2012.
- [6] S. Sreenath, U. Saravanan, V. Kalyanaraman, "Beam and shell element model for advanced analysis of steel structural members" Journal of Colloid and Interface Science, Volume 361, pp. 90-96, 2011.
- [7] CEN. EN 1993-1-5, Eurocode 3: Design of Steel Structures - Part 1-5: Plated structural elements, Brussels, Belgium, 2006.
- [8] B. Zhao, A. Sanzel, F. Morente, J.-M. Franssen, P. Vila Real, F. Wald, Fire Design of Steel Members with Welded or Hot-rolled Class 4 Cross-sections, Report, RFCS, 2015.
- [9] F. Morente, B. Zhao, J.-M. Franssen, P. Vila Real, F. Wald, Definition of numerical Benchmark investigation for WP1 of FIDESC 4 Project, 2012.
- [10] J. Hricak, M. Jandera, F. Wald, "Local buckling of class 4 sections beams", COST Action TU0904 – Benchmark studies, V. of num. models in fire eng., 84-91, CTU, 2014.
- [11] CEN, EN 1090-2, Execution of steel structures and aluminium structures - Part 2: Technical requirements for steel structures, Brussels, Belgium, 2008.
- [12] ECCS, "Ultimate limit state calculation of sway frames with rigid joints", Technical Committee 8 - Structural Stability, Publication n. 33, 1984.

USE OF MICROSIMULATION IN THE ADAPTATION TO PORTUGAL OF THE HCM 2000 METHODOLOGY FOR BASIC FREEWAY SEGMENTS

J. Macedo*, A. Benta and L. Picado-Santos

** Department of Civil Engineering/RISCO, University of Aveiro
Campus Universitário de Santiago, 3810-193 Aveiro, Portugal
E-mail: jmacedo@ua.pt*

Keywords: Freeways, Microsimulation, Level of Service, Traffic Engineering.

Abstract. *Portugal is one of the European countries with higher spatial and population freeway network coverage. The sharp growth of this network in the last years instigates the use of methods of analysis and the evaluation of their quality of service in terms of the traffic performance, typically performed through internationally accepted methodologies, namely that presented in the Highway Capacity Manual (HCM). Lately, the use of microscopic traffic simulation models has been increasingly widespread. These models simulate the individual movement of the vehicles, allowing to perform traffic analysis. The main target of this study was to verify the possibility of using microsimulation as an auxiliary tool in the adaptation of the methodology by HCM 2000 to Portugal. For this purpose, were used the microscopic simulators AIMSUN and VISSIM for the simulation of the traffic circulation in the A5 Portuguese freeway. The results allowed the analysis of the influence of the main geometric and traffic factors involved in the methodology by HCM 2000. In conclusion, the study presents the main advantages and limitations of the microsimulators AIMSUN and VISSIM in modelling the traffic circulation in Portuguese freeways. The main limitation is that these microsimulators are not able to simulate explicitly some of the factors considered in the HCM 2000 methodology, which invalidates their direct use as a tool in the quantification of those effects and, consequently, makes the direct adaptation of this methodology to Portugal impracticable.*

1 INTRODUCTION

In the last years, Portugal increased very significantly their road network namely in terms of freeways. Between 2000 and 2013 the total length of the Portuguese freeway network increased more than 106%, from 1486 km (2000) to 3065 km (2013) [1,2]. Thus, Portugal is one of the European countries with higher spatial and population freeway network coverage (6th among the 28 countries of the European Union). This sharp growth of the infrastructure, combined with the increase of traffic demand, means that it is necessary to use methods to analyse and evaluate the quality of the service that is provided in this type of road infrastructure. Traditionally, the evaluation of the quality of service is performed through internationally accepted methodologies, namely those that are recommended in the Highway Capacity Manual (HCM) [3]. With these methodologies is possible the determination of the level of service in the various components of a freeway (basic freeway segments, ramp segments, weaving segments).

However, from a theoretical point of view the simple and direct transposition to the Portuguese reality of a methodology developed to another country raises some reservations, since all the elements that compose the road environment (infrastructure, vehicle and driver) are somewhat different from the United States reality for which it was developed HCM [3].

Lately, the use of microscopic traffic simulation models has been increasingly widespread. These models seek to recreate in a virtual environment the individual vehicle movements within a traffic system, and from that representation to enable a set of traffic analysis.

The main target of this study was to verify the possibility of using microsimulation as an auxiliary tool in the adaptation of the methodology by HCM 2000 to Portugal. For this purpose, the microscopic simulators AIMSUN and VISSIM were used for the simulation of the traffic circulation in the A5 Portuguese freeway. This allowed to identify the main advantages and limitations of the microsimulators AIMSUN and VISSIM in modelling the traffic circulation in Portuguese freeways.

Furthermore, this work tried to verify if the microscopic simulators used (AIMSUN and VISSIM) are able to represent the influence of all the factors involved, in order to, in a second phase, quantify their influence to the Portuguese reality.

2 MICROSCOPIC TRAFFIC SIMULATION MODELS

In recent years there has been a huge growth in the use of microscopic traffic simulation models. These models consist of software tools that try to recreate, in a virtual environment as realistically as possible, the individual movement of vehicles in a traffic system. Their potentialities rendered traffic simulation an important role as decision support tool in the field of traffic engineering, since they enable a wide range of traffic analysis. According to Caltrans [4], microsimulation is the dynamic and stochastic modelling of individual vehicle movements within a system of transportation facilities. Each vehicle is moved through the network of transportation facilities on a split second by split second basis according to the physical characteristics of the vehicle (length, maximum acceleration rate, etc.), the fundamental rules of motion (e.g. acceleration times time equals velocity, velocity times time equals distance) and rules of driver behaviour (car following rules, lane changing rules, etc.). Thus, in the microscopic traffic simulation the dynamics of each vehicle is represented based on several behaviour theories: car-following; lane-changing; and gap acceptance models [5, 6]. The more

recent microsimulators also represent and simulate cyclists and pedestrians in addition to motor vehicles.

This work used two of the most popular microsimulation software available worldwide: AIMSUN and VISSIM. Further information about these microsimulation software can be found in [7, 8, 9].

3 HCM 2000 METHODOLOGY FOR BASIC FREEWAY SEGMENTS

The HCM 2000 methodology for basic freeway segments can be used to analyse the capacity, level of service (LOS), lane requirements and effects of traffic and design features in this component of the freeways facilities [3]. According to HCM 2000 [3] a basic freeway segment is a segment of freeway outside of the influence area of ramps or weaving areas of the freeway and can be characterized by three performance measures: density in terms of passenger cars per kilometre per lane; speed in terms of mean passenger car speed; and volume-to-capacity (v/c) ratio. Each of these measures is an indication of how well traffic flow is being accommodated by the freeway. To estimate the level of service of a freeway the measure used is the density calculated using the methodology and speed-flow curves presented in the Figure 1 [3].

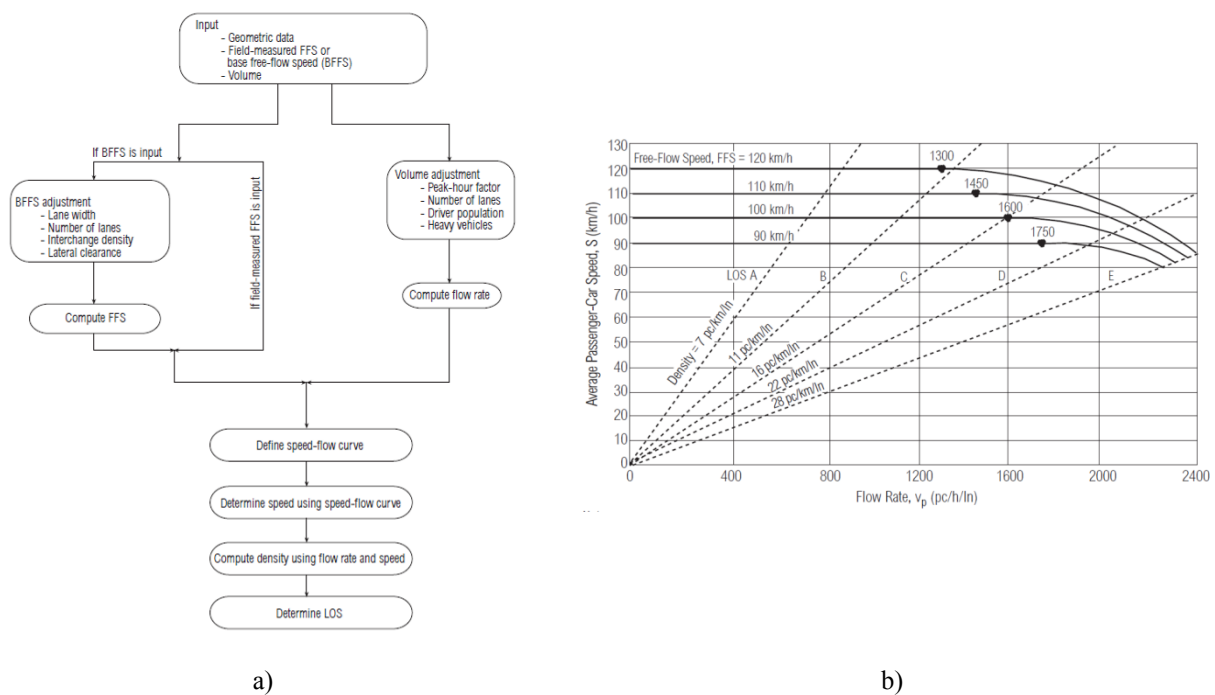


Figure 1. a) HCM 2000 basic freeway segments methodology; b) Speed-flow curves and LOS [3]

The determination of the density (D) is performed in an indirect way by computing the passenger-car equivalent flow rate (v_p), based on traffic volume for peak-hour, and the average passenger-car speed (S) of the traffic stream. The equation used is as follows:

$$D = \frac{v_p}{S} \quad (1)$$

As can be observed in the Figure 1a) the parameters that can influence the LOS are: lane width; number of lanes; interchange density; lateral clearance; peak-hour factor; driver population; heavy vehicles (traffic composition). Further information can be found in [3]

4 APPROACH USED

The first step consisted in the comparison of the speed-curves observed in the A5 Portuguese freeway that links Lisbon to Cascais (Figure 2) with those that are presented in the HCM 2000.



Figure 2. A5 freeway

In order to perform the analysis of the ability of each of the two microscopic traffic simulators used, AIMSUN and VISSIM, to represent the macroscopic behaviour of traffic streams in basic freeway segments, a typical day was simulated in the coded A5 freeway and the results obtained were analysed (Figure 3).

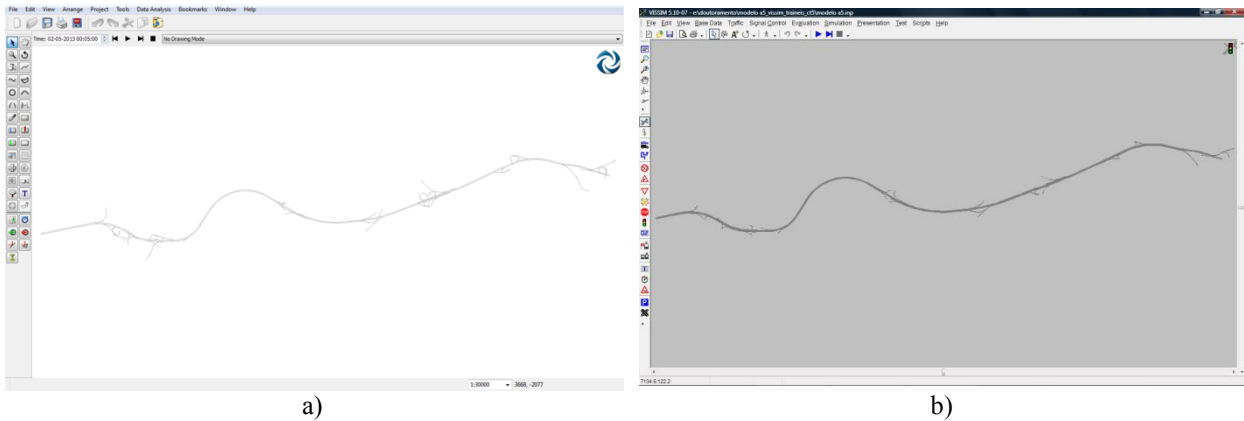


Figure 3. Microsimulation Models of the A5 Freeway: a) AIMSUN; b) VISSIM

To carry out a sensibility analysis to some of the parameters (lane width; lateral clearance; traffic composition) used in the HCM 2000 methodology, it was coded in each of the microsimulators an experimental track, inspired in the approach used by Manstetten et al. [10] (Figure 4).

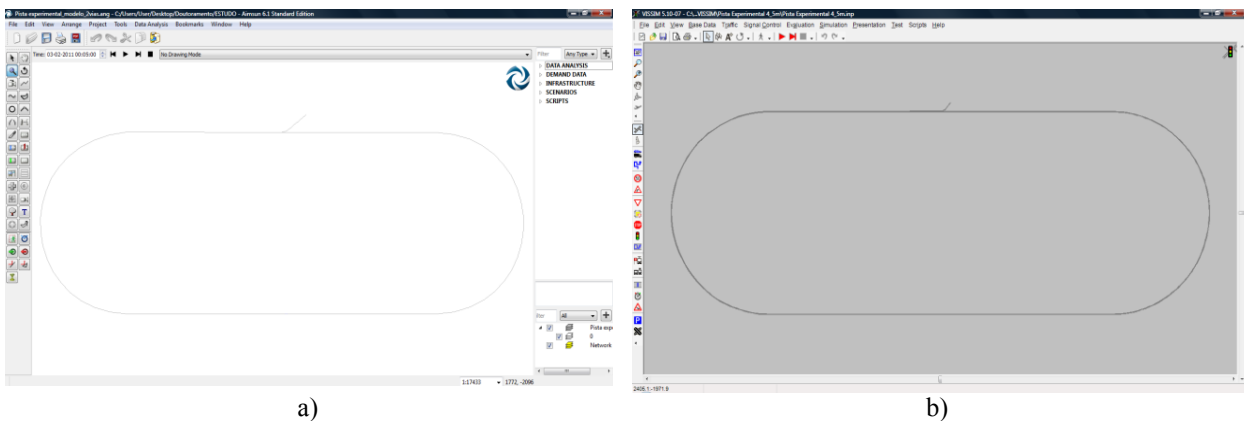


Figure 4. Experimental track used in the sensibility analysis: a) AIMSUN; b) VISSIM

The models were calibrated trying to represent the speed-flow represented in the HCM 2000 using base conditions [3].

5 RESULTS AND DISCUSSION

This section presents the obtained results during the study. First of all, was applied the HCM 2000 methodology to some segments of the A5 freeway. The results obtained are presented in the Figure 5.

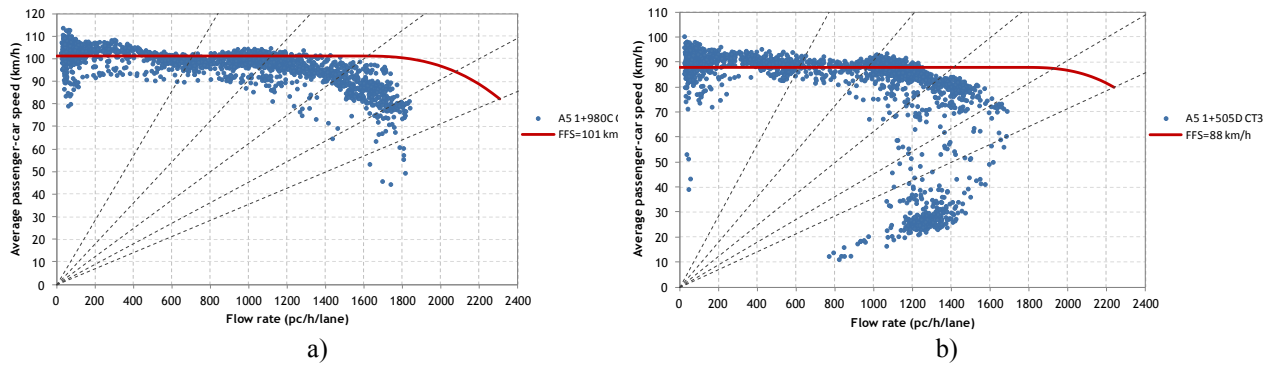


Figure 5. Speed-flow curves observed versus HCM 2000 curves: a) Lisbon-Cascais; b) Cascais-Lisbon

It can be concluded that the HCM 2000 methodology is not able to represent satisfactorily the speed-flow curve observed in the A5 freeway. This suggests that an adaptation of the HCM 2000 methodology is necessary to the Portuguese reality.

Using the models constructed in the simulators a comparison between the observed and the simulated data was performed. The Figure 6 presents that results obtained during the calibration (Figure 6a) and validation (Figure 6b) in the AIMSUN-VISSIM results were very similar.

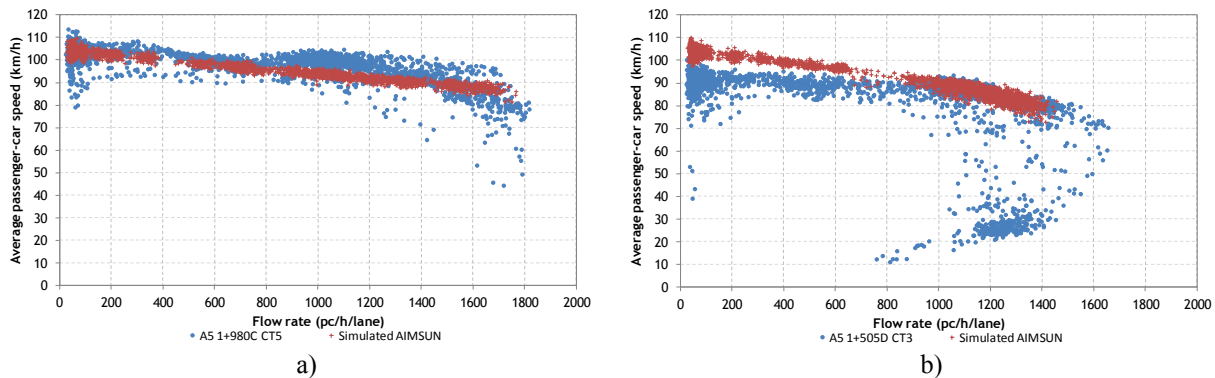


Figure 6. Speed-flow curves observed versus simulated in AIMSUN: a) calibration; b) validation

Observing Figure 6 is possible to perceive that the microsimulators can represent the traffic flow at the A5 freeway. However, the results showed in the Figure 6b allow to conclude that this representation is still not perfect.

Finally, Figure 7 presents some of the results obtained from the sensibility analysis using the AIMSUN. The results presented correspond to the analysis of the influence of lane width and heavy vehicles (traffic composition and grades). Also here the results obtained with the VISSIM were similar to those that were obtained with the AIMSUN [11].

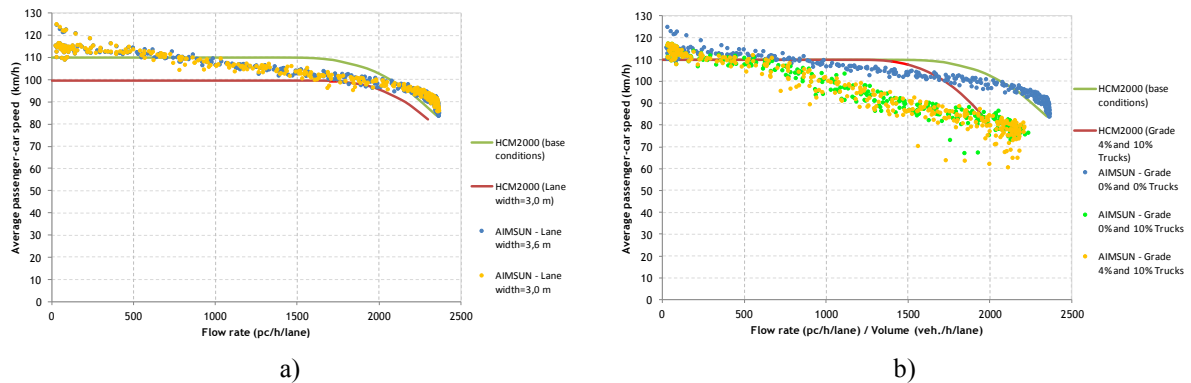


Figure 7. Sensibility analysis using the AIMSUN: a) influence of lane width; b) influence of heavy vehicles

The results show that the influence of these factors on the traffic streams are not well represented in the simulators. This invalidates their direct use as a tool in the quantification of those effects and, consequently, makes the direct adaptation of this methodology to Portugal impracticable.

6 CONCLUSIONS

A study on the assessment of the possibility of use of microsimulation in the adaptation to Portugal of the HCM 2000 methodology of basic freeway segments was presented. The study presents the main advantages and limitations of the microsimulators AIMSUN and VISSIM in modelling the traffic circulation in Portuguese freeways. The main limitation is that these microsimulators are not able to simulate explicitly some of the factors considered in the HCM 2000 methodology, which invalidates their direct use as a tool in the quantification of those effects and, consequently, makes the direct adaptation of this methodology to Portugal impracticable. This study ends providing solutions on how these limitations can be overcome, so that the adaptation of the HCM 2000 methodology to Portugal (or other country) can be achieved in the future.

REFERENCES

- [1] INE: Estatísticas dos Transportes 2013, Instituto Nacional de Estatística, Lisboa, 2014.
- [2] INE: Estatísticas dos Transportes 2000, Instituto Nacional de Estatística, Lisboa, 2002.
- [3] TRB: Highway Capacity Manual 2000. Transportation Research Board, National Research Council, Washington, D.C., U.S.A, 2000.
- [4] Caltrans: Guidelines for Applying Traffic Micro Simulation Modeling Software. 2002.
- [5] M. Brackstone, M. McDonald: Car-following: a historical review, Transportation Research Part F: Traffic Psychology and Behaviour, 2(4) 181-196, 1999.
- [6] T. Toledo: Driving Behaviour: Models and Challenges, Transport Reviews: A Transnational Transdisciplinary Journal, 27(1) 65-84, 2007.
- [7] J. Barceló: Fundamentals of traffic simulation. Vol. 145. New York: Springer, 2010.
- [8] TSS: AIMSUN Version 6.1 User's Manual, TSS-Transport Simulation Systems, 2011.
- [9] PTV: VISSIM 5.10 User manual, PTV AG, 2008.

- [10]D. Manstetten, W. Krautter, T. Schwab: Traffic simulation supporting urban control system development. Proceedings of the 4th world conference on ITS, Seoul, 1998.
- [11]J. Macedo, A. Benta, L. Picado-Santos: Utilização da microssimulação no desenvolvimento de uma metodologia de avaliação dos níveis de serviço em autoestradas. Proceedings of the 7th Congresso Rodoviário Português, Lisbon, 2013.

Benchmarking of Optimization Algorithms

J. Meier*, T. Schanz

* *Gruner AG*

Basel, Switzerland

E-mail: joerg.meier@vint.de

Keywords: Optimization, Parameter Back Calculation, Benchmarking.

Abstract. *In this paper, we present an empirical approach for objective and quantitative benchmarking of optimization algorithms with respect to characteristics induced by the forward calculation. Due to the professional background of the authors, this benchmarking strategy is illustrated on a selection of search methods in regard to expected characteristics of geotechnical parameter back calculation problems. Starting from brief introduction into the approach employed, a strategy for optimization algorithm benchmarking is introduced. The benchmarking utilizes statistical tests carried out on well-known test functions superposed with perturbations, both chosen to mimic objective function topologies found for geotechnical objective function topologies. Here, the moved axis parallel hyper-ellipsoid test function and the generalized Ackley test function in conjunction with an adjustable quantity of objective function topology roughness and fraction of failing forward calculations is analyzed. In total, results for 5 optimization algorithms are presented, compared and discussed.*

1 MOTIVATION

For numerical simulations, it is essential to use a model parameter set which generates a realistic system response. In practice, parameter back calculation based on the direct approach is often used for this purpose in which mathematical optimisation algorithms are a critical component. Many different optimization algorithms are known and are available within the literature (for an overview, see e.g. [11] or [7]). These algorithms use a variety of approaches to perform the search for optimal parameter combinations. However, the performance and convergence of the different optimization algorithms itself varies strongly, and also depend strongly on the optimization problem to solve. Exorbitant computational costs or, in the worst case, an improper or random parameter set will be returned if an unsuitable optimization algorithm is selected. Therefore, a suitable optimization algorithm has to be carefully selected for each problem.

For optimization algorithms, the performance by means of “finding the optimum reliable” and “low computational cost” cannot be assessed in a closed mathematical form in most of the cases. However, we may use a statistical analysis of the solution obtained from optimization runs to make conclusions on some properties of the optimization algorithm and the search-performance. For this approach, the success rates of finding the optimum is treated as a stochastic value and statistical measures are applicable. Hereafter the approach used and some results are presented.

2 EMPIRICAL BENCHMARKING APPROACH

The parameter identification approach using the direct back analysis method consists of an iterative procedure controlled by an optimization algorithm. The model parameters are iteratively changed in such a way to achieve better agreement between the model results and the measured values, e.g. the field measurements. This agreement (or disagreement) is measured by the objective function $f(x)$. The aim of the optimization algorithm is therefore to iteratively minimize the objective function value.

The computational cost caused by this iterative process is mainly influenced by the number of forward calculations (usually numerical simulations) requested by the optimization algorithm. The processor usage of the optimization algorithm itself on the other hand is usually neglectable. A typical single forward calculation used in Geotechnics (e.g. Finite Element model of an excavation pit) requires often 5 min calculation time or more while the optimization algorithm itself needs less than 1 sec. Minimizing the computational cost of an optimization sequence is therefore equivalent with minimizing the number of forward calculations.

For the statistical approach applied here, no “real life” forward calculation has been used to avoid high calculation time. Therefore, the normal calculation scheme for an objective function value has been altered by substituting the time-consuming forward calculation by a well-defined and well-known test function. This substitution has no influence on the iterative process controlled by the optimization algorithm nor have the optimization algorithms to be adapted. From view of the optimization algorithm, an objective function value is still calculated based on a parameter vector.

As stated by [2] and also by the experience of the authors (e.g. [6, 8, 14]), many objective functions from the field of (geo-)technics have a globally convex shape, in which often secondary (locally optimal) solutions are present. Furthermore many objective functions show a certain ‘roughness’ or ‘noise’ at a smaller scale. Additionally for some parameter vectors a forward calculation can fail reproducible (e.g. no convergence in the Finite Element Method) and no objective function value can be calculated accordingly.

In view of these facts, two test functions have been chosen for the benchmarking presented: Firstly, the Moved axis parallel hyper-ellipsoid function, which has no secondary optima and one global optimum [10]. Secondly, the Ackley test function in its generalized form, which shows several secondary optima of varying objective function values and a single global optimum (see [1] for details).

Both test functions exhibit no roughness or failed parameter vectors. In order to incorporate both characteristics the original test function $f(x)$ is superposed with a noise field $r(x)$ according to Eq. (1) and (2). In Eq. (2) $srnd(\blacksquare)$ is a pseudo-random number generator returning equal-distributed numbers ranging from 0.0 to 1.0, while for one and the same argument (\blacksquare) always the same number is returned. The control variable τ is the noise scaling factor. According to Eq. (3) a parameter vector x is considered “failed” if the pseudo-random number for x is smaller or equal to a predefined failure probability p_f .

$$f^*(x) := f(x) + r(x) \quad (1)$$

$$r(x) := \tau \left(\frac{1}{2} - \frac{1}{n} \sum_{i=1}^n srnd(x_i) \right) \quad (2)$$

$$srnd(x) \leq p_f \quad (3)$$

The majority of optimization algorithms will not find the exact location of the test function global optimum (x^*), but will rather move asymptotically towards x^* due to underlying paradigms. The optimization sequence is considered to be successful, if the parameter set x_{min} with the smallest objective function value is located within Ψ as defined by Eq. (4).

$$\Psi = \left\{ x_{min} \mid \|x_{min} - x^*\|_2 \leq d_\Psi \right\} \quad (4)$$

The search range Ω and d_Ψ has been chosen as follows (please note that the relative size of Ψ for both test functions is equal compared to Ω):

- Ackley Test Function: $-1.0 \leq x_i \leq +2.0$ with $d_\Psi = 0.1$
- Moved axis parallel hyper-ellipsoid function: $-10.0 \leq x_i \leq +20.0$ with $d_\Psi = 1.0$

To assess the probability of which an optimization algorithm is able to converge within Ψ on a test function for given values of p_f and τ , a large number of optimization sequences is repeatedly run. For each sequence, the start parameter sets are chosen randomly within Ω and the number of forward calculation is limited to 500. The quotient of successful sequences over the total number of sequences is considered as success rate p . The number of optimization sequences is increased until the success rate is stabilizing, what usually corresponds to some 10'000 runs.

3 RESULTS

The empirical benchmarking approach described above has been applied to 5 selected optimization algorithms. Namely, Monte-Carlo method (MC), a gradient descent method (GD) (e.g. [12, 11]), an evolutionary-genetic algorithm (EG) [e.g. 11], the Simplex-Nelder-Mead optimizer (SNM) [9] and the particle swarm optimizer (PSO) [5, 4]. For each algorithm both test functions have been used with $n = \{2, 3, 4, 6, 8 \text{ and } 10\}$ unknown parameters.

The diagrams of Figure 3 show on the vertical axis the success rate p . over the noise control variable τ and, respectively, the failure rate p_f . The main conclusions are:

- The MC method performs well for $n = 2$. For higher n it clearly suffers from the “curse of dimensionality” [3].

- The GD performs works very nice for smooth objective function topologies with no secondary optima. It performs very badly if secondary optima are present, as it is the case for the Ackley test function. The GD is also not robust to noise and failing forward calculations.
- The SNM optimizer is much more robust than the GD. Nevertheless, due to its local character the success rate for the Ackley test function is $\sim 50\%$ even for the ideal case of $\tau = 0$ and $p_f = 0$.
- The EG algorithm class is very popular among many researchers due to its high robustness. This robustness is also visible in Figure 3. The major drawback of this method is its need for a large number of forward calculations as also stated by [13].
- For both test function the PSO (10 particles) used shows the best performance values. It outperforms clearly all other tested algorithms including the EG method. This finding is in agreement with the experience of other researchers, e.g. [13].

The results of Figure 3 show clearly how different the optimization algorithms behave for the two test functions. This illustrates how the nonlinearity of the objective function has a strong influence to the performance of the optimization algorithm.

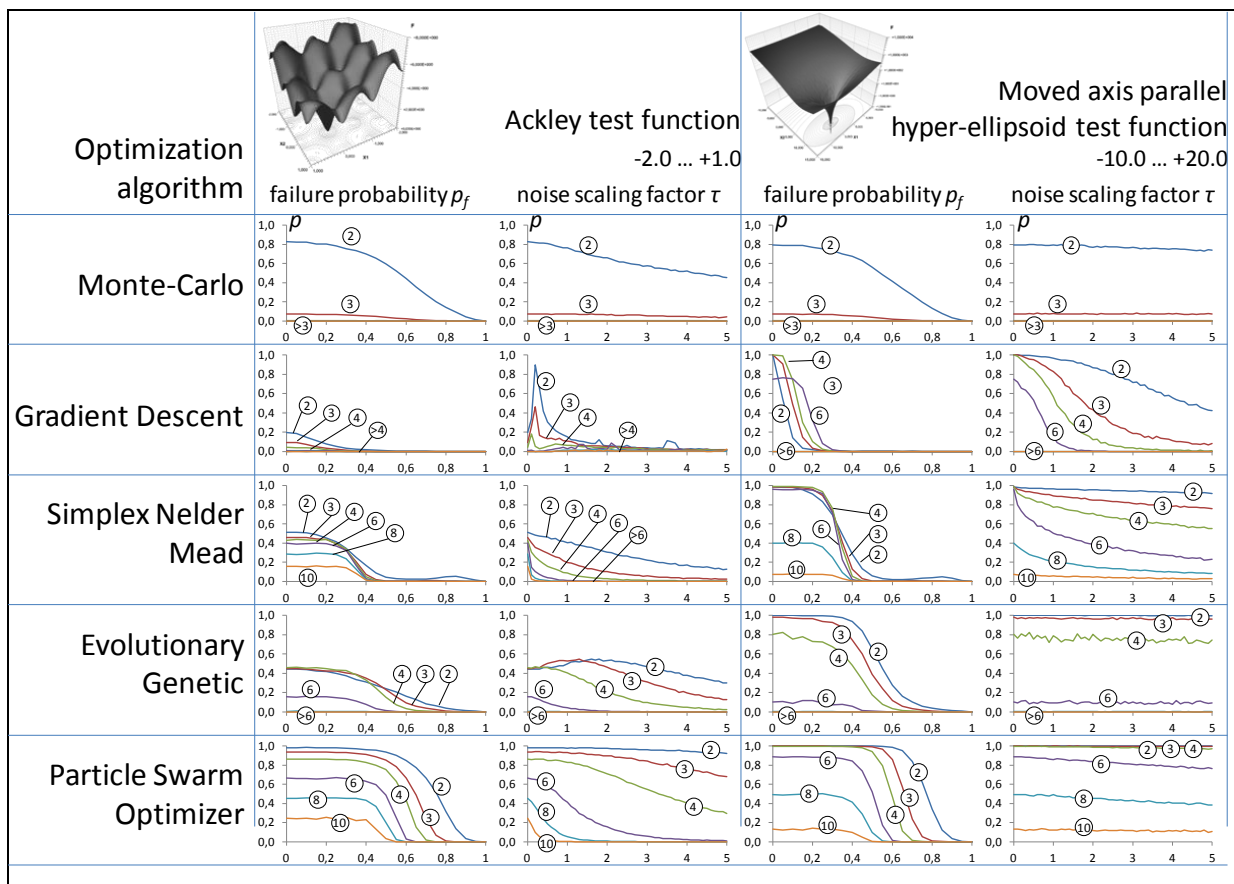


Figure 1: Results of the 5 tested optimization algorithms

4 CONCLUSION AND OUTLOOK

In the present paper an approach for impartial and quantitative benchmarking of optimization algorithms has been briefly presented and applied to 5 selected optimization algorithms. Of all the optimization algorithms tested, the PSO shows the best performance. However, if an objective function with a severely different nonlinearity is present, or if the number of unknown parameters n increases strongly the PSO may be outperformed by other algorithms.

The next step will be to apply the benchmarking to more algorithms and to define a rating function based on the performance profiles to provide an objective rating method for optimization algorithms.

REFERENCES

- [1] Ackley, D. H. (1987): A connectionist machine for genetic hill climbing. Boston: Kluwer Academic Publishers.
- [2] Chen, S. (2009): Locust Swarms - A New Multi-Optima Search Technique. 2009 IEEE Congress on Evolutionary Computation (CEC 2009), p. 1745 - 1752.
- [3] Dixon, L.C.W.; Gomulka, J.; Hersom, S.E. (1976): Reflections on the global optimization problem. In: Dixon, L.C.W. (ed.) Optimization in action, pp. 398-435. London: Academic Press.
- [4] EBERHARDT, R. C.; KENNEDY, J. (1995): A new optimizer using particle swarm theory. Proceedings of the Sixth International Symposium on Micro Machine and Human Science, Nagoya, Japan, IEEE Service Center, Piscataway, NJ, 39 – 43.
- [5] KENNEDY, J.; EBERHARDT, R. C. (1995): Particle Swarm Optimization. Proceedings of IEEE International Conference on Neural Networks, Volume IV, S. 1942 – 1948, Perth, Australia, IEEE Service Center, Piscataway, NY.
- [6] Knabe, T.; Schweiger, H. F.; Schanz, T. (2012): Calibration of constitutive parameters by inverse analysis for a geotechnical boundary problem. Canadian Geotechnical Journal 49(2): 170-183, 10.1139/t11-091
- [7] MEIER, J. (2008): Parameterbestimmung mittels inverser Verfahren für geotechnische Problemstellungen. Dissertationsschrift, Fakultät Bauingenieurwesen, Bauhaus-Universität Weimar.
- [8] Most, T.; Knabe, T. (2009): Reliability analysis of the bearing failure problem considering uncertain stochastic parameters. Comput. Geotech (2009), doi:10.1016/j.compgeo.2009.11.003.
- [9] NELDER, J. A.; MEAD, R. (1965): A simplex method for function minimization. Computational Journal 7, p. 308 - 313.
- [10] Polheim, H. (1999): Evolutionäre Algorithmen-Verfahren, Operatoren und Hinweise für die Praxis. Springer.
- [11] SPALL, J. C. (2003): Introduction to stochastic search and optimization: estimation, simulation and control. Wiley-Interscience series in discrete mathematics.

- [12] SPELLUCCI, P. (1993): Numerische Verfahren der nichtlinearen Optimierung. Birkhäuser Verlag, Basel Boston Berlin, ISBN 3-7643-2854-1.
- [13] Vaz, A. I. F.; Vicente, L. N. (2006): A particle swarm pattern search method for bound constrained nonlinear optimization. *J Glob Optim* (2007) 39:197–219, DOI 10.1007/s10898-007-9133-5.
- [14] Zimmerer, M. M. (2010): Identifikation konstitutiver Parameter von weichen feinkörnigen Böden, Beitrag zum Konsolidationsverhalten von Ton, Dissertation, Bauhaus-Universität Weimar, Schriftenreihe des DFG Graduiertenkollegs 1462 Modellqualitäten (1).

THE INFLUENCE OF CRACKS AND OVERESTIMATION ERRORS ON THE DEFLECTION OF THE REINFORCED CONCRETE BEAMS IN THE RIGID FINITE ELEMENT METHOD

M. Musiał

*Wroclaw University of Technology
Department of Civil Engineering
Wybrzeże Wyspiańskiego 27
50-370 Wrocław
Poland*

E-mail: michal.musial@pwr.edu.pl

Keywords: beam, crack, deflection, reinforced concrete, RFEM.

Abstract. *This article presents the Rigid Finite Element Method in the calculation of reinforced concrete beam deflection with cracks. Initially, this method was used in the shipbuilding industry. Later, it was adapted in the homogeneous calculations of the bar structures. In this method, rigid mass discs serve as an element model. In the flat layout, three generalized coordinates (two translational and one rotational) correspond to each disc. These discs are connected by elastic ties. The genuine idea is to take into account a discrete crack in the Rigid Finite Element Method. It consists in the suitable reduction of the rigidity in rotational ties located in the spots, where cracks occurred. The susceptibility of this tie results from the flexural deformability of the element and the occurrence of the crack. As part of the numerical analyses, the influence of cracks on the total deflection of beams was determined. Furthermore, the results of the calculations were compared to the results of the experiment. Overestimations of the calculated deflections against the measured deflections were found. The article specifies the size of the overestimation and describes its causes.*

1 INTRODUCTION

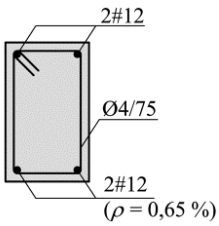
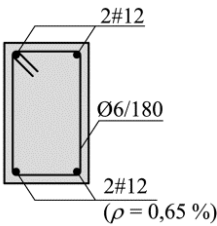
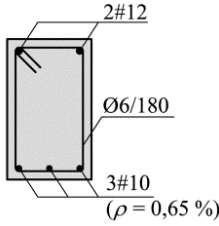
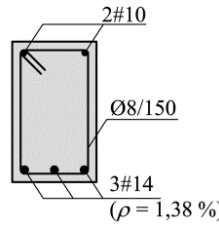
A phenomenon characteristic of reinforced concrete elements subjected to bending is the formation of cracks perpendicular to the axis of the tension zone. Cracks in concrete occur after the tension exceeds the tensile strength of concrete and they have fundamental influence on its operation. They cause, among others, increase in deflections [1]. In addition, in hyperstatic structures they are associated with redistribution of internal forces. In this paper, the rigid finite element method [2] was used in the computational analyses, which enables taking into account the cracks of the reinforced concrete element in a discreet way. A detailed description of the method is contained in [3-5].

2 LABORATORY TESTS

2.1 Test elements

Experimental tests were performed on four sets of beams. Each set consisted of three elements having the same dimensions (3300 x 150 x 250 mm). The synthetic summary of the test elements and their properties is presented in the form of a table (Table. 1).

Tab. 1. The summary of the test elements

Set	B-I	B-II	B-III	B-IV
Cross-section				
f_{cm} [MPa]	51.7	51.2	45.6	41.1
$f_{ctm,spl}$ [MPa]	3.58	3.21	3.03	2.79
E_{cm} [GPa]	30.3	29.6	28.5	30.0
f_{ym} [MPa]	563	563	548	555
E_s [GPa]	202	202	200	202
M_R [kNm]	26.96	27.00	26.62	53.29
M_{cr} [kNm]	7.35	6.18	5.87	5.60

where: ρ – tensioned reinforcement ratio, f_{cm} – mean compressive strength of concrete, $f_{ctm,spl}$ – mean tensile strength of concrete at splitting, E_{cm} – mean Young's modulus of concrete, f_{ym} – mean yield strength of reinforcing steel (longitudinal reinforcement), E_s – mean Young's modulus of reinforcing steel (longitudinal reinforcement), M_R – mean flexural load bearing capacity of the beam, M_{cr} – mean cracking moment.

2.2 Test procedure

The beams were loaded in a three-point bending test. During the study, deflection in the middle of the span and on the supports was recorded by means of inductive gauges with an accuracy of 0.001 mm. From the measurements, actual deflection was calculated at the centre of the span. After cracking of each beam, an inventory of cracks for at least five steps of load was performed. Due to the nature of calculations using its own numerical model, the focus was on the number and spacing of cracks. A detailed description of the tests is given in [6].

2.3 Measurement results

Deflections in the middle of the span recorded in the test are shown in the graphs (Figs. 1-4).

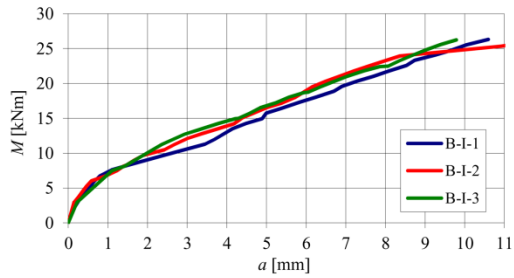


Fig. 1. Beam deflection in set B-I

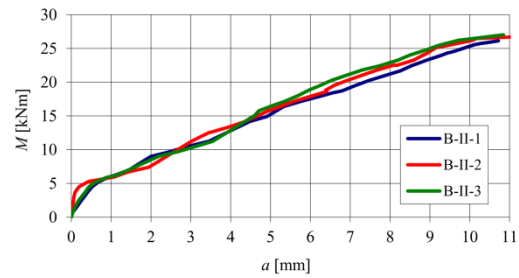


Fig. 2. Beam deflection in set B-II

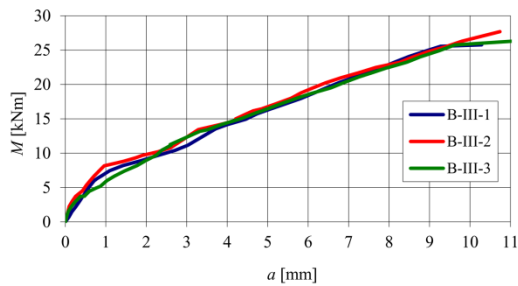


Fig. 3. Beam deflection in set B-III

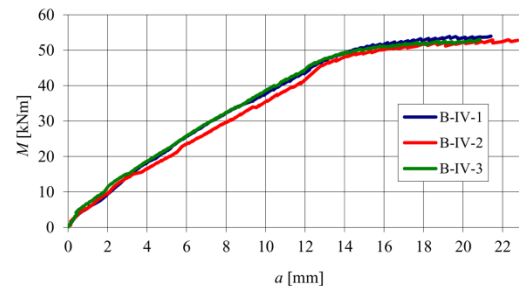


Fig. 4. Beam deflection in set B-IV

4 NUMERICAL CALCULATIONS, DISCUSSION OF THE RESULTS

Numerical calculations with the developed model were performed for selected load steps, at which cracks in the beam were drawn. The results are shown in the form of histograms for each of the beams (Figs. 5-8). The numerical model presented enabled the separation of deflections originating from flexural deformability of the element from crack effect. The following designations were applied: a_b – deflection dependent on the flexural deformability, a_{cr} – calculated deflection dependent on cracks, a_e – measured deflection.

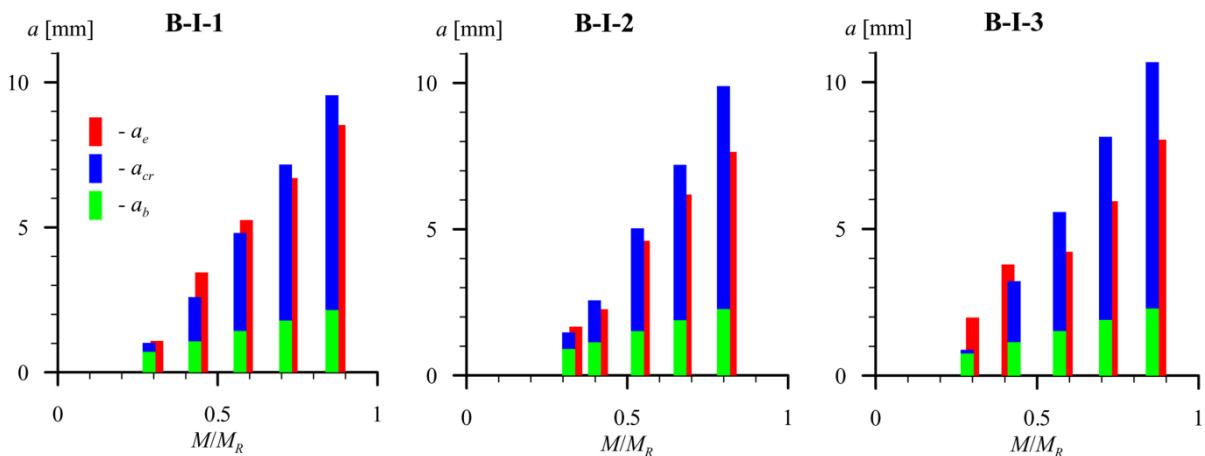


Fig. 5. Summary of results for set B-I

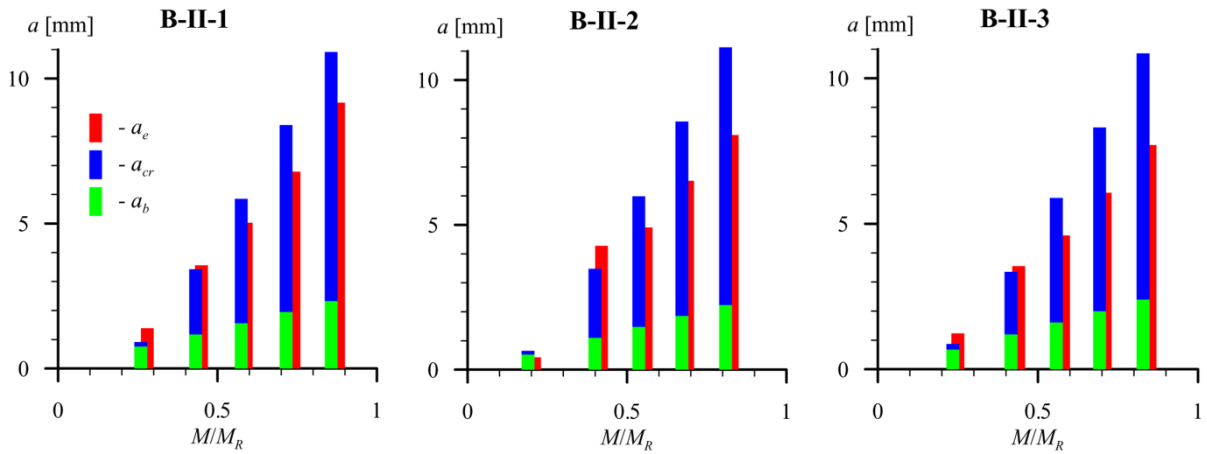


Fig. 6. Summary of results for set B-II

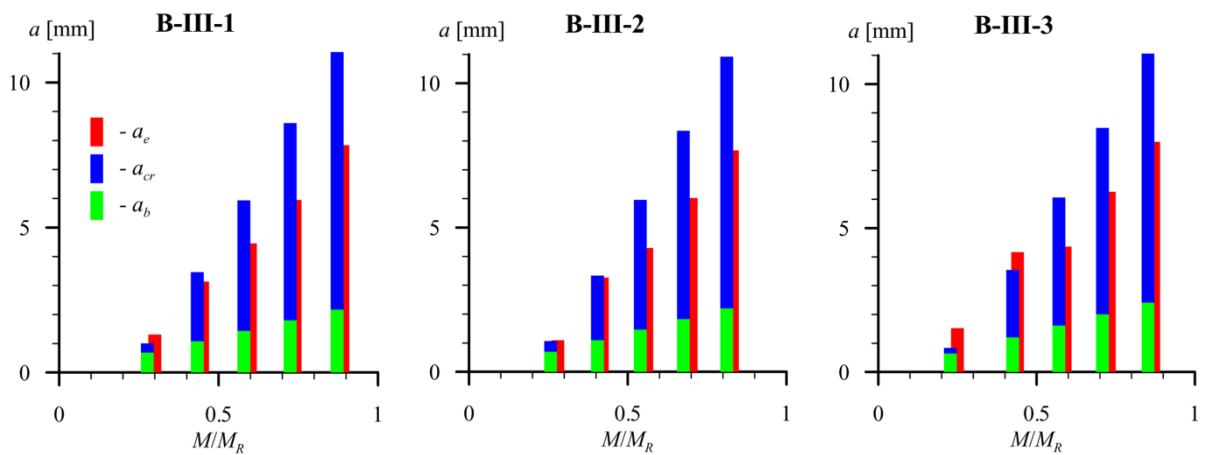


Fig. 7. Summary of results for set B-III

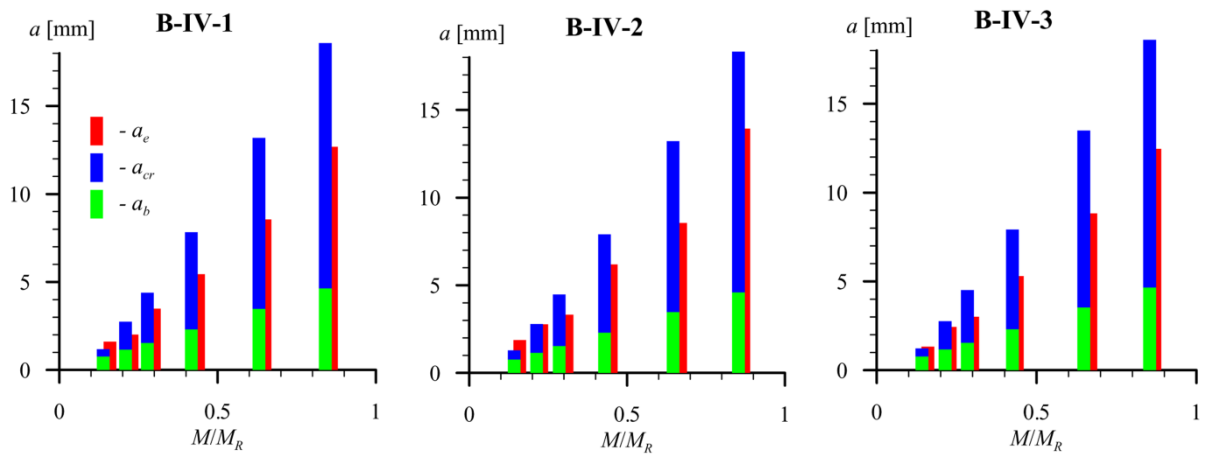


Fig. 8. Summary of results for set B-IV

The analysis performed lead to the following conclusions:

- deflections of elements caused by the flexural deformation of the element are multiplied in a quasi-linear manner over the range of loads in the case of elements less (sets BI, B-II, B-III) and more reinforced (set B-IV);

- along with an increase in the load, the share of the crack effect in deflection increases up to 75% (more reinforced elements) or 80% (less reinforced elements) in the final phase of the element operation;
- in the developed numerical model, the re-estimation of deflections takes place, it is greater the greater the severity of the load is.

Re-estimation of deflections has its base in the established theoretical model. It is assumed that the crack opens all the way up to the neutral axis. This is a simplification because the cracks formed in the final phase of the element's operation (closer to the supports) are subjected to a much smaller bending moment and they open to a less degree (they demonstrate lower rotational susceptibility).

In order to observe certain regularity, graphs (Figs. 9-12) are listed below. They include the impact of the global deflection multiplier δ as a function of the severity of the load. This factor allows the transition from the calculated deflection at to the actual (measured) deflection a_e , and it must be interpreted in accordance with the following relation (1).

$$a_t \cdot \delta = a_e. \tag{1}$$

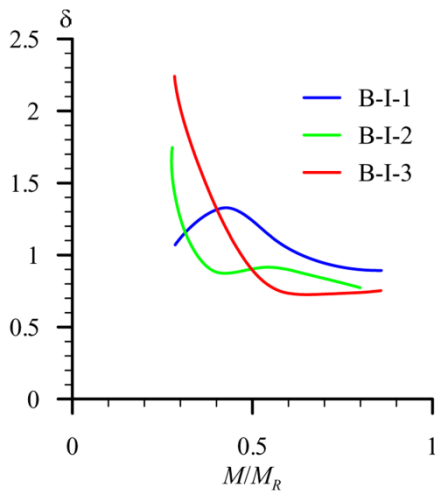


Fig. 9. Coefficient δ for beams in set B-I

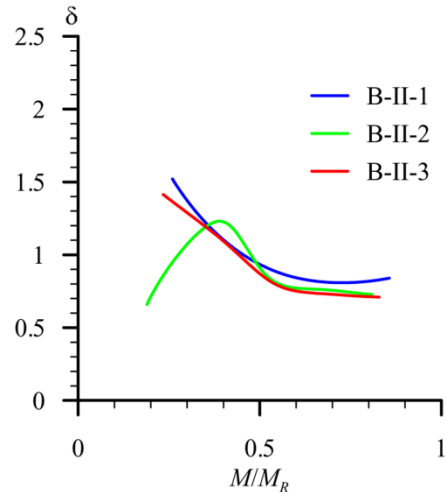


Fig. 10. Coefficient δ for beams in set B-II

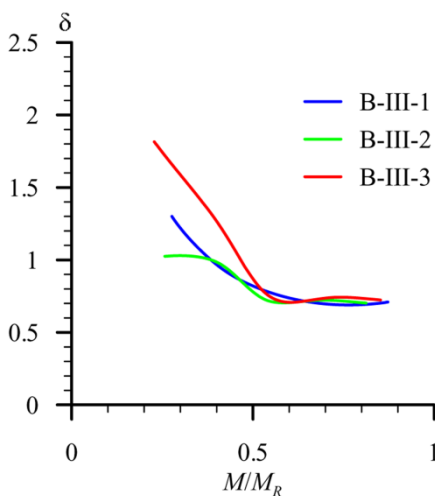


Fig. 11. Coefficient δ for beams in set B-III

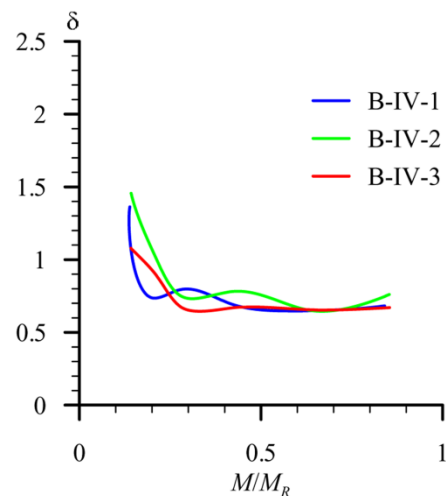


Fig. 12. Coefficient δ for beams in set B-IV

From these graphs, it can be seen that in the initial phases of the element operation, the coefficients are characterized by significant divergence. It is a consequence of the fact that the cracking process in these areas is very random and chaotic. An important observation is the fact that the re-estimation error stabilizes the ranges: 0.5-1.0 for less reinforced beams and 0.3-1.0 for more reinforced beams, and the coefficient δ is then approx. 0.78 and approx. 0.65, respectively (for other reinforcement degrees it is recommended to determine the coefficient from the linear interpolation). From an engineering point of view, these ranges are the most important, because rationally designed elements operate in these ranges. This allows us to consider the presented method to be effective, provided that the correction coefficient δ will be taken into account.

Another more advanced way to calibrate the presented method would be to modify the rotational susceptibility resulting from cracks. An additional reducing coefficient proportional, e.g. to the bending moment, should be applied.

4 SUMMARY

The paper presents a rigid finite element method for calculating deflections of reinforced concrete beams with cracks. Detailed analyses performed using own computational model showed its usefulness in civil engineering. The method of the calculation enabled the separation of part of the deflection resulting from the flexural deformability of the element and from the cracking phenomenon. The percentage of cracking in the total deflection at the high degree of effort reaches even 75-80%, depending on the degree of the beam reinforcement. The developed method produces a slight overestimation of the calculated deflections, which has its origin in the adopted model of the crack.

REFERENCES

- [1] M. Kamiński, M. Szechiński, A. Ubysz: Theoretical and practical fundamentals of calculating of reinforced concrete elements deflections (in Polish). Lower Silesian Publishing House, Wroclaw, 1998.
- [2] E. Wittbrodt, I. Adamiec-Wójcik, S. Wojciech: Dynamics of Flexible Multibody Systems. Rigid Finite Element Method. Springer, Berlin, 2006.
- [3] M. Musiał, A. Ubysz: Rotational ductility of crack in static and dynamic calculations of reinforced concrete bar structures. K. Gürlebeck, T. Lahmer, F. Werner eds. 19th International Conference on the Applications of Computer Science and Mathematics in Architecture and Civil Engineering, IKM 2012, Weimar, Germany, 2012.
- [4] M. Musiał, M. Kamiński, A. Ubysz: Free vibration frequencies the cracked reinforced concrete beams-methods of calculations. K. Gürlebeck, C. Könke eds. 18th International Conference on the Applications of Computer Science and Mathematics in Architecture and Civil Engineering, IKM 2009, Weimar, Germany, 2009.
- [5] M. Musiał: Static analysis of reinforced concrete beams with rigid finite elements method (in Polish). Modelling in Engineering, vol. 12, no. 43, 211-218, 2012.
- [6] M. Musiał: Vibrations of reinforced concrete beams with consideration of discrete crack model (in Polish) - PhD dissertation, Wroclaw University of Technology, Wroclaw, 2010.

AMELIORATING EMPLOYABILITY IN CONSTRUCTION THROUGH BIM INNOVATION

A. R. Nasir *, H- J. Bargstädt

** Institute of Construction Engineering and Management, Department of Civil Engineering,
Bauhaus Universität Weimar
Marienstraße 7a, 99423-Weimar, Germany
E-mail: abdur.nasir@uni-weimar.de*

Keywords: Construction, low-skilled labor, employability, BIM, task instructions.

Abstract. *Low-skilled labor makes a significant part of the construction sector, performing daily production tasks that do not require specific technical knowledge or confirmed skills. Today, construction market demands increasing skill levels. Many jobs that were once considered to be undertaken by low or un-skilled labor, now demand some kind of formal skills. The jobs that require low skilled labor are continually decreasing due to technological advancement and globalization. Jobs that previously required little or no training now require skilful people to perform the tasks appropriately.*

The study aims at ameliorating employability of less skilled manpower by finding ways to instruct them for performing constructions tasks. A review of exiting task instruction methodologies in construction and the underlying gaps within them warrants an appropriate way to train and instruct low skilled workers for the tasks in construction. The idea is to ensure the required quality of construction with technological and didactic aids seeming particularly purposeful to prepare potential workers for the tasks in construction without exposing them to existing communication barriers. A BIM based technology is considered promising along with the integration of visual directives/animations to elaborate the construction tasks scheduled to be carried on site.

1 INTRODUCTION

The global construction industry is currently observing a growing mismatch between skills that employers want and what the global labor markets can supply, resulting in growing unemployment, shortage of skills and polarization of wages among its labor. The high unemployment rate usually occurs in an industry due to its high dependency on low skilled workers [1] where construction section is no exception. An illustration of it can be perceived through the two populous construction industries of China and India, where low and un-skilled labor in construction sector sums to at least three-fourth of their total construction workforce [2, 3]. The shortage of skilled workers have been a known concern in the construction sector with studies predicting their need in high numbers to meet the expected turnover and growth expectations for future [4, 5]. The polarity is the wages has also been observed, where the less skilled labor in the construction sector earns very less than that of a skilled. This in turn can result into less motivation for these less skilled labors to end their occupation in not so brightly imaged construction sector.

One of the underline causes for these growing mismatches include the much globalization and technological change. On one hand it has resulted into immense benefits to economies and construction workers, where increased construction technology with more automation and new sources of low cost labor has driven a path to productive growth. However, on the other hand it has also change the employment pattern significantly where for now the sector's demand for labors has moved away from less skilled to high skilled jobs [6]. Other causes could be the lack of training provision in the construction sector [7], aging construction workforce [8], increasing pressures of indulging local people as labor force [9] and less educated labor [10]. To overcome these, the study looks to find ways of educating and training the existing less skilled construction manpower through virtual instructions in order to contribute towards their employability.

2 EMPLOYABILITY OF LESS SKILLED

The construction industry plays an important role in regard to creating employment opportunities. The long-standing figure of more than 111 million for the total construction workforce revealed in 2001[11] backs the fact of construction as a big employer, although the old figure must have been augmented highly in recent times. Taking the social role, the construction industry also bears the potential of employing world's poorest and most vulnerable people [9]. The sector creates prospects for low-skilled or entry-level workers and to those migrating from the countryside in addition to absorbing those with few academic qualifications [11]. These less skilled labors, that have sufficient knowledge of the particular trade to do respective work and simple job with the help of simple equipment and tools, look for employability in construction to satisfy basic needs of their families with low demands of professional qualifications [12].

A study pertaining to low skilled workers defined 'employability' in the year 2004 as *the capacity and the willingness to be and to remain attractive in the labor market by anticipating changes in tasks and work environment and reacting to these changes in a proactive way* [13]. The same can be transformed for the construction sector by treating construction as the work environment. To achieve the goal of the employability for these low skilled labors in the construction sector, the imminent challenge in hand is to deal with their existing and probable communication barriers on the construction site.

3 INEFFECTIVE COMMUNICATION

Effective communication between all parties involved in a project is a must for successful project completions and high profitability [14]. Likewise, effective communication has always been a key success factor for a construction project. In construction, the complex communication patterns make the interaction between stakeholders very difficult to achieve appropriately [15]. Problems like conflicts and low productivity are caused due to a broken communication among construction workers [16]. Lack of understanding and misunderstanding of instructions are common examples which arise in construction owing to language differences [17]. Among others, poor communication of task instructions is one of the major delay factors to a project. According to [18], typical methodology to produce highly inefficient and difficult to understand tasks instructions result into delays, poor quality and compromised safety.

Construction contractors rely upon using verbal instructions for instructing tasks to labors on sites due to their limited capacity and resources [19]. This reliance on human-variable verbal instructions along with the poor quality of construction drawings leads to situations like inadequate productivity, workface questions, rework and unsafe conditions on the site [20, 21, 22]. To overcome the shortcomings lying under the typical instruction methodology, [19] came up with the idea of paper based field instruction template. The aim was to make the human variable process uniform with written instructions alongside relevant construction drawings on a piece of paper.

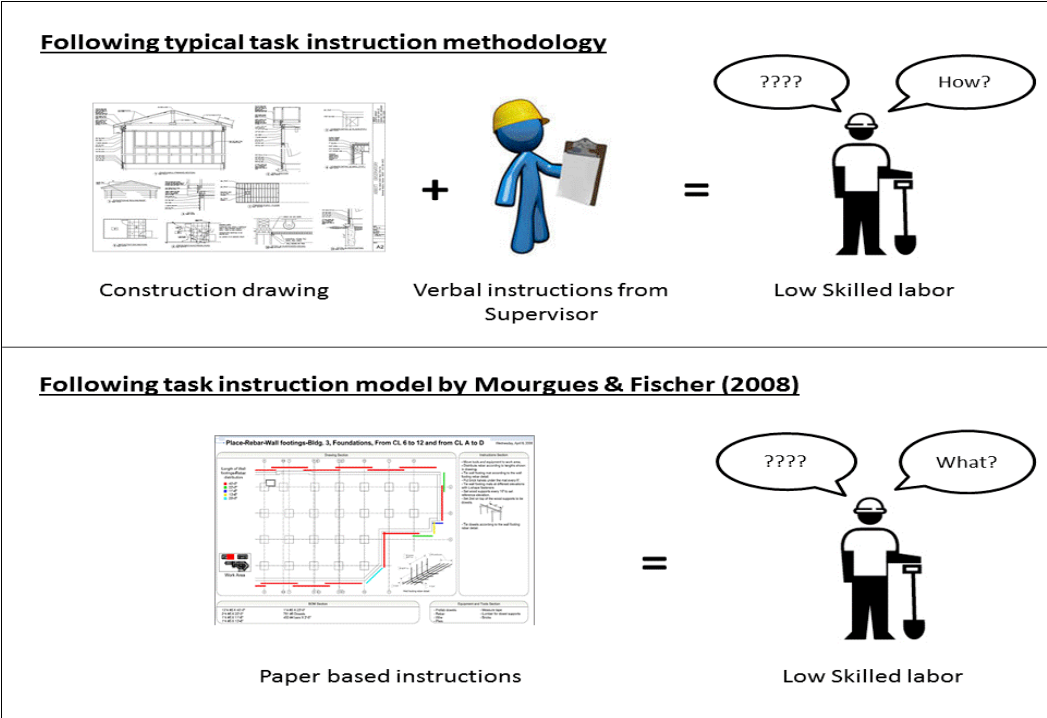


Fig. 1: Existing Task Instruction Practices Among Low Skilled Construction Labor

However, communication with the low skilled construction labor will still remain ineffective after following either the typical verbal instructions or the recently developed field instructions template methodology as shown in Fig. 1. The reason could be lack of knowledge among these low skilled workers about particular tasks and the instances of multiple languages barriers in this globalized construction world. Video based instruction with no language use might perhaps be a useful tool for educating and training these less skilled workers. A study conducted for

designing of computer based safety training for language barrier affected Hispanic construction workers shows that among the use of video, audio and images, videos enhanced the memorability of a training module.

4 BIM POTENTIAL

Building Information Modeling (BIM) has been a widely research area in recent times. With its intelligent and object-oriented parametric models having capabilities of parametric digital representation, decision making process has been greatly improved. Sharing of knowledge and communication between project participants in the Architecture, Engineering and Construction industry has been the important traits of BIM [23]. Besides various benefits of BIM utilized by the industry, its use as a teaching and learning platform has also grown in the universities and colleges. One study with BIM based knowledge repository has also revealed prospects for teaching residential construction courses to Construction Engineering and Management (CEM) students [24]. One more study has also proposed a BIM based teaching approach to prove the effectiveness of BIM as an integrated learning tool in construction [25]. A study focused on measuring benefits of BIM as a learning tool envisaged that BIM provides less expensive virtual environment for learning by doing for project management and physically repetitive construction tasks [26].

However, less has been investigated for using the potential of BIM as a learning tool for construction labors specifically those under the less skilled category. Through the exploration of the knowledge integration subject within BIM, less skilled construction labors could also be educated for performing construction tasks easily as compared to much random and disorganized present practice.

5 CONCEPT FOR VIRTUAL CONSTRUCTIONS

To elaborate the video based construction tasks to the low skilled workers, this paper proposes a framework for a digital instructing environment. The idea is to first prepare the 3D animations of construction tasks for elaborating the steps required to execute a particular task. These video based task instructions in a 3D animated environment with ‘how-to-do’ theme will elaborate the sequential steps to those workers for easily following on the ground.

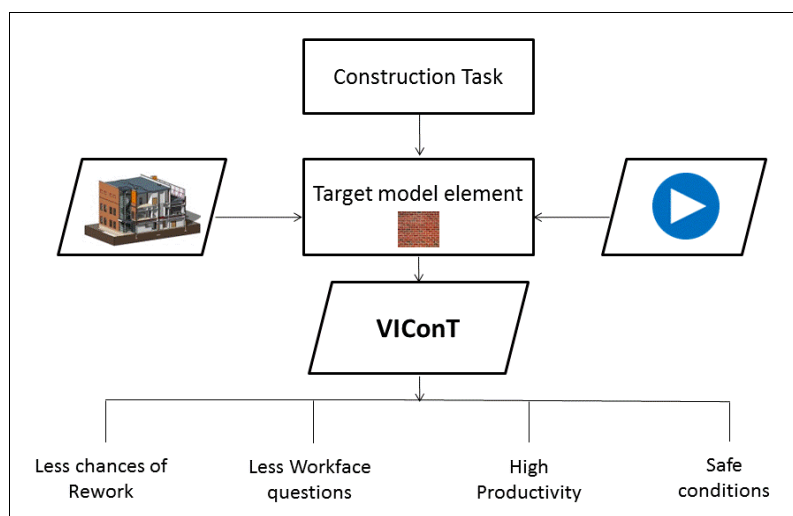


Fig. 2: Approach Intended for Virtual Instructions for Construction Tasks

These easily understandable videos will then be connected digitally in a BIM model. The idea is to relate the videos to that model object in a BIM model with which the relevancy is high and admissible. Fig. 2 represent the approach wherein for an individual construction task, video based instructions are connected to relevant BIM model object to develop a digital product 'VIConT' (Virtual Instructions for Construction Tasks). This approach will perhaps lead to less chances of rework, less workforce questions, increased productivity and safer conditions for labors to work with.

6 CONCLUSION

The study reinforces the idea of using 3D animation videos for elaborating construction tasks to low skilled construction labor. Labors with high illiteracy level as well as communication barriers like language and reading will get benefits due to high probability of easy understandings from 3D animated task tutorials. These videos linked with relevant objects of a BIM model will ease the path of having a digital instructing environment on project site. The approach of 'VIConT' can be used by construction contractors where their representatives like supervisors, with little knowledge of operating BIM tools, can elaborate the tasks to their workers. This inexpensive process will not only lead to lesser field mistakes and inefficiencies but will also increase the prospects of higher employability of low skilled manpower in the construction sector. Through this practice, the social commitment of the construction industry will surely be enhanced. The idea will be taken forward to the next step by the development of 3D animations pertaining to construction tasks usually performed by low skilled labors.

REFERENCES

- [1] S. R. Cunningham and Z. Mukherjee: Labor Market Recovers Unevenly. Business Cycle Conditions. Vol. II, No. 4. 2013.
- [2] Centre for Development Policy and Research: Survey Results Document Exploitative Labour Conditions in China's Construction Sector. Development Viewpoint. Number 78. 2014.
- [3] R. Hajela: Shortage of skilled workers: a paradox of the Indian economy. SKOPE Research Paper, 111. 2012.
- [4] Construction Users Roundtable: Confronting the Skilled Construction Workforce Shortage. WP-401, 2004.
- [5] Construction Labor Research Council. Craft Labor Supply Outlook 2005-2015, 2005.
- [6] R. Dobbs, A. Madgavkar, D. Barton, E. Labaye, J. Manyika, C. Roxburgh and S. Madhav. The world at work: Jobs, pay, and skills for 3.5 billion people. McKinsey Global Institute. 2012.
- [7] R. Liska and B. Weldzius: Attracting and maintaining a skilled construction work force. Research Summary No. 135-1, The Construction Industry Institute, Austin, Tex. 2002.
- [8] D. Olsen, M. Tatum and C. Defnall: How Industrial Contractors are Handling Skilled Labor Shortages in the United States, 48th ASC Annual International Conference Proceedings. Associated Schools of Construction. 2012.
- [9] H. J. Bargstädt, A. R. Nasir, and E. Ignatova: Can BIM support better working conditions for low-skilled labor? Proceedings of the 14th International Conference on Construction Applications of Virtual Reality. Sharjah, UAE, 2014.

- [10] N. Ehwany, M. Metwally: Labor market competitiveness and flexibility in Egypt. Cairo, Egypt: Economic Research Forum for the Arab Countries, Iran & Turkey (Working paper, 29). 2001.
- [11] J. Wells: The construction industry in the twentyfirst century: Its image, employment prospects and skill requirements: report for discussion at the Tripartite Meeting on the Construction Industry in the Twenty-first Century: Its Image, Employment Prospects and Skill Requirements, Geneva, 2001.
- [12] H. Lingard, K. Brown, L. Bradley, C., Bailey and K. Townsend: Improving employees' work-life balance in the construction industry, Project alliance case study. *Journal of Construction Engineering and Management*, 133(10), 807-815. 2007.
- [13] J. Sanders, and A. De Grip: Training, task flexibility and the employability of low-skilled workers. *International Journal of Manpower*, 25(1), 73-89. 2004.
- [14] A. Dainty, D. Moore and M. Murray: *Communication in construction: Theory and practice*. Routledge. 2007.
- [15] Ö. Wikforss and A. Löfgren: Rethinking communication in construction. In 4th Nordic Conference on Construction Economics and Organisation. 2007.
- [16] F. Y. Y. Ling, M. F. Dulaimi and M. Chua: Strategies for managing migrant construction workers from China, India, and the Philippines. *Journal of Professional Issues in Engineering Education and Practice*. 2012.
- [17] J. English: The communication problems experienced by workforce on-site, and their possible solutions. *Journal of Construction Research*, Vol. 3, No. 2, 311-321. 2002.
- [18] 3DVIA. "Work Instructions for AEC. Improve project efficiency and worker safety", <http://www.3ds.com/fileadmin/Industries/Architecture-Engineering-Construction/Pdf/brochures/work-instruction-for-construction.pdf> (accessed 21 May 2015).
- [19] C. Mourgues and M. Fischer: A work instruction template for cast-in-place concrete construction laborers. 2008.
- [20] C. Mourgues, M. Fischer and D. Hudgens: Using 3D and 4D models to improve jobsite communication—virtual huddles case study. *Proceedings of CIB 24th W78 Conference & 14th EG-ICE Workshop & 5th ITC@ EDU Workshop*, Maribor, Slovenia, 91-97. 2007.
- [21] Z. Gao, R. C. Walters, E. J. Jaselskis and T. J. Wipf: Approaches to Improving the Quality of Construction Drawings from Owner's Perspective. *Journal of Construction Engineering and Management*, 132(11), 1187-1192. 2006.
- [22] P. F. Kaming, P. O. Olomolaiye, G. D. Holt and F. C. Harris: Factors influencing craftsmen's productivity in Indonesia. *International Journal of Project Management*, 15(1), 21-30. 1997.
- [23] R. Masood, M. K. N. Kharal and A. R. Nasir: Is BIM Adoption Advantageous for Construction Industry of Pakistan? *Procedia Engineering*, 77, 229-238. 2014.
- [24] P. Meadati and J. Irizarry: BIM—a knowledge repository. *Proceedings of the 46th Annual International Conference of the Associated Schools of Construction*, Vol. 12. 2010.
- [25] J. L. Kim: Use of BIM for effective visualization teaching approach in construction education. *Journal of Professional Issues in Engineering Education and Practice*, 138(3), 214-223. 2011.
- [26] W. Lu, Y. Peng, Q. Shen and H. Li: Generic model for measuring benefits of BIM as a learning tool in construction tasks. *Journal of Construction Engineering and Management*. 2012.

PARAMETER IDENTIFICATION APPLYING IN COMPLEX THERMO-HYDRO-MECHANICAL PROBLEMS LIKE THE DESIGN OF BUFFER ELEMENTS

L. Nguyen-Tuan^{*}, T. Lahmer, M. Datcheva, E. Stoimenova and T. Schanz

**Institute of Structural Mechanics and Juniorprofessorship Optimisation and Stochastics,
Bauhaus-Universität Weimar
Marienstrasse 15, 99423 Weimar, Germany
E-mail: long.nguyen.tuan@uni-weimar.de*

Keywords: Parameter Identification, Coupled THM Problem, Sensitivity Analysis, Particle Swarm Optimisation, Confidence Interval.

Abstract. *This study contributes to the identification of coupled THM constitutive model parameters via back analysis against information-rich experiments. A sampling based back analysis approach is proposed comprising both the model parameter identification and the assessment of the reliability of identified model parameters. The results obtained in the context of buffer elements indicate that sensitive parameter estimates generally obey the normal distribution. According to the sensitivity of the parameters and the probability distribution of the samples we can provide confidence intervals for the estimated parameters and thus allow a qualitative estimation on the identified parameters which are in future work used as inputs for prognosis computations of buffer elements. These elements play e.g. an important role in the design of nuclear waste repositories.*

1 INTRODUCTION

Identifying parameters for coupled THM analysis in unsaturated soils is a complicated problem due to a large set of parameters and a variety of variables in the forward calculation (i.e. displacements, temperature, pore water pressure and air pressure). Some authors attempted to identify constitutive model parameters for unsaturated soils by means of back analysis, for instance [1, 2]. They drew an objective function in different subspaces and found the minimum of the objective function assuming that the other parameters are kept constant. In fact, model parameters vary in the search space during the searching process. Beside that the confidence of the identified parameters have not been assessed. In [3] model parameters for describing the elasto-plastic behaviour have been identified for unsaturated soils. The authors have chosen six parameters for identification based on qualitative arguments. However, the quality of the identified parameters has not been assessed quantitatively.

Therefore, in this paper a novel back analysis approach is proposed comprising model parameter identification and an assessment of the reliability of the identified model parameters. Parameter samplings are carried out based on metaheuristic optimization methods, in which parameters are varied under the control of the computational paradigms such as the Particle Swarm Optimisation (PSO) [4]. The confidence intervals are determined based on these parameter samplings by means of probability distribution functions, see e.g. [5]. The approach can be applied for back analysing a variety of geotechnical problems, in particular it is well suited for parameter identification problems including large sets of model parameters and multi-response measurements.

This proposed strategy is applied to identify the model parameters for the simulation of the behaviour of buffer elements in high-level nuclear waste facilities. The clayey buffer elements in nuclear waste repository play the role as engineered barriers. The behaviour of the clay barrier is highly complex. It involves coupled THM phenomena, which take place due to the simultaneous heating (generated by the radioactive waste) and hydrating of the barrier (due to the inflow of water from the surrounding rock) and mechanical forces (due to swelling phenomenon of the buffer). It requires a fully coupled nonlinear THM numerical analysis for simulating water/vapour transport, heat conduction, and modelling of complex thermo-elasto-plastic stress-strain behaviour. The results of the back analysis approach are finally compared and discussed considering experimental data in this paper.

2 PARAMETER IDENTIFICATION VIA BACK ANALYSIS

2.1 Back analysis strategy

The back analysis strategy is illustrated in Fig. 1. Firstly, the mathematical models for the forward calculation are selected. In coupled THM analysis, we use multi-physical relations described in Table 1, which are implemented in finite element code, CODE_BRIGHT [6]. Afterwards, the numerical solution of the forward problem is compared with experimental data by means of an objective function i.e. a weighted sum of squared errors approach, where the latter is minimised by means of nonlinear optimisation, in particular by PSO method [4]. The sampling process is carried out based on the replication of optimisations. Each optimisation begins by an initial values of parameters. The initial values of parameters are uniformly distributed within their prescribed ranges. The sampling process generates n_p samples of parameters by means of iterating n_p times of the optimisation with the PSO method. Next, a sensitivity analy-

Table 1: Constitutive relations in coupled THM analysis

Variables	Constitutive equation	Notation
Liquid and gas advective flux	Darcy's law	q_l, q_g
Vapour and air non-advective fluxes	Fick's law	i_g^w, i_l^a
Conductive heat flux	Fourier's law	i_c
Liquid phase degree of saturation	Retention curve	S_l, S_g
Stress tensor	Mechanical constitutive model	σ

- Parameters involved in modelling net stress driven processes ($d\sigma \neq 0$):
 $\mathcal{M} = (k_{io}, \alpha_i, p_{ref}, \lambda(0), r, \beta, k, p_{s0}, p^c, M, \alpha, e_o, p_o^*)$
- Parameters involved in modelling suction driven processes ($ds \neq 0$):
 $\mathcal{H} = (P_0, \lambda, \phi_0, k_o, \kappa_{s0}, \alpha_{ss}, \alpha_{sp})$
- Parameters involved in modelling temperature driven processes ($dT \neq 0$):
 $\mathcal{T} = (\tau, D, n_D, \lambda_{sat}, \lambda_{dry}, \alpha_0, \alpha_1, \alpha_3, \rho)$

Therefore the vector of model parameters reads:

$$\mathbf{x} = (\mathcal{H}, \mathcal{T}, \mathcal{M}) \quad (1)$$

The vector of model response \mathbf{y}^{calc} is composed as follows:

$$\mathbf{y}^{calc} = (y_{tm}^d(\mathbf{x}))^{calc} = (S_l(tm), \sigma_{yy}(tm), T(tm), s(tm))^{calc} \quad (2)$$

where $S_l(tm)$ is the degree of saturation over time t at observation point m , $\sigma_{yy}(tm)$ is the vertical stress, $T(tm)$ is the temperature, and $s(tm)$ is suction.

3.2 Results

Figure 3 presents the histograms and scaled Student probability density distribution (PDF), in which model parameters are normalised from 0 to 1 corresponding to their minimum and maximum boundaries, respectively. From Figure 3, it is clear that these parameters have their distribution close to the normal distribution. The figure also indicates that the high sensitive parameters have narrow ranges of their probability density functions (i.e. $P_0, \lambda, \mathbf{k}_0$). Less sensitive parameters have wider ranges of their probability density distributions (i.e. $\lambda_{sat}, \kappa_{s0}, n_D$). For the non-sensitive model parameters, the probability distributions show no pattern and significantly deviate from the normal distribution. From this, we derive that the confidence intervals for these parameters may not be reliably estimated. The confidence intervals are estimated considering typical confidence coefficients ($\gamma_c = 95\%$), which means that the expected value of each of the identified model parameters is with 0.95 probability within to the confidence interval. Table 2 presents the mean value, the upper (CI_U) and the lower (CI_L) bound of the confidence interval. The result in Fig. 3 shows that in general the parameters, which are highly sensitive (e.g. $\mathbf{k}_0, \lambda, P_0$), have a more pronounced peakedness. In contrast, the low sensitivity parameters (e.g. $\lambda_{sat}, \kappa_{s0}, n_D$) have less pronounced peakedness.

Table 2: Confidence intervals of the optimal parameters

	P_0	λ	\mathbf{k}_0	λ_{sat}	κ_{s0}	n_D
Mean	1.51	0.339	2.03E-16	1.33	0.0071	0.79
CI_L	1.45	0.328	1.55E-16	1.28	0.0012	0.73
CI_U	1.58	0.349	2.50E-16	1.38	0.013	0.86

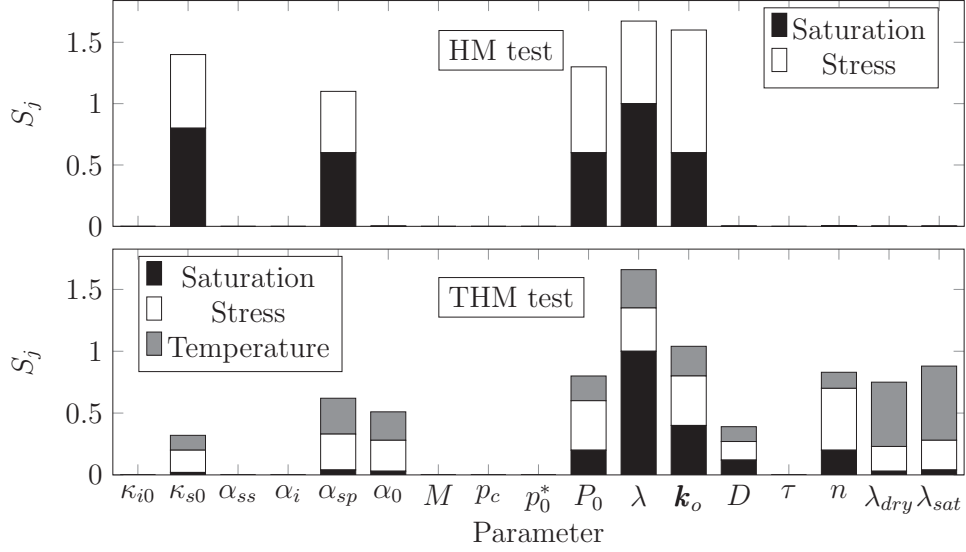


Figure 2: Sensitivity indices S_j .

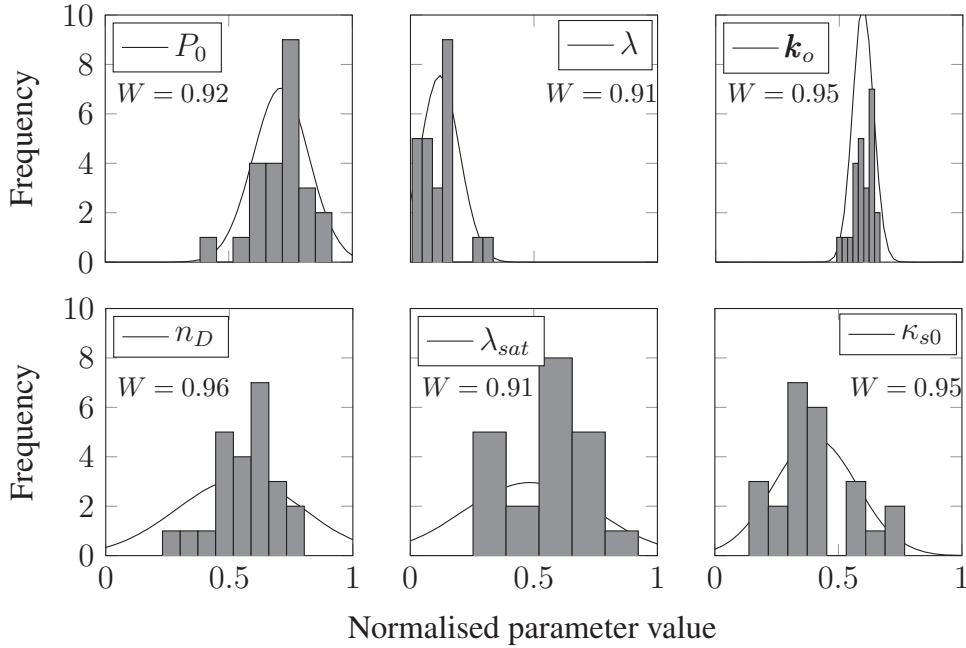


Figure 3: Histogram and PDF of the parameter samplings

4 CONCLUSIONS

We propose a back analysis approach combining model parameter identification and the assessment of the reliability of identified model parameters. The obtained results show that it is a promising method for model parameter identification, especially in coupled multi-physical process simulations involving complex non-linear constitutive laws. The reliability of an identified parameter depends on its sensitivity revealed under the particular boundary conditions taking place in the forward problem. The approach can be applied for back analysing a variety of geotechnical problems, especially, it is designed for parameter identifications of problems having a large set of constitutive model parameters and a large set of model responses.

Acknowledgements

This research was supported by the Deutsche Forschungsgemeinschaft (DFG) through the research grants SCHA 675/17-1 and LA 2869/4-1. These financial supports are gratefully acknowledged.

REFERENCES

- [1] M. Hofmann, T. Most, G. Hofstetter, Parameter identification for partially saturated soil models, in: 2nd International Conference on Computational Methods in Tunnelling, Ruhr University Bochum, 2009.
- [2] T. Schanz, M. Zimmerer, M. Datcheva, Identification of coupled hydro-mechanical parameters with application to engineered barrier systems, in: Toll et al. (Ed.), *Unsaturated Soils: Advances in Geo-Engineering – 1st European Conference on Unsaturated Soils*, Durham, UK, 2008, pp. 797–803.
- [3] Y. Zhang, D. Gallipoli, C. Augarde, Parameter identification for elasto-plastic modelling of unsaturated soils from pressuremeter tests by parallel modified particle swarm optimization, *Computers and Geotechnics* 48 (0) (2013) 293–303.
- [4] J. Kennedy, R. Eberhart, Particle swarm optimization, in: *Proceedings of IEEE International Conference on Neural Networks*. IV, 1995, pp. 1942–1948.
- [5] D. C. Montgomery, G. C. Runger, *Applied Statistics and Probability for Engineers*, John Wiley & Sons Inc., 2002.
- [6] DIT-UPC, *CODE BRIGHT user's guide*, Universitat Politècnica de Catalunya, Barcelona, Spain, 2009.
- [7] S. S. Shapiro, M. B. Wilk, An analysis of variance test for normality (complete samples), *Biometrika* 52 (3/4) (1965) 591–611.

EVALUATION OF THE METRIC TRIFOCAL TENSOR FOR RELATIVE THREE-VIEW ORIENTATION

V. Rodehorst

Bauhaus-Universität Weimar
Faculties media and civil engineering
Bauhausstr. 11, 99423 Weimar, Germany
E-mail: volker.rodehorst@uni-weimar.de

Keywords: Relative Orientation, Calibrated Camera, Metric Trifocal Tensor, Evaluation

Abstract. *In photogrammetry and computer vision the trifocal tensor is used to describe the geometric relation between projections of points in three views. In this paper we analyze the stability and accuracy of the metric trifocal tensor for calibrated cameras. Since a minimal parameterization of the metric trifocal tensor is challenging, the additional constraints of the interior orientation are applied to the well-known projective 6-point and 7-point algorithms for three images. The experimental results show that the linear 7-point algorithm fails for some noise-free degenerated cases, whereas the minimal 6-point algorithm seems to be competitive even with realistic noise.*

1 INTRODUCTION

The automatic and reliable calculation of the relative camera pose and orientation from image correspondences is one of the challenging tasks in photogrammetry and computer vision. If cameras view an arbitrary 3D scene from two distinct positions, the mapping of each point depends on its unknown spatial depth. However, the projection ray of a point in the first view reprojects onto the second view as a line on which the corresponding point must be located. This relation which is independent of the scene structure is called *epipolar geometry* (see Figure 1). The *baseline* \mathbf{b} joining the two projection centers \mathbf{C} and \mathbf{C}' intersect with the image planes at the *epipoles* \mathbf{e} and \mathbf{e}' . Thus, for each image the epipole is the projection of the other camera center. An image point \mathbf{x} in one view generates an *epipolar line* \mathbf{l}' in the other view and all these lines pass through the particular epipole. The plane defined by an object point \mathbf{X} and the two projection centers is called *epipolar plane*.

Algebraically, we can describe this relation between points and lines in different planar coordinate systems with help of the *fundamental matrix* [1, 2]. Given at least $n \geq 8$ image point pairs $\mathbf{x}_i \leftrightarrow \mathbf{x}'_i$ in the image planes which are distributed in general position (i.e. are not collinear), we can linearly compute the 3×3 fundamental matrix \mathbf{F} with seven degrees of freedom, so that all epipolar lines $\mathbf{l}'_i = \mathbf{F}\mathbf{x}_i$ can be derived. The *essential matrix* describes the same relation in the calibrated case where the interior orientation is known. An interesting aspect of the minimal 5-point algorithms is their stability, even if points from coplanar objects are observed. An overview and evaluation of relative pose estimation methods for image pairs can be found in [3].

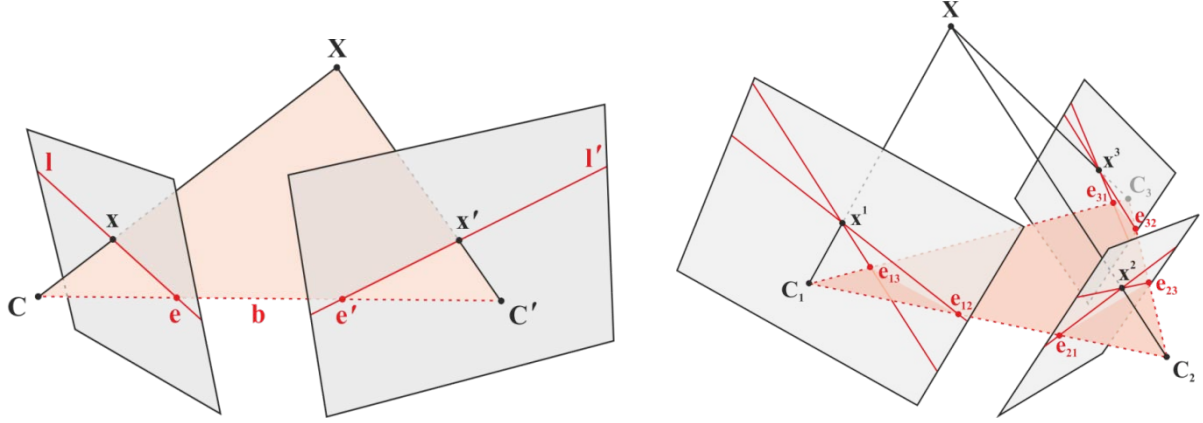


Figure 1: Epipolar geometry (left) and trifocal geometry (right)

2 TRIFOCAL TENSOR

Although two views are enough to determine depth, the point correspondence between two views is not unique, since a point is related to a line instead of a point. By extending the geometry to three views, the point correspondence ambiguity can be removed using the third view. If an object point is identified in two images and the projection centers are not collinear, the position in the third image can be predicted unambiguously by intersection of the corresponding epipolar lines (see Figure 1). The three projection centers \mathbf{C}_j define a so-called *trifocal plane* which introduces three additional constraints on the epipols

$$\mathbf{e}_{23}^\top \mathbf{F}_{12} \mathbf{e}_{13} = \mathbf{e}_{31}^\top \mathbf{F}_{23} \mathbf{e}_{21} = \mathbf{e}_{32}^\top \mathbf{F}_{13} \mathbf{e}_{12} = 0. \quad (1)$$

Algebraically, the trifocal tensor relates image points or lines seen in three views in a similar way like the fundamental matrix relates points in two views. The tensor depends on image coordinates only without an explicit spatial point or line. In this paper we concentrate on point coordinates only. Given at least $n \geq 7$ image point correspondences across three images $\mathbf{x}_i^1 \leftrightarrow \mathbf{x}_i^2 \leftrightarrow \mathbf{x}_i^3$ which are distributed in general position (i.e. are not collinear), we can compute the $3 \times 3 \times 3$ trifocal tensor $\mathbf{T} = [\mathbf{T}_1, \mathbf{T}_2, \mathbf{T}_3]$ with 18 degrees of freedom, where each submatrix \mathbf{T}_j is singular with rank two. At first, the image points \mathbf{x}_i^1 , \mathbf{x}_i^2 and \mathbf{x}_i^3 must be conditioned separately by translation to the origin and scaling to a mean distance of $\sqrt{2}$ using the 3×3 similarity transformations \mathbf{T}_1 , \mathbf{T}_2 and \mathbf{T}_3 . Then, the trifocal tensor for the conditioned image points $\tilde{\mathbf{x}}_i$ can be derived from the *point-point-point* relation [5]

$$[\tilde{\mathbf{x}}^2]_{\times} \left(\sum_{j=1}^3 \tilde{\mathbf{x}}_j^1 \tilde{\mathbf{T}}_j \right) [\tilde{\mathbf{x}}^3]_{\times} = \mathbf{0}. \quad (2)$$

where $[\]_{\times}$ denotes a 3×3 skew-symmetric matrix. For each point triplet we get four constraints on the elements of \mathbf{T} which can be combined into a $4n \times 27$ design matrix \mathbf{A} . Its derivation is omitted for simplicity but the complete matrix can be found in [4]. The linear homogeneous equation system of the form $\mathbf{A}\mathbf{t} = \mathbf{0}$ can be solved for the 27 elements of vector \mathbf{t} with help of *singular value decomposition* (SVD). After reshaping the solution vector row-wise into the $3 \times 3 \times 3$ tensorial slices, we have a basic trifocal tensor $\tilde{\mathbf{T}}$ for the conditioned points.

However, the trifocal tensor has 27 elements but only 18 degrees of freedom. This basic linear approach does not satisfy the eight remaining algebraic constraints. In [5] a method is proposed that takes the basic tensor as initial estimate and finds a geometrically valid tensor that satisfies all internal constraints. At first, the two epipols \mathbf{e}_{21} and \mathbf{e}_{31} are extracted from $\tilde{\mathbf{T}}$ as the left and right null-vectors according to

$$[\mathbf{u}_1, \mathbf{u}_2, \mathbf{u}_3]^\top \mathbf{e}_{21} = \mathbf{0} \quad \text{with} \quad \mathbf{u}_j^\top \mathbf{T}_j = \mathbf{0}^\top \quad \text{and} \quad [\mathbf{v}_1, \mathbf{v}_2, \mathbf{v}_3]^\top \mathbf{e}_{31} = \mathbf{0} \quad \text{with} \quad \mathbf{T}_j \mathbf{v}_j = \mathbf{0}. \quad (3)$$

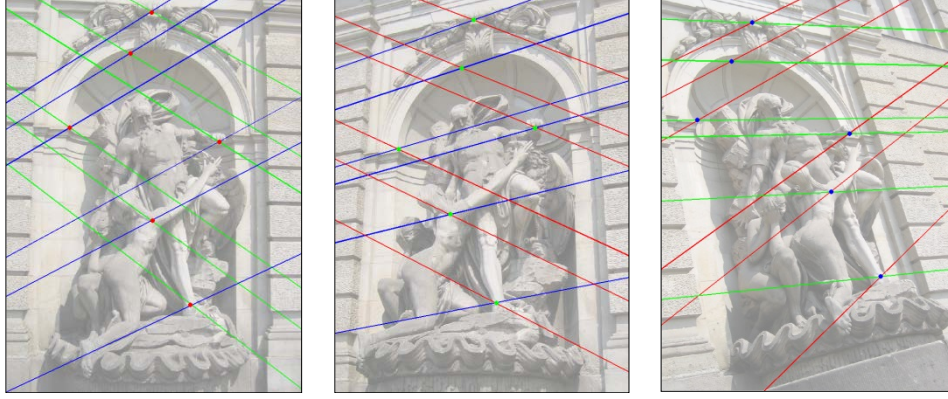


Figure 2: Trifocal geometry computed from of six corresponding image point triplets. The example shows the Prometheus fountain at Berlin University of the Arts

Then, a 27×18 matrix \mathbf{E} is assembled such that $\mathbf{t} = \mathbf{E}\mathbf{a}$, where \mathbf{E} expresses the linear relationship of the unknown projection matrices \mathbf{P}_2 and \mathbf{P}_3 with known epipols

$$\tilde{\mathbf{T}}_{jkl} = a_{jl}e_{31_k} - e_{21_j}b_{kl} \quad \text{for } j, k, l = 1, 2, 3 \quad (4)$$

and vector \mathbf{a} contains the remaining 18 elements a_j^k and b_j^l . Now, we have to minimize the algebraic error of $\|\mathbf{A}\mathbf{E}\mathbf{a}\|$ subject to $\|\mathbf{E}\mathbf{a}\| = 1$ using a constrained *direct linear transformation* (DLT) algorithm. After reshaping the 27 elements of the solution vector into tensor form, the final \mathbf{T} for the original points can be obtained by deconditioning

$$\mathbf{T}_j = \mathbf{T}_2^{-1} \left(\sum_{k=1}^3 \mathbf{T}_{1kj} \tilde{\mathbf{T}}_k \right) \mathbf{T}_3^{-\top} \quad \text{for } j = 1, 2, 3. \quad (5)$$

Similarly to the fundamental matrix, there exists also a *minimal* algorithm to determine the trifocal tensor from exactly six point correspondences across three images [6]. An example of the computed trifocal geometry is given in Figure 2.

3 CALIBRATED TRIFOCAL TENSOR

In many applications we are able to calibrate the cameras in beforehand. Taking advantage of the known interior orientation stored in the upper-triangular 3×3 *calibration matrix* \mathbf{K} and the metric parameterization of the transformation functions should stabilize the reconstruction process. For the metric 3D reconstruction from three calibrated views we can parameterize the trifocal tensor with five parameters for the relative orientation of the first two cameras and six parameters for the exterior orientation of the third camera.

Since each image point correspondence $\mathbf{x}_i^1 \leftrightarrow \mathbf{x}_i^2 \leftrightarrow \mathbf{x}_i^3$ provides three constraints, we need at least $n \geq 3\frac{2}{3}$ point triplets to determine the eleven unknown parameters. However, the problem is still not solved satisfactorily due to its algebraic complexity and lack of efficient algorithms. For example [7] parameterizes the relative orientation by the two translation vectors \mathbf{t}_2 and \mathbf{t}_3 and the two quaternions \mathbf{q}_2 and \mathbf{q}_3 for the rotations. These 14 parameters are further reduced by fixing the first baseline to unit length using the constraint $\mathbf{t}_2^\top \mathbf{t}_2 = 1$ and normalizing the quaternions with $\mathbf{q}_2^\top \mathbf{q}_2 = 1$ and $\mathbf{q}_3^\top \mathbf{q}_3 = 1$. The detailed estimation procedure for this metric trifocal tensor is studied in [8].

A minimal algorithm for the metric trifocal tensor is sketched in [9] where only four points in three calibrated views are used. However, in case of noisy point correspondences, the reprojected fourth object point will not exactly coincide with the observed image point and therefore the authors demonstrates the enormous complexity by visualizing the remarkable solution space. The minimal parameterization of the trifocal tensor in [10] uses projective line geometry in order to provide necessary and sufficient constraints. Finally, in [11] a new meaningful parametrization with non-collinear pinholes from a quotient Riemannian manifold is proposed.

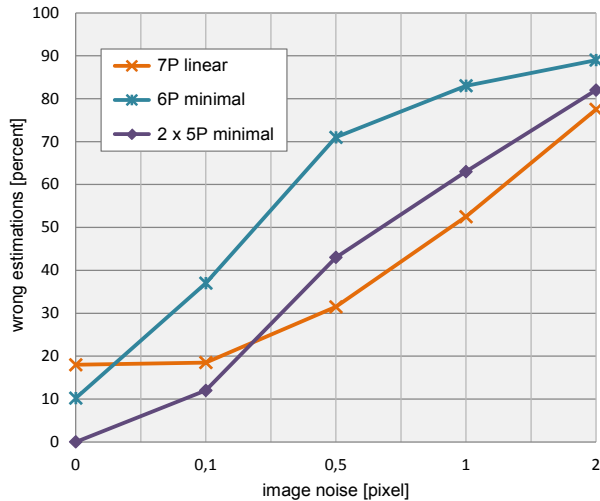


Figure 3: Comparison of the relative orientation of three views using synthetic data

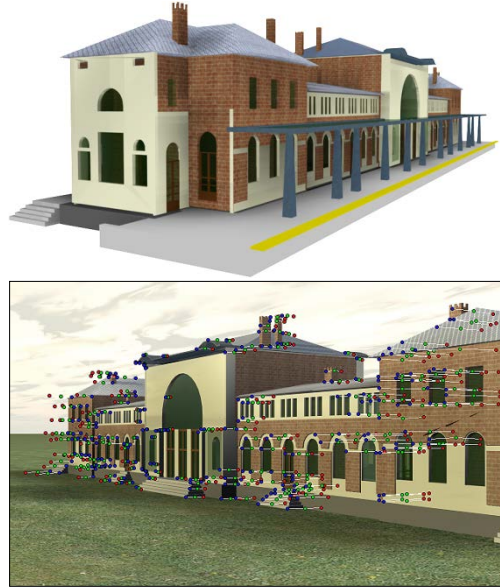


Figure 4: Textured 3D model with matched image feature triplets

However, in this paper we simply compute the linear trifocal tensor from the normalized image triplets $\tilde{\mathbf{x}}_i^1 \leftrightarrow \tilde{\mathbf{x}}_i^2 \leftrightarrow \tilde{\mathbf{x}}_i^3$ by applying the inverted calibration matrices $\tilde{\mathbf{x}}_i = \mathbf{K}^{-1}\mathbf{x}_i$. The fundamental matrices contained in the trifocal slices should now describe the individual rotations and translations. Since both baselines are thereby fixed to unit length, we have to find a proper scaling for the second baseline. At first spatial coordinates are triangulated using the camera pairs $(\mathbf{P}_1, \mathbf{P}_2)$ and $(\mathbf{P}_1, \mathbf{P}_3)$. Then, the mean distance of the object points to the common camera \mathbf{P}_1 defines the scale ratio. Note that this simple linear version does not incorporate all the partly unknown and complicated polynomial constraints that are required for an optimal metric trifocal tensor. Nevertheless, the computation of the direct linear solution is fast and unique. In contrast to the fundamental matrix this version of the metric trifocal tensor works for planar point configurations too.

4 EXPERIMENTAL RESULTS

To evaluate the relative orientation of three images, we analyzed the following approaches

- The metric trifocal tensor which is based on the *linear 7-point algorithm* [5,4]
- The *minimal 6-point algorithm* [6,4] with normalized image coordinates
- The *minimal 5-point algorithm* [3] for two image pairs with recovery of different scaling

using synthetically generated data with ground truth. At first 100 spatial object points are randomly generated in general position and projected into the images using simulated cameras. The camera positions are also selected arbitrarily, but the view directions are restricted to the approximate location of the point cloud. The image coordinates range from 1 to 1024 and are displaced with Gaussian noise. Every technique is examined 10,000 times to obtain statistically significant results. Critical point configurations or camera motions are not explicitly checked for these synthetic experiments and may lead to false estimations.

The experimental results are summarized in Figure 3. In the tested metric case, the minimal 5-point algorithm for calibrated image pairs performs always better than the minimal 6-point algorithm for three uncalibrated images. It seems that because of some missing constraints the linear 7-point algorithm fails for some degenerated cases although the input data is noise-free. However, with realistic noise the two additional point triples stabilize the approach and the linear 7-point algorithm overtakes the minimal 5-point algorithm.

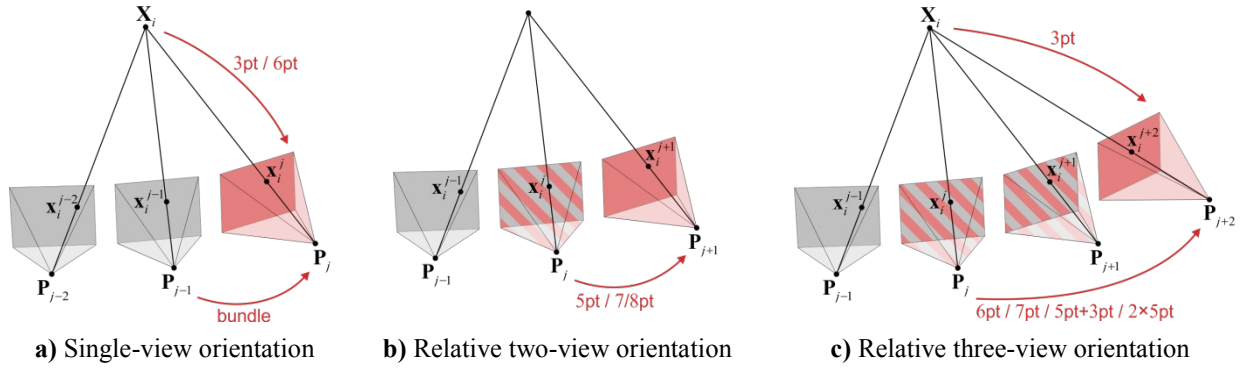


Figure 5: Tested strategies for camera path estimation

The following tests demonstrate the performance of the proposed multi-view algorithms. Figure 4 shows our synthetic 3D model of the railway station in Bonn together with the results of the automatically detected and matched image features. The camera generates 120 images while moving around the building and keeping it in view. On average 960 corner features are extracted from each image which typically yields 310 correspondences over three successive views. Additionally, we add some normal distributed noise with a standard deviation of 0.5 pixels to the measured image coordinates in order to emphasize the differences between the tested strategies (see Figure 5).

To compare the general projective methods, we removed the known calibration information of the synthetic camera from the images points and recovered the camera motion according to the metric algorithms [3,4].

- **One view:** if an initial reconstruction from two or three images is available, the subsequent camera positions may be recovered from the spatial coordinates using single-view orientation methods:
 - **Projective:** the new camera position can be determined from at least six object coordinate projections using the over-determined *spatial resection* [5]. The matching object coordinates may be identified by analyzing the image point correspondences to the existing reconstruction.
 - **Metric:** in order to prevent that the reconstruction error is shifted to the interior orientation, the camera motion can be computed with help of the *minimal 3-point* pose estimation algorithm [4]. For this experiment the required three points are selected randomly and the method is repeated 100 times. Finally, the solution with the lowest reprojection error is taken as result.
 - **Bundle:** if the camera motion is somewhat smooth with a relative small baseline, the new camera position may be computed with incremental *bundle adjustment* [5,4] only, where the initial values are taken from the last camera of the already processed sequence.
- **Two views:** many techniques for pose or ego-motion estimation rely on two successive views. Subsequently, we compare the following relative orientation methods for camera pairs [3]:
 - **Projective:** very simple and computational effective is the over-determined *8-point algorithm* for the fundamental matrix.
 - **Metric:** a little more robust is the *minimal 5-point algorithm* for computing the essential matrix. In our implementation the five points are selected randomly and the algorithm is applied 100 times. Finally, the solution with the lowest sampson distance is taken as result.
- **Three views:** Finally we present the strategies for camera path estimation which are based on the relative orientation of camera triplets:
 - **Projective:** we apply the *minimal 6-point* algorithm for the general projective trifocal tensor. The required six points are selected randomly and the method is repeated 100 times. Finally, the solution with the lowest reprojection error is taken as result.
 - **Metric 1:** the first metric method consists of the *minimal 5-point* algorithm to compute the essential matrix for the first two cameras followed by the *minimal 3-point* algorithm for the pose of the third camera.
 - **Metric 2:** the second alternative uses the *minimal 5-point* algorithm to compute the essential matrix for the first and second camera pair. Then we triangulate spatial coordinates and take the

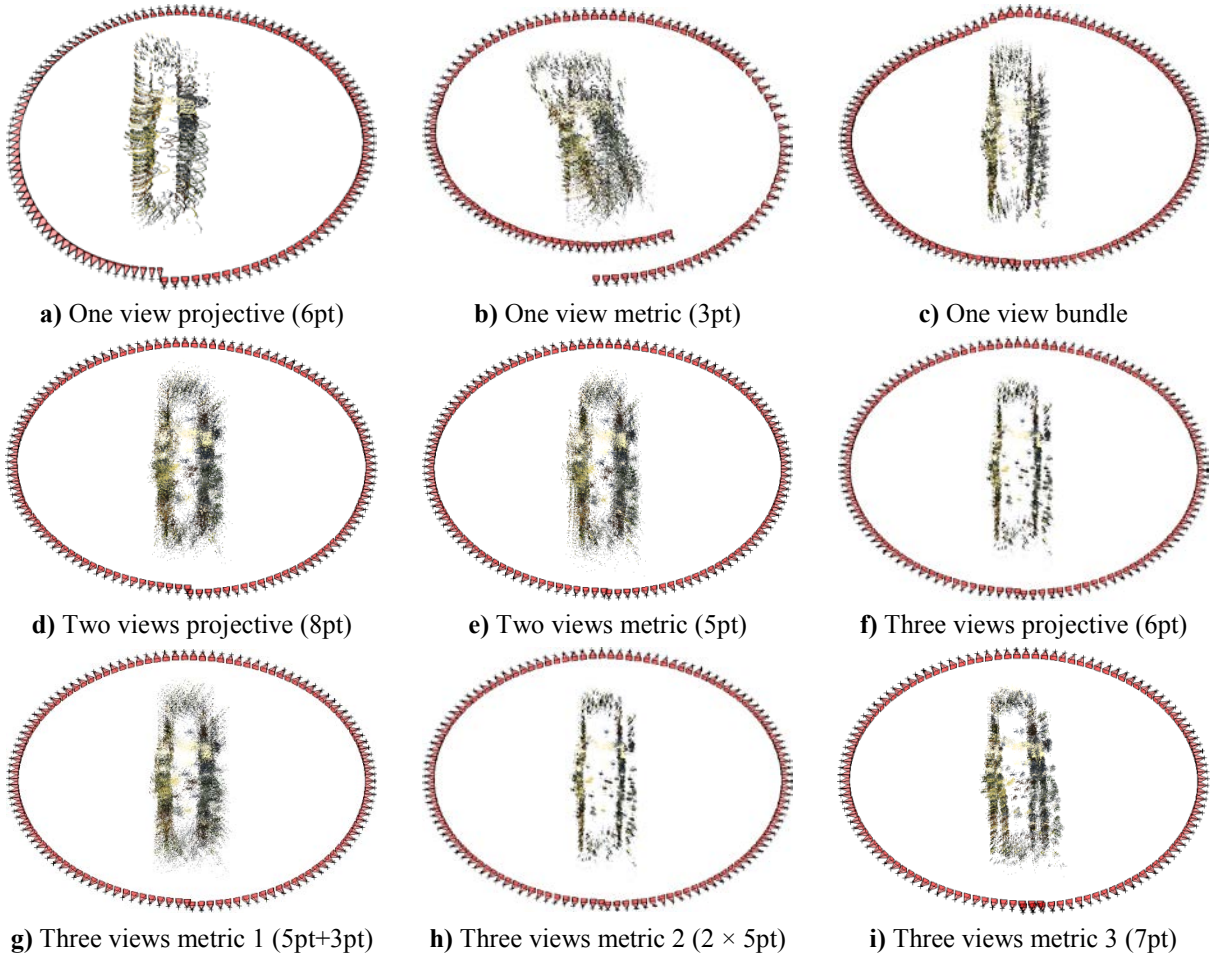


Figure 6: Strategies to reconstruct the object structure and camera motion using different image orientation techniques

mean distance of the object points to the common camera to find a proper scale ratio for the baselines.

- **Metric 3:** as last method we demonstrate the results of the proposed over-determined *7-point algorithm* for the metric trifocal tensor.

In a next step these initial reconstructions should be improved by extending the baselines for better triangulation. At first the image features must be tracked as long as possible to maximize the camera distance. For the exemplary sequence of the railway station an image point is on average visible in 4.5 subsequent views. However, some features can be tracked up to 22 frames which extend the triangulation angle from 3 to 66 degrees. For the following experiment we started from the two-view metric reconstruction. Then we selected all image points which are observable in at least four images and triangulated the object coordinates using all involved views. Thereby, the number of points is reduced to approximately the half while the accuracy of the spatial coordinates is apparently better. As already mentioned, the final step of a reconstruction algorithm should be the global optimization using bundle adjustment in order to obtain maximum accuracy. In contrast to the preceding step, which modifies the spatial objects points only, improves the metric bundle adjustment the cameras as well.

5 SUMMARY AND OUTLOOK

Our experiments of the calibrated metric case have shown that for single-image orientation the minimal 3-point algorithm and for the relative orientation of image pairs the minimal 5-point algorithms perform best, especially in presence of noise. For the relative orientation of three calibrated images we also

recommend applying the minimal 5-point algorithm independently to the image pairs and recovering the different scaling using the depth ratio of corresponding object coordinates. However, even though the metric trifocal tensor based on the linear 7-point algorithm does not enforce all necessary metric constraints, it can be more stable than the 5-point algorithms due to the possibility of over-determined estimation. Our detailed investigations of the relative orientation methods in [3] have shown that in general, the estimation of camera rotation is more reliable than the translation. The minimal 5-point algorithms often provide multiple solutions. The best selection criterion is a combination of a preceding cheirality test with the minimal number of points followed by the computation of the Sampson distance over all available points.

The registration of individual reconstructions based on spatial points suffers from critical surfaces and inaccurate triangulated object coordinates. Therefore we recommend determining a spatial similarity transformation using a single-view overlap for image pairs and a double-view camera consistency for image triplets. In case of a moving camera that captures video frames at high frequency the extension of the baseline is essential to improve the triangulation accuracy. However, the sequential approach accumulates the estimation errors over time and the reconstructed path tend to drift. To reduce this effect, the result necessarily should be improved with a global optimization technique like bundle adjustment.

Nevertheless, if the initial reconstruction is far from the correct solution, the non-linear optimization step is not able to work wonders. The general projective approaches are simple and quite helpful, if no calibration information is available so far. However, if coplanar points on dominant planes are observed the spatial resection with the 6-point algorithm, the relative two-image orientation with the minimal 7-point or linear 8-point algorithm and the relative orientation of image triplets with the minimal 6-point algorithm will fail. Unfortunately, all relative orientation algorithms produce wrong estimates from time to time. If a camera path over several hundred frames needs to be reconstructed only one miscalculation may corrupt the whole path. Thus, additional multi-camera constraints [3,4] are required to give stable results for extensive camera path reconstructions.

REFERENCES

- [1] R.I. Hartley: In defense of the eight-point algorithm, In T-PAMI, 19(6), 580—593, 1997.
- [2] H.C. Longuet-Higgins: A computer algorithm for reconstructing a scene from two projections, *Nature*, vol. 293, 133—135, 1981.
- [3] V. Rodehorst, M. Heinrichs and O. Hellwich: Evaluation of Relative Pose Estimation Methods for Multi-Camera Setups, IAPRS 37(B3b), 135—140, 2008.
- [4] V. Rodehorst: Photogrammetric Computer Vision for spatio-temporal 3D reconstruction, habilitation thesis, Technische Universität Berlin, 2013.
- [5] R.I. Hartley and A. Zisserman, 2004: Multiple view geometry in computer vision, Cambridge University Press, 2nd edition, 1—672, 2004.
- [6] P.H.S. Torr and A. Zisserman: Robust parameterization and computation of the trifocal tensor, *Image and Vision Computing*, 15(8), 591—605, 1997.
- [7] W. Förstner: New orientation procedures, In IAPRS, 33(3), 297—304, 2000.
- [8] S. Abraham: Kamera Kalibrierung und metrische Auswertung monokularer Bildfolgen, Shaker Verlag, 1—170, 2000.
- [9] D. Nistér and F. Schaffalitzky: Four points in two or three calibrated views: theory and practice, In *IJCV*, 67(2), 211—231, 2006
- [10] J. Ponce, M. Hebert and M. Trager: Trinocular geometry revisited, submitted to *IJCV*, 2015.
- [11] S. Leonardos, R. Tron and K. Daniilidis: A metric parametrization for trifocal tensors with non-coplanar pinholes, In *CVPR*, 259—267, 2015.

OPERATIONAL PROPERTIES OF THE LAGUERRE TRANSFORM

M.M. Rodrigues

*CIDMA - Center for Research and Development in Mathematics and Applications
Department of Mathematics, University of Aveiro, Campus Universitário de Santiago,
3810-193 Aveiro, Portugal.
E-mail: mrodrigues@ua.pt*

Keywords: Inequalities; Differential operators; Integral operators; Laguerre transform.

Abstract. *The Laguerre polynomials appear naturally in many branches of pure and applied mathematics and mathematical physics. Debnath introduced the Laguerre transform and derived some of its properties. He also discussed the applications in study of heat conduction and to the oscillations of a very long and heavy chain with variable tension. An explicit boundedness for some class of Laguerre integral transforms will be present.*

1 INTRODUCTION

The Laguerre polynomials appear naturally in many branches of pure and applied mathematics and mathematical physics (see e.g. [2, 3, 4, 6]). Debnath [2] introduced the Laguerre transform and derived some of its properties. He also discussed the applications in study of heat conduction [4] and to the oscillations of a very long and heavy chain with variable tension [3].

This paper is devoted to the study of the generalized Laguerre transform and some operational properties. Here we present and prove of the results presented in [1]. In fact, for the interested reader we refer [1], where it is presented a more detailed study of the generalized Laguerre transform.

2 PRELIMINARIES

The Laguerre transform of a function $f(x)$ is denoted by $\tilde{f}_\alpha(n)$ and defined by the integral

$$L\{f(x)\} = \tilde{f}_\alpha(n) = \int_0^\infty e^{-x} x^\alpha L_n^\alpha(x) f(x) dx, \quad n = 0, 1, 2, \dots \quad (1)$$

provided the integral exists in the sense of Lebesgue, where $L_n^\alpha(x)$ is a generalized Laguerre polynomial of degree n with order $\alpha > -1$, and satisfies the following differential equation

$$\frac{d}{dx} \left[e^{-x} x^{\alpha+1} \frac{d}{dx} L_n^\alpha(x) \right] + n e^{-x} x^\alpha L_n^\alpha(x) = 0. \quad (2)$$

The sequence of Laguerre polynomial $(L_n^\alpha(x))_{n=0}^\infty$ have the following property:

$$\int_0^\infty e^{-x} x^\alpha L_n^\alpha(x) L_m^\alpha(x) dx = \binom{n+\alpha}{n} \Gamma(\alpha+1) \delta_{nm}, \quad (3)$$

where δ_{nm} is Kronecker function defined by

$$\delta_{nm} = \begin{cases} 1, & \text{if } n = m \\ 0, & \text{if } n \neq m \end{cases}$$

and

$$\Gamma(\alpha+1) = \int_0^\infty x^\alpha e^{-x} dx.$$

The inverse of the Laguerre transformation is then

$$f(x) = \sum_{n=0}^{\infty} (\delta_n)^{-1} \tilde{f}_\alpha(n) L_n^\alpha(x) \quad (0 < x < \infty),$$

where

$$\delta_n = \binom{n+\alpha}{n} \Gamma(\alpha+1).$$

3 EXPLICIT BOUNDEDNESS FOR SOME CLASS OF LAGUERRE INTEGRAL TRANSFORMS

Here, we consider the generalized integral transform defined, for $x \geq 0$, by

$$(\alpha, \beta, n I_-^\delta f)(x) = \int_x^\infty (t-x)^{\delta-1} e^{-\beta(x)t} t^\alpha L_n^\alpha(c(t,x)) f(t) dt \quad (4)$$

with $\beta(x)$ a non-negative continuous function on $]0, +\infty[$. When $\delta = 1, \beta(x) \equiv 1, x = 0$ and such that $c(t, 0) \equiv t$, the integral transform (4) coincide with (1), and when $\alpha = 0, n = 0, \beta(x) \equiv 0$ the integral transform (4) multiplied by $\frac{1}{\Gamma(\delta)}$ coincide with the classical Riemann Liouville fractional integral of order δ

$$\begin{aligned} \frac{1}{\Gamma(\delta)} (\alpha, \beta, n I_-^\delta f)(x) &\equiv (I_-^\delta f)(x) \\ &= \frac{1}{\Gamma(\delta)} \int_x^\infty (t-x)^{\delta-1} f(t) dt, \quad x > 0 \end{aligned} \quad (5)$$

with $0 < \delta < 1$ (see [8]).

Now, we will study the generalized fractional integral transforms (4), and two of their modifications in the space $\mathcal{L}_{v,r}$ of the complex value Lebesgue measurable functions f on \mathbf{R}_+ such that for $v \in \mathbf{R}$

$$\|f\|_{v,r} = \left(\int_0^\infty |t^v f(t)|^r \frac{dt}{t} \right)^{1/r} < \infty, \quad 1 \leq r < \infty, \quad (6)$$

$$\|f\|_{v,\infty} = \operatorname{ess\,sup}_{t>0} (t^v |f(t)|) < \infty. \quad (7)$$

In what follows we obtain the boundedness of the fractional integral transform (4) as operators mapping the space $\mathcal{L}_{v,r}$ into the spaces $\mathcal{L}_{v-\delta-\alpha,r}$.

Theorem 3.1 *Let $\beta(x) = \frac{1}{x}$, $c(t,x) = \frac{t}{x}$ and $1 \leq r \leq \infty$. The operator $\alpha, \beta, n I_-^\delta f$ is bounded from $\mathcal{L}_{v,r}$ into $\mathcal{L}_{v-\delta-\alpha,r}$ and*

$$\|\alpha, \beta, n I_-^\delta f\|_{v-\delta-\alpha,r} \leq C_{\alpha,\beta,\delta,v} \|f\|_{v,r}. \quad (8)$$

Proof: Let $1 \leq r < \infty$. Using (6) and making the change of variable $t = xu$, we obtain

$$\begin{aligned} \|\alpha, \beta, n I_-^\delta f\|_{v-\delta-\alpha,r} &= \left(\int_0^\infty \left| x^{v-\delta-\alpha} (\alpha, \beta, n I_-^\delta f)(x) \right|^r \frac{dx}{x} \right)^{1/r} \\ &= \left(\int_0^\infty \left| x^{v-\delta-\alpha} \int_x^\infty (t-x)^{\delta-1} e^{-\frac{t}{x}} t^\alpha L_n^\alpha\left(\frac{t}{x}\right) f(t) dt \right|^r \frac{dx}{x} \right)^{1/r} \\ &= \left(\int_0^\infty \left| x^{v-\frac{1}{r}} \int_1^\infty (u-1)^{\delta-1} e^{-u} u^\alpha L_n^\alpha(u) f(ux) du \right|^r dx \right)^{1/r} \end{aligned}$$

$$\begin{aligned}
&\leq \int_1^\infty \left(\int_0^\infty \left| x^{v-\frac{1}{r}} (u-1)^{\delta-1} e^{-u} u^\alpha L_n^\alpha(u) f(ux) \right|^r dx \right)^{1/r} du \\
&\leq \int_1^\infty (u-1)^{\delta-1} e^{-u} u^{\alpha-v} |L_n^\alpha(u)| \left(\int_0^\infty |t^v f(t)|^r \frac{dt}{t} \right)^{1/r} du \\
&= \|f\|_{v,r} \int_1^\infty (u-1)^{\delta-1} e^{-u} u^{\alpha-v} |L_n^\alpha(u)| du.
\end{aligned}$$

From relation (2.19.3.8) in [7], we have

$$\begin{aligned}
C_{\alpha,\beta,\delta,v} &= \int_1^\infty (u-1)^{\delta-1} e^{-u} u^{\alpha-v} L_n^\alpha(u) du \\
&= \frac{(1+\alpha)_n}{n!} B(\delta, -\alpha+v-\delta) \\
&\quad \times {}_2F_2(\alpha-v+1, 1+\alpha+n; \alpha-v+1+\delta, 1+\alpha; -1) \\
&\quad + \frac{(1+v-\delta)_n}{n!} \Gamma(\alpha-v+\delta) \\
&\quad \times {}_2F_2(1-\delta, 1+v-\delta+n; 1-\alpha+v-\delta, 1+v-\delta; -1), \tag{9}
\end{aligned}$$

where $(\cdot)_n$ denote the Pochhammer symbol and $B(\cdot, \cdot)$ denote the Beta function.

For $r = \infty$ we have

$$\begin{aligned}
|x^{v-\delta-\alpha} {}_{\alpha,\beta,n}I_-^\delta f| &= \left| x^{v-\delta-\alpha} \int_x^\infty (t-x)^{\delta-1} e^{-\frac{t}{x}} t^\alpha L_n^\alpha\left(\frac{t}{x}\right) f(t) dt \right| \\
&\leq \int_1^\infty (u-1)^{\delta-1} e^{-u} u^{\alpha-v} |L_n^\alpha(u)| |t^{-v}(t^v f(t))| du \\
&\leq \|f\|_{v,\infty} \int_1^\infty (u-1)^{\delta-1} e^{-u} u^{\alpha-v} |L_n^\alpha(u)| du \\
&= \|f\|_{v,\infty} C_{\alpha,\beta,\delta,v}.
\end{aligned}$$

This completes the proof. ■

Acknowledgement: This work was supported by Portuguese funds through the CIDMA - Center for Research and Development in Mathematics and Applications, and the Portuguese Foundation for Science and Technology (“FCT–Fundação para a Ciência e a Tecnologia”), within project UID/MAT/ 0416/2013.

REFERENCES

- [1] L.P. Castro, V.N. Huy, M.M. Rodrigues and N.M. Tuan: Some properties of Laguerre transform, submitted.
- [2] L. Debnath: On Laguerre Transforms. Bull. Calcutta Math. Soc., **52**, 69-77, 1960.
- [3] L. Debnath: Applications of Laguerre transform on the problem of oscillations of a very long and heavy chain. Ann. Univ. Ferrara, N. Ser., Sez. VII, **9**, 149-151, 1961.
- [4] L. Debnath: Application of Laguerre transform to heat conduction problem. Ann. Univ. Ferrara, N. Ser., Sez. X, 17-19, 1962.
- [5] L. Debnath and B. Dambaru: Integral transforms and their applications, 2nd ed., Chapman & Hall/CRC, Boca Raton, FL, 2006.
- [6] J. McCully: The Laguerre transform. SIAM Review 2, 185-191, 1960.
- [7] A.P. Prudnikov, Yu.A. Brychkov and O.I. Marichev: Integrals and Series Vol.2: Special Functions. Gordon and Breach Science Publisher, New York etc., 1988.
- [8] S.G. Samko, A.A. Kilbas and O.I. Marichev: Fractional integrals and derivatives: theory and applications. Gordon and Breach, New York, 1993.
- [9] C.J. Tranter: Integral transform in mathematical physics. Methuen’s monographs on physical subjects, Methuen IX, London, 1951.

OPTIMISING ACOUSTIC RESONATORS FOR SONOFUSION EXPERIMENTS WITH EVOLUTIONARY ALGORITHMS

M. J. Stokmaier^{*}, A. G. Class, T. Schulenberg, and R. T. Lahey Jr.

^{*}*Dynardo GmbH*

Steubenstrasse 25, 99423 Weimar

E-mail: Markus.Stokmaier@dynardo.de

Keywords: evolutionary algorithm, hybrid EA, global optimization, resonator optimization.

Abstract. *The sizing of simple resonators like guitar strings or laser mirrors is directly connected to the wavelength and represents no complex optimisation problem. This is not the case with liquid-filled acoustic resonators of non-trivial geometries, where several masses and stiffnesses of the structure and the fluid have to fit together. This creates a scenario of many competing and interacting resonances varying in relative strength and frequency when design parameters change. Hence, the resonator design involves a parameter-tuning problem with many local optima. As its solution evolutionary algorithms (EA) coupled to a forced-harmonic FE simulation are presented. A new hybrid EA is proposed and compared to two state-of-the-art EAs based on selected test problems. The motivating background is the search for better resonators suitable for sonofusion experiments where extreme states of matter are sought in collapsing cavitation bubbles.*

1 INTRODUCTION

1.1 The optimisation problem of resonator tuning

An important fraction of **parameter tuning problems** in science and engineering is well-behaved in the manner that small variations in the parameter set entail only small changes in the system responses in most parts of the parameter space. The next important question for classifying optimisation (or just function minimisation w.l.o.g.) problems is whether there are local minima apart from the global minimum. Tuning a guitar string is easy because a gradient-following scheme allows to reach the global optimum of matching the frequency target. Minimising the displacement at the middle of the string when it is in forced stationary oscillation by varying tension, cross section, and forcing frequency is also easy as there are many different standing wave patterns with nodes in the centre that can be found by gradient-following. The situation changes, however, when asked to minimise the string displacement at a shifted position, say 2 cm away from the middle. If gaining sufficient problem understanding for an analytical solution is impossible or impractical, then many standing wave patterns have to be tried experimentally or by simulation, i. e. via numerical experiment.

The difficulty level of function minimisation problems depends on (a) the existence of local minima (uni-/multimodal), (b) the number of dimensions, (c) separability (sequential 1D-minimisation along coordinate axes possible?), (d) whether there is structure in the distribution of minima, (e) the existence of cliffs, (f) noise, (g) neutral plateaus, and (h) the relation among attractor sizes (what percentage of the search space funnels into the deepest valley(s)?).

Designing a liquid filled structure which can exhibit a vibration mode allowing the maximisation of the sound pressure amplitude of a standing acoustic wave in the liquid can be easy or hard. In the case of a spherical vessel it is a simple 1D problem of matching the masses and stiffnesses of liquid and solid. But if the geometry becomes more complex, if the number of subsystems in coupled oscillation increases, if the number of masses and stiffnesses multiplies, then the parameter tuning problem becomes harder. Then, simulations for exploring the design space are needed to support the design process, and efficient global optimisation algorithms can be of great help to make this exploration much more goal-oriented.

1.2 Background: the sonofusion experiment

When cavitation bubbles implode, then the bubble's noncondensable gas content is being compressed in the final phase of implosion. At the end, the kinetic energy from the surrounding liquid is transformed into potential energy and concentrated in a tiny amount of gas. If the surface tension manages to conserve the spherical symmetry, then this energy concentration mechanism is capable of raising the energy density by many orders of magnitude above the initial level of the sound wave in the liquid. In fact, the compression-heated gas can turn into light-emitting plasma, an effect which is called *sonoluminescence (SL)*. Where is the limit of this energy concentration mechanism? Could fusion conditions be reached? Could SL become *sonofusion (SF)* [6, 11, 12]? This debated question has too often been asked in the form: "Who will be the first to achieve thermonuclear fusion on the tabletop?". Perhaps it could be more fruitfully put this way: Any SL experiment turns into an SF experiment when deuterium is added to the liquid up front and neutron and tritium detection to the backend. This simply adds one more signal channel to the otherwise sparse data available for characterising SL plasma.

In a cooperation of the Institute of Nuclear and Energy Technologies (IKET) at the Karlsruhe Institute of Technology (KIT) with the Department of Mechanical, Aerospace, and Nu-

clear Engineering (MANE) at the Rensselaer Polytechnic Institute (RPI) the question has been addressed why the resonators used for the SF experiments of Taleyarkhan et al. [11, 12] are not reproducible with reliable performance and how better resonator designs can be proposed so that the acoustic pressure is maximised and reproducible manufacturing becomes possible. In order to do this, forced-harmonic finite element (FE) analyses of the piezo-driven and liquid-filled acoustic resonators have been subject to parameter tuning with global (GS) and local search (LS) methods like EAs and the downhill-simplex method.

2 EVOLUTIONARY ALGORITHMS (EA) FOR REAL-WORLD PARAMETER TUNING PROBLEMS

When using a blackbox optimiser, a list of tuning parameters $\vec{x} \in \mathbb{R}^n$ (or¹ $\in [0, 1]^{n \cdot m}$) is called chromosome or genotype representation of a candidate solution. In real-world applications the phenotype representation of the genotype solution \vec{x} is often a sequence of simulation and postprocessing from which a scalar quality measure $f_{\text{obj}}(\vec{x})$ is distilled. The blackbox optimiser ignores any intermediate phenotype features and merely deals with the response f_{obj} . Deciding to treat a real-world problem with a blackbox optimiser means favouring the advantage of being able to use a generic algorithm of known features over the advantage of being able to leverage detailed phenotype information and human problem understanding during the automated optimisation run. The latter has to be shifted up front (intelligent problem setup and parametrisation for making the task principally (and perhaps efficiently) solvable) which represents an effort, and it may also be used afterwards (learning from solutions found by the optimiser which were undiscovered by previous approaches) which represents another benefit.

2.1 Historic and state-of-the-art EAs

In the 1950s and 60s both things were new and emerging: the knowledge about the substance carrying genetic information in living beings and computer programs made of zeros and ones. It inspired researchers both ways, some wanted to simulate evolution to prove assumptions of how it works in nature, i. e. see how a generation cycle of repetitive random mutation and recombination operations can turn random code of symbols into meaningful code, whereas others wanted to derive efficient optimisation routines for technical real-world problems. Some of these works went far beyond their time in their wide conceptual scope and sophisticated implementations (e. g. [2, 7]). From the 1970s on, two somewhat more narrowly framed EA paradigms, evolution strategies (ES) and genetic algorithms (GA), gained popularity. The good thing about them is that they allow exemplary understanding of several important properties and features of EAs like *gene pool diversity*, *selection pressure*, *exploitation vs. exploration*, or thinking about the geometry of mutation operations, the genotype population, and f_{obj} .

In a classic **genetic algorithm (GA)** the search is coordinate system-dependent because most mutation steps are parallel to coordinate system axes and because component-wise recombinations of two candidate solutions \vec{x} and \vec{y} can only reach the corners of axis-aligned cuboids. GAs stall on diagonal valleys and are often inefficient on nonseparable problems. However, they show the meaning of gene pool diversity and recombination: in many real-world problems not each parameter is heavily coupled with each other parameter; e. g. when subsets of parameters belong to components of a system to be optimised, like the components of a power plant, then it makes sense to try component-wise recombinations of solutions created by re-

¹in a binary instead of real-coded setup when n parameters are coded with m bits each

combination operators like n -point crossover. The exploration-exploitation conflict appears as the difficulty to choose a good mutation probability: only the mutation operator creates new information, but if its activity is too high, good information is too often destroyed and cannot accumulate in the gene pool.

Classic **evolution strategies (ES)** can teach different lessons: that mutation operators have to be seen as distributions, that the population acts as a low-pass filter scanning for large-scale gradients under small-scale noise, that not all random number distributions retain their shape when the dimension is increased, how self-adaptation can lead to case-sensitive convergence behaviour, and that a local search algorithm can perform a global search when damped self-adaptation leads to the right speed of sinking down from larger to smaller scales in the genotype space. The shortcomings of classic ES are their poor global search power.

Modern EAs are able to lessen or avoid these shortcomings by making creative use of the grown toolbox of mutation and recombination operators and by inventing new ones. In the spirit of [2] they constructively go beyond mere abstractions of nature’s EAs. The most performant modern ES, **CMA-ES** [4], adapts its mutation operator in the form of an arbitrarily rotated and stretched multivariate normal distribution (MVN) based on analysing genotype population statistics (instead of mutation & inheritance) and with the result that the population cloud moves and stretches like an amoeba. Another modern EA is **differential evolution (DE)** [10]. It creates a similar tendency of amplifying deviations of the genotype population from the spherical shape by adding vector differences of two population members to a third one. This operation is coordinate system-independent. At the same time, a GA-style component-wise crossover operator acts on each each new chromosome. A third example of the state of the art is **particle swarm optimisation (PSO)** [5] where movements of orbiting particles are modelled through inertia, friction, and attraction. The orbit attractors are stored high-quality solutions once encountered by the swarm (exploitation) while inertia and randomness push exploration. PSO searches more globally when multiple attractors are kept active by not communicating them throughout the full swarm. Similar to the problem of dwindling gene pool diversity in GAs, PSO would have the issue that orbital planes are restricted subspaces of the search space. Therefore, the particle motions are randomised out of the orbital planes.

Hybridising EAs is a way to combine yet more operators and their effects. One goal is to make the algorithm more robust by damping the negative effect if particular operations lead to drag in certain landscapes. Another goal is to increase efficiency, assuming that it can be beneficial if the genetic material produced by one scheme is fed into the next one.

2.2 A simple hybrid EA scheme

The developed in-house hybrid EA [8] can be called tier-based hybrid EA (THEA) as each offspring population is created in five tiers or segments whereby these segments represent ES-, GA-, and DE-like EA paradigms. $\mathcal{P}_g = \{\vec{x}_i\}$ is the evaluated and sorted parent population. The offspring population of same size is initialised and divided into five segments or tiers $\mathcal{P}_{g+1} = \{\mathcal{P}_{elite}, \mathcal{P}_{mutants}, \mathcal{P}_{fp-mutants}, \mathcal{P}_{CO}, \mathcal{P}_{DE}\} = \{\vec{x}'_1, \dots, \vec{x}'_{n_1}, \vec{x}'_{n_1+1}, \dots, \vec{x}'_{n_4}, \vec{x}'_{n_4+1}, \dots, \vec{x}'_N\}$, where $n_1 = N_{elite}$, the size of the first tier, $n_2 = N_{elite} + N_{mutants}$ and so on. The offspring generation loop iterates in the following manner: for i in $1, 2, \dots, N$:

- **if \vec{x}'_i in 1st tier (“elite”):** Copy \vec{x}_i , leave the best chromosome \vec{x}_1 untouched, mutate the others weakly (isotropic mutation step distribution, i. e. ES-style).
- **if \vec{x}'_i in 2nd tier (“mutants”):** Copy \vec{x}_i and mutate each vector component with a probability $P_{mut} < 1$ (GA-style: not all components are mutated).

- **if \vec{x}'_i in 3rd tier (“free parent choice mutants”):** Randomly choose one parent \vec{x}_k , copy it, and mutate (GA-style). The random choice is an exponential distribution favouring better parents (GA-style: also the worst can be chosen).
- **if \vec{x}'_i in 4th tier (“CO-bunch”):** Randomly choose (with exponential selection pressure) two numbers $k, l \in [1, N]$, ($k \neq l$) and form the chromosome \vec{x}'_i by recombining \vec{x}_k with \vec{x}_l . This means using a crossover (CO) operator like in genetic algorithms (GA). The two CO operators are uniform CO and line recombination with subsequent isotropic mutation. A GA-style mutation with damped step size follows.
- **if \vec{x}'_i in 5th tier (“DE-bunch”):** Randomly choose three different parents $\vec{x}_k, \vec{x}_l, \vec{x}_o$ to treat them as in DE. \vec{x}_k is chosen with selection pressure, the others without. The difference vector $\vec{x}_o - \vec{x}_l$ is scaled with a random number $\in [0.2, 0.8]$ and added to \vec{x}_k . The CO-step is skipped. A GA-style mutation with damped step size follows.

The advantage of the segmented offspring generation is the flexibility to tune the EA blend. One can smoothly fade between extreme cases (e. g. $N_{CO} = N$ is a pure GA) and all kinds of mixtures allowing to either find the most robust blend or to tune to test problems representing a relevant problem class. Since the underlying assumption is that chromosomes generated in one segment are beneficial input for others, only larger population sizes between $40 \leq N \leq 100$ have been used on the resonator tuning task with 10-40 free design parameters. THEA incorporates no self-adaptive features. The only time-varying state variable is a general mutation step size parameter σ which decays exponentially over time. The forced convergence at a fixed rate (as in simulated annealing) is seen as a practical advantage when confronted with a time-consuming simulation to optimise (no risk of premature or delayed convergence).

2.3 Test problems for tuning, benchmarking, and choosing algorithms

Computationally slim test problems enable easy evaluation and benchmarking of blackbox optimisers which is needed during algorithm development and also by prospective applicants for decision making. In order to make a correct choice for the EA tuning of SF resonators, three test problems have been selected as representative and relevant: the Genitor F101 function [13], the CEC-2011 FM-synthesis problem [3], and the charged marble problem [9]. The functions are smooth, multimodal, and they have only weak structures in their distributions of minima. 400 random-initialised optimisation runs were conducted on each problem. Each run included 9600 function calls by the EA and a budget of 400 evaluations for finishing off with local search (downhill-simplex). THEA was compared with CMA-ES and PSO. Table 1 shows the pairwise comparison of the resulting statistics with the Wilcoxon signed ranks test. In agreement with that data, both CMA-ES and THEA but not PSO have been applied to tuning the resonator FE model.

3 OPTIMISED RESONATOR GEOMETRIES

The resonator design used in [11] was rebuilt several times with small variations by the cooperating team at RPI. It is based on manually manufactured glass parts and manual assembly and proved to be very sensitive. Subsequent FEM simulation of this design at IKET and a sensitivity study conducted on the FE model showed that the sensitivity can be explained by the large manufacturing tolerances. The goal of the current project was to propose a resonator redesign with

Table 1: Wilcoxon signed ranks test on EA statistics

The nonparametric Wilcoxon signed ranks test has been applied to statistics of 400 EA+LS runs per algorithm on three selected test problems. The listed p -values indicate the probability of the null hypothesis to be valid, i.e. that the samples come from the same distribution. The comparisons have been declared a tie if $p > 0.1$. The three competing setups of CMA-ES are (A) an own implementation based on Hansen’s educational code “baremaes.py” (<https://www.lri.fr/~hansen/>), (B) his performance code in Python, and (C) the latter with population size-doubling random restarts [1]. The PSO versions are (A) the implementation by Marcel Caraciolo (<https://github.com/marcelcaraciolo/pyppo>) with $c_1 = c_2 = 2.05$, and (B) an own implementation with $\alpha = 0.7298$ and $\psi = 2.9922$ and local neighbourhood degree 2. All population sizes were set to 80 except CMA-ES-C starting with 10.

	CMA-ES-A	CMA-ES-B	CMA-ES-C	PSO-A	PSO-B
charged marbles (8D)					
THEA wins?	win	win	win	win	tie
p -value	7.33e-21	1.66e-14	5.01e-17	1.41e-14	2.39e-01
FM-synthesis (6D)					
THEA wins?	tie	defeat	win	tie	win
p -value	9.72e-01	5.02e-02	7.80e-05	5.06e-01	4.69e-21
F101 (10D)					
THEA wins?	win	defeat	win	win	win
p -value	1.80e-05	4.79e-09	1.93e-09	4.70e-33	4.39e-62

much smaller manufacturing tolerances by making precision-machining of the assembly parts possible. The goal is a high- Q system providing a resonance with strong sound pressure amplitude for a given driving voltage while at the same time avoiding elevated sound pressures near fluid-structure interfaces. Only centrally positioned bubble clusters can implode symmetrically. Bubbles in other places destroy the sound field. The function f_{obj} to minimise is thus $-p_{max}$ on the central axis with a penalty on elevated wall pressure ratios $r_{wp} = p_{max}/p_{wall}$. As f_{obj} is highly multimodal, any new geometry needs to be parametrised and globally optimised in order to be properly evaluated. Figure 1 shows a proposed resonator geometry overcoming many of the shortcomings of the old design. It is displayed in two versions corresponding to two global optimisation results. The first run yielded the design with $p_{max} = 81$ bar and $r_{wp} = 0.30$. In order to search for solutions with lower r_{wp} the penalty has been raised for two more optimisation runs. The first was a local search starting from the old solution which couldn’t substantially lower r_{wp} . The other run, a new global search, yielded the design depicted in the lower row with $p_{max} = 32.6$ bar and $r_{wp} = 0.16$. 32.6 bar Seems quite low in comparison to 81, but it is still 30 % more than the p_{max} of the optimised FE model of the existing resonators (not shown here; driven by just one piezo ring; serving as reference for new designs). There are two limitations: if the p_{max} per driving voltage is too low, then heating due to elevated driving voltages will occur. If r_{wp} is too high, then beyond a certain voltage threshold cavitation on walls will occur while the pressure amplitude in the central region of interest is not yet high enough. Efficient cooling makes it possible to accept lower- Q resonators, drive them with higher voltage, and benefit from a low- r_{wp} layout. A renewed dedicated campaign of experimental resonator trials is necessary to explore the tradeoffs between p_{max} , r_{wp} , and heating. Simulation-based optimisation techniques help understand the tradeoffs and guide experimental work.

4 CONCLUSION

Designing new resonators for SF experiments involves a hard parameter tuning problem. Comparing design points without pre-optimisation makes little sense. With local search techniques performant resonator setups can only be found with a lucky starting point. Yet, with

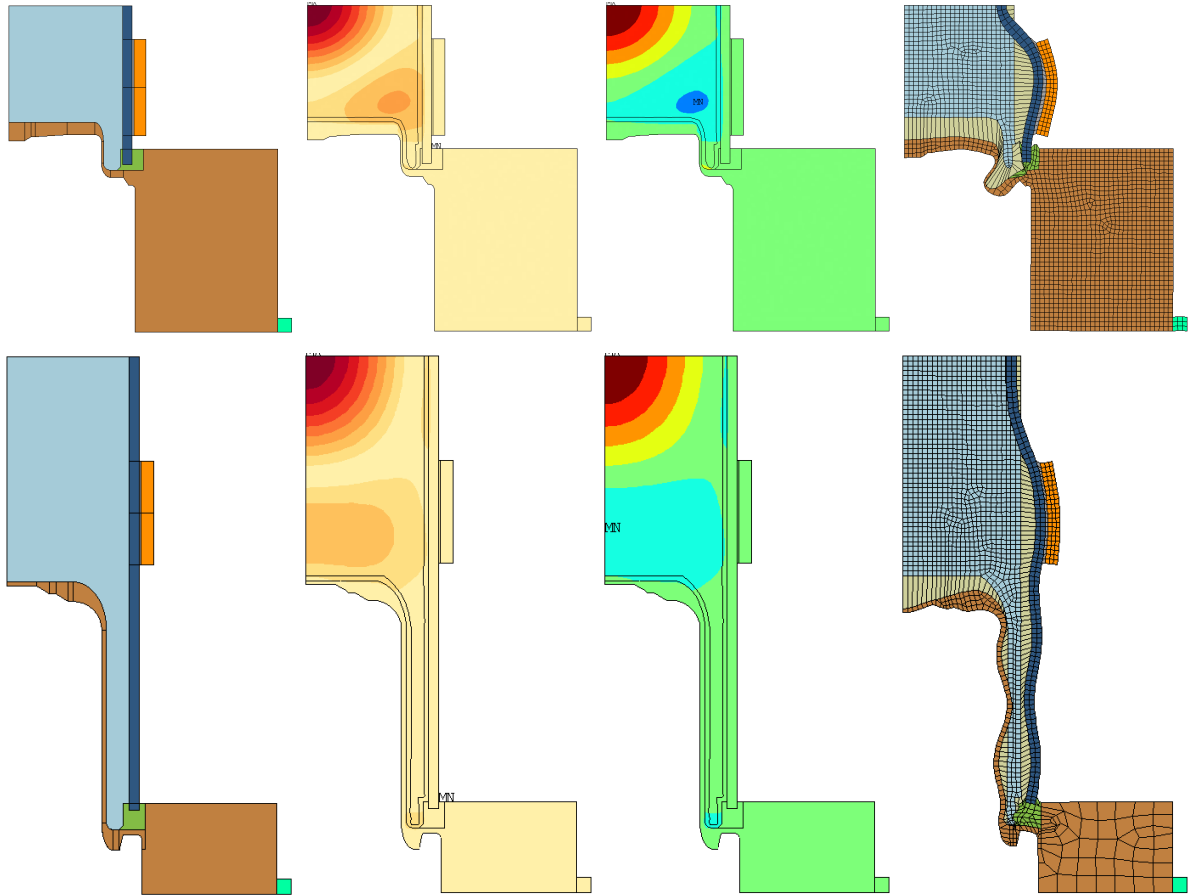


Figure 1: Optimised resonator geometry

Two optimised resonator designs are shown. As the FE model (Ansys[®] Mechanical APDL) is 2D-axisymmetric and has a horizontal symmetry plane, only a quarter of the cross section is shown. The materials are glass (blue), aluminium (brown), acetone (light blue), piezo driver (orange), silicone (green), soft fixation (cyan). The four picture types from left to right are: geometry, pressure amplitude, pressure snapshot (red – pressure, blue – tension), and deformed mesh (displacement scaling = 800). Both designs are the results of random-initialised global searches with THEA and subsequent downhill-simplex local search on the same base geometry and parametrisation. The only difference is the threshold setting for where the smooth wall pressure ratio-based penalty function sets in. The EA run leading to the upper design was with $N = 80$ over $G = 30$ generations followed by 960 iterations of the downhill-simplex (DS) algorithm. The second EA run was over $G = 39$ generations and 600 DS iterations. The scanned frequency intervals were 16-24 kHz in the first and 18-28 kHz in the second case for the EA search; LS was allowed to shift the range. The found working points are at $f = 25.9$ kHz, $p_{\max} = 81$ bar, $r_{\text{wp}} = 0.30$ and $f = 20.9$ kHz, $p_{\max} = 32.6$ bar, $r_{\text{wp}} = 0.16$, respectively. The higher wall pressure ratio of the upper design is mirrored by the existence of the elliptical dark blue region in the pressure snapshot. It has the same close distance from the surfaces of piston and glass wall. In the course of the local search the maximum pressure on the two surfaces becomes equal. Since LS starting on the upper design with the sharpened penalty could not reduce r_{wp} and since the resonator had to become longer to host more antinodes along the central axis, it can be inferred that it was necessary to give the sound field more room to decay towards the pistons and that the change in the mode shape involves surmounting a hill in f_{obj} .

an efficient global optimiser at hand the iterative development cycle towards deeper problem understanding and better resonator designs becomes quicker and much more systematic. EA hybridisation is a way to incorporate and combine lessons learnt from historic paradigm-driven EA approaches. Segmentation of the offspring population is a simple hybridisation approach offering the advantage of flexible EA blending ratios.

REFERENCES

- [1] A. Auger, N. Hansen: A restart CMA evolution strategy with increasing population size: Proc. IEEE Congress on Evolutionary Computation (2005), pp. 1769–1776.
- [2] H. J. Bremermann: Numerical optimization procedures derived from biological evolution processes. *Cybernetic Problems in Bionics* (1968), pp. 597–615.
- [3] S. Das, P. N. Suganthan: Problem Definitions and Evaluation Criteria for the CEC 2011 Competition on Testing Evolutionary Algorithms on Real-World Optimization Problems. Tech. Rep., Jadavpur University (2010).
- [4] N. Hansen, A. Ostermeier: Completely Derandomized Self-Adaptation in Evolution Strategies. *Evolutionary Computation* **9** (2001), pp. 159–195.
- [5] J. Kennedy, R. Eberhart: Particle swarm optimization. Proc. IEEE International Conference on Neural Networks (1995), pp. 1942–1948.
- [6] R. I. Nigmatulin, I. Sh. Akhatov, A. S. Topolnikov, R. Kh. Bolotnova, N. K. Vakhitova, R. T. Lahey Jr., R. P. Taleyarkhan: Theory of supercompression of vapor bubbles and nanoscale thermonuclear fusion. *Physics of Fluids* **17** (2005), p. 107106.
- [7] J. Reed, R. Toombs, N. A. Baricelli: Simulation of biological evolution and machine learning: I. Selection of self-reproducing numeric patterns by data processing machines, effects of hereditary control, mutation type and crossing. *Journal of Theoretical Biology* **17** (1967), pp. 319–342.
- [8] M. J. Stokmaier, A. G. Class, T. Schulenberg, R. T. Lahey Jr.: Sonofusion: EA optimisation of acoustic resonator. *PAMM* **12-1** (2012), pp. 623-624.
- [9] M. J. Stokmaier, A. G. Class, T. Schulenberg: A hard optimisation test function with symbolic solution visualisation for fast interpretation by the human eye. Proc. IEEE Congress on Evolutionary Computation (2013), pp. 2251–2258.
- [10] R. Storn, K. Price: Differential Evolution A Simple and Efficient Heuristic for Global Optimization over Continuous Spaces. *Journal of Global Optimization* **11-4** (1997), pp. 341–359.
- [11] R. P. Taleyarkhan, C. D. West, J. S. Cho, R. T. Lahey Jr., R. I. Nigmatulin, R. C. Block: Evidence for Nuclear Emissions During Acoustic Cavitation. *Science* **295** (2002), p. 1868.
- [12] R. P. Taleyarkhan, J. S. Cho, C. D. West, R. T. Lahey Jr., R. I. Nigmatulin, R. C. Block: Additional Evidence for Nuclear Emissions During Acoustic Cavitation. *Phys. Rev. E* **69** (2004), p. 036109.
- [13] D. Whitley, S. Rana, J. Dzubera, K. E. Mathias: Evaluating evolutionary algorithms. *Artificial Intelligence* **85** (1996), pp. 245–276.

SECTION OPTIMIZATION AND RELIABILITY ANALYSIS OF ARCH-TYPE DAMS INCLUDING COUPLED MECHANICAL-THERMAL AND HYDRAULIC FIELDS

Tan Fengjie *, Tom Lahmer and Manju Gyaraganahalli Siddappa

*Institute of Structural Mechanics
Faculty of Civil Engineering, Bauhaus-University
E-mail: fengjie.tan@uni-weimar.de*

Keywords: Arch Dam, Section Optimization, Coupling Thermal and Hydraulics, Genetic Algorithm, Reliability Analysis

Abstract. *From the design experiences of arch dams in the past, it has significant practical value to carry out the shape optimization of arch dams, which can fully make use of material characteristics and reduce the cost of constructions. Suitable variables need to be chosen to formulate the objective function, e.g. to minimize the total volume of the arch dam. Additionally a series of constraints are derived and a reasonable and convenient penalty function has been formed, which can easily enforce the characteristics of constraints and optimal design. For the optimization method, a Genetic Algorithm is adopted to perform a global search. Simultaneously, ANSYS is used to do the mechanical analysis under the coupling of thermal and hydraulic loads. One of the constraints of the newly designed dam is to fulfill requirements on the structural safety. Therefore, a reliability analysis is applied to offer a good decision supporting for matters concerning predictions of both safety and service life of the arch dam. By this, the key factors which would influence the stability and safety of arch dam significantly can be acquired, and supply a good way to take preventive measures to prolong the service life of an arch dam and enhances the safety of structure.*

1 INTRODUCTION

Nowadays, more and more arch-dams have been built to protect from natural disaster, irrigate plants, generate electricity power, etc. The structure of an arch dam has the advantage of using upstream curvature to transfer water pressures to the basement on both sides of the valley, which means the stability of dam body relies on the reactive force from the basement of abutment instead of its own weight.

For arch dams, the main loads influencing the structure most are water loading, self-weight and fluctuation of temperature, which are main cases contributing to the deformation of arch dams. A proper method selected for shape optimization decides the efficiency of design process. With the development of heuristic algorithms [4-5], it became popular to apply this kind of optimization into shape optimization of structural design for its characters of global search.

Reliability analysis is involved to judge the structure after optimization and provides predictions of both safety and service life of the arch dam, which can supply a good way to take preventive measures to prolong, at the service life and enhance the safety of the dam body

2 SHAPE OPTIMAL DESIGN PROCEDURES

2.1 Description of the shape of arch dam

Generally, the function of upstream curve is assumed to be a cubic equation along height direction (z coordinate direction), which can be written in form of $y(z) = a_0 + a_1z + a_2z^2 + a_3z^3 \dots$. In order to solve this function, three height control points, $z = z_1, z_2, z_3$ are selected

$$\begin{aligned} y(z = 0) &= 0 \\ y(z = H) &= -\beta_2 t_b \\ \frac{dz}{dy}(z = \beta_1 H) &= 0 \end{aligned} \quad (1)$$

Where t_c, t_b are the width of dam crest and bottom; β_1, β_2 are coefficients obtained according to experiences. And the same procedure for acquiring the function of the sectional thickness, $T_c(z) = b_0 + b_1z + b_2z^2 + b_3z^3 \dots$, and a linear function is used to stand for the change of thickness, and the coefficients can be found by the following equations:

$$\begin{aligned} T_c(z = 0) &= t_c \\ T_c(z = H) &= t_b \end{aligned} \quad (2)$$

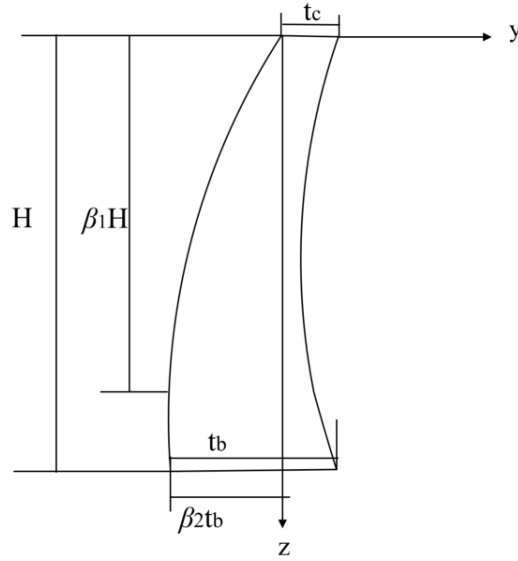


Fig1 Central Section of Arch Dam

2.2 Objective function

Generally, the objective function of the shape optimization is defined to ensure either minimal stresses of the structure or minimal volumes of dam body. In this case, for the sectional optimization, the objective function is determined by the minimum area of dam section:

$$f(\hat{\mathbf{x}}) = \text{area}(\hat{\mathbf{x}}) = \int |y_d(z) - y_u(z)| dz \quad (3)$$

By introducing exterior penalty terms, the objective function with constraints can be transferred to an unconstrained optimization problem.

$$F_{obj} = f(\hat{\mathbf{x}}) + \delta_k \sum_{i=1}^m [\max\{0, g_i(\hat{\mathbf{x}})\}]^2 \quad (4)$$

where $f(\hat{\mathbf{x}})$ is the cost function, $g_i(\hat{\mathbf{x}})$ is the i th constraint condition, lb, ub are respectively lower and upper boundaries of $\hat{\mathbf{x}}$ and δ_k are non-negative penalty factors. In this study, the variables defining the shape of arch dams section are $\beta_1, \beta_2, t_c, t_b$ which are included in the vector

$$\hat{\mathbf{x}} = [\beta_1, \beta_2, t_c, t_b]^T. \quad (5)$$

2.3 Constrained conditions

(1) Stress constraint

For the assurance of normal working during service life, the maximum stress of arch dam must be under allowed stress. Then, the stress constraint can be expressed as follows:

$$g_1 = \frac{\sigma_1}{[\sigma_1]} \leq 1 \quad (6)$$

$$g_2 = \frac{\sigma_3}{[\sigma_3]} \leq 1 \quad (7)$$

in which, g_i is the constraint condition, σ_1, σ_3 are respectively the maximum strain stress and maximum compressive stress.

(2) Geometric constraint

Generally, for any convenient construction, the geometrical constraints are expressed as the degrees of overhang on the upstream and downstream side, which is represented by 's'. According to [3], the principle degree of overhang [s] is 0.3, so, the geometrical constraint is:

$$g_3 = \frac{s}{[s]} \leq 1 \quad (8)$$

(3) Stability Constraint:

Any design for an arch dam must fulfil the slope stability requirements. Consequently, stability against sliding must be taken into consideration by introducing coefficients of sliding resistance, which are given by the sliding resistance K_i . The constraint condition can be written as:

$$g_4 = \frac{[K_i]}{K_i} \leq 1, \quad (9)$$

where the $[K_i]$ is the minimum allowable coefficient of sliding resistance for the i th point, and K_i is the coefficient of sliding resistance of i th point.

2.4 GA method of unconstrained minimization

The idea of GA [9] is to realize globally optimal designs in a given search region mimicking the procedure of natural selection. After randomly generating an original population, the next generation is produced by crossing over and mutation. New generations are formed from the last generation.

2.5 Coupled Thermo-Hydro-Mechanical Field Analysis

As the structural behavior of dams is visibly dominated by three fields - thermal, hydraulic and mechanical – we choose a coupled-analysis approach here. A coupled-field analysis is an analysis that takes into account the interaction between two or more disciplines of engineering. The procedure for a coupled/field analysis depends on which fields are being coupled, but two distinct methods can be identified: direct and sequential.

The couplings between the procedure of heat transfer, fluid flow and stress/deformation in porous geological media like concrete has become an increasingly important subject in many engineering disciplines. The two-way coupling process reveals continuing reciprocal interaction among different processes in a complex way, see Figure 2.

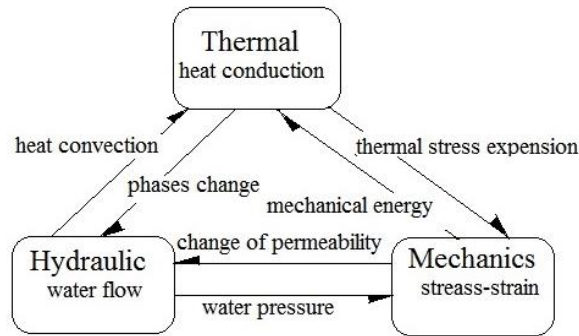


Fig2. Reciprocal Interaction among Different Process

3 NUMERICAL EXAMPLES FOR ARCH DAM SECTIONAL OPTIMIZATION COUPLING THERM–HYDRO -MECHANICS FIELDS

The example used in this paper is an arch dam with the height of 88m, density of 2355kg/m^3 , Young's modulus of $2.6\text{e}+10$ Pa, and the Poisson's ratio of 0.25.

The loads considered in the optimal procedure are: dead load, hydrostatic pressure on the upstream face and uplift pressure on the foundational interface. Besides, a realistic assessment of loading from water flow and temperature loading are also considered for the coupled response of shape optimization.

In order to create the shape of the arch dam, 4 proper shape design variables are selected to model the dam:

$$\left\{ \begin{array}{l} \hat{\mathbf{x}} = [\beta_1, \beta_2, t_c, t_b]^T \\ 0.6 \leq \beta_1 \leq 0.9 \\ 0.3 \leq \beta_2 \leq 0.6 \\ 3\text{m} \leq t_c \leq 10\text{m} \\ 10\text{m} \leq t_b \leq 55\text{m} \end{array} \right. \quad (10)$$

The first principal stress and third principal stress results of initial structure and optimized structure are shown in Figure 3a-d, and the summary of the comparison between initial and optimal structures are tabulated in the Table1. It can be observed that the area is reduced by 14.58% compared with the initial structure.

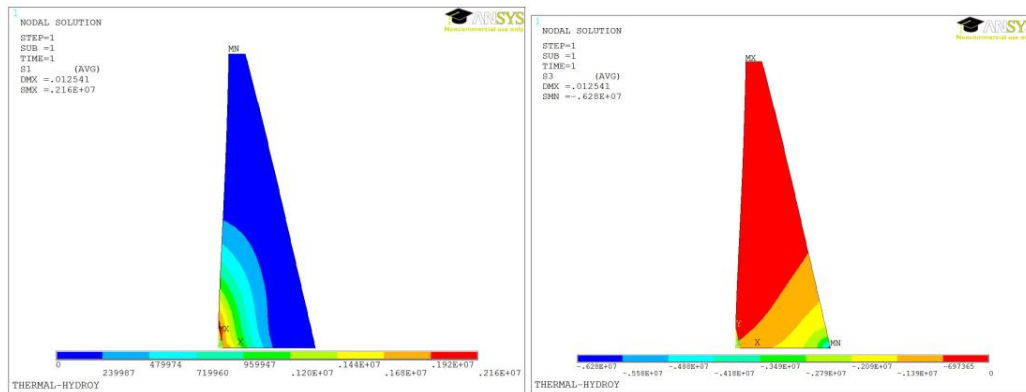


Fig3a. The First Principal Stress of Initial Dam

Fig3b. The Third Principal Stress of Initial Dam

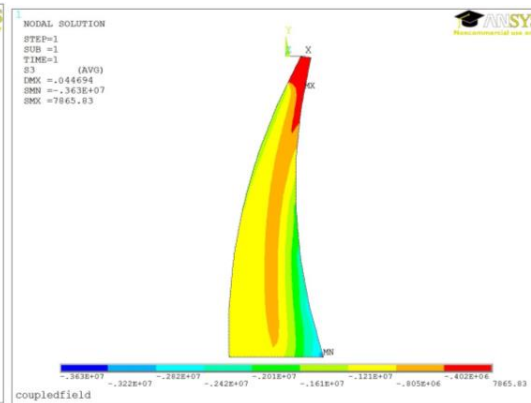
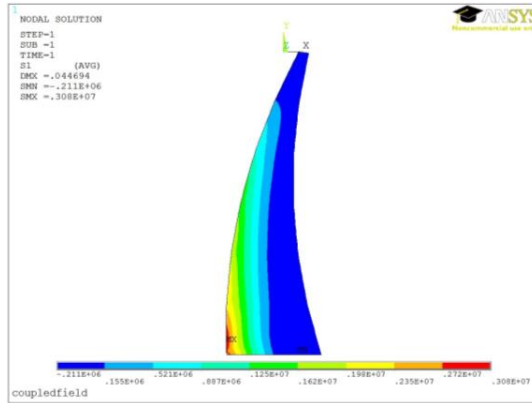


Fig3c. The First Principal Stress of Optimal Dam

Fig3d. The Third Principal Stress of Optimal Dam

Table 1. The Comparison of initial structure and optimal structure

	Height (m)	Width of dam crest (m)	Width of dam bottom (m)	Sectional area (m^2)	Max principal tensile stress (MPa)	Max principal compressive stress (MPa)
Initial	88	5	30	1540	2.16	6.28
Optimal	88	3	27.564	1344.826	3.08	3.63

4 RELIABILITY ANALYSIS

After optimization, a newly designed dam under constraint conditions is obtained to fulfill the requirements of structural safety. Therefore, a reliability analysis is taken to offer a decision supporting for matters on predictions of both safety and service life of arch dam. The most general method to solve stochastic problems in structural mechanics is the Monte Carlo method. The sampling selects the values of uncertain variables randomly according to their probability distribution functions. For a simple approach in structural reliability analysis, the sampling includes each random variable assigned randomly to a given sample value x_i and the limit state function $Z=g(\mathbf{x})$ is then checked. If the number of simulations is n , and among them, there are n_f times failed, according to Bernoulli theory, the frequency of random event $Z<0$ in the n -times independent experiments, $\frac{n_f}{N}$, converges to the failure probability. Therefore, the failure probability can be expressed as

$$\hat{P}_f = \frac{n_f}{N} = \int_{-\infty}^{+\infty} I[g_X(x)]f_X(x)dx = E\{I[gX(x)]\} \quad (11)$$

where the $I(x)$ is indicator function, and when $x<0$, $I(x)=1$, $x>0$, $I(x)=0$. With this, the estimated value of failure probability is:

$$\hat{P}_f = \frac{1}{N} \sum_{i=1}^N I[gX(x)]. \quad (12)$$

4.1 Reliability analysis results:

For the reliability analysis of the dam, the material properties values are used as random variables. The material properties will give the resistance to the structure. As the structure gets old there will be deterioration in structure due to change in the properties. The reliability analysis results are carried out respectively with Monte Carlo direct simulation and second order reliability method from the normal distribution with mean μ and standard deviation σ . The Table 2 shows the mean, standard deviation and probability distribution considered in this case, and Figure 4, 5 show the distribution of random variables.

Table 2. The Mean Standard Deviation and Probability Distribution

Description	Density of concrete (kg/m^3)	Modulus of Elasticity (MPa)	Probability distribution
Mean	2400	26000	Normal
Standard Deviation	240	2600	Normal

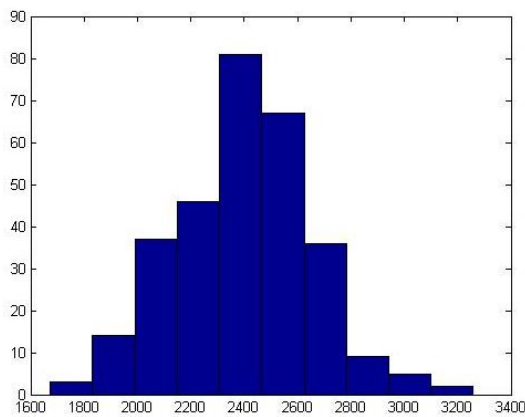


Figure 4. The Normal Distribution of Density

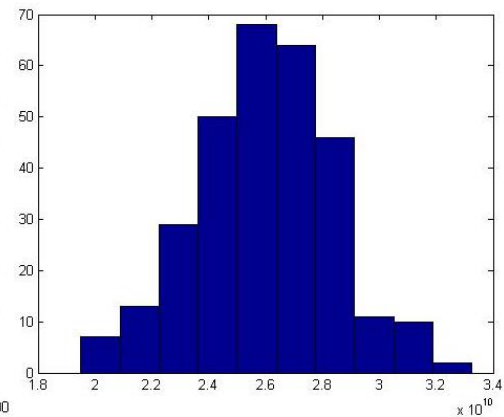


Figure 5. The Normal Distribution of Young's Modulus

Table 3. Reliability Analysis Results

	Reliability index β	Probability of failure P_f
Monte Carlo direct simulation	2.67	0.0036
Second Order Method	2.905	0.0033

5 CONCLUSIONS

A sectional optimization of an arch-type dam is carried out. The optimization is processed under a thermal-hydraulic-mechanical field analysis with the application of GA method. The area of the arch dam section was visibly reduced. The problem with the chosen GA method is that is a global search method, which would be very time consuming when the number of variables is raised. More suitable optimization techniques need to be applied and tested w.r.t their suitability.

The variation of temperature provides significant stresses due to thermal expansion. This effect may be taken stronger into consideration in further analyses. Due to the low permeability of concrete, the seepage field has very little effect on stress and deformations of structure. However seepage can cause significant stresses if the concrete is deteriorated.

REFERENCES

- [1] Y. W. CHUN, E. J. HAUG: Two-Dimensional Shape Optimal Design, International Journal for Numerical Methods in Engineering, 13, 311-336, 1978.
- [2] M. Kegl: Shape Optimal Design of Structures: An Efficient Shape Representation Concept, 49, 1571-1588, 2000.
- [3] Bofang Zhu, Bin Rao, Jinsheng, Jia, and Yinsheng Li: Shape Optimization of Arch Dams for Static and Dynamic Loads. J.Struct.Eng.118,2996-3015,1992.
- [4] S.M.Seyedpoor, J.Salajegheh: Adaptive Neuro-Fuzzy Inference System for High-Speed Computing in Optimal Shape Design of Arch Dams Subjected to Earthquake Loading, Mechanics Based Design of Structures and a Machines, 37,31-59,2009.
- [5] Omid Bozorg Haddad, Mahsa Mirmomeni, and Miguel A. Marino: Optimal Design of Stepped Spillways Using the HBMO Algorithm, Civil Engineering and Environmental Systems, 27,81-94,2010.
- [6] XiaoLi Zou: Reliability Analysis of Fatigue Crack Growth with JC Method Based on Scientific Materials, Applied Mechanics and Materials, 63-64, 882-885,2011.
- [7] Jalal Akbari, Mohammad Taghi Ahmadi, Hamid Moharrami: Advances in Concrete Arch Dams Shape Optimization, Applied Mathematical Modelling, 35, 3316-3333,2011.
- [8] Carsten Ebenau, Jens Rottschaefer, Georg Thierauf: An Advanced Evolutionary Strategy with An Adaptive Penalty Function for Mixed-Discrete Structural Optimization, Advances in Engineering Software,36, 29-38, 2005.
- [9] Rahul Malhotra, Narinder Singh, Yaduvir Singh: Genetic Algorithms: Concepts, Design for Optimization of Process Controllers, Computer and Information Science, 4, 39-54, 2011.

RULE BASED EXPANSION OF STANDARD CONSTRUCTION PROCESSES

H. -J. Bargstädt*, R. S. Tarigan

** Institute for Construction Engineering and Management
Bauhaus-Universität Weimar
Marienstrasse 7a, 99423 Weimar
E-mail: hans-joachim.bargstaedt@uni-weimar.de*

Keywords: Construction Management Knowledge, Decision Support, BIM.

Abstract. *The paper introduces a systematic construction management approach, supporting expansion of a specified construction process, both automatically and semi-automatically. Throughout the whole design process, many requirements must be taken into account in order to fulfil demands defined by clients. In implementing those demands into a design concept up to the execution plan, constraints such as site conditions, building code, and legal framework are to be considered. However, complete information, which is needed to make a sound decision, is not yet acquired in the early phase. Decisions are traditionally taken based on experience and assumptions. Due to a vast number of appropriate available solutions, particularly in building projects, it is necessary to make those decisions traceable. This is important in order to be able to reconstruct considerations and assumptions taken, should there be any changes in the future project's objectives.*

The research will be carried out by means of building information modelling, where rules deriving from standard logics of construction management knowledge will be applied. The knowledge comprises a comprehensive interaction amongst bidding process, cost-estimation, construction site preparation as well as specific project logistics – which are usually still separately considered. By means of these rules, favourable decision taking regarding prefabrication and in-situ implementation can be justified. Modifications depending on the available information within current design stage will consistently be traceable.

1 INTRODUCTION

The objective of this research is to demonstrate theoretical possibilities in order to provide detailed specification supporting decisions making in construction projects. It is particularly concerning issues that have not been determined by clients and therefore designers and contractors are completely in charge at free disposal as contracting parties. Background of the research is based in the well-established facts in construction project, that thorough requirements are hardly specified by clients. In contrast, designers are often required to provide alternative solutions in a swift manner. In this case, decisions taken by expert designers are based on a long-term experience, the reasoning behind them are however often cannot continuously be traced by other parties. This leads mainly to problems during design and construction stage, since changes in such long period are unavoidable. Those changes often occur in terms of objective function of the project regarding quality, cost and schedule. Changes emerge furthermore within project constrain, in the design and the work preparation as well as during execution when responding the dynamic of site. Following this, on one hand contractors are hardly able to reconstruct considerations taken by designers during the design process. On the other hand, the lack of complete information typically requires the designers to utilize assumption as a temporary feasible solution. In this case, decisions taken by designer are traditionally based on partial knowledge as illustrated in Figure 1.

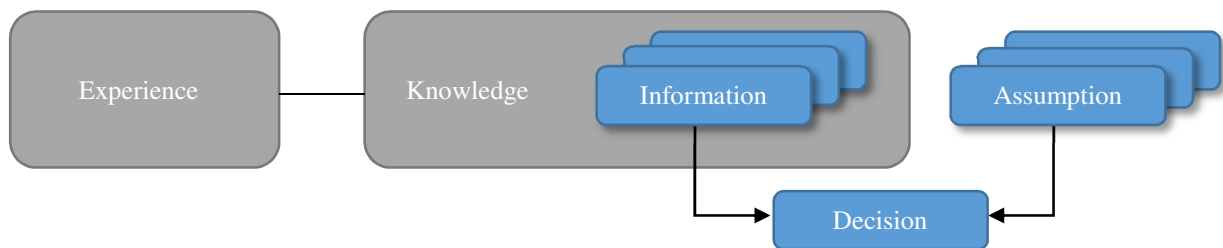


Figure 1: Decisions are traditionally taken based on experience and assumptions.

This paper is going to be compiled as follow: Section 2 will describe basic approach to classify construction management knowledge in regards to construction project delivery type and functional requirements of buildings. Hence Building Information Modelling (BIM) as current possible tool in transferring the knowledge will be proposed. Section 3 will present the concept of rules in expanding construction processes due to standard logic of construction management knowledge. Section 4 will expose examples on how simple construction management knowledge can be represented by means of additional information embedded within the BIM-design tool. Section 5 will draw conclusion and future works.

2 CLASSIFICATION OF CONSTRUCTION MANAGEMENT KNOWLEDGE

The main concern of how to enable traceability of the decisions taken during the early design process is to make the road map of a standard construction process accessible, where construction management knowledge is represented. This knowledge will be classified at different level of granularities, in order to support flexibility when choosing decision path through all different project stages. This is necessary, reflecting the facts that numerous execution alternatives exist, particularly in building construction projects. Hence, decisions and other alternatives should be kept available in transparent manner as a guideline through all different project phases. Furthermore the design elaborating process in such complex construction project is not carried

out sequentially from feasibility study up to execution planning anymore. It is common that during the early design phases, clients and designers have already had specific ideas regarding construction details. Those ideas are however hardly to be transformed in a traditional sequential service structure of architects and engineers, e.g. in Germany called “HOAI” [1] and in USA called “AIA” [2], where only the lowermost performance profile at each design stage is defined.

2.1 Construction Project Delivery Types

The inappropriate type of construction project delivery typically causes an expensive modification of the design and construction process. This fact requires therefore a consideration of project delivery type in early design stage. Hence, clients decide in which project stage contractors should have been involved, in order to engage construction management knowledge. In referring to this decision, designers should be aware of the consequent risks, since designers are not only liable for delivering design performance but also for warranting result to be brought of each design stage. In regards to HOAI, Table 1 illustrates several common types of project delivery [3][4], that make use of different design phase as working basis for contractors. In a traditional design process, designers for example prepare construction documents along with execution drawing; however this method is particularly suitable only for project delivery type number 1, since designers are solely liable for the constructability of the design. Contractor undertakes risks that only based on its own design such as in project delivery type number 4, 5 and 6. Problems occur traditionally at type 2 and 3, where contractors typically can neither rely on design nor on detailed specification provided by clients. The challenge of each project delivery type is how to coordinate interfaces throughout the design processes to be consistently traceable at the time of handover of the design to contractors.

Nr.	Procurement Method	Specification	Contractor Business Type	Working Basis
1	Design Bid Build	Detailed	Single Contractor	Phase 5
2	Design Bid Build	Detailed	General Contractor	Phase 5
3	Design Bid Build	Detailed	Partial General Contractor	Phase 5
4	Design Build	Functional	General Contractor	Phase 3, 4
5	Design Build	Functional	Partial General Contractor	Phase 3, 4
6	Design Build	Functional	Contractor led Design Build	Phase 1, 2

Table 1: HOAI-based working basis for contractor in several types of project delivery.

2.2 Functional Requirements of Buildings

Decision taken according to aforementioned type of project delivery is closely related to demand and desire of clients to be actively involved within design and construction phase. The more clients desire to undertake control of the project, the less designers and contractors are in charge at free disposal as contracting parties. This fact indicates the relevance of building typology, which is implied by its functional requirements. Should projects be procured through functional specification, it is important to consider prestigious aspect of the building, since then clients hardly influence the design anymore. In regards to HOAI, building typology is in general defined through several criteria and reference samples, for which demands on architects involved are described. Those criteria range from buildings that require minimal demands on the architect’s performance up to buildings that indicate extreme difficulties of the design process. Buildings which make minimal demands on the architect’s performance, for example multi-storey car parks, will be suitable for a design build procurement method. For such buildings with stringent requirements and complex interrelation like concert halls, detailed specification is legally needed.

2.3 Application of Building Information Modelling (BIM)

According to National Building Information Model Standard Project Committee [5], Building Information Modelling (BIM) is “*a digital representation of physical and functional characteristics of a facility. A BIM is a shared knowledge resource for information about a facility forming a reliable basis for decisions during its life-cycle; defined as existing from earliest conception to demolition*”. An application of BIM in context of construction management modelling is facilitated by so called parametric modelling, which refers to the relationship among all elements in a project model that enable change simultaneously and can be controlled both automatically by system and semi automatically by user. Moreover process integration can be enhanced through BIM, since parametric objects serve as knowledge container that can be used continuously throughout the design and construction stage.

3 RULES TO EXPAND CONSTRUCTION PROCESSES

In expanding construction processes, constrains arise from each type of project delivery types are firstly and foremost to be systematically identified. In order to make those constrains accessible to be considered by designers during design processes, information templates should be placed within semantic description. Hence construction management modelling serves as working templates, where designers and contractors can feed in knowledge. Rules that embedded in a logical formulas will control the automatic and semi-automatic expansion of the processes. A “what-if-scenario” will be applied. In regards to terms of contract, some decisions paths that are taken along with expansion possibilities cannot be reversed.

Furthermore patterns during construction process should be captured, in order to understand the semantic amongst trade work activities during construction process and subsequently be integrated within Building Information Model. Process patterns for example have been identified when generating a work plan schedule, so that some tasks can be automatically linked together as a work sequence, through rules. Those patterns refer to logical dependencies amongst the tasks such as technological constraints and available resources. However, there are dependence amongst some tasks, for example in a specific site condition, which should only be semi-automatically decided by authorized person [6].

Further approach in order to determine pattern of construction process can already be adopted. In infrastructure projects, working sequence is specifically defined by technological constraints amongst activities of machine and equipment. In building construction projects, particularly finishing trade works, constraints consist of rather on how to prioritize and organize tasks. That what is here known as soft constraints can be handled through weighting certain strategies of each trades work [7]. In combination with various dependency of logistic components, infinite number of strategies can be developed [8]. A more reliable decision support system in executing trades works is characterized by considering the multi-layer constraints [9], where working space and weather condition are additionally included. How to deal with all of those constraints is a representation of construction management knowledge, which can be used to trace decision that supposedly will be taken by contractor in the future.

A consideration of dynamic condition of the construction process in the early design process enables designer to compress specifically vast numbers of design solutions. The complexity of production site during construction process will be hence controllable. When designers understand how the works will be executed, that is to say the language of contractors, the intended

purpose of the building project as well as the proposed standard level of architecture, which represent the demand of clients, can be clearly articulated. Aforementioned considerations are even more crucial in order to procure building projects precisely in regards to meeting technical and quality requirements.

4 EXAMPLE

A simple demonstration of a parametric modelling of window type will be carried out by utilizing a BIM-geometric tool. Window`s utilization in a building is closely related to the type of façade that either opted by client, since they have already been used by or during previous projects; or selected by designer that has already had preferred supplier for the building products in the proposed design. During the design elaboration process, several considerations of the construction process are taken. For example the function of the façade, whether the load of the building is to be borne with it or not; that means the decision taken is simply either punctuated façade or non-punctuated façade. When load is not to be borne, further façade types such as post and rail façade, element façade, curtain wall, etc. are possible to be used. Additional construction aspect that needs to be considered is the side of assembly, whether the mounting process takes place from outside or inside of the building. This aspect will lead either to the requirement of the auxiliary component such as scaffolding or the machinery required such as forklift and crane.

When a punctuated façade is opted for, position and size of the wall opening are significant points for the windows to be mounted. Since loads are to be borne in this case and depending on the wall material, steel reinforcement in concrete wall for instance should be considered. It means there are constraints to be implied in regards to the wall opening in the course of windows design process. Following simple modelling demonstrates the relationship of those elements. Supposed that windows in a punctuated façade should be positioned at least 300 mm from the edge of the wall. The distance between windows should not be less than 600 mm. The height of the sill will additionally be determined as 1100 mm, when presumably that the wall is designed for an office function. For window type size 1100 mm x 1100 mm, a minimum wide space of the wall required is 2000 mm as illustrated Figure 2. These constraints will be applied as preconfigured parameters of a wall opening in a window class as illustrated in Figure 3.

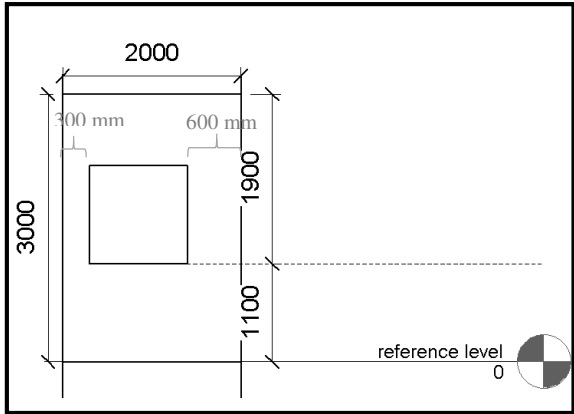


Figure 2: A window family consists of a 2000 mm wide wall and an opening inserted

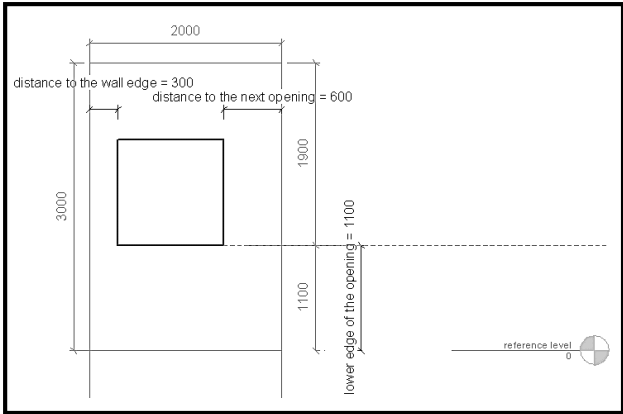


Figure 3: Distances of the opening in the wall-element are preconfigured as parameters

Moreover the wall opening can serve as a placeholder for subsequent detailing of the window. When standard details of some building elements are already acquainted in the early design stage,

it is possible to embed those details within model elements and treat them in several modes of view. In regards to HOAI and AIA, those different modes of building elements are available to be retrieved in every design stage to guide clients during design elaboration process.

5 CONCLUSION AND FUTURE WORKS

Well-structured and reasonable information is a basis of all reliable construction knowledge. A transformation of organized information into knowledge however can only be ensured by means of semantic description. Hence, to provide construction management knowledge as templates accessible for the design process, the corresponding logic and its parameters of construction management have to be aggregated in an appropriate semantic. This paper proposes a construction management modelling method, which will assist designers during the design process by integrating several construction process knowhow in building information model. The possibilities to expand construction processes through the modelling method are defined typically by constraints arise from construction project delivery type and functional requirements of the building. By using a simple geometric example it is demonstrated that several construction management parameters can be embedded in early design stage. This will be starting point for the future works to develop the construction management modelling method. It would hence to be expected, that those parameters and their interfaces are going to establish a logical consequence of the functionality, construction and form.

REFERENCES

- [1] Das Bundesministerium der Justiz und für Verbraucherschutz, HOAI 2013, [July 01, 2015], http://www.gesetze-im-internet.de/hoai_2013/.
- [2] The American Institute of Architects, Guide, Instructions and Commentary to the 2013 AIA Digital Practice Documents, [July 01, 2015], <http://www.aia.org/contractdocs/AIAB095713>.
- [3] U. Bauch, H.-J. Bargstädt, Praxis-Handbuch Bauleiter: Bauleistungen sicher überwachen ; mit 21 Tabellen, Müller, Köln, 2015.
- [4] H. Rosenheinrich, Entscheidungshilfe zur Vergabestrategie von Hochbauprojekten, VDG, Verlag und Datenbank für Geisteswissenschaften, Weimar, 2003.
- [5] NBIMS-US, What is a BIM, [June 18, 2015], <http://www.nationalbimstandard.org/faq.php#faq1>.
- [6] S. Hollermann, H.-J. Bargstädt, Work Planning Based on a Building Information Model, in: Y.-C. Lin, S.-C.J. Kang (Eds.), CONVR 2012: Proceedings of the 12th International Conference on Construction Applications of Virtual Reality; November 1-2, 2012, Taipei Taiwan, Taiwan Univ. Press, Taipei, 2012, pp. 64–72.
- [7] U. Beißert, Constraint-basierte Simulation zur Terminplanung von Ausführungsprozessen: Repräsentation baubetrieblichen Wissens mittels Soft Constraints, Verl. der Bauhaus-Universität, Weimar, 2012.
- [8] J.K. Voigtmann, Simulation bauleistungsprozesse, 1. Aufl., Bauhaus-Universitätsverlag Weimar, Kromsdorf, 2014.
- [9] A. Elmahdi, H.-H. Le, H.-J. Bargstädt, Multi-Layer Constraint and Decision Support System for Construction Operation: A simulation framework for the exterior construction works in high rise building, in: SIMUL 2011 The Third International Conference on Advances in System Simulation, pp. 94–100.

IFC-BASED MONITORING INFORMATION MODELING FOR DATA MANAGEMENT IN STRUCTURAL HEALTH MONITORING

Kay Smarsly* and Eike Tauscher

Bauhaus University Weimar, Germany
Email: kay.smarsly@uni-weimar.de

Keywords: Monitoring Information Modeling, Structural Health Monitoring (SHM), Building Information Modeling (BIM), Industry Foundation Classes, Wireless Sensor Networks.

Abstract. *This conceptual paper discusses opportunities and challenges towards the digital representation of structural health monitoring systems using the Industry Foundation Classes (IFC) standard. State-of-the-art sensor nodes, collecting structural and environmental data from civil infrastructure systems, are capable of processing and analyzing the data sets directly on-board the nodes. Structural health monitoring (SHM) based on sensor nodes that possess so called “on-chip intelligence” is, in this study, referred to as “intelligent SHM”, and the infrastructure system being equipped with an intelligent SHM system is referred to as “intelligent infrastructure”. Although intelligent SHM will continue to grow, it is not possible, on a well-defined formalism, to digitally represent information about sensors, about the overall SHM system, and about the monitoring strategies being implemented (“monitoring-related information”). Based on a review of available SHM regulations and guidelines as well as existing sensor models and sensor modeling languages, this conceptual paper investigates how to digitally represent monitoring-related information in a semantic model. With the Industry Foundation Classes, there exists an open standard for the digital representation of building information; however, it is not possible to represent monitoring-related information using the IFC object model. This paper proposes a conceptual approach for extending the current IFC object model in order to include monitoring-related information. Taking civil infrastructure systems as an illustrative example, it becomes possible to adequately represent, process, and exchange monitoring-related information throughout the whole life cycle of civil infrastructure systems, which is referred to as monitoring information modeling (MIM). However, since this paper is conceptual, additional research efforts are required to further investigate, implement, and validate the proposed concepts and methods.*

1 INTRODUCTION

Civil infrastructure systems, such as bridges, roads and tunnels, are gradually deteriorating. In Germany, for example, an estimated amount of €7.2bn is missing every year that is required for maintaining existing civil infrastructure [1]. In order to assess the condition of civil infrastructure, structural health monitoring (SHM) systems are deployed to collect monitoring data, i.e. structural, environmental, and operational data. Different sensors, such as accelerometers, displacement transducers or temperature sensors, installed in the civil infrastructure systems are connected to (tethered or wireless) sensor nodes that forward the collected data sets to computer systems. With recent advances in embedded computing and microcontroller technologies, state-of-the-art sensor nodes are capable of intelligent on-board data processing enabling the sensor nodes autonomously processing, analyzing, and condensing the monitoring data in a fully decentralized manner [2]. SHM systems being composed of sensor nodes that possess so called “on-chip intelligence” are referred to as “intelligent SHM systems”, and the infrastructure system being equipped with an intelligent SHM system is referred to as “intelligent infrastructure” [3].

To facilitate efficient sensor data management, existing standards allow semantic modeling of sensor information (or sensor metadata), such as sensor type, sampling rate, location, or manufacturer [4-6]. However, with respect to intelligent SHM systems, sensor information is only a small subset of monitoring-related information [7]. Unlike sensor information, which primarily includes local information about single sensors, monitoring-related information includes, for example, information on the configuration and topology of the (tethered or wireless) sensor network, interaction protocols used, hardware specifications, monitoring strategies, or algorithms embedded into the sensor nodes. Although the trend of incorporating intelligent SHM systems into civil infrastructure systems, forming a coherent “intelligent infrastructure” unit, will continue to grow, semantic modeling and digital representation of monitoring-related information is still in its infancy. Specifically, the logics and coherences inherent to intelligent SHM systems – both tethered and wireless systems – cannot adequately be modeled using existing approaches. While building information modeling (BIM) technologies mature and become mandatory in many areas in building and construction industries [8], monitoring information modeling (MIM) has received little attention.

This conceptual paper discusses opportunities and challenges towards monitoring information modeling for intelligent SHM systems in civil engineering. The conceptual MIM approach proposed in this paper builds upon the widely used BIM standard, i.e. the Industry Foundation Classes (IFC) developed as an open data format for the exchange of building information. When implementing the proposed approach in prospective research efforts, it can be expected that the integration of monitoring-related information into existing IFC-based building information models enables a consistent digital representation not only of building information, but also of all relevant monitoring information about the SHM systems throughout the whole life cycle of the civil infrastructure system being monitored.

2 IFC-BASED BUILDING INFORMATION MODELING

Building information modeling, i.e. the integrated, object-based coordination of building information, has begun to emerge as a fruitful technology in various areas of civil engineering. Supporting interoperability and information exchange, BIM is mandatory in publicly-funded building projects in several European countries, such as the U.K., the Netherlands, Denmark, Finland and Norway, and – as recommended by the European Parliament – it will be mandatory in all EU member states by 2016 [8]. The use of BIM technology requires a continuous digital

workflow based on a common data format. In accordance with the ISO 10303 standard [9], which specifies a technology for model-based digital product data exchange, the Industry Foundation Classes (IFC) have been developed starting in 1994. In recent years, increasing attention has been paid to extending the IFC object model. Both in the scientific community and in engineering practice, it has been recognized that the possibilities of digitally representing building information using the existing IFC standard (IFC version 4) are very limited in several areas.

In IFC version 4, several aspects of sensor information can be mapped into the IFC object model. However, IFC version 4 primarily supports sensor types that are related to building automation systems. To map sensor information, the IFC entity `IfcSensor`, provided by the IFC object model, must be used [10]. An `IfcSensor` object is classified by assigning a predefined sensor type, which is provided by the enumeration `IfcSensorTypeEnum`. For sensors not predefined in `IfcSensorTypeEnum`, the sensor type `USERDEFINED` must be used; the sensor type must be specified by assigning an `IfcSensorType` object using objectified relations. In addition to sensor types, further sensor information can be mapped into the IFC object model, such as information about manufacturer and about sensor energy consumption using predefined IFC property sets. Some IFC property sets are applicable to all `IfcSensor` objects in general, while more specific sensor information is only applicable to predefined sensor types. Many sensor types relevant to SHM systems, such as accelerometers or strain gauges, are not predefined. Since these sensors must be mapped as user-defined types, applicable property set definitions are not available, which makes it difficult to store and to retrieve the sensor information [11].

In summary, IFC-compliant mapping of sensor information is possible in principal, but semantic mapping and digital representation of monitoring-related information is not supported in IFC version 4 (e.g. information on the configuration and topology of the sensor network, interaction protocols used, hardware specifications, monitoring strategies, or algorithms embedded into the sensor nodes). In particular, mapping monitoring-related information with respect to intelligent SHM systems, which include sensor nodes possessing on-chip intelligence, is not possible using the IFC standard. A major challenge when mapping such information are the dynamic logics inherent to intelligent SHM systems. Because the type of a sensor node is largely determined by its implemented logic, it is not possible to apply the standardized IFC object typing to intelligent sensor nodes and to the dynamic relationships between communicating sensor nodes. Consequently, it is necessary to extend IFC version 4 in order to be able to specify this logic (e.g. in terms of algorithms embedded into the sensor node) for modeling an intelligent sensor node as part of an IFC-compliant building information model. In the following section, a conceptual approach towards extending the IFC object model for semantic modeling of monitoring-related information is discussed.

3 A CONCEPTUAL APPROACH TOWARDS SEMANTIC MODELING OF MONITORING-RELATED INFORMATION

A semantic model supporting monitoring information modeling is to be developed, which will be integrated, in further steps, into the IFC object model, resulting in a monitoring-related IFC model labeled “IFC Monitor”. Focusing on civil infrastructure systems, the development of the semantic model is a three-step process comprising of (i) a review of available SHM regulations and guidelines, (ii) a review of existing sensor models and modeling languages, and (iii) the definition and classification of specific monitoring-related information relevant to intelligent SHM systems.

3.1 Structural health monitoring regulations and guidelines

In several countries, regulations and guidelines related to monitoring of civil infrastructure systems have been established. However, most regulations and guidelines promote “conventional” monitoring activities (such as visual inspections or non-destructive testing), rather than automated SHM activities. In Germany, for example, the DIN 1076 standard, first published in 1930, is the legal basis for monitoring and inspecting civil infrastructure systems [12]. For automated SHM activities, a number of guidelines has been proposed by several research groups, institutes, and committees. For example, the “Guidelines for Structural Health Monitoring”, proposed by the Intelligent Sensing for Innovative Structures (ISIS) Canada Research Center, provide practicing engineers with detailed guidelines for SHM systems [13]; a “Guideline and Recommendations for SHM” are proposed in a book chapter published by Wenzel [13]; the “FIB Bulletin No. 22” of the International Federation for Structural Concrete (FIB) summarizes the important inspection and measuring methods [14]; and the “Guideline for Structural Health Monitoring”, published by the Structural Assessment Monitoring and Control (SAMCO) network in association with the German Federal Institute of Materials Research and Testing (BAM), introduces SHM procedures and technologies and gives recommendations for their application [15].

3.2 Sensor models and modeling languages

A broad wealth of standards exists that enable semantic modeling of sensor information (or sensor metadata), such as sensor type, sampling rate, location, or manufacturer. For example, the Sensor Web Enablement (SWE) initiative of the Open Geospatial Consortium (OGC), an international consortium of industry, academic and government organizations, provides standardized web services and communication protocols for the web-based integration of sensors and sensor networks in order to make all types of sensors as well as sensor data repositories accessible via the Web. As a part of the SWE initiative, the Sensor Model Language (SensorML) provides a sensor information model and XML encodings for describing sensors and processes associated with sensor measurements [4]. To overcome the general problem of too much data and not enough knowledge, the semantic sensor Web (SSW) couples sensor technologies and semantic Web technologies [5]. Extending the SWE standards of the OGC with semantic Web technologies, the World Wide Web Consortium (W3C) has initiated the Semantic Sensor Networks Incubator Group (now transitioned into the Semantic Sensor Networks Community Group), which has defined an ontology for modeling sensors and sensor networks [6]: The Semantic Sensor Network (SSN) ontology can describe sensors in terms of capabilities, measurement processes, observations, and deployments. The SSN ontology covers large parts of the OGC standards (e.g. SensorML), i.e. it can interpret sensor metadata advertised in SensorML documents, but it is not constrained by the OGC standards.

Fig. 1 illuminates the SSN ontology in more detail. As can be seen from Fig. 1, the ontology enables the description of sensors, including their measuring capabilities and measuring properties (accuracy, resolution, response time, etc.), features of interest as well as the corresponding sensing processes. In addition, concepts for operating and survival ranges, often part of a given sensor specification, are included.

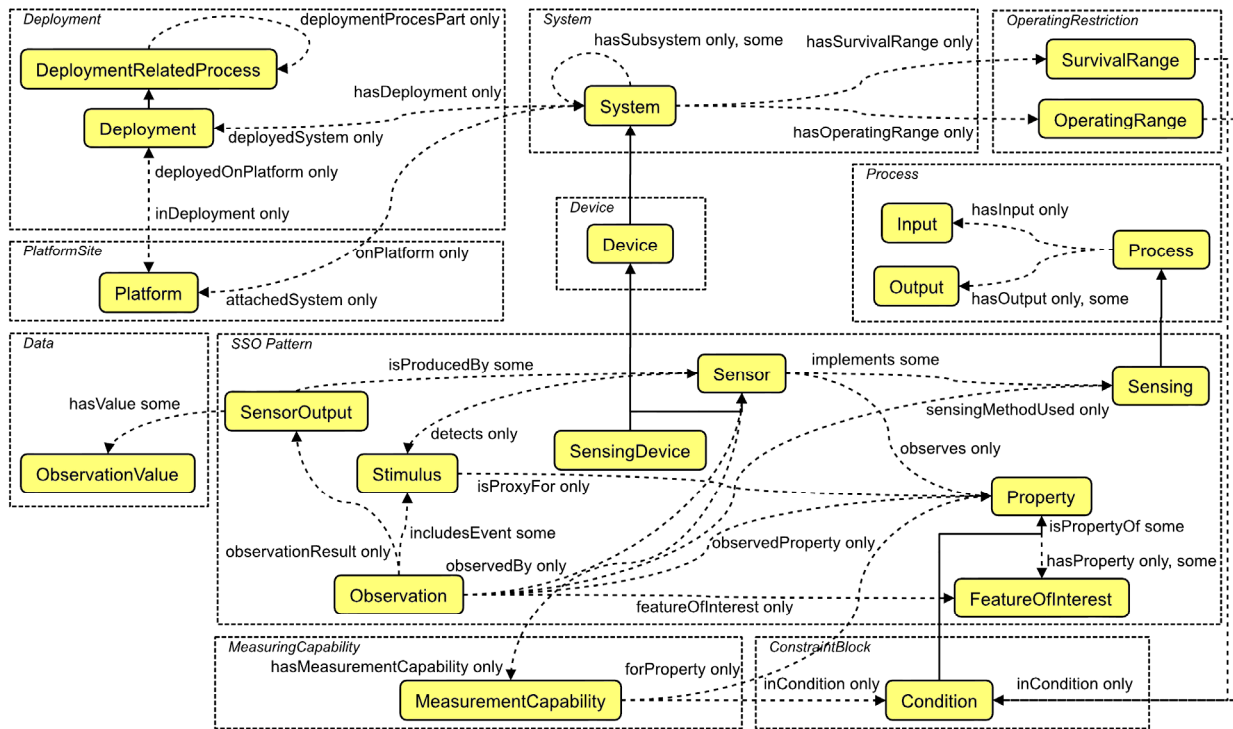


Figure 1: Classes and properties of the SSN ontology, subdivided by conceptual modules (source: [9], modified)

3.3 Monitoring-related information for intelligent SHM systems

Covering a plenitude of semantic modeling features, existing sensor models (or modeling languages) are truly useful for semantic modeling of sensors and sensor networks. While some monitoring-related information, such as hardware specifications, can be mapped by existing standards, it is not possible to map all aspects necessary to describe intelligent SHM systems. First, it is not possible to map the inherent, dynamic logics of intelligent sensor nodes that are implicitly specified by the algorithms embedded. Furthermore, it is not possible to map SHM-specific information on the configuration and topology of the (tethered or wireless) sensor network, interaction protocols used, or monitoring strategies implemented. In conclusion, these aspects must be defined and classified when developing a semantic model for mapping monitoring-related information. In order to define and clarify monitoring-related information, it is useful to distinguish between global and local monitoring-related information.

3.4 A conceptual approach towards IFC-based mapping of monitoring-related information

A conceptual approach towards defining a semantic model is proposed for mapping monitoring-related information based on the Industry Foundation Classes. The IFC Industry Foundation Classes are used to close the gap between sensor models and building information modeling, because the IFC are the most important standard for building information modeling in the construction industry. When defining a semantic model, particular emphasis is put on intelligent SHM systems deployed to civil infrastructure systems. As elucidated in the previous subsections, available SHM regulations/guidelines (subsection 3.1), existing sensor models/modeling languages (subsection 3.2), and specific monitoring-related information relevant to intelligent SHM systems (subsection 3.3) may serve as a conceptual basis. As shown in Fig. 2, a reference model, mapping the information stemming from existing SHM regulations/guidelines and sensor models/modeling languages, is to be generated. In addition, a monitoring-related model, representing the specific monitoring-related information, is to be

defined. In a further step, both models, the reference model and the monitoring-related model, are to be coupled in order to achieve a semantic model used to extend the existing IFC 4 object model. The extended IFC 4 object model, as shown in Fig. 2, is termed “IFC Monitor”, representing a monitoring-related extension of the existing IFC standard.

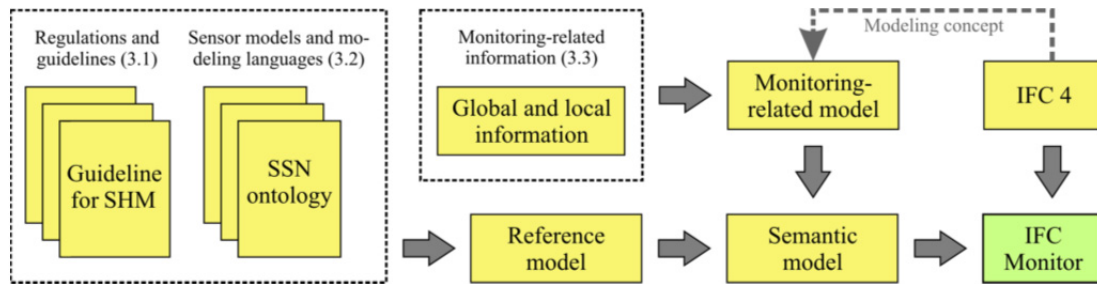


Figure 2: Conceptual approach towards IFC-based mapping of monitoring-related information

SUMMARY AND DISCUSSION

This conceptual paper has discussed opportunities and challenges towards monitoring information modeling (MIM) for intelligent structural health monitoring systems in civil engineering, focusing on civil infrastructure systems. The conceptual MIM approach proposed in this paper builds upon the widely used BIM standard, i.e. the Industry Foundation Classes (IFC) developed as an open data format for the exchange of building information. As has been showcased in this paper, several SHM regulations and guidelines as well as sensor models and modeling languages are available for semantic modeling and digital representation of sensor information. However, sensor information is only a small subset of monitoring-related information, which cannot adequately be modeled using existing standards. As illustrated in this paper, specific monitoring-related information relevant to intelligent SHM systems is defined and classified. The set of available SHM regulations/guidelines, existing sensor models/modeling languages and specific monitoring-related information serves as a basis to define a semantic model for digital representation of monitoring-related information. The semantic model, used to extend the existing IFC 4 standard, results in an extended IFC model, labeled “IFC Monitor”.

Since this paper is conceptual, additional research efforts are required to further investigate, implement, and validate the conceptual MIM approach proposed herein. It can be expected that implementing this conceptual approach into existing, IFC-based building information models would enable a consistent digital representation of all relevant monitoring information about the SHM systems throughout the whole life cycle of civil infrastructure systems, thus substantially enhancing the monitoring quality and the assessment of civil infrastructure.

REFERENCES

- [1] German Bundestag, 2014. Verkehrsinfrastruktur chronisch unterfinanziert. Press release. Berlin, Germany: German Bundestag, Committee on Transport and Digital Infrastructure. Available at: https://www.bundestag.de/dokumente/textarchiv/2014/49449197_kw07_pa_verkehr/215644 [Accessed: 28/05/2015].
- [2] K. Dragos and K. Smarsly, 2015. Decentralized infrastructure health monitoring using embedded computing in wireless sensor networks. In: Sextos, A. and Manolis, G. D.

- (eds.). *Dynamic Response of Infrastructure to Environmentally Induced Loads*. Cham, Switzerland: Springer International Publishing AG.
- [3] K. Dragos and K. Smarsly, K., 2015. A Comparative Review of Wireless Sensor Nodes for Structural Health Monitoring. In: *Proceedings of the 7th International Conference on Structural Health Monitoring of Intelligent Infrastructure*. Turin, Italy, 07/01/2015.
- [4] OGC, 2014. OGC SensorML: Model and XML Encoding Standard. Open Geospatial Consortium (OGC), Wayland, MA, USA.
- [5] A. P. Sheth and S. S. Sahoo, 2008. Semantic Sensor Web. *IEEE Internet Computing*, 12(4), pp. 78-83.
- [6] L. Lefort, et al., 2011. Semantic Sensor Network XG Final Report. W3C Incubator Group, World Wide Web Consortium (W3C), Cambridge, MA, USA.
- [7] K. Law, K. Smarsly and Y. Wang, 2014. Sensor Data Management Technologies for Infrastructure Asset Management. In: M. L. Wang, J. P. Lynch and H. Sohn (eds.). *Sensor Technologies for Civil Infrastructures*. Pp. 3-32. Woodhead Publishing, Ltd., Sawston, UK.
- [8] European Parliament, 2015. Directive 2014/24/EU of the European Parliament and of the Council. Brussels, Belgium.
- [9] ISO, 2014. ISO 10303:2014 – Industrial automation systems and integration - Product data representation and exchange. International Organization for Standardization (ISO), Geneva, Switzerland.
- [10] BuildingSMART, 2013a. Industry Foundation Classes Release 4 (IFC4). Documentation for 7.2.3.9 IfcSensor. March 12, 2013. Available at: <http://www.buildingsmart-tech.org/ifc/IFC4/final/html/link/ifcsensor.htm> [Accessed: May 20, 2015]
- [11] BuildingSMART, 2013b. Industry Foundation Classes Release 4 (IFC4). Documentation for 4.2.1 Property Sets for Objects. March 12, 2013. Available at: <http://www.buildingsmart-tech.org/ifc/IFC4/final/html/link/property-sets-for-objects.htm>
- [12] DIN, 1999. DIN 1076:1999-11 – Ingenieurbauwerke im Zuge von Straßen und Wegen - Überwachung und Prüfung. Normenausschuss Bauwesen (NABau) within the Deutsches Institut für Normung e.V. (DIN), Beuth Verlag GmbH, Berlin, Germany.
- [13] A. A. Mufti, 2001. *ISIS Design Manual 2: Guidelines for Structural Health Monitoring. Intelligent Sensing for Innovative Structures (ISIS)*, Winnipeg, MB, Canada.
- [14] H. Wenzel, H., 2009. *Guideline and Recommendations for SHM*. In: *Health Monitoring of Bridges*, John Wiley & Sons, Ltd, Chichester, UK.
- [15] FIB, 2003. FIB Bulletin No. 22 – Monitoring and safety evaluation of existing concrete structures. International Federation for Structural Concrete (FIB), Lausanne, Switzerland.
- [16] W. Rücker, F. Hille and R. Rohrmann, 2006. *Guideline for Structural Health Monitoring. Report “F08b”*. German Federal Institute of Materials Research and Testing (BAM), Berlin, Germany.

THE PROBLEM OF PARTIAL REINFORCING AN INTERFACE CRACK EDGE BY A RIGID PATCH PLATE UNDER IN-PLANE AND ANTIPLANE LOADS

Iu. Vasileva

Bauhaus-Universität Weimar
Coudraystrae 13B, room 205, 99423 Weimar, Germany
E-mail: yu.vasilyeva@gmail.com

Keywords: Interface Crack, Rigid Patch Plate, Riemann-Hilbert Matrix Problem, Stress Intensity Factors.

Abstract. *The stress state of a piecewise-homogeneous elastic body, which has a semi-infinite crack along the interface, under in-plane and antiplane loads is considered. One of the crack edges is reinforced by a rigid patch plate on a finite interval adjacent to the crack tip. The crack edges are loaded with specified stresses. The body is stretched at infinity by specified stresses. External forces with a given principal vector and moment act on the patch plate. The problem reduces to a Riemann-Hilbert boundary-value matrix problem with a piecewise-constant coefficient for two complex potentials in the plane case and for one in the antiplane case. The complex potentials are found explicitly using a Gaussian hypergeometric function. The stress state of the body close to the ends of the patch plate, one of which is also simultaneously the crack tip, is investigated. Stress intensity factors near the singular points are determined.*

1 INTRODUCTION

In recent years considerable attention has been focused on interfacial fracture problems with the replacement of conventional materials by a variety of composite materials. Interfacial defects, such as cracks, inclusions, pre-fracture zones and others, play an important role in the fracture behavior. Serious stress concentrations will arise near the ends of the defects, from which debonding, cracking, damage and so on may emanate. Therefore investigations on such defects are important for structural integrity assessments.

Several investigations on mixed plane and antiplane problems for homogeneous and piecewise-homogeneous elastic bodies with a cut have been conducted. Works by Popov G. [1], Cherepanov G. [2], Ballarini R. [3], Mkhitarian S., Melkounian N. and Lin B. [4], Hakobyan V., Dashtoyan L. and Hakobyan L. [5] and many others provide examples of recent contributions. The mixed problems considered in this paper differ from other problems in that the cut is located between two elastic materials and boundary conditions are of a different type: the stress vector on one part and the strain vector on another part, are specified on different parts of the same edge of the cut. The analytic solution of this problem is unknown in the case of a piecewise-homogeneous body.

2 IN-PLANE PROBLEM

Consider a piecewise-homogeneous elastic isotropic body that is modeled on the form of the plane $\zeta = x + iy$, composed of two half-planes $y > 0$ and $y < 0$ which are different in their properties. A semi-infinite open crack is located at the interface $y = 0$ of the media. The upper crack edge is partially reinforced by a rigid patch plate along the interval $0 \leq x \leq l$. The remaining part of the upper crack edge and the whole of the lower crack edge are loaded with given stresses. Boundary conditions of the problem have the form

$$\begin{aligned} u^+(x) + iv^+(x) &= s_1(x) + is_2(x) + i\varepsilon x, \quad x \in (0, l] \\ \tau_{xy}^+(x) + i\sigma_y^+(x) &= p_1^+(x) + ip_2^+(x), \quad x \in (l, +\infty) \\ \tau_{xy}^-(x) + i\sigma_y^-(x) &= p_1^-(x) + ip_2^-(x), \quad x \in (0, +\infty) \end{aligned} \quad (2.1)$$

where $u + iv$ is the strain vector, $\tau_{xy} + i\sigma_y$ is the stress vector, $s_1(x)$, $s_2(x)$, $p_1^\pm(x)$, $p_2^\pm(x)$ are given functions, ε is the angle of rotation of the patch plate. Superscripts plus and minus refer to the values of the functions on the upper and lower edges of the crack, respectively.

Along the ray $(-\infty, 0]$, the half-planes are joined such that, on crossing the joining line, the strain and stress vectors change continuously. The upper half-plane has a shear modulus μ_1 and a Poisson's ratio ν_1 , and the lower half-plane μ_2 and ν_2 , respectively. The normal longitudinal stresses σ_{x1}^∞ and $\sigma_{x2}^\infty = \sigma_{x1}^\infty \mu_2(1 + \kappa_1)/[\mu_1(1 + \kappa_2)]$ act at infinity in the half-planes $y > 0$ and $y < 0$, respectively. Here, $\kappa_j = 3 - 4\nu_j$ for plane strain and $\kappa_j = (3 - \nu_j)/(1 + \nu_j)$ ($j=1,2$) for plane stress state. The stresses σ_y^∞ and τ_{xy}^∞ vanish at infinity. The principal vector of the external forces acting on the patch plate and the moment of these forces about the crack tip are further specified. The stresses can have integrable singularities at the points $\zeta = 0$ and $\zeta = l + i0$.

It is required to define the stress state of the composite plane.

Due to the Kolosov-Muskhelishvili formulae for a piecewise-homogeneous plane [2] the stresses, the rotation and the displacements can be expressed in terms of two piecewise-analytic functions (complex potentials) $\Phi(\zeta)$, $\Omega(\zeta)$ in $\mathbb{C} \setminus [0, +\infty)$. Thus, boundary conditions (2.1) reduce to the matrix Riemann-Hilbert problem with a piecewise-constant coefficient for the

complex potentials:

$$\begin{pmatrix} \Phi^+(x) \\ \Omega^+(x) \end{pmatrix} = \begin{pmatrix} 0 & \kappa_1^{-1} \\ -m & -\alpha \end{pmatrix} \begin{pmatrix} \Phi^-(x) \\ \Omega^-(x) \end{pmatrix} + \begin{pmatrix} 2\mu_1\kappa_1^{-1}[s'(x) + i\varepsilon] \\ \beta_1 p^-(x) - 2\mu_1\kappa_1^{-1}\beta_2[s'(x) + i\varepsilon] \end{pmatrix}, \quad x \in (0, l)$$

$$\begin{pmatrix} \Phi^+(x) \\ \Omega^+(x) \end{pmatrix} = \begin{pmatrix} 0 & -1 \\ -m & 1 - m \end{pmatrix} \begin{pmatrix} \Phi^-(x) \\ \Omega^-(x) \end{pmatrix} + \begin{pmatrix} p^+(x) \\ \beta_1 p^-(x) - \beta_2 p^+(x) \end{pmatrix}, \quad x \in (l, +\infty)$$

$$m = \frac{\mu_1 + \mu_2\kappa_1}{\mu_2 + \mu_1\kappa_2}, \quad \alpha = \frac{\mu_1(\kappa_1 + \kappa_2) - 2\mu_2\kappa_1}{\kappa_1(\mu_2 + \mu_1\kappa_2)}, \quad \beta_1 = \frac{\mu_1(1 + \kappa_2)}{\mu_2 + \mu_1\kappa_2}, \quad \beta_2 = \frac{\mu_1\kappa_2 - \mu_2\kappa_1}{\mu_2 + \mu_1\kappa_2}$$

$$s'(x) = s'_1(x) + is'_2(x), \quad p^\pm(x) = p_2^\pm(x) - ip_1^\pm(x)$$

The functions $\Phi(\zeta)$, $\Omega(\zeta)$ are allowed to have integrable singularities at the points $\zeta = 0$ and $\zeta = l \pm i0$. They must be bounded at infinity.

The solution of the Riemann-Hilbert problem is found explicitly using a Gaussian hypergeometric function [6]. On the basis of this solution, the angle of rotation is obtained and the asymptotic of the stresses near the points $\zeta = 0$ and $\zeta = l \pm i0$ is studied. The stress intensity factors are defined.

The stresses close to the point $\zeta = l + i0$ behave in the same way as the stresses close to the tip of a stamp that is rigidly coupled with a medium [7]. Close to the point $\zeta = l - i0$ they are bounded.

The asymptotic of the stresses near the crack tip $\zeta = 0$ on the ray $(-\infty, 0]$ has the form

$$\sigma_y(x) - i\tau_{xy}(x) = \frac{K_I^2 - iK_{II}^2}{\sqrt{2\pi}|x|^{\gamma-i\delta_2}} + \frac{K_I^1 - iK_{II}^1}{\sqrt{2\pi}|x|^{1-\gamma-i\delta_1}} + O(1), \quad x \rightarrow 0 - 0 \quad (2.2)$$

where γ , δ_1 , δ_2 are constants which depend only on the elastic parameters of the composite plane, K_I^j, K_{II}^j ($j = 1, 2$) are the stress intensity factors. The parameter γ takes values from the interval $[1/2, 1)$ and there is a range of values of the elastic parameters for which $\gamma = 1/2$. If $\mu_2/\mu_1 > 0.124$ then the parameter $\gamma > 1/2$ and $\delta_1 = \delta_2$. In addition to described asymptotic (2.2), the stresses near the crack tip can also have singularities of the type $\zeta^{-1/2+i\delta} \ln \zeta$. The latter occurs in case of multiple eigenvalues of the matrix-coefficients of the Riemann-Hilbert problem.

3 ANTIPLANE PROBLEM

Consider the same body as in section 2 in \mathbb{R}^3 . Suppose the crack is located along the half-plane $y = 0, x > 0$. On the upper crack edge along the strip $y = 0, 0 \leq x \leq l$ the longitudinal displacements are known:

$$w^+(x, 0, z) = s_3(x), \quad x \in [0, l], \quad z \in (-\infty, +\infty) \quad (3.1)$$

where w is the strain vector component in the z -direction, $s_3(x)$ is a given function. The remaining part of the upper crack edge and the whole of the lower crack edge are loaded with the given longitudinal shear stresses:

$$\begin{aligned} \tau_{yz}^+(x, 0, z) &= p_3^+(x), \quad x \in (l, +\infty), \quad z \in (-\infty, +\infty) \\ \tau_{yz}^-(x, 0, z) &= p_3^-(x), \quad x \in (0, +\infty), \quad z \in (-\infty, +\infty) \end{aligned} \quad (3.2)$$

where τ_{yz} is the stress vector component along the crack surfaces, $p_3^\pm(x)$ are given functions.

Along the half-plane $y = 0$, $x < 0$ the half-spaces have continuous contact. Specified shear stresses τ_{xz1}^∞ and $\tau_{xz2}^\infty = \mu_2 \tau_{xz1}^\infty / \mu_1$ act at infinity of the half-spaces $y > 0$ and $y < 0$, respectively. The shear stress τ_{yz}^∞ vanishes at infinity. The principal vector of the external forces acting on the strip $y = 0$, $0 \leq x \leq l$ is further specified.

All the given functions $s_3(x)$, $p_3^\pm(x)$ in (3.1)-(3.2) are dependent only on the variable x . Therefore, the antiplane stress state is implemented in the body. It can be defined by one analytic function [8] (complex potential) $F(\zeta)$, $\zeta \in \mathbb{C} \setminus [0, +\infty)$, which satisfies the boundary conditions

$$\operatorname{Re}F^+(x) = \mu_1 s_3'(x), \quad x \in (0, l)$$

$$\operatorname{Im}F^+(x) = -p_3^+(x), \quad x \in (l, +\infty)$$

$$(\mu_1 - \mu_2)\operatorname{Im}F^+(x) + (\mu_1 + \mu_2)\operatorname{Im}F^-(x) = -2\mu_2 p_3^-(x), \quad x \in (0, +\infty).$$

The problem reduces again to a matrix Riemann-Hilbert boundary-value problem with a piecewise-constant coefficient for the complex potential $F(\zeta)$ in the class of symmetric functions. The solution of the problem is found explicitly using a Gaussian hypergeometric function. On the basis of this solution, the asymptotic of the stresses near the points $\zeta = 0$ and $\zeta = l \pm i0$ is investigated. The stress intensity factors are defined.

In this case, near the right end of the path plate $\zeta = l + i0$ the stresses have the traditional power singularity of order $1/2$, and at the point $\zeta = l - i0$ they are bounded. The asymptotic of the stresses near the crack tip $\zeta = 0$ on the half-plane $y = 0$, $x < 0$ has the form

$$\tau_{xz} - i\tau_{yz} = -\frac{iK_{\text{III}}^2}{\sqrt{2\pi}|x|^{1-\gamma_0}}e^{-i\pi(1-\gamma_0)} - \frac{iK_{\text{III}}^1}{\sqrt{2\pi}|x|^{\gamma_0}}e^{-i\pi\gamma_0} + O(1), \quad x \rightarrow 0 - 0$$

where $\gamma_0 \in [1/2, 1)$ is a real constant which depends only on the shear moduli of the body, K_{III}^1 , K_{III}^2 are the stress intensity factors close to the crack tip.

Acknowledgments: The research is supported by the German Academic Exchange Service (DAAD), project 91531467, and the Russian Foundation for Basic Research (RFBR), project 13-01-00003.

REFERENCES

- [1] G. Ya. Popov: The Concentration of Elastic Stresses near Punches, Cuts, Thin Inclusions and Reinforcements. Nauka, Moscow, 1982.
- [2] G. P. Cherepanov: Fracture Mechanics of Composite Materials. Nauka, Moscow, 1983.
- [3] R. Ballarini: A certain mixed boundary value problem for bimaterial interface. Int. J. Solid Structures, **32**, 279-289, 1995.
- [4] S.M. Mkhitarian, N. Melkounian, B.B. Lin: Stress-strain state of a cracked elastic wedge under anti-plane deformation with mixed boundary conditions on its faces. Int. J. Fract., **108**(4), 291-315, 2001.
- [5] V.N. Hakobyan, L.L. Dashtoyan, L.V. Hakobyan: On Anti-plane Stress State of Compound Space with Crack Under Mixed Conditions. Izv NAN Armenii Mekhanika, **62**(4), 1622, 2009.

- [6] Yu.O. Vasil'eva, V.V. Sil'vestrov: The problem of an interface crack with a rigid patch plate on part of its edge. *J. Appl. Math. and Mech.*, **75**(6), 716–730, 2011.
- [7] N. I. Muskhelishvili: *Some Basic Problems of the Mathematical Theory of Elasticity*. Noordhoff International Publishing, Leiden, 1977.
- [8] G.C. Sih: Stress distribution near internal crack tip for longitudinal shear problems. *J. appl. Mech.*, **32**, 51–58, 1965.

SOME RESULTS IN FRACTIONAL CLIFFORD ANALYSIS

N. Vieira*

*CIDMA - Center for Research and Development in Mathematics and Applications
Department of Mathematics, University of Aveiro, Campus Universitário de Santiago,
3810-193 Aveiro, Portugal.
E-mail: nloureirovieira@gmail.com

Keywords: Fractional monogenic polynomials, Fischer decomposition, Fractional Dirac operator, Riemann-Liouville fractional derivative, Stationary transport operator.

Abstract. *What is nowadays called (classic) Clifford analysis consists in the establishment of a function theory for functions belonging to the kernel of the Dirac operator. While such functions can very well describe problems of a particle with internal $SU(2)$ -symmetries, higher order symmetries are beyond this theory. Although many modifications (such as Yang-Mills theory) were suggested over the years they could not address the principal problem, the need of a n -fold factorization of the d'Alembert operator.*

In this paper we present the basic tools of a fractional function theory in higher dimensions, for the transport operator ($\alpha = \frac{1}{2}$), by means of a fractional correspondence to the Weyl relations via fractional Riemann-Liouville derivatives. A Fischer decomposition, fractional Euler and Gamma operators, monogenic projection, and basic fractional homogeneous powers are constructed.

1 INTRODUCTION

In the last decades the interest in fractional calculus increased substantially. This fact is due to on the one hand different problems can be considered in the framework of fractional derivatives like, for example, in optics and quantum mechanics, and on the other hand fractional calculus gives us a new degree of freedom which can be used for more complete characterization of an object or as an additional encoding parameter.

Over the last decades F. Sommen and his collaborators developed a method for establishing a higher dimension function theory based on the so-called Weyl relations [1, 3, 2]. In more restrictive settings it is nowadays called Howe dual pair technique (see [6]). Its focal point is the construction of an operator algebra (classically $\mathfrak{osp}(1|2)$) and the resulting Fischer decomposition.

The aim of this paper is to present a Fischer decomposition, when considering the fractional Dirac operator defined via Riemann-Liouville derivatives, where the fractional parameter is equal to $\frac{1}{2}$ (which leads to the case of the stationary transport operator). The results presented here correspond to a restriction of correspondent ones presented in [7] for the particular case of $\alpha = \frac{1}{2}$.

In the Preliminaries we recall some basic facts about Clifford analysis and fractional calculus. In Section 3, we introduce the corresponding Weyl relations for this fractional setting and the notion of a fractional homogeneous polynomial. In the same section we present the fractional correspondence to the Fischer decomposition. In the final section we construct the projection of a given fractional homogeneous polynomial into the space of fractional homogeneous monogenic polynomials. We also calculate the dimension of the space of fractional homogeneous monogenic polynomials.

2 PRELIMINARIES

We consider the d -dimensional vector space \mathbb{R}^d endowed with an orthonormal basis $\{e_1, \dots, e_d\}$. We define the universal real Clifford algebra $\mathbb{R}_{0,d}$ as the 2^d -dimensional associative algebra which obeys the multiplication rules $e_i e_j + e_j e_i = -2\delta_{i,j}$. A vector space basis for $\mathbb{R}_{0,d}$ is generated by the elements $e_0 = 1$ and $e_A = e_{h_1} \cdots e_{h_k}$, where $A = \{h_1, \dots, h_k\} \subset M = \{1, \dots, d\}$, for $1 \leq h_1 < \dots < h_k \leq d$. An important subspace of the real Clifford algebra $\mathbb{R}_{0,d}$ is the so-called space of paravectors $\mathbb{R}_1^d = \mathbb{R} \oplus \mathbb{R}^d$, being the sum of scalars and vectors. An important property of algebra $\mathbb{R}_{0,d}$ is that each non-zero vector $x \in \mathbb{R}_1^d$ has a multiplicative inverse given by $\frac{\bar{x}}{\|x\|^2}$. Now, we introduce the complexified Clifford algebra \mathbb{C}_d as the tensor product

$$\mathbb{C} \otimes \mathbb{R}_{0,d} = \left\{ w = \sum_A w_A e_A, w_A \in \mathbb{C}, A \subset M \right\},$$

where the imaginary unit i of \mathbb{C} commutes with the basis elements, i.e., $ie_j = e_j i$ for all $j = 1, \dots, d$.

An \mathbb{C}_d -valued function f over $\Omega \subset \mathbb{R}_1^d$ has representation $f = \sum_A e_A f_A$, with components $f_A : \Omega \rightarrow \mathbb{C}$. Properties such as continuity are understood component-wisely. Next, we recall the Euclidean Dirac operator $D = \sum_{j=1}^d e_j \partial_{x_j}$, which factorizes the d -dimensional Euclidean Laplacian, i.e., $D^2 = -\Delta = -\sum_{j=1}^d \partial_{x_j}^2$. A \mathbb{C}_d -valued function f is called *left-monogenic* if

it satisfies $Du = 0$ on Ω (resp. *right-monogenic* if it satisfies $uD = 0$ on Ω). For more details about Clifford algebras and monogenic function we refer [2].

The most widely known definition of the fractional derivative is the so-called Riemann-Liouville definition:

$$(D_{a+}^{\alpha} f)(x) = \left(\frac{d}{dx}\right)^n \frac{1}{\Gamma(n-\alpha)} \int_a^x \frac{f(t)}{(x-t)^{\alpha-n+1}} dt, \quad n = [\alpha] + 1, \quad a, x > 0. \quad (1)$$

where $[\alpha]$ means the integer part of α . In [4] fractional derivative (1) was successfully applied in the definition of the fractional correspondent of the Dirac operator in the context of Clifford analysis. In fact, for the particular case of $\alpha = \frac{1}{2}$, the fractional Dirac operator corresponds to $\mathbf{D} = \sum_{j=1}^d e_j \mathbf{D}_j = \sum_{j=1}^d e_j (D_j + Y_j)$, where $D_j = \partial_{x_j}$ and $Y_j = \frac{1}{2(\xi_j - x_j)}$ with $\xi = (\xi_1, \dots, \xi_d)$ the observer time vector. Moreover, we have that $\mathbf{D}\mathbf{D} = D$ with D the Euclidian Dirac operator, i.e., the stationary transport operator. A \mathbb{C}_n -valued function f is called *fractional left-monogenic* if it satisfies $\mathbf{D}u = 0$ on Ω (resp. *fractional right-monogenic* if it satisfies $u\mathbf{D} = 0$ on Ω). We observe that due to the definition of \mathbf{D} we have that

$$\mathbf{D} \left(\prod_{i=1}^d (\xi_i - x_i)^{\frac{1}{2}} \right) = 0, \quad (2)$$

i.e., $\prod_{i=1}^d (\xi_i - x_i)^{\frac{1}{2}}$ is a fractional monogenic function. The fractional power $(\xi_i - x_i)^{\frac{1}{2}}$ corresponds to $(\xi_j - x_j)^{\frac{1}{2}}$ if $\xi_j \geq x_j$, or $(x_j - \xi_j)^{\frac{1}{2}} i$ if $\xi_j < x_j$, with $j = 0, 1, \dots, d$. From now until the end of the paper, we consider paravectors of the form $\underline{x} = \mathbf{x}_0 + \mathbf{x}$, where $\mathbf{x} = \sum_{j=1}^d e_j \mathbf{x}_j$ with $\mathbf{x}_j = \frac{\xi_j - x_j}{2}$.

3 WEYL RELATIONS AND FRACTIONAL FISCHER DECOMPOSITION

The aim of this section is to provide the basic tools for a function theory for the fractional Dirac operator defined via fractional Riemann-Liouville derivatives for the particular case of $\alpha = \frac{1}{2}$.

3.1 Fractional Weyl relations

Now we introduce the fractional correspondence of the classical Euler and Gamma operators. Furthermore, we show that the two natural operators \mathbf{D} and \mathbf{x} , considered as odd elements, generate a finite-dimensional Lie superalgebra in the algebra of endomorphisms generated by the partial fractional Riemann-Liouville derivatives, the basic *vector variables* \mathbf{x}_j (seen as multiplication operators), and the basis of the Clifford algebra e_j .

In order to obtain our results, we use some standard technique in higher dimensions, namely we study the commutator and the anti-commutator between \mathbf{x} and \mathbf{D} . We start proposing the following fractional Weyl relations

$$[\mathbf{D}_i, \mathbf{x}_i] = \mathbf{D}_i \mathbf{x}_i - \mathbf{x}_i \mathbf{D}_i = -\frac{1}{2}, \quad (3)$$

with $i = 1, \dots, d$. This leads to the following relations for \mathbf{x} and \mathbf{D} :

$$\{\mathbf{D}, \mathbf{x}\} = \mathbf{D}\mathbf{x} + \mathbf{x}\mathbf{D} = -2\mathbf{E} + \frac{d}{2}, \quad [\mathbf{x}, \mathbf{D}] = \mathbf{x}\mathbf{D} - \mathbf{D}\mathbf{x} = -2\mathbf{\Gamma} - \frac{d}{2}, \quad (4)$$

where \mathbb{E} , Γ are, respectively, the fractional Euler and Gamma operators of order $\frac{1}{2}$, and have the following expressions

$$\mathbb{E} = \sum_{i=1}^d \mathbf{x}_i \mathbf{D}_j, \quad \Gamma = \sum_{i < j} e_i e_j (\mathbf{x}_i \mathbf{D}_j - \mathbf{D}_i \mathbf{x}_j). \quad (5)$$

From (5) we derive

$$[\mathbf{x}, \mathbb{E}] = \frac{1}{2} \mathbf{x}, \quad [\mathbf{D}, \mathbb{E}] = -\frac{1}{2} \mathbf{D}, \quad (6)$$

which allow us to conclude that we have a finite dimensional Lie superalgebra generated by \mathbf{x} and \mathbf{D} , isomorphic to $\mathfrak{osp}(1|2)$. Now we introduce the definition of fractional homogeneity of a polynomial by means of the fractional Euler operator.

Definition 3.1 *A polynomial P_l is called fractional homogeneous of degree $l \in \mathbb{N}_0$, if and only if $\mathbb{E}P_l = -\frac{l}{2} P_l$.*

We observe that from the previous definition the basic fractional homogeneous powers are given by $\prod_{j=1}^d \mathbf{x}_j^{\beta_j}$, with $l = |\beta| = \beta_1 + \dots + \beta_d$. In combination with the first relation in (6) this definition also implies that the multiplication of a fractional homogeneous polynomial of degree l by \mathbf{x} , results in a fractional homogeneous polynomial of degree $l + 1$, and thus may be seen as a raising operator. Moreover, we can also ensure that for a fractional homogeneous polynomial P_l of degree l , $\mathbf{D}P_l$ is a fractional homogeneous polynomial of degree $l - 1$. Furthermore, Weyl's relations (3) enable us to construct fractional homogeneous polynomials, recursively.

3.2 Fractional Fischer decomposition

A fractional Fischer inner product of two fractional homogeneous polynomials P and Q would have the following form

$$\langle P(\mathbf{x}), Q(\mathbf{x}) \rangle = \text{Sc} \left[\overline{P(\partial_{\mathbf{x}})} Q(\mathbf{x}) \right], \quad (7)$$

where $\partial_{\mathbf{x}}$ represents \mathbf{D}_j , and $P(\partial_{\mathbf{x}})$ is a differential operator obtained by replacing in the polynomial P each variable \mathbf{x}_j by the corresponding fractional derivative, i.e. $D_j + Y_j$. From (7) we have that for any polynomial P_{l-1} of homogeneity $l - 1$ and any polynomial Q_l of homogeneity l the relation $\langle \mathbf{x} P_{l-1}, Q_l \rangle = \langle P_{l-1}, \mathbf{D}Q_l \rangle$. This fact allows us to obtain the following result:

Theorem 3.2 *For each $l \in \mathbb{N}_0$ we have $\Pi_l = \mathcal{M}_l + \mathbf{x} \Pi_{l-1}$, where Π_l denotes the space of fractional homogeneous polynomials of degree l and \mathcal{M}_l denotes the space of fractional monogenic homogeneous polynomials of degree l . Moreover, the subspaces \mathcal{M}_k and $\mathbf{x} \Pi_{l-1}$ are orthogonal with respect to the Fischer inner product (7).*

The proof is analogous to the proof of Theorem 3.5 in [7] but considering $\alpha = \frac{1}{2}$, and therefore we omit it from the paper. As a result of the previous theorem we obtain the fractional Fischer decomposition with respect to the fractional Dirac operator \mathbf{D} .

Theorem 3.3 *Let P_l be a fractional homogeneous polynomial of degree l . Then*

$$P_l = M_l + \mathbf{x} M_{l-1} + \mathbf{x}^2 M_{l-2} + \dots + \mathbf{x}^l M_0, \quad (8)$$

where each M_j denotes the fractional homogeneous monogenic polynomial of degree j . More specifically, $M_0 = P_0$ and $M_l = \{u \in P_l : \mathbf{D}u = 0\}$.

The spaces represented in (8) are orthogonal to each other with respect to the Fischer inner product (7). This is a consequence of the construction of the fractional Euler operator \mathbb{E} (see (5)), and in particular of (4).

3.3 Explicit formulae

Here we obtain an explicit formula for the projection $\pi_{\mathcal{M}}(P_l)$ of a given fractional homogeneous polynomial P_l into the space of fractional homogeneous monogenic polynomials. We start with the following auxiliary result:

Theorem 3.4 *For any fractional homogeneous polynomial P_l and any positive integer s , we have $\mathbf{D}\mathbf{x}^s P_l = g_{s,l} \mathbf{x}^{s-1} P_l + (-1)^s \mathbf{x}^s \mathbf{D} P_l$, where $g_{2k,l} = k$ and $g_{2k+1,l} = k + l + \frac{d}{2}$.*

Proof: The proof follows, by induction and straightforward calculations, from the commutation between \mathbf{D} and \mathbf{x}^s using the relations $\mathbf{D}\mathbf{x} = -2\mathbb{E} + \frac{d}{2} - \mathbf{x} \mathbf{D}$ and $\mathbb{E}\mathbf{x} = \mathbf{x} \mathbb{E} - \frac{1}{2}\mathbf{x}$. ■

Let us now compute an explicit form of the projection $\pi_{\mathcal{M}}(P_l)$.

Theorem 3.5 *Consider the constants $c_{j,l}$ defined by $c_{0,l} = 1$, and $c_{j,l} = \frac{(-1)^j \Gamma(\frac{d}{2} + l - 1 - [\frac{j}{2}])}{\Gamma(\frac{d}{2} + 1) \Gamma(1 + 2[\frac{j}{2}])}$, where $j = 1, \dots, l$ and $[\cdot]$ represents the integer part. Then the map $\pi_{\mathcal{M}}$ given by*

$$\pi_{\mathcal{M}}(P_l) := P_l + c_{1,l} \mathbf{x} \mathbf{D} P_l + c_{2,l} \mathbf{x}^2 \mathbf{D}^2 P_l + \dots + c_{l,l} \mathbf{x}^l \mathbf{D}^l P_l$$

is the projection of the fractional homogeneous polynomial P_l into the space of fractional homogeneous monogenic polynomials.

Proof: Let us consider the linear combination

$$r = a_0 P_l + a_1 \mathbf{x} \mathbf{D} P_l + a_2 \mathbf{x}^2 \mathbf{D}^2 P_l + \dots + a_l \mathbf{x}^l \mathbf{D}^l P_l,$$

with $a_0 = 1$. If there are constants a_j , $j = 1, \dots, l$, such that $r \in \mathcal{M}_l$, then r is equal to $\pi_{\mathcal{M}}(P_l)$. Indeed, we know that $P_l = \mathcal{M}_l \oplus \mathbf{x} P_{l-1}$ and $r = P_l + Q_{l-1}$, with $Q_{l-1} = \sum_{i=1}^l a_i \mathbf{x}^i \mathbf{D}^i P_l$. Applying Theorem 3.4, we get

$$\begin{aligned} 0 &= \mathbf{D}(\pi_{\mathcal{M}}(P_l)) \\ &= \mathbf{D} P_l + a_1 \mathbf{D} \mathbf{x} \mathbf{D} P_l + a_2 \mathbf{D} \mathbf{x}^2 \mathbf{D}^2 P_l + \dots + a_l \mathbf{D} \mathbf{x}^l \mathbf{D}^l P_l \\ &= (1 + a_1 g_{1,l-1}) \mathbf{D} P_l + (-a_1 + a_2 g_{2,l-2}) \mathbf{x} \mathbf{D}^2 P_l + (a_2 + a_3 g_{3,l-3}) \mathbf{x}^2 \mathbf{D}^3 P_l \\ &\quad + \dots + ((-1)^{l-1} a_{l-1} + a_l g_{l,0}) \mathbf{x}^{l-1} \mathbf{D}^l P_l. \end{aligned}$$

Hence if the relation $(-1)^{j-1} a_{j-1} + a_j g_{j,l-j} = 0$ holds for each $j = 1, \dots, l$, then the function r is fractional monogenic. By induction we get $a_j = \frac{(-1)^j \Gamma(\frac{d}{2} + l - 1 - [\frac{j}{2}])}{\Gamma(\frac{d}{2} + 1) \Gamma(1 + 2[\frac{j}{2}])}$. ■

Theorem 3.6 *Each polynomial P_l can be written in a unique way as $P_l = \sum_{j=0}^l \mathbf{x}^j M_{l-j}(P_l)$, where $M_{l-j}(P_l) = c'_j \sum_{n=0}^j c_{j,l-n} \mathbf{x}^n \mathbf{D}^n \mathbf{D}^{l-j} P_l$ with $j = 0, \dots, l$, and the coefficients c'_j are defined by $c'_j = \frac{(-1)^j \Gamma(\frac{d}{2} + l - 1 - [\frac{j}{2}])}{\Gamma(\frac{d}{2} + 1) \Gamma(1 + 2[\frac{j}{2}])}$.*

The proof of this result is analogous to the proof of Theorem 3.9, for $\alpha = \frac{1}{2}$, in [7], and therefore we omit it from the paper.

Acknowledgement: This work was supported by Portuguese funds through the CIDMA - Center for Research and Development in Mathematics and Applications, and the Portuguese Foundation for Science and Technology (“FCT-Fundação para a Ciência e a Tecnologia”), within project UID/MAT/ 0416/2013. N. Vieira was also supported by FCT via the FCT Researcher Program 2014 (Ref: IF/00271/2014).

REFERENCES

- [1] H. De Bie and F. Sommen: Fischer decompositions in superspace. Le Hung Son et al eds. Function spaces in complex and Clifford analysis, National University Publishers, Hanoi, 2008.
- [2] R. Delanghe, F. Sommen and V. Souček: Clifford algebras and spinor-valued functions. A function theory for the Dirac operator. Mathematics and its Applications-Vol.53, Kluwer Academic Publishers, Dordrecht etc., 1992.
- [3] H. De Ridder, H. De Schepper, U. Kähler and F. Sommen: Discrete function theory based on skew Weyl relations. Proc. Am. Math. Soc., **138**-No.9, 3241-3256, 2010.
- [4] R.A. El-Nabulsi: Fractional Dirac operators and deformed field theory on Clifford algebra. Chaos Solitons Fractals, **42**-No.5, 2614-2622, 2009.
- [5] U. Kähler and N. Vieira: Fractional Clifford analysis. S. Bernstein, U. Kähler, I. Sabadini and F. Sommen eds. Hypercomplex Analysis: New perspectives and applications, Trends in Mathematics, Birkhäuser, Basel, 2014.
- [6] B. Ørsted, P. Somberg and V. Souček: The Howe duality for the Dunkl version of the Dirac operator. Adv. Appl. Clifford Algebr., **19**-No.2, 403–415, 2009.
- [7] N. Vieira: Fischer Decomposition and Cauchy-Kovalevskaya extension in fractional Clifford analysis: the Riemann-Liouville case. Proc. Edinb. Math. Soc., II. Ser., in press.

A GENERIC FRAMEWORK SUPPORTING DISTRIBUTED COMPUTING IN ENGINEERING APPLICATIONS

J. Wiggenbrock^{*1,2} and K. Smarsly¹

¹*Bauhaus University Weimar
Coudraystr. 7, 99423 Weimar, Germany
Email: jens.wiggenbrock@uni-weimar.de*

²*South Westphalia University of Applied Sciences
Lindenstraße 53, 59872 Meschede, Germany*

Keywords: Data Modeling, Distributed Engineering Applications, Message-oriented Middleware, Computing in Civil Engineering.

Abstract. *Modern distributed engineering applications are based on complex systems consisting of various subsystems that are connected through the Internet. Communication and collaboration within an entire system requires reliable and efficient data exchange between the subsystems. Middleware developed within the web evolution during the past years provides reliable and efficient data exchange for web applications, which can be adopted for solving the data exchange problems in distributed engineering applications. This paper presents a generic approach for reliable and efficient data exchange between engineering devices using existing middleware known from web applications. Different existing middleware is examined with respect to the suitability in engineering applications. In this paper, a suitable middleware is shown and a prototype implementation simulating distributed wind farm control is presented and validated using several performance measurements.*

1 INTRODUCTION

A general trend in engineering applications are interconnected subsystems that in total form a distributed engineering system. Every subsystem may include sensors and actuators supporting the overall task of the engineering system. A common general requirement of distributed engineering systems is the need for reliable and efficient data exchange between the interconnected subsystems. Examples of such engineering systems are industrial assembly lines, home automation, wired or wireless structural health monitoring [1] [2] or, more specifically, wind farms being composed of single wind turbines representing interconnected subsystems.

There exists a number of proprietary and enterprise-specific approaches for reliable and efficient data exchange between interconnected and spatially distributed subsystems. The approaches provide data exchange protocols, network topologies and, also, several specifications for additional cabling that must be considered when implemented in terms of an engineering system required to connect the subsystems. Disadvantages of these approaches are high expenses because of the additional cabling. Furthermore, the engineering system is technology-dependent and, as such, hardly expandable.

Modern, collaborative web applications, such as groupware and social networks, also require reliable and efficient data exchange between the subsystems. Here, the web servers and the web browsers are considered subsystems forming the entire system “web” that is connected through the Internet. In the area of web applications, there exists well-established middleware for data exchange between the subsystems (i.e. web servers and web browsers). This middleware can advantageously be adopted to implement reliable and efficient data exchange in distributed engineering applications.

In this paper, a generic framework for reliable and efficient data exchange between engineering devices is presented, using existing middleware usually deployed in web applications. Starting with a brief overview of modern collaborative web applications, the principles of existing middleware are elucidated. Then, selection criteria for suitable middleware with respect to data exchange in engineering applications are defined, and existing middleware is examined. Based on the selection results, the middleware being most appropriate to be adopted to engineering applications is taken as a basis for a prototype implementation. Finally, the prototype implementation is validated using several performance measurements.

2 MESSAGE-ORIENTED MIDDLEWARE FOR ENGINEERING APPLICATIONS

“Message-oriented middleware” is a generic term describing a software that operates as message exchange service. The software can be divided into a server, which provides the exchange service, and participating clients, which require message exchange between each other. A message refers to all types of data and command packets being exchanged. The following paragraphs describe state-of-the-art message-oriented middleware for engineering applications.

2.1 Principles of message-oriented middleware

Today, most devices that are connected to the Internet are located behind a router with an integrated firewall. As shown in Figure 1, the router grants Internet access to the devices behind the router. Vice versa, the devices behind the router cannot be accessed from the

Internet directly. To give an example, the mobile phone shown in Figure 1 cannot establish a connection to the public web server, and the web server cannot establish a connection to any device, such as the mobile phone mentioned above.

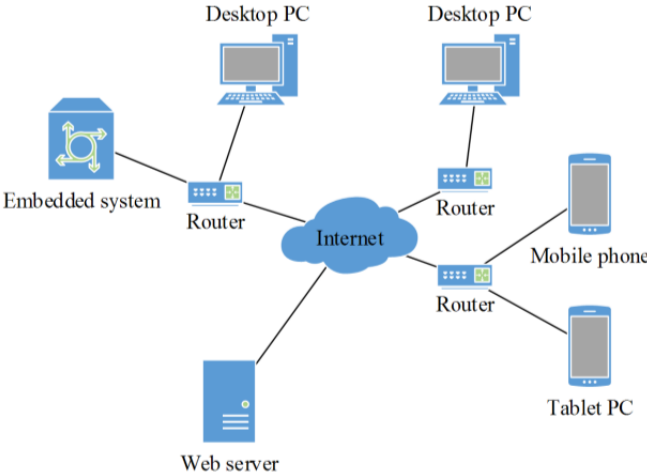


Figure 1: Topology of various devices connected through the Internet

In summary, the topology shown in Figure 1 shields the devices behind the router and basically protects the devices from external access. However, considering engineering applications, establishing a connection to a device behind a router can become a serious issue if the connection is needed for the engineering application.

A well-known solution for reliable and efficient data exchange between devices connected through the Internet is the establishment of a public server, based e.g. on the File Transfer Protocol (FTP). The common, unidirectional and indirect way to transfer a file between the devices via FTP is shown in Figure 2. The desktop PC connects with the public FTP server and uploads a file (green arrows). Once the file is uploaded, the mobile phone connects with the public FTP server and downloads the file (red arrows). Technically, the FTP server operates as a middleware for file exchange.

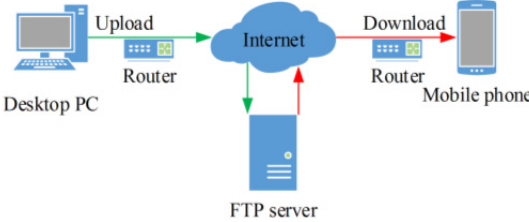


Figure 2: Indirect, unidirectional data exchange over a public FTP server

Both operations, upload and download, are executed independently from each other and must explicitly be initiated by the respective client device, i.e. the upload process must be finished before the download process is started. Unfortunately, traditional file exchange protocols, such as FTP, generally do not provide any possibility to notify participating clients when the upload process is finished or when changes at the server occur. Thus, additional means for notifying participating clients, such as email or phone calls, are needed, which, however, leads to delays in the data exchange process.

Eradicating the drawbacks illustrated above, message-oriented middleware (MOM) enables data exchange between various devices based on a different concept. Negotiating on a central server allows near real-time data exchange between participating clients, as shown in Figure 3

and in Figure 4 [3]. Message-oriented middleware provides different communication protocols, such as “message passing”, “message queueing”, and “publish/subscribe”. While “message passing” and “message queueing” are mostly used for concurrent programming in local applications, publish/subscribe is a well-established model for asynchronous distributed computing considered herein.

A public server provides topic-oriented communication channels and takes on their central mediation. First, all participating clients connect to the public server. Then, the clients register with the server and “subscribe” to a specific topic. Finally, the server compiles a list of all clients and topics, and it manages the communication. To receive data, a client sends a message with the topic of interest to the server. The server processes the list of clients and topics, and it forwards the message to the clients subscribed to the topic of interest. Figure 3 and Figure 4 show different publish/subscribe architectures. Figure 3 presents a simple architecture of one client publishing in one topic, a server, and two subscriber clients. Figure 4 presents a simple architecture of two clients publishing in the same or in different topics, a server, and one subscriber client.

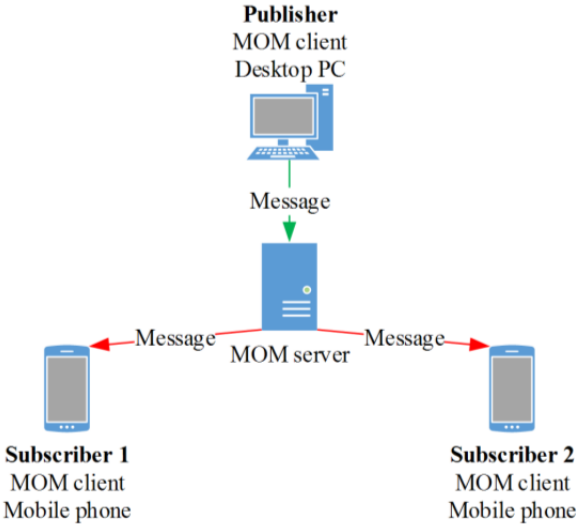


Figure 3: Publish/subscribe architecture with one publisher and two subscribers

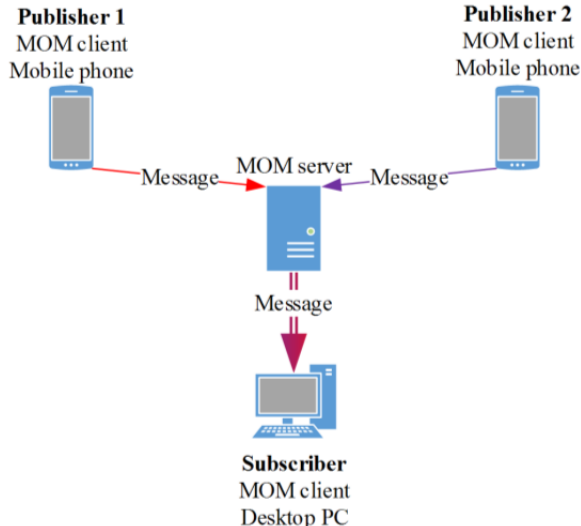


Figure 4: Publish/subscribe architecture with two publishers and one subscriber

2.2 Selection criteria for message-oriented middleware for engineering applications

Automated, distributed engineering applications are widely used in a number of areas. The most critical component in distributed engineering applications is the communication system [4]. Essential features, which every distributed engineering application must provide, are defined as follows:

- Fast data exchange: Data packets have to be delivered with low and predictable latency
- Reliable data exchange: Data must be equipped with error-correcting code
- Durability: The lifetime of engineering applications may be several decades; the engineering systems have to be maintained over the lifetime

When using message-oriented middleware in engineering applications, specific requirements must be met. The following criteria are identified for selecting suitable message-oriented middleware for distributed engineering applications. Based on these criteria, Table 1 summarizes the middleware examined in this study.

- **Hosting:** Does the middleware provide self-hosting on an independent server?
- **Data security:** Does the middleware provide authentication and encryption or is a plugin available?
- **Future security:** Is the development within the next years ensured by a vivid community?
- **Usability:** Does the middleware provide a programming interface, which can easily be integrated into existing engineering applications?

Table 1: Middleware examined in this study

Middleware	Host	Data security	Future security	Usability	Remarks
Redis http://redis.io/	Self-host	Not integrated	Server and clients are open source	<u>Server:</u> Independent application on Linux/Windows <u>Clients:</u> Supporting many programming languages	Popular NoSQL-database with publish/subscribe function
Google Cloud pub/sub API https://cloud.google.com/pubsub/docs	Cloud-host	HTTPS	Beta version, potential for future Google services	<u>Server:</u> Managed service <u>Clients:</u> Supporting .NET, Java and JavaScript	First (beta) release in 03/2015
Apache Kafka http://kafka.apache.org/	Self-host	SSL implemented in last version	Server and clients are open source	<u>Server:</u> Independent application on Linux/Windows <u>Clients:</u> Supporting several progr. languages	Originally developed by LinkedIn
PUSHER https://pusher.com/	Cloud-host	SSL implemented	Server not available, Clients are open source	<u>Server:</u> Managed service <u>Clients:</u> Supporting .NET, Java and JavaScript	Describes itself as “Leader in realtime technologies”
Socket.io + NODE.js http://socket.io/	Self-host	SSL implemented	Server and clients are open source	Server and client only available in JavaScript	Popular event-driven JavaScript server architecture
RabbitMQ http://www.rabbitmq.com	Self-host	SLL implemented but depends on Erlang crypto application	Server and clients are open source.	<u>Server:</u> Independent application on Linux/Windows written in Erlang <u>Clients:</u> Supporting several progr. languages	Implements the open Advanced Message Queuing Protocol enabling own client developments
ASP.NET SignalR http://signalr.net	Self-host	Over IIS-Server / OWIN	Open source	<u>Server:</u> Integrates in existing C# or ASP.NET appl’s on Linux/Windows <u>Clients:</u> Supporting C#, Java, JavaScript	Started as open source project; now core feature of ASP.NET

As can be seen from Table 1, “Apache Kafka”, “RabbitMQ” and “SignalR” are matching all defined selection criteria. In addition, SignalR provides a so called server module that can be integrated directly into existing engineering applications [5]; this enables the server to perform further processing on the messages and to distribute the messages according to additional filter rules. Finally, SignalR is chosen in this study as an appropriate basis for the prototype implementation simulating decentralized wind farm control.

3 A GENERIC FRAMEWORK SUPPORTING REAL-TIME DATA EXCHANGE FOR DECENTRALIZED WIND FARM CONTROL

Representing an illustrative example of a distributed engineering application, decentralized collaborative control of a wind farm is chosen as a proof of concept of the proposed framework. Today, wind turbines in a wind farm are usually operated without considering wake effects between the wind turbines. Figure 5 shows a wind farm with highlighted wake fields affecting wind turbines lying behind other wind turbines. Minimizing the wake effects increases the wind farm power efficiency. In recent years, different approaches towards wind farm power efficiency optimization have been proposed. Park et al., for example, propose a cooperative control strategy, adjusting the yaw control of the nacelle, the pitch control of the rotor blades and the induction factor of the generator to alter the wake field of each wind turbine [6, 7]. It is evident that automated real-time control of the wind turbines in a collaborative way can substantially increase the overall performance of a wind farm in terms of power efficiency. In this paper, collaborative control of a wind farm is simulated, serving as a proof of concept of the proposed framework.

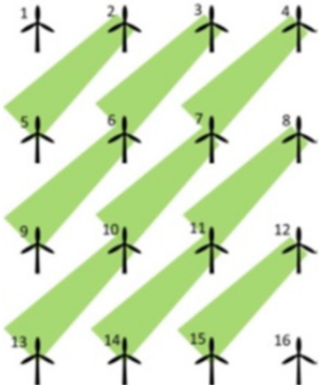


Figure 5: Wind farm with highlighted wake fields affecting wind turbines lying behind other wind turbines (figure source: [4])

It is assumed that for cooperative control, the location (i.e. latitude and longitude) of each wind turbine within the wind farm, the actual settings (i.e. yaw angle, rotor blade pitch, and induction factor), the power output, and the environmental data (i.e. wind direction and wind speed) of each wind turbine is needed to calculate the optimum settings for each wind turbine relevant to collaborative wind farm power maximization. The optimum settings of each wind turbine contain improved yaw angle, rotor blade pitch, and induction factor. It is further assumed that real-time computational optimization is done by a central control unit within a procedure carried out in regular intervals. Each wind turbine sends the described data sets to the central control unit. In this study, the central control unit runs an engineering application simulating the wind farm optimization model proposed by Park et al. The calculated data sets containing the optimum settings are sent to the respective wind turbine in through messages.

Assuming that the messages, which contain the data sets described above, are sent in human readable text format (JSON or XML), one message has a size of less than 100 bytes (about 10 bytes per value). In this study, data exchange between the central control unit and the wind turbines 10 times per minute will be sufficient for wind farm control.

The SignalR middleware used in this study has originally been developed to integrate real-time communication in ASP.NET web applications [8]. A SignalR server is based on the programming language C# and provides server and client integration in underlying applications running on Windows and Linux. Clients for Java and JavaScript are also available. The ability of SSL encryption is a further feature of SignalR. Figure 6 presents the architecture of the proposed generic framework, which basically consists of one server that represents the central control unit, and two clients that represent two wind turbines. Both, server and clients, include specific SignalR libraries that provide a hub class. The hub class is the interface to handle all SignalR communications within the distributed engineering application. Furthermore, the hub class provides a programmable interface for external access, which keeps the main part of the application encapsulated. Data exchange between subsystems is done by invoking hub class methods that pass the data sets of the wind turbines as method parameters.

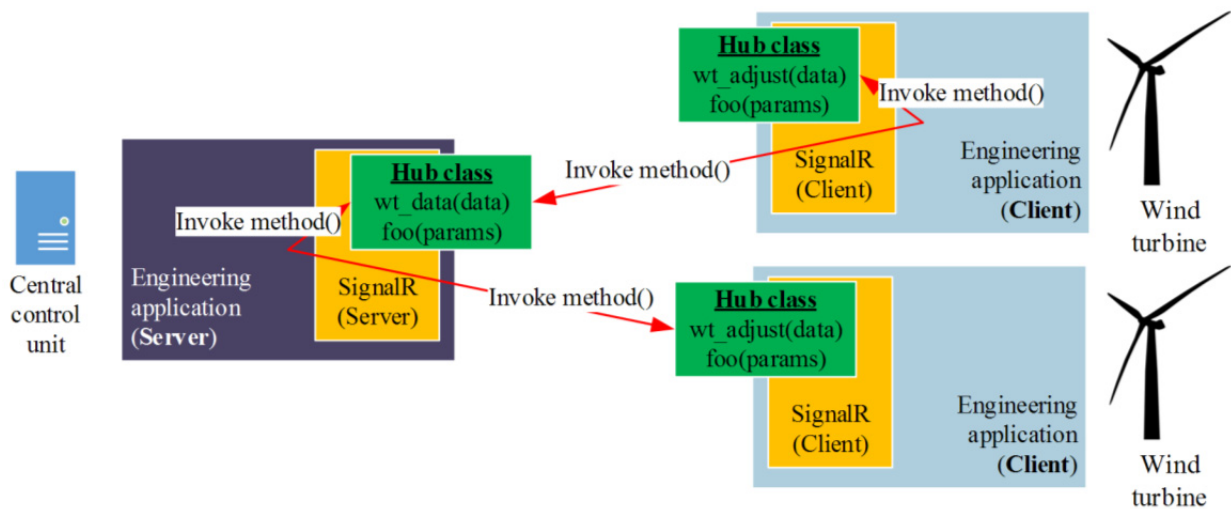


Figure 6: SignalR-based example application for wind farm control

As mentioned earlier, the wind turbines technically act as the clients and the central control unit acts as the server. Figure 7 shows the wind farm control as a closed control circuit. The clients, in pre-defined intervals, collect the environmental data and the wind turbine settings required for real-time optimization. Once having collected all data sets, the clients invoke the server method “wt_data”, passing the collected data sets to the server.

As shown in Figure 7, the “wt_data” server method passes the collected data sets to the server engineering application, which then calculates the optimum settings for each wind turbine. After the calculations are done, the server engineering application invokes the client method “wt_adjust” on every client, passing the optimum settings for adjusting the respective wind turbine. Thus, the optimum settings are transmitted to the server. Finally, the “wt_adjust”-method passes the optimum settings to the wind turbine, which adopts the optimum settings to adjust the wind turbine actuators.

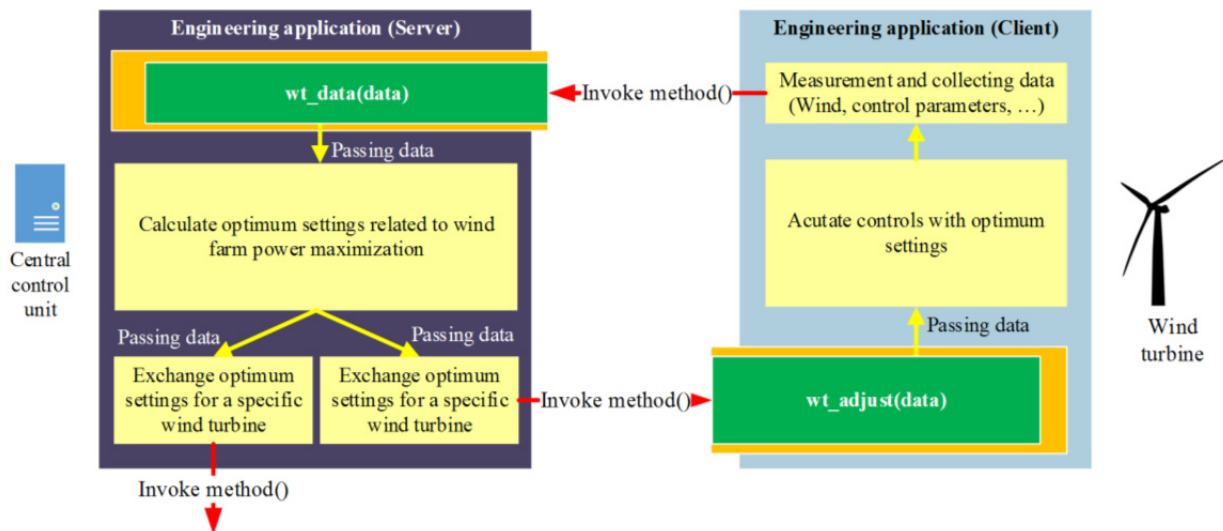


Figure 7: Closed control circuit enabling wind farm optimization

The above described framework has been implemented into a prototype application simulating distributed wind farm control. The prototype application has been written in the programming language C#. As a result, the program is executable on different computer systems and operating systems, entailing an easy integration into existing systems, such as existing wind turbine control systems. Performance measurements have been conducted on the prototype application to validate the reliability and the efficiency of the data exchange. The test environment defined for the performance measurement is shown in Figure 7, measuring the message response times from client to server and back to the client. The time difference, also called latency, is an acknowledged performance indicator used to compare different system variations. Table 2 presents the performance measurement results for different system variations.

		Client		
		Desktop PC, Windows 7	Desktop PC, Linux Ubuntu 14.10	Raspberry Pi 1, Debian Raspbian
Server	Desktop PC, Windows 7	2 ms	3 ms	20 ms
	Desktop PC, Linux Ubuntu 14.10	270 ms	70 ms	90 ms
	Raspberry Pi 1, Debian Raspbian	730 ms	520 ms	550 ms

Table 2: Performance measurement results

Summarizing the performance measurement results, it can be concluded that the proposed framework is usable for reliable and efficient data exchange supporting distributed computing in engineering applications, specifically for decentralized wind farm control as simulated herein. However, the different response times on desktop PCs running Linux as server are unexpected and may open a field for further research.

4 SUMMARY AND CONCLUSIONS

This paper has presented a generic framework for reliable and efficient data exchange in engineering applications. Principles of existing middleware, well-established in the field of web applications, have been adopted to distributed engineering applications. Specifically, selection criteria for reliable and efficient data exchange in engineering applications have been defined and matched with existing middleware. Based on the selection criteria, SignalR has been examined in detail for a prototype implementation simulating distributed wind farm control. As a result, the prototype implementation has shown that SignalR is universally applicable to different engineering systems as a reliable and efficient middleware for data exchange. Performance measurements have demonstrated that the performance strongly depends on the roles of the subsystems (e.g. server or client) as well as on the computer systems and operating systems used (e.g. Windows and the Microsoft .NET Framework or Linux and the Mono .NET Framework).

5 ACKNOWLEDGEMENTS

The authors would like to gratefully acknowledge the generous support offered by Professor Stefan Breide and Professor Jürgen Willms (South Westphalia University of Applied Sciences, Germany).

REFERENCES

- [1] K. Smarsly, K. Lehner and D. Hartmann, “Structural Health Monitoring based on Artificial Intelligence Techniques,” in *Proceedings of the International Workshop on Computing in Civil Engineering*, Pittsburgh, PA, USA, 2007.
- [2] K. Smarsly, K. H. Law and M. König, “Autonomous Structural Condition Monitoring based on Dynamic Code Migration and Cooperative Information Processing in Wireless Sensor Networks,” in *Proceedings of the 8th International Workshop on Structural Health Monitoring 2011*, Stanford, CA, USA, 2011.
- [3] M. Qusay and E. Curry, *Middleware for Communications*, New Jersey, USA: John Wiley & Sons, Ltd, 2004.
- [4] K. H. Law, K. Smarsly and Y. Wang, “Sensor Data Management Technologies for Infrastructure Asset Management,” in *Sensor Technologies for Civil Infrastructures*, Sawston, UK, Woodhead Publishing, Ltd., 2014, pp. 3-32.
- [5] J. S. Lang and J. R. Irving, “Creating a Prototype Web Application for Spacecraft Real-Time Data Visualization on Mobile Devices,” in *SpaceOps 2014 International Conference on Space Operations*, Pasadena, CA, USA, 2014.
- [6] J. Park, S. Kwon and K. H. Law, “Wind Farm Power Maximization Based On A Cooperative Static Game Approach,” in *Proceedings of the SPIE Smart Structures/NDE Conference*, San Diego, CA, USA, 2013.
- [7] J. Park and K. H. Law, “A Bayesian optimization approach for wind farm power maximization,” in *Proceedings of the SPIE Smart Structures/NDE Conference*, San Diego, CA, USA, 2015.
- [8] G. A. Valdez, “SignalR: Building real time web applications,” Microsoft, 17 12 2012. [Online]. Available: <http://blogs.msdn.com/b/webdev/archive/2012/12/17/signalr-building-real-time-web-applications.aspx>. [Accessed January 9, 2015].